Novel Growth Factor Delivery Systems from Self-Assembling Peptide (SAP) Hydrogels

Kiara Anaya Fay Bruggeman

November 2016

A thesis submitted for the degree of Doctor of Philosophy

of The Australian National University.

The research described in this thesis is my own original work, except where otherwise acknowledged.

Kiara Bruggeman

04 November 2016

For my dad, who taught me to think about how things work,
and for my mom, who taught me to change them

Acknowledgements

The work described in Chapters 4 and 7 was performed primarily by Alexandra Rodriguez (ANU) and the team at the Florey Neuroscience Institute under Dr. Clare Parish, including Ting Wang, Jessica Kauhausen, and Rebecca Sheean. My primary contribution to this work was material characterisation and synthesis of the PDL-xyloglucan material used in for Chapter 7. Similarly, in section 5.4, biological testing was performed as above, with my contribution being release profile experimental design and analysis. Biological testing discussed in section 5.3 was performed by Rui Li working under Dr. Richard Williams at Deakin university, and my contribution to this section was synthesising fucoidan-gold nanoparticle complexes and using them for molecular interaction analysis. The work described in Chapters 6, 8, and 9 was primarily performed by me. In Chapter 8 the scanning electron microscopy was performed partially by Francesca Maclean (ANU) and the cell culture and MTT assays were performed by Yi Wang (ANU). In Chapter 9, the lysine coated nanoparticles used were prepared by Tina Zhang (ANU).

K. F. Bruggeman was supported by a Natural Sciences and Engineering Research Council of Canada (NSERC) Postgraduate Scholarship Doctoral (PGS D) award. D. R. Nisbet was supported by a NHMRC Career Development Fellowship (APP1050684). R. J. Williams was supported via an Alfred Deakin Research Fellowship. C. L. Parish was supported by a Senior Medical Research Fellowship provided by the Viertel Charitable Foundation. This research was supported by funding from the National Health and Medical Research Council, Australia and an Australian Research Council Discovery Project (DP130103131). Access to the facilities of the Centre for Advanced Microscopy (CAM) with funding through the Australian Microscopy and Microanalysis Research Facility (AMMRF) is gratefully acknowledged. The Florey Institute of Neuroscience and Mental Health acknowledges the support from the

Victorian Government's Operational Infrastructure Support Grant. We wish to thank Dr Thomas Gengenbach and the CSIRO for conducting the XPS analysis. Thank you to Andy Rodda with nanoscope images for 3D illustrations of material interactions.

I would like to thank my three supervisors for all of their help and support. You've all worked hard both with me and behind the scenes to make sure my PhD was a success. Dave, you've always supported my research even more than I did myself, and were always eager to hear my latest updates. I'm glad to have had such an enthusiastic supervisor pushing me further and making me feel that my work really matters. Rich and Clare, you haven't let the distance stop you from being great supervisors. Rich, you've provided a backbone of understanding from which for me to draw, and Clare, I'll never forget you showing me live brain surgery. Your comments and contributions have helped me to become a better writer, a better researcher, and hopefully soon even a doctor. Thank you all for turning a lazy bum into a productive researcher, and thank you for your patience during the transition.

Of course thank you to everyone in the LΛB group for their constant support. Thank you for help in the lab, for reviewing my papers, and for listening to who knows how many presentations about release profiles and still being interested. And thank you to admin team in the research school of engineering for making sure all my exciting travels could happen and all my chemicals got to the lab.

To the original LΛB girls, Francesca and Owlex, it has been such an amazing journey with you. It's because of you that this degree really is of philosophy. I've learned so much more than biomaterials and I'm happy to have shared that journey with you. I probably won't remember which growth factors do what a few years from now, but I will remember you. I'll remember our deep and meaningful conversations, our battles against the science gods and the LΛB unicorns, and I'll remember the amazing people beside me throughout my PhD. Owlex, you are so genuine and caring, and you make any group better for your presence. Francesca, you are intimidatingly thorough and you are always the high bar in my mind of

how well something could be done. You are both amazing people, and you've made me into a better person too.

To Ben, my chef, chauffeur, dog sitter, pillow, and entertainment system, thanks for everything. Thanks for fancy cocktails and pizza on the couch. Thanks for letting me blather at you and thanks for the hugs. Mostly, thanks for making my worries not seem so bad just by being around and thanks for making me smile.

To all my friends for making this PhD experience a fun one. Thank you for the nights out, the afternoons at the bar, and the sunny BBQs. I cannot thank you all enough. Thanks to my housemates the Ipimians, Lachlan and Aley (and formerly Owlex), who ensure I can always go home to a happy place. Special thanks to Kate, for 'bearing' (grrr!) with me throughout nano. This PhD wouldn't have been possible without you (because an undergraduate degree is a prerequisite for the program). I've learned so much from you and admire you in so many ways. Special thanks to Megan, from Stargate marathons to emails from across the globe for over a decade now you've always been there for me to soothe my woes and share in my joys. And special thanks to Brendan, you are not, in fact, the wind beneath my wings, but you are a great drinking buddy and you always make me feel a little better about the fact that if I am going mad at least I'm not the only one.

They say the pen is mightier than the sword, but what kind of scientist would I be if I didn't test that? Thanks to all my friends in the Ancient Arts Fellowship for your unwavering support, even after I bashed your heads repeatedly with a sword. You've always been ready to knock some sense into me. I have to say that the sword, the axe, and the spear are all pretty mighty, though the mightiest of all are the people wielding them.

To all my sistas at FitSistas, you've had such a positive impact on my life in such a short time. You've helped me punch out my frustrations, climb to new and contorted heights, and you've even instilled in me the value of a healthy breakfast. You've provided balance in a hectic PhD life. You make hard work enjoyable. I never thought I'd get into exercise and

I've never been happier to be proven wrong. Thank you for pushing me further, thank you for keeping me going, and thank you for always having a smile—even at 6:30 in the morning.

To my family. You've made me who I am and you've put up with who I am. Father unit, "strong like fencepost, smart like… nuclear engineer," you are solid and persistent. When I had to stick it out those long nights in the lab, that was the element of you in me. When I had to do things the right way instead of the easy way, that was you. And when I had to do things again because they didn't work the first time, that was you. And they did work that time, or the next, because hard work does pay off. Mother unit, you were there in my head when I thought up new ideas that hadn't been tried yet. When the results came back exactly the opposite of what was expected, it was the element of you in me that found new ways of looking at the information to find benefit and novelty. And when I covered my desk with toys and unicorns that was you too, because what's life without whimsy and what's a workplace without some balance. Because of you both I made it through this PhD, and I did it with a smile. Alas, there is one more to consider, brother unit, who just couldn't wait his turn to finish. Thank you for your long distance help with statistics, thanks for generally being not just a brother but a friend, and thanks for bringing the wonderful Iryna-unit into the family.

And finally, to Eunoia, always there for me with a smile and a cuddle: woof woof bark bark.

Abstract

Growth factors are important signalling molecules in regenerative medicine and tissue engineering, but their inherent instability, lasting only minute to hours *in vivo*, presents an obstacle to sustained and controlled delivery. This is particularly difficult to achieve in the brain, where the blood brain barrier (BBB) prevents systemic delivery. For this reason, much research is currently directed at incorporating growth factors into supportive tissue engineering materials that mimic the natural extracellular matrix (ECM). In this case temporally controlled and sequential delivery must come from selectively delaying the release of some growth factors from the material. Here, we aim to develop novel growth factor delivery systems to provide temporally controlled growth factor delivery from self-assembling peptide (SAP) hydrogel materials specifically.

We use minimalist and tissue-specific Fmoc-SAP hydrogels, a novel class of material designed around biologically recognisable peptide sequences, engineered to self-assemble at physiological conditions into supportive nanofibres. We demonstrate the biocompatibility of three distinct sequences *in vivo* with cell grafts into an intact brain, as well as the tissue-specificity of the materials, with the brain protein laminin derived SAPs showing superior performance. We also demonstrate their ability to improve cell graft treatment efficacy in an ischemic brain injury in rats, showing improved sensorimotor recovery, increased neuronal differentiation, and reduced cortical atrophy compared to the unsupported cell graft treatment.

We demonstrate that these materials stabilise growth factors to provide sustained delivery, with release detected out to 6 weeks. Sustained delivery of growth factors is a common goal in growth factor delivery, and here we go beyond that by providing novel systems for temporally controlled delivery, allowing the sequential delivery of multiple growth factors

required to achieve their full therapeutic potential. We have successfully demonstrated systems to provide a short delay of 4 hours, a long delay of 6 days, and stimuli-responsive control of the delivery profiles. Covalent attachment of the polysaccharide chitosan to the growth factor increased physical associations with the SAP nanofibres, delaying its release by 4 hours. Using emulsion electrospinning to create polymer nanofibres loaded with growth factor, we then cut short fibres to mix into the SAP hydrogel. The polymer provided an additional barrier to diffusion, delaying the release from the hydrogel by 6 days. Covalent attachment of growth factor to UV-sensitive nanoparticles allowed for counter-intuitive control over growth factor delivery, with UV exposure reducing the growth factor released. We were also able to use this system to tune the shape of the temporal release profile to provide a constant dose delivery with no initial burst. These novel systems demonstrate an improved level of control of growth factor delivery without sacrificing the tissue engineering material properties, and represent a significant contribution to the field of tissue engineering.

List of Publications

A. Rodriguez, T. Wang, **K. Bruggeman**, C. Horgan, R. Li, R. Williams, C. Parish, D. Nisbet, "*in vivo* assessment of grafted cortical neural progenitor cells and host response to functionalised self-assembling peptide hydrogels and the implications for tissue repair", *Journal of Materials Chemistry B*, 2014, vol. 2, pp. 7771-7778

Rui Li, Sivapriya Pavuluri, **Kiara Bruggeman**, Benjamin M. Long, Andrew J. Parnell, Anne Martel, Steven R. Parnell, Frederick M. Pfeffer, Andrew J.C. Dennison, Kevin R. Nicholas, Colin J. Barrow, David R. Nisbet, Richard J. Williams, "Coassembled nanostructured bioscaffold reduces the expression of proinflammatory cytokines to induce apoptosis in epithelial cancer cells", *Nanomedicine: Nanotechnology, Biology and Medicine*, 2016, vol. 12, pp. 1397-1407

Alexandra L. Rodriguez, Ting-Yi Wang, **Kiara F. Bruggeman**, Rui Li, Richard J. Williams, Clare L. Parish, David R. Nisbet, "Tailoring minimalist self-assembling peptides for localized viral vector gene delivery", *Nano Research*, 2016, vol. 9, pp. 674-684

Kiara F Bruggeman, Alexandra L Rodriguez, Clare L Parish, Richard J Williams, David R Nisbet, "Temporally controlled release of multiple growth factors from a self-assembling peptide hydrogel", *Nanotechnology*, 2016, vol. 27

Ting-Yi Wang*, **Kiara F Bruggeman* (co first author)**, Jessica A Kauhausen, Alexandra L Rodriguez, David R Nisbet, Clare L Parish, "Functionalized composite scaffolds improve the engraftment of transplanted dopaminergic progenitors in a mouse model of Parkinson's disease", Biomaterials, 2016, vol. 74, pp. 89-98

Ting-Yi Wang, **Kiara AF Bruggeman**, Rebecca K Sheean, Bradley J Turner, David R Nisbet, Clare L Parish, "Characterization of the Stability and Bio-functionality of Tethered

Proteins on Bioengineered Scaffolds IMPLICATIONS FOR STEM CELL BIOLOGY AND TISSUE REPAIR", *Journal of Biological Chemistry*, 2014, vol. 289, pp. 15044-15051

Conor C Horgan, Alexandra L Rodriguez, Rui Li, **Kiara F Bruggeman**, Nicole Stupka, Jared K Raynes, Li Day, John W White, Richard J Williams, David R Nisbet, "Characterisation of minimalist co-assembled fluorenylmethyloxycarbonyl self-assembling peptide systems for presentation of multiple bioactive peptides", *Acta Biomaterialia*, 2016, vol. 38, pp. 11-22

Table of Contents

List of Figures

NOMENCLATURE

1D	1-dimensional
2D	2-dimensional
3D	3-dimensional
APF	Australian Phenomics Facility
ATCC	American Type Culture Collection
BBB	blood brain barrier
BDNF	brain derived neurotrophic factor
BET	Brunauer-Emmett-Teller
bFGF	basic fibroblast growth factor
bGDNF	blended glial cell-line derived neurotrophic factor
BSA	bovine serum albumin
CD	circular dichroism
CE	coefficient of error
$CHCl_3$	chloroform
CNS	central nervous system
CNTF	ciliary neurotrophic factor
CO_2	carbon dioxide

CRT	cell replacement therapy
CSIRO	Commonwealth Scientific and Industrial Research Organisation
CV	coefficient of variance
D	aspartic acid
DA	dopamine/dopaminergic
DAPI	4',6-diamidino-2-phenylindole
DCM	dichloromethane
DDIKVAV	aspartic acid-aspartci acid-isoleucine-lysine-valine-alanine-valine
DDIKVAVK	aspartic acid-aspartci acid-isoleucine-lysine-valine-alanine-valine-lysine
DI H_2O	deionised water
DIKVAV	aspartic acid – isoleucine – lysine – valine – alanine – valine
DIPEA	N,N-diisopropylethylamide
DIV	days *in vitro*
DMA	dimethylaminoethyl methacrylate
DMEM	Dulbecco's Modified Eagle Medium
DMF	dimethylformamide
DTAB	dodeoyltrimethyl-ammonium bromide
DYIGSRF	aspartic acid-tyrosine-isoleucine-glycine-serine-arginine-phenylalanine
E	embryonic day

ECM	extracellular matrix
ED	ethylenediamine
EDAC	N-(3-dimethylaminopropyl)-N'-ethylcarbodiimide hydrochloride
EGF	epidermal growth factor
ELISA	enzyme linked immunosorbent assay
EPO	erythroprotein
ET1	endothelin-1
FBS	foetal bovine serum
Fe_3O_4	iron (II, III) oxide
FGF	fibroblast growth factor
FGFb	basic fibroblast growth factor
FITC	fluorescein isothiocyanate
Fmoc	fluorenylmethyloxycarbonyl
FOV	field(s) of view
FRGDF	phenylalanine-arginine-glycine-aspartic acid-phenylalanine
FTIR	Fourier transform infrared
G'	storage modulus
G"	loss modulus
GDNF	glial cell-line derived neurotrophic factor

GFAP	glial fibrillary acidic protein
GFP	green fluorescent protein
GNP	gold nanoparticle
GRDGS	glycine-arginine-aspartic acid-serine
HAMC	hyaluronan methylcellulose
HBSS	Hank's balanced salt solution
HBTU	O-Benzotriazole-N,N,N',N'-tetramethyl-uronium-hexafluoro-phosphat
HCl	hydrochloric acid
hESC	human embryonic stem cells
hMFC	human mammary fibroblast cell
HOBt	hydroxybenzotriazole
iBDNF	immobilised brain derived neurotrohpic factor
ICV	intracerebroventricular
IFN-γ	interferon-γ
iGDNF	immobilised glial cell-line derived neurotrophic factor
IKVAV	isoleucine-lysine-valine-alanine-valine
IL	interleukin
IL-10	interleukin 10
IPA	isopropanol

K	lysine
LPS	lipopolysaccharide
MAC	methacrylamide chitosan
mGDNF	emulsion glial cell-line derived neurotrophic factor
MMP	matrix metalloproteinase
MSC	mesenchymal stem cell
MTT	3-(4,5-dimethylthiazol-2-yl)-2,5-diphenyltetrazolium bro
MWCO	molecular weight cut-off
Na_3VO_4	sodium orthovanadate
NaCl	sodium chloride
NaF	sodium fluoride
NaOH	sodium hydroxide
NBM	neurobasal media
NGF	nerve growth factor
NH_3^+	amine
NHS	N-hydroxysuccinimide
NP	nanoparticle
NSC	neural stem cell
PBA	phenylboronic acid

PBS	phosphate buffered saline
PBST	phosphate buffered saline with Tween20
PCL	poly-ε-caprolactone or polycaprolactone
PCLEEP	poly-ε-caprolactone ethyl ethylene phosphate
PDGF	platelet derived growth factor
PDL	poly-D-lysine
PEG4SH	poly(ethylene glycol)-tetrathiol
PEO	Poly(ethylene oxide)
PFA	paraformaldehyde
PLA	polylactic acid
PLGA	poly(lactide-co-glycolide)
PLLA	poly-L-lactic acid
PNIPAAm	poly(N-isopropylacrylamide)
PSA	polysebacic acid
PSC	pluripotent stem cells
RGC	retinal ganglion cell
RGD	arginine-glycine-aspartate
SAP	self-assembling peptide
SD	standard deviation

SDS	sodium dodecylsulfate
SEM	scanning electron microscopy
SEM	standard error of the mean
SF	short fibres
sGDNF	soluble glial cell-line derived neurotrophic factor
SHH	sonic hedgehog
SMCC	4-(N-Maleimidomethyl)cyclohexane-1-carboxylic acid 3-sulfo-N-hydroxysuccinimide ester sodium salt
SPPS	solid phase peptide synthesis
TBS	tris buffered saline
TBST	tris buffered saline with Tween20
TEM	transmission electron microscopy
TES	triethylsilane
TFA	trifluoroacetic acid
TGF-β1	transforming growth factor beta-1
TH	tyrosine hydroxylase
TiO_2	titanium dioxide
TNF	tissue necrosis factor
tris	tris(hydroxymethyl)aminomethane

UF	unaryl formate
UV	ultraviolet
VEGF	vascular endothelial growth factor
VM	ventral midbrain
XPS	x-ray photochemical spectroscopy
xylo	xyloglucan
YIGSR	tyrosine-isoleucine-glycine-serine-arginine

Chapter One

Introduction

1.1 Background

Regenerative medicine, or tissue engineering, relies on the formation of new tissue from exogenous or endogenous cells. To encourage this new growth within damaged tissue, tissue engineering scaffold materials are used to support the cells and provide physical, chemical, and biological cues to guide cell growth and differentiation. These cues are designed to mimic the extracellular matrix (ECM) environment of healthy tissue, which provides support and guidance to cells in healthy tissue.

1.1.1 The Extracellular Matrix (ECM)

The extracellular matrix is a complex aqueous environment surrounding and connecting cells. It is composed of water, proteins, and polysaccharides and structurally speaking the two major components are cellularly secreted fibrous proteins and proteoglycan hydrogels.[1] The ECM interacts dynamically with cells, with each affecting the other.[1] As such, the exact nature of the ECM is different in different tissues, and reciprocally the tissue specific properties of the ECM affect cell behaviour. When using tissue engineering materials as a synthetic ECM, tuning these properties can be used to can direct cell fate. Stiffness is an excellent example of the tissue-specificity of the ECM and of how ECM properties can direct

cell fate. It is obvious that different tissue types have different stiffnesses, with bone tissue, for example, being much stiffer/harder than brain tissue, which is comparatively soft. Naïve mesenchymal stem cells (MSCs) grown on similar materials varying only in stiffness were effectively directed into neurogenic, myogenic, and osteogenic cell types.[2] Similarly cells grown in 3D environments compared to traditional 2D culture plates show more *in vivo* like behaviour,[3] with the specific morphology/topography capable of improving or directing cell growth, for instance with parallel aligned nanofibres to promote neurite extension via contact guidance.[4] And of course, the ECM also provides biological signals specific to the individual tissue and to regulate processes required for morphogenesis or homeostasis.[1] Early in this thesis the effect on cell fate of distinct biological epitopes from different tissue specific proteins is investigated, while the goal of this thesis is to engineer methods for controlling the delivery of growth factors, which are used within the ECM to allow intercellular communication, initiating signal transduction and regulating gene transcription.[1]

1.1.2 Tissue Engineering Materials

There are many types of tissue engineering materials currently being explored and developed, all with pros and cons. Natural materials can provide more biological cues and mimicry, while synthetic materials are more easily controlled and customised. In all cases mimicking the nature of the ECM is desired, and as such nanofibrous materials and hydrogels (mimicking the two major structural components of the ECM) are very common. Electrospinning is a popular approach for the development of nanofibrous materials due to its simplicity, low cost, and versatility.[5] The method produces a sheet of overlapping nanofibres, providing a 3D microenvironment for cells despite macroscopically appearing as a 2D sheet, and are therefore well suited for bandaging and wrapping applications. Hydrogels provide an aqueous environment analogous to that of the ECM and their flexible 3D structure makes them suited for implantation in 3D voids or injury sites. Many hydrogel

materials also undergo shear-thinning,[6] meaning that they can flow readily through a needle and reform in situ to perfectly fit a void and fully interface with surrounding tissue.

The materials used throughout this thesis, self-assembling peptide (SAP) hydrogels, are a semi-synthetic material presenting nanofibrous structures within a fluid hydrogel environment. Most hydrogel materials are formed from an interconnected network of hydrated molecular chains. In SAP hydrogels, however, the network forms between comparatively large supramolecular assemblies rather than individual molecules, meaning that the interconnecting fibres exist on a biologically structurally relevant scale (~10 nm diameter).[7-9] The material provides the nanofibre morphology, while also providing an aqueous hydrogel environment with shear-thinning capability to allow it to fill an irregular 3D void or injury site. Specifically, SAP materials designed around biologically relevant peptide sequences are used here to provide the biomimicry of natural materials. The specific peptide composition makes the material inherently biocompatible, with biocompatible degradation by-products.[8] Meanwhile, the minimalist bottom-up fabrication of the materials, consisting of a specific peptide molecule synthesised from individual amino acids, makes their material composition and properties controllable like synthetic materials.

1.1.3 Growth Factors in Regenerative Medicine

Growth factors are natural proteins and important signalling molecules in regenerative medicine. They exist in the ECM, either bound to other ECM proteins or soluble within the aqueous environment, to bind to receptors on the cell surface to initiate biological processes.[10] In regenerative medicine they encourage growth of new tissues and specific cell types. Unlike the tissue engineering materials, which provide constant support, growth factors can be used to encourage different activities at different stages of regeneration. For example, for angiogenesis, first vascular endothelial growth factor (VEGF), fibroblast growth factor (FGF), and angiopoietin-2 can be used to provide disrupt pre-existing blood vessels and induce migration to form new ones, then angiopoietin-1 and platelet derived growth

factor BB (PDGF-BB) can be used to stabilise newly formed blood vessels.[11] Biological processes require growth factors not just in a specific order, but with specific timing as well. For example, demyelination involves many growth factors with different temporal presentation profiles in the cortex, including initial presentation lasting 2 weeks for glial cell line derived neurotrophic factor (GDNF), initial and sustained presentation of FGF-2, and delayed presentation starting after 1 week for transforming growth factor beta-1 (TGF-β1).[12] However, growth factors are inherently short-lived, and *in vivo* enzymatic degradation results in very short growth factor half-lives, as low as 3 min for basic fibroblast growth factor (bFGF)[13] and 45 min for nerve growth factor (NGF).[14]

1.1.4 Drug (including Growth Factor) Delivery in the Brain

Neurotrophic growth factors have demonstrated great potential for neural tissue regeneration, where these is limited capacity for healing, in both promoting regeneration and delaying disease progression.[15,16] Brain-derived neurotrophic factor (BDNF),[17] nerve growth factor (NGF),[18] and GDNF[19] have all been used *in vivo* to support cells and slow the progression of neurodegenerative disorders. The use of growth factors can also prevent secondary degeneration after injury or stroke by protecting the surrounding parenchyma.[15] However, growth factor delivery to brain tissue is particularly challenging.

Systemic drug delivery to the brain is hampered by the blood brain barrier (BBB), a selective membrane that prohibits most drugs in the bloodstream from entering the brain based on chemical structure and size.[20] Strategies do exist to overcome this obstacle, such as the use of prodrugs, a modified form of the drug being delivered with chemical properties (i.e.: lipophilicity) at all it to pass through the selective BBB and then undergo reactions into the active form of the drug on the other side.[20] This allows drugs to bypass the chemical specificity of the BBB, but not the size exclusivity. Growth factors are protein molecules and comparatively large (e.g.: 27 kDa for BDNF) relative to standard pharmaceutical drug molecules like the prodrug L-DOPA (0.197 kDa). There are also methods of disrupting the

BBB, such as with pulsed lasers,[21] but this removes all selectivity, preventing the BBB from performing its useful function. In both cases, the delivery occurs from the bloodstream, meaning there is time for growth factor degradation to occur and the chance for off target side effects.[10] Currently direct delivery is achieved with implanted mechanical micro pumps or indwelling cannulas, which are highly invasive.[22] While these methods are not well suited for regenerative medicine applications focusing on natural tissue growth to repair, they do all offer a high degree of temporal control, as drugs can be administered sequentially or devices programmed for different delivery patterns. That level of temporal control is highly desirable, and tissue engineering materials will not be able to operate fully independently until they can provide a similar level of control. For this reason, temporally controlled growth factor delivery from tissue engineering materials is a growing research field, with a focus on achieving complex delivery patterns (i.e.: multiple growth factors delivered with distinct delivery profiles from the same material).[22] Current techniques of incorporating drug delivery into tissue engineering materials, examined in detail in Literature Review (Chapter Two) of this thesis, generally rely on modifying the tissue engineering material to control release. This approach limits their ability to deliver multiple independently controlled drugs and potentially detracts from their material function as ECM mimics.

1.2 Thesis Outline

1.2.1 Hypothesis

We hypothesize that SAP hydrogels can be used to provide a greater degree of temporal control of growth factor delivery. This thesis investigates SAP material properties and their interactions with other chemicals to design improved growth factor delivery systems. Specifically, we hypothesise that these systems will be able to provide distinct options for temporally controlling the delivery of growth factors beyond the stabilised and sustained delivery common in the field while maintaining the biomimetic properties of the SAP hydrogels.

1.2.2 Thesis Aims

This thesis describes work investigating SAP materials and strategies to use them to provide temporally controlled delivery of growth factors. The work focuses on applications in brain tissue repair, where growth factor delivery is particularly challenging. The overall aim is to increase the diversity of growth factor delivery/release profiles options from SAP materials, and for this thesis delivery strategies for three distinct modified profiles have been developed, in addition to the sustained delivery achieved from unmodified growth factor mixed with unmodified SAP hydrogel:

Short (Hours) Delay

Growth factor release from the SAP hydrogel is delayed for a short time, several hours, relative to the unmodified growth factor. To achieve this a polysaccharide molecule, chitosan, is covalently attached to the growth factor to create a bulkier growth factor with increased interactions with the SAP fibres causing it to remain in hydrogel longer before diffusing out. This achievement is discussed in full in Chapter Six.

Long (Days) Delay

Growth factor release from the SAP hydrogel is delayed for a long time, several days, relative to the unmodified growth factor. To achieve this the growth factor was mixed into electrospun nanofibres via emulsion electrospinning, and the electrospun scaffold was cut into short loose fibres that were mixed into the SAP hydrogel. The growth factor in the electrospun fibres was extensively delayed due to the time required to first diffuse from the fibres into the SAP hydrogel environment, and only then from the SAP hydrogel into the surrounding environment. This achievement is discussed in full in Chapter Eight.

Stimuli Responsive

The temporal profile of growth factor release from the SAP hydrogel is controlled by external stimulation in a counter-intuitive way. To achieve this the growth factor was

covalently attached to titanium dioxide (TiO_2) nanoparticles via a UV-sensitive coating. The nanoparticle bound growth factor displayed a unique release profile relative to that of free growth factor regardless of UV stimulation, and by controlling UV exposure the release profile was also controlled. The nanoparticles diffused out of the hydrogel irrespective of UV exposure, but the UV exposure affected the amount of growth factor that remained bound to and therefore was release with the nanoparticles. The UV caused the growth factor to leave the nanoparticle and become free to interact with and physically adsorb to the SAP nanofibres, with that adsorption slowing their release. For this reason, UV exposure decreased the growth factor released rather than increasing it, as is the normal approach for photo-triggered drug delivery. This system was also used to tune the shape of the release profile rather than delaying it. The increasing release rate observed from the nanoparticles was adjusted via UV exposure to a constant rate of delivery with no initial burst. This achievement is discussed in full in Chapter Nine.

1.2.3 Thesis Structure

Chapter Two-Chapter Four provide background information. Chapter Two comprises a literature review of common tissue engineering materials and current methods of incorporating growth factor and other drug delivery strategies. In writing this review I was able to identify common themes in delivery strategies as well as the areas currently lacking, specifically achieving temporal control beyond sustained delivery while maintaining material properties of the base tissue engineering material. Chapter Three covers all the methods used for the work discussed through this thesis, and Chapter Four discusses work to which I contributed evaluating the SAP materials for their biocompatibility and efficacy in treatments *in vivo*.

The heart of the novelty and advancement of the field described in this thesis is covered in Chapter Six, Chapter Eight, and Chapter Nine, which cover the research led by me to

develop innovate methods of temporally controlled growth factor delivery from SAP hydrogels, achieving short delay, long delay, and stimuli responsive delivery respectively.

Chapter Five and Chapter Six discuss the work done to achieve temporally controlled growth factor delivery in the form of a short (hours) delay in release from the SAP hydrogel, as well as the unmodified delivery profile obtained from unmodified growth factors diffusing out of an unmodified SAP hydrogel. Chapter Six discusses this achievement itself, while Chapter Five discusses projects in which I was involved that provided the insights to achieve the work done in Chapter Six, investigating physical associations between SAP nanofibres and other, non-growth factor therapeutic agents. Chapter Six also includes a discussion on improved presentation of drug delivery data, focusing on release rates rather than cumulative release, which is done throughout this thesis.

Chapter Seven and Chapter Eight discuss work done to achieve temporally controlled growth factor delivery in the form of a long (days) delay in release from the SAP hydrogel. Chapter Eight discusses this achievement itself, while Chapter Seven discusses projects in which I was involved working on growth factor incorporation into electrospun materials that allowed for a composite material to be developed for the growth factor delivery described in Chapter Eight.

Chapter Nine discusses the work done to achieve stimuli-responsive temporal control of growth factor delivery. This work is fully contained in one chapter.

Finally, Chapter Ten discusses the overall conclusions from the thesis as well as future perspectives for this work and the field. The appendices include supplementary information for Chapter Six (Appendices A), as well as full published works to which I have contributed, including work discussed only briefly in this thesis (Appendices B-E) and additional work combining different sequence SAP hydrogels not discussed in this thesis (Appendix F).

Chapter Two

Literature Review

2.1 Chapter Details

This chapter provides a review of current approaches to drug delivery, and specifically growth factor delivery, from tissue engineering materials. This chapter is also a review article manuscript in preparation.

2.2 Abstract

Tissue engineering scaffolds are designed to mimic physical, chemical, and biological features of the extracellular matrix (ECM), thereby providing a constant static support that is crucial to improved regenerative medicine outcomes. Beyond mechanical and structural support, the next generation of these materials must also consider the dynamic presentation and delivery of drugs or growth factors to guide new and regenerating tissue development. These two aspects have been explored expansively separately, but they must interact synergistically to achieve optimal regeneration. This review explores common tissue engineering materials types, electrospun polymers and hydrogels, and strategies used for incorporating drug delivery systems into these scaffolds.

2.3 Introduction

The goal of tissue engineering for regenerative medicine is to stimulate the growth of new, healthy tissue. Strategies to achieve this include encouraging the activation of host cells for the repair of damaged tissue or tissue replacement with new cells via cell replacement therapy (CRT).[23] In either case, specifically designed tissue engineering materials or scaffolds are used to mimic the natural extracellular matrix (ECM) and provide an intermediate supportive environment. The material degrades away as it is replaced by new, healthy ECM from regenerating tissue.

The ECM is an incredibly complex aqueous environment that connects individual cells within a tissue, both structurally and functionally. Nanofibrous structural proteins are a major component of the ECM,[1] and cell behaviours are heavily influenced by cues from the surrounding microenvironment, provided by the tissue-specific ECM.[24] These cues vary widely, including physical, chemical, and biological properties. For cells to behave as they would in healthy ECM, the synthetic scaffolds must be as mimetic as possible of the desired tissue's ECM.[25]

Much research has been done investigating and optimising one material property at a time to mimic the ECM. For example, extensive work has been done tuning material stiffness[2,26] and the nano-/microscale morphology,[27] and these properties have both been shown to significantly affect cell differentiation and proliferation.[28,29] While tuning an individual biochemical or physical cue can enable study of its effect in isolation and enhance material performance, multiple biomimetic cues often have a synergistic effect, such that the overall benefit is greater than the combined individual benefits.[29,30] This makes it important to include and optimise as many aspects of the ECM as synthetically possible to achieve the greatest therapeutic benefit.

While tissue engineering materials are designed with degradation in mind, this can be over a relatively long timescale (months to years) so in the context of drug delivery the long-term materials can be considered static compared to growth factors and other drugs. They provide a constant, static, environment that is mimetic of the ECM and supportive of new tissue growth and regeneration. Another important factor in directing cell growth and behaviour is the more dynamic presentation of secreted, soluble growth factors into the ECM.[24] Growth factors are protein signalling molecules that have an important role in determining cell fate and behaviour, and they are inherently short-lived[10] in the order of minutes to hours.[31] Different growth factors are needed at different stages of tissue growth/regeneration, and the order and timing of their delivery is important.[11] For example, for angiogenesis, angiopoietin-1 and platelet derived growth factor BB (PDGF-BB) stabilise newly formed blood vessels after vascular endothelial growth factor (VEGF), fibroblast growth factor (FGF), and angiopoietin-2 provide the disruption of pre-existing vessels and migration to form new immature vessels.[11] Furthermore, in neuroscience applications epidermal growth factor (EGF), which increases proliferation of neural stem/progenitor cells (NSPs), is best delivered initially for 7 days, followed by erythroprotein (EPO) to protect and reduce apoptosis in the new cells.[22] In addition to the order of delivery, different growth factors require different durations. The demyelination process, for example, involves many growth factors with different temporal presentation profiles in the cortex, including: initial presentation lasting 2 weeks for glial cell line derived neurotrophic factor (GDNF), initial sustained presentation for FGF-2, and delayed presentation starting after 1 week for transforming growth factor beta-1 (TGF-β1).[12] While designing static ECM mimetic materials focuses on ongoing presentation of biological cues, here a variety of presentation or delivery profiles is required to create the optimal dynamic environment for tissue regeneration.

To provide this dynamic environment, growth factors, and other drugs, are being incorporated into tissue engineer materials. When developing drug delivery strategies, there

are several important issues that need to be considered. Drugs, including growth factors, function best at doses within a therapeutic window; concentrations above this window can be toxic or produce harmful side effects, while lower concentrations can be ineffective.[10,32] This means a design consideration needs to be the control of the timing and rate of the drug delivery, whilst being mindful of its *in situ* properties. In particular, protein growth factors require sustained presentation, yet are unstable in a physiological environment and degrade within minutes to hours.[14,31,33] *in vivo*, enzymatic degradation results in very short growth factor half-lives, as low as 3 min for basic fibroblast growth factor (bFGF)[13] and 45 min for nerve growth factor (NGF).[14] It is also important to consider the delivery or release profile; most commonly a sustained release is desirable[34] but sometimes a burst release is required for immediate response or a pulsatile release is required to mimic natural processes.[32] The delivery site is another major consideration, as drugs can have negative side effects to non-target tissues.[20]

In an effort to control drug dosage, maximise delivery, and reduce cytotoxicity, the targeted delivery of drugs to the site of therapeutic need is an area of intense research focus.[20] Delivery and targeting methods are becoming increasingly specific; for example, in cancer treatment, shielded cytotoxic chemotherapy drugs that are detrimental to the surrounding healthy tissue, can be introduced globally into the blood stream where they undergo localised and selective release only around cancerous cells.[35] Localisation of drug delivery can also be achieved simply by incorporating the drug delivery system into a tissue engineering material, as we are discussing here. The tissue engineering material must be implanted at the specific injury or disease site, providing a base for highly localised drug delivery. This is particularly advantageous for regeneration of tissues shielded from the bloodstream, such as the brain, which is protected from systemic drug delivery by a highly selective membrane called the blood brain barrier (BBB).[20] Sustained and controlled delivery to the brain can be achieved using intracerebroventricular (ICV) infusion or micropumps, however, this is very invasive and causes significant tissue damage as well as the chance of potentially fatal infection so

much research has focused on using tissue engineering scaffolds as growth factor delivery vehicles as well.[22,36]

Tissue engineering materials can be used as a reservoir for sustained and controlled drug delivery as they are minimally invasive (small implants or injections) and their biodegradability means they require no additional surgery for removal. Note that when using a reservoir, temporally controlled delivery must be achieved via controlled delay in release from the reservoir. This review discusses methods of incorporating drugs into tissue engineering materials and efforts to control their delivery/presentation. We will discuss a variety of drug delivery systems, with a particular focus on growth factor delivery. We will explore methods in the two most common classes of tissue engineering materials, electrospun materials and hydrogels, including brief contextual explanations of the fabrication and material properties of these materials themselves. Drug delivery systems will be evaluated based on their applicability with growth factors, ability to provide temporally controlled delivery of multiple distinct drugs, and their effect on the properties of the tissue engineering material.

2.4 Electrospun Materials

Electrospinning produces a scaffold in the form of a mesh of nano- to microscale polymer fibres, either randomly oriented or aligned in parallel.[37] The final material is a sheet that is 3-dimensional (3D) at the micro scale and provides a structural mimic of the fibrous structural proteins abundant in the ECM.[38]

To produce these materials, a high voltage is applied between a collection plate and spinneret (metal needle) from which a polymer solution is slowly dispensed (Figure 2.1). This method is simple and versatile; it can be used with any materials that can be dispersed in the spinning solution enough to pass through the spinneret. The competing forces of surface tension holding the solution in place and electrostatic attraction, pulling the charged solution

towards the collection plate deform the solution droplet at the end of the spinneret into a Taylor cone shape with charge concentrated at the peak.[5] The concentrated charge allows the electrostatic forces to finally overcome the surface tension and a very thin stream of the spinning solution is drawn out towards the collection plate.[5] The spinning solution consists of the final scaffold material, generally a natural or synthetic polymer, dissolved in volatile solvents. The volatility of the solvents is such that they are lost to the atmosphere between the spinneret and collection plate, so that only thin fibres of the scaffold material are collected.[5]

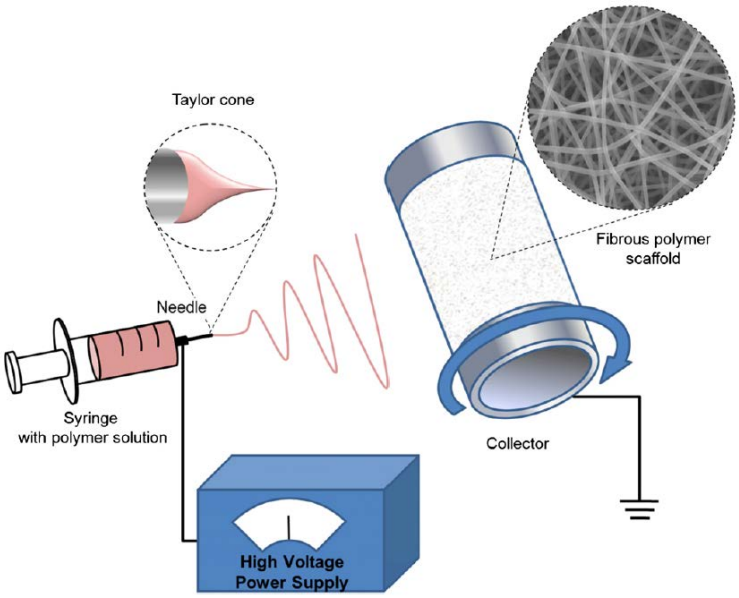

Figure 2.1: Scheme of the electrospinning system with major components.[5] A high voltage is applied between the needle of the spinning solution and the collecting plate, which causes a charge build up at the solution surface and the formation of a Taylor cone. Fibres of the spinning solution are pulled toward the collector to form a fibrous polymer scaffold. (© IOP Publishing. Reproduced with permission. All rights reserved)

The operating parameters (applied voltage, working distance between spinneret and collector, solution flow rate) and solution properties (solvents, scaffold material concentration, additional surfactants or other additives) can be adjusted and optimised to tune fibre diameter, porosity, fibre consistency, and final scaffold thickness.[5] Fibre alignment can be controlled by changing the collector type. Randomly aligned fibres accumulate on a

stationary collection plate, while a rapidly rotating collection drum forces fibre alignment because it collects fibres like winding a spool of thread.[37]

Electrospinning can be used with natural or synthetic scaffold materials and can accommodate many additives, including living cells.[37,39] The tissue response to electrospun nanofibrous scaffolds along with methods of tuning their surface and bulk properties, have been well explored and reviewed.[5,37,38,40-42] On the micro-scale, the nanofibrous structure can be used to promote specific cell growth, such as neurite extension, via contact guidance.[4] The 2D nature of these materials makes them ideal for wrapping or bandaging applications where additional support or a barrier is required from the scaffold. One major drawback of these materials is their inability to fill voids, which limits their ability to fully interface with the healthy tissue surrounding an irregularly shaped disease/injury site, and therefore inhibits its full therapeutic potential.[43]

2.4.1 Emulsion Electrospinning

When creating an electrospun scaffold material, the polymer used to form the scaffold is first dissolved to create the spinning solution. As the polymer initially exists in solution, it is possible, via emulsion electrospinning, to add drugs or other active agents directly into this solution to produce a homogeneously loaded scaffold material.[44] With electrospun materials being suited for bandaging applications, drug loaded electrospun mats have been prepared for wound dressings, such as antibacterial tetracycline hydrochloride loaded poly-ε-caprolactone (PCL)/polylactic acid (PLA) blend electrospun materials.[45] These materials showed superior performance to commercial Comfeel wound dressings, with improved water-uptake capacity, 600% vs. 100% respectively, as well as adding effective antibacterial properties, showing continuous release of tetracycline hydrochloride over 48 hours and effectively killing all E. coli and S. aureus in agar plates.[45]

This approach can be used for protein growth factors, whose large size and instability can be an obstacle for delivery from the blood stream across size-selective membranes such as

the BBB. Human β-nerve growth factor (NGF), in the presence of the stabilising carrier protein bovine serum albumin (BSA), has been successfully electrospun with PCL dissolved in chloroform ($CHCl_3$)[46] and PCL/poly-ε-caprolactone ethyl ethylene phosphate (PCLEEP) blend in dichloromethane (DCM).[47] The materials demonstrated a sustained, continuous release for 28[46] to 90 days[47] with bioactivity unaffected by the harsh solvents confirmed by neurite outgrowth from PC12 cells *in vitro*.[47] Both brain derived neurotrophic factor (BDNF) and ciliary neurotrophic factor (CNTF) have been simultaneously loaded into electrospun silk fibroin/poly(ethylene oxide) (PEO) blend, which showed a greater increase in the axonal growth of rat retinal ganglion cells (RGCs) compared to fibres loaded with just one growth factor or fibres alone.[48]

This method is effective for achieving a single, sustained release profile of growth factors, and while it can be used to deliver multiple growth factors concurrently, it does not offer control over the release or temporal distinction between multiple loaded drugs. To achieve more control of the release properties, more individually customisable methods must be used.

2.4.2 Radially Layered Fibres

Coaxial electrospinning uses concentric spinnerets with distinct spinning solutions in order to produce radially layered fibres.[49] This method can be used to shield a drug loaded core with a degradable or porous outer sheath in order to delay and control the release of the drug.[49] Similar to the wound dressing mats discussed above, biodegradable poly(lactide-co-glycolide) (PLGA) nanofibrous mats have been prepared with tetracycline hydrochloride in the core of each fibre.[49] Optimal mats were produced using a smaller amount of drug in the sheath as well, and these mats provided sustained release for 10 days with a reduction in the initial burst release (defined as the percentage of total release achieved in the first hour) from 62 to 44% compared to blended single-layer fibres.[49]

The coaxial method can also be used to layer different drugs to provide successive release of multiple agents.[50] Han and Steckl developed a model electrospun material with three distinct radial layers to deliver multiple drugs with distinct release profiles (Figure 2.2).[50] Using colour dyes as model drugs the dye in the hygroscopic outer sheath layer displayed a burst release, while the dye in the core showed sustained release for 50 hours as it was slowed by an intermediate hydrophobic layer and the other sheath.[50] This method could be employed for any active agent stable in the electrospinning solution, and can also provide a non-solvent layer for active agents unstable in the volatile electrospinning solution.

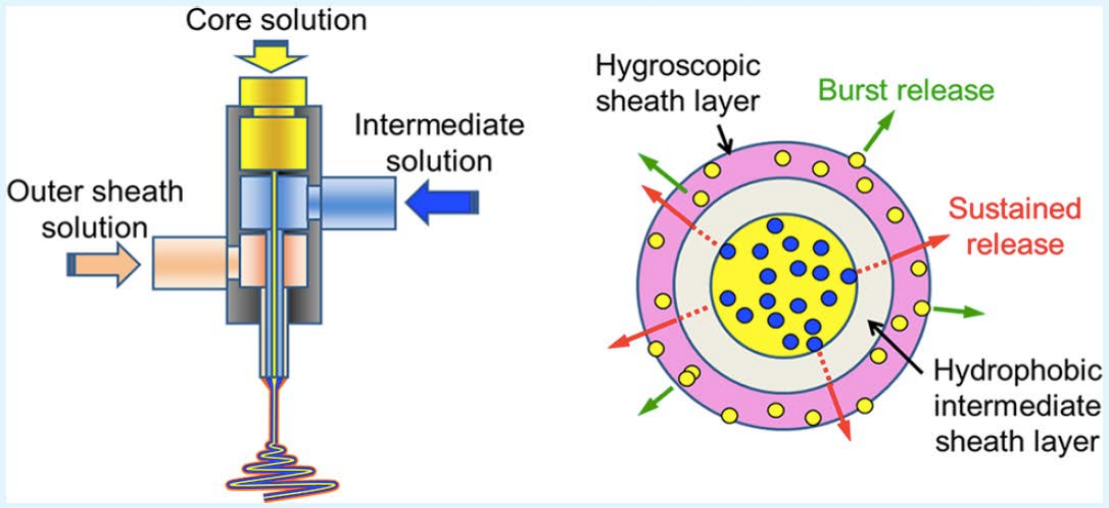

Figure 2.2: Triaxial electrospinning of radially layered fibres.[50] Three concentric needles are used to dispense separate spinning solutions to create fibres with three distinct radial layers. Dye added to the other layer displayed a burst release while the dye in the core displayed a sustained release after travelling through the intermediate sheath layer. (Reprinted with permission from Han, D. & Steckl, A.J. *ACS Appl. Mater. Interfaces*, 5, 8241-8245 (2013). Copyright 2013 American Chemical Society.)

2.4.3 Immobilisation onto Electrospun Materials

Drugs can be immobilised permanently onto an electrospun scaffold by attaching them using strong covalent bonds (preferably formed through bonding of an otherwise inactive site on the drug molecule). Immobilised drugs can be detected by surrounding cells but not consumed; making this approach applicable to mimic the delivery of secreted, extracellularly active intercellular signalling molecules such as some protein growth factors. Growth factors

play an important role in cellular activity, and function as a mechanism for rapid communication between surrounding cells in other parts of the tissue. However, due to this transient signalling role, growth factors naturally degrade rapidly under normal physiological conditions, lasting only minutes to hours when introduced *in vivo* in soluble form.[31] For the growth factor to have prolonged effectiveness a sustained delivery system, such as covalent immobilisation to an electrospun scaffold, is required.

Click chemistry has be used to chemically immobilise therapeutic agents, including cyclodextrins,[51] and bioactive peptide sequences,[52,53] to the surface of electrospun materials. Growth factors can be covalently chemically immobilised through direct reactions with amine or carboxylic acid moieties present in their protein structure.[54] Alternatively, commercially available crosslinking molecules, such as succinimidyl-4-(N-maleimidomethyl) cyclohexane-1-carboxylate (SMCC),[31,36,55] can be used to link two materials by reacting with specific functional groups present on each material. SMCC connects two different molecules between the amine groups of one and the thiol groups of the other, such as by connecting an aminolysed electrospun polymer surface to the thiol group of a free cysteine residue in a protein growth factor.[36] This results in the alteration of one, relatively small chemical moiety on the protein. The immobilised growth factors therefore remain biologically active and their degradation depends on the degradation of the polymer scaffold, allowing them to be presented on the scaffold surface for orders of magnitude longer than soluble growth factors.[31,36,55]

Our group has immobilised GDNF onto electrospun PCL scaffolds using SMCC and have shown that GDNF maintained its biofunctionality for at least 7 days in a neural progenitor cell culture and remained detectable by enzyme linked immunosorbent assay (ELISA) after 120 days of storage in PBS or artificial cerebrospinal fluid.[31] The biofunctionality was confirmed by ongoing ErK phosphorylation in the neural stem line

SN4741 as well as improved viability and number of tyrosine hydroxylase immunoreactive (TH+) cells.[31]

The covalent immobilisation method is not entirely efficient, and some unattached protein remains bound to the scaffold through physical interactions, and can therefore de-absorb over time.[36,55] It is possible that this combination of soluble and immobilised growth factor act synergistically, with the soluble component diffusing from the implanted scaffold to create a concentration gradient, an important aspect of growth factor function,[10] directing nearby cells toward the electrospun material and the immobilised drug. Although unquantified, this could potentially mitigate the lack of void filling capacity of the electrospun scaffolds since the diffused soluble component spreads through the void to interact with the surrounding tissue, potentially encouraging the tissue-material interface to migrate toward the scaffold. Covalent immobilisation strategies are limited however, as they are only relevant to drugs that can be used by cells non-destructively, where only repeated surface recognition but not internalisation is required. This method is also static; it cannot be used to provide a temporally varied drug delivery profile. It can be used to allow materials to present ongoing biochemical cues in addition to the physical cues, either of drugs that are required indefinitely or to increase the biomimetic quality of the scaffold material by immobilising biological components of the ECM. The inherent properties of electrospun materials do put some limitations on their biomimicry, and this is one of the main reasons why hydrogel materials are often more suitable.

2.5 Hydrogel Materials

A cellularly secreted proteoglycan hydrogel is a major component of the ECM, meaning that hydrogels can be intrinsically biomimetic.[1] Hydrogels consist of highly hydrated interconnected chains, connected through physical or chemical crosslinking, forming an aqueous matrix. Chemical crosslinking involves the formation of covalent bonds and is an

irreversible procedure resulting in a strong network that can only be degraded by breaking those bonds, typically via hydrolysis, enzymatic action, or a specific stimulus (such as photo-degradable hydrogels[56]). Physical crosslinking, however, occurs reversibly through the secondary bonds between the chain molecules. As these forces are relatively weak, they allow the hydrogel to undergo shear thinning, where applied shear stress disrupts the physically bound network and breaks the continuous gel material into many small domains (Figure 2.3).[6] These smaller gel domains can easily move past and around one another, so that the bulk material flows with minimal resistance.[6] When the stress is removed the domains interconnect again to recreate the structure allowing the gel to recover its initial stiffness.[6]

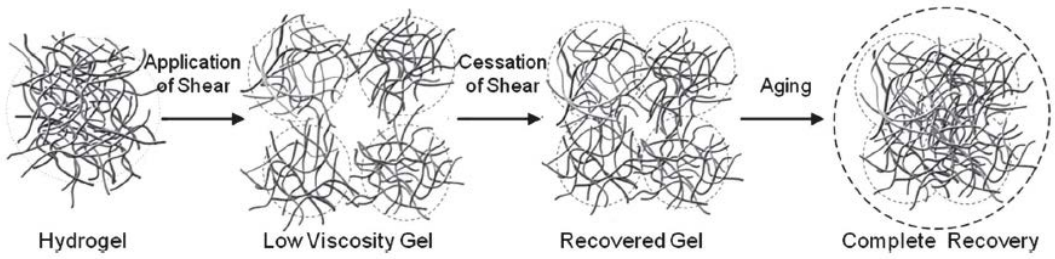

Figure 2.3: Hydrogel shear thinning and recovery.[6] Application of shear stress causes the hydrogel network to break into smaller domains, which flow easily around each other. When the stress is removed, the small domains reintegrate into a larger hydrogel network. (Reproduced with permission from The Royal Society of Chemistry)

This is a very attractive property for tissue engineering applications as the engineered material can be injected directly to the site of therapeutic need via a minimally invasive needle rather than surgically implanted. Shear-thinning also increases their void filling ability, as the thinned hydrogel flows throughout the entire injury site before the domains reassemble and the material returns to its more solid-like gel state to create a perfectly fitted implant.[57] The true ECM is a dynamic environment, constantly changing and undergoing stress,[1] so materials based on reversible and reformable physical interactions can potentially provide a more adaptable and appropriate scaffold.

An important class of physically formed hydrogels for biomedical applications are those that mimic the natural fabrication of the ECM, exploiting the spontaneous self-assembly of bioinspired amphiphilic molecules (such as synthetic polymers, proteins, peptides, polysaccharides, and their derivatives) into higher order structures.[42,57-60] Self-assembly occurs when there is a balance between the intermolecular repulsive and solvating forces, which drive the material towards a homogeneous solution, and attractive forces and insolubility, which drive the material towards precipitation or separation. The intermolecular interactions can include hydrophobic interactions, hydrogen bonds, π-π stacking of aromatic groups, and charge-charge interactions.[57] A stimulus is usually applied to reduce the solvation and promote intermolecular attractions, allowing the molecules to organise into interconnected network structures under thermodynamic or kinetic control. Starting from a state of overpowering repulsive and/or solvating forces is preferable, as this provides a homogeneous distribution of nucleation points throughout the solution. The stimulus must be presented as uniformly as possible to ensure homogeneity, and the rate at which the stimulus is applied must be adjusted to promote ordered structures and avoid uncontrolled aggregation or precipitation.[61] The extent and nature of the stimulus can have an effect on the final material properties. Adjusting pH affects the charge on free amine or carboxylic acid groups present,[57] increasing salt concentration in the aqueous medium shields surface charges and reduces their effect,[57] and hydrophobic interactions are strengthened by increased temperature.[57] The catalytic action of enzymes has also been used to modify these interactions due to the formation/cleavage of bonds. For biological applications it is important that the molecular assembly occurs under physiological conditions (pH 7.4, salt concentration 150 mM, temperature 37 °C) to ensure the desirable hydrogel structure is retained *in vivo*.[62] For more information relating the cellular response to synthetic and natural hydrogels, particularly in the central nervous system, the interested reader is directed to our review.[37]

2.5.1 Direct Addition of Drugs into Hydrogels

The self-organising and shear thinning nature of physical hydrogels makes direct incorporation into the gel material much simpler than with electrospun materials. Soluble additives that interact with the structures can be co-assembled into the material as it forms, or can be mixed into the aqueous component of the hydrogel post assembly by simply applying minimal shear stress to thin the gel temporarily without destroying/disrupting the beneficial structures (e.g.: with a bench top vortex mixer), and then allowing the gel to reform.[63] NGF was mixed into the self-assembling diblock copolypeptide hydrogels $K_{180}L_{20}$ and $E_{180}L_{20}$ and showed ongoing bioactive effect for at least 4 weeks *in vivo* in mice. This study demonstrated prolonged hypertrophy and a larger region of effect compared to NGF injected in a buffer solution.[64] Although the loading is simple, the release profile of drugs and growth factors from hydrogels is dependent on interactions between the two materials. From MAX8 peptide hydrogels for example, positively charged proteins diffuse out while negatively charged proteins adsorb to the hydrogel showing little diffusion.[65] While the electrostatic properties of different growth factors inherently result in different release profiles, so as with electrospun materials controlling the release profile again requires more involved methods. Unmodified diffusion of growth factor from hydrogels can occur very rapidly,[66] so for growth factors in particular, for which rapid degradation means sustained delivery is required, just slowing the diffusion to provide more long-term delivery is an important goal.

2.5.2 Immobilisation of Drugs in Hydrogels

Non-covalent affinity interactions can be used to either permanently or non-permanently immobilise growth factors within a hydrogel. Thesis systems are particularly applicable to growth factors, as many natural growth factors have known binding partners, biological molecules with known affinities for the target growth factor.[54,67] For example, biotin tagged interferon-γ (IFN-γ) and platelet derived growth factor AA (PDGF-AA) have been

immobilised to a streptavidin functionalised methacrylamide chitosan (MAC) hydrogel via the well-known biotin-streptavidin conjugation.[68] These materials showed improved neural regeneration *in vivo* in spinal cord injury in rats, showing increased neuron count relative to treatment with the hydrogel material alone.[68] Similar immobilised IFN-γ in chitosan hydrogel materials were tested with NSCs.[69] When cultured in hydrogels functionalised with either immobilised or soluble IFN-γ, both conditions resulted in a similar improvement in neuronal differentiation compared to medium alone, but the immobilised drug showed fewer semi-committed and immature neurons, indicated by the lower co-presentation of nestin and βIII tubulin.[69] The binding pairs can be used individually, or as one link in a chain. For example, collagen hydrogels have been modified with epidermal growth factor (EGF) covalently attached to a peptide designed to bind to collagen, which was observed to improve proliferation and neuronal differentiation of neural stem cells (NSCs).[70]

Delayed release can be achieved by covalent immobilisation to the hydrogel material of a molecule with a weaker affinity for the drug being released. The drug is not fully immobilised to the scaffold, but held in place by a strong affinity through reversible physical bonds. This has been achieved for heparin-binding drugs by first immobilising heparin within the hydrogel.[71] In this work, a bi-domain peptide was covalently bound to a fibrin matrix through a transglutaminase substrate on the N-terminus, and a heparin-binding domain on the C-terminus was used to electrostatically immobilise heparin to the matrix.[71] The heparin-binding drug, basic fibroblast growth factor (bFGF), was in turn semi-immobilised through its electrostatic interaction with heparin, and its release from the hydrogel was delayed.[71] This approach is widely applicable to heparin binding growth factors, and has also been adapted for some non-heparin-binding factors. NGF is non-heparin binding, but its C-terminus contains several basic residues surrounded by hydrophobic residues, which is similar to a heparin-binding domain.[66] Using a high molar excess of immobilised heparin, the release of NGF was slowed from the fibrin matrix, allowing a continuous release over 15 days

compared to 1 day from fibrin alone and resulting in a 100% improvement in neurite growth compared to fibrin and NGF alone.[66]

This heparin binding domain system is diverse, with 15 binding proteins identified so far from the platelet-derived growth factor (PDGF)/VEGF, FGF, transforming growth factor beta (TGT-β), and neurotrophin families.[72] This variety shows versatility of this controlled release method for delaying the release of individual proteins, but it also highlights a significant drawback of this technique: the release profile cannot be tailored for one drug without affecting the release profile of other loaded heparin-binding drugs. Also, this method is dependent on chemical modification of the hydrogel scaffold itself, which could alter some of the specifically engineered scaffold properties, particularly stiffness, a property that plays a major role in driving cell differentiation.[2,26] This could mean that control of the dynamic environment is attained at the expense of control of the static environment.

Many affinity binding pairs occur naturally, including the commonly explored heparin binding affinity discussed above that can be used with many growth factors. Natural affinity binding pairs can occur in the form of: ECM-integrin, receptor-ligand, protein-protein, and antibody-antigen.[67] These non-covalent linkages are a requirement of the dynamic nature biological processes. New binding partners can be discovered via screening against peptide/protein libraries, or else new partners can be evolved *in vitro* through random mutagenesis or *in silico* using computational models to directly design binding structures.

A similar delivery effect has been achieved with enzyme sensitive linkages. Therapeutic peptide sequences flanked with matrix metalloproteinase (MMP) enzyme degradable sequences were chemically crosslinked to a PEG hydrogel structure, such that host MMP cleaved the bonds holding the therapeutic peptide in place resulting in a sustained delivery.[73] This method has been confirmed *in vivo* in mice with proangiogenic SPARC sequences promoting increased vascularisation.[73] This system is interesting as it allows drug delivery

dependent on local conditions, but being dependent on gel degradation for delivery it again does not fully utilise the potential of the hydrogel material as a biomimetic structural scaffold.

2.5.3 Spatial Control of Multiple Drugs in Hydrogels

Fine 3D spatial control over drug incorporation in hydrogel materials is possible using 2-photon technology to attach molecules.[74,75] In this method lasers are used to precisely determine where in the 3D hydrogel photochemical reactions occur to chemically immobilise therapeutic or binding agents. Immobilisation of a single therapeutic agent, the peptide sequence glycine-arginine-aspartic acid-serine (GRDGS) containing the RGD integrin binding sequence from fibronectin, has been used to spatially guide neurite outgrowth.[76] This method has been adapted to provide independent control over multiple therapeutic agents via protein binding agents.[75] Multiple protein binding agents can be immobilised first, before washing the hydrogel material with the appropriate protein solutions to allow the physical association with the binding agent to hold them in place (Figure 2.4).[75] The nature of this procedure means that all reactive chemistry is performed before any sensitive proteins are introduced into the material.[75] The method is also widely applicable to other proteins, requiring only a common biotin or barstar modification.[75] The number of spatially distinct regions is limited to the number of biotin-streptavadin style binding pairs can be incorporated. Combining this technique with work being done on injectable preformed hydrogel materials with shape memory[77] might lead to fine spatial control of drugs within an injectable hydrogel matching an irregularly shaped injury site. However, this method does not offer advances in the way of temporally controlled delivery.

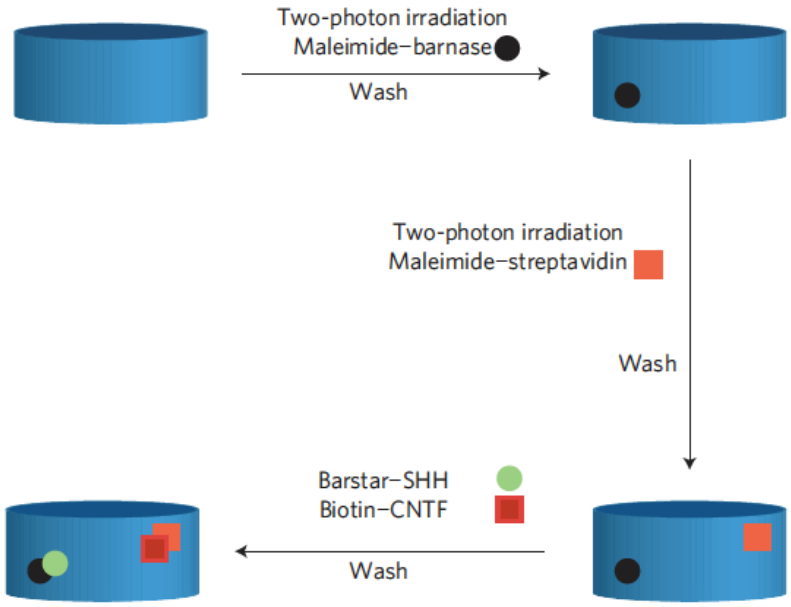

Figure 2.4: Method for the simultaneous immobilisation of (sonic hedgehog) SHH and CNTF.[75] Two-photon irradiation is provided sequentially to chemically bind one half of each binding pair. The entire hydrogel is immersed in the material but fine spatial control of the two-photon irradiation limits the immobilisation reaction. Once all the first halves are bound individually, a final wash off all the binding proteins combined is used to lock them in place only where the relevant binding pair has been immobilised. (Reproduced with permission from Nature Publishing Group)

2.5.4 Bioactive Sequences in Self-Assembling Peptide (SAP) Hydrogels

SAP hydrogels are growing in popularity as tissue engineering materials, they offer some uniquely attractive properties as well as the option to use desired bioactive signals directly as the material structure. SAPs exist in the semi-synthetic middle ground of tissue engineering materials. While all the individual amino acids used are natural materials, the peptide sequences are synthetically manufactured. The stepwise synthesis of the sequence of amino acid residues in the SAP means it is completely controllable, with no variation and high purity. However, because they are made from biocompatible natural materials SAP hydrogels have a very high level of biodegradability and biocompatability.[78]

Physical intermolecular interactions under the right conditions drive self-assembly into supramolecularly organised fibril structures much thicker than the single molecule polymer chains comprising the matrix of traditional hydrogels.[6,57] This fibrillar nature allows SAPs to

occupy a structural middle zone as well, displaying advantageous structural properties of both hydrogels and electrospun materials. As physical hydrogels, SAPs are highly hydrated, completely 3D, undergo shear thinning (so are injectable), and display void-filling behaviour, while also acting similarly to electrospun materials by providing supportive fibrous structures mimetic of the ECM structural proteins.[8]

Commercially available SAPs consisting of long repetitive peptides, such as $RADA_{16}$ and MAX8, are biocompatible, but do not provide the ECM-mimetic biochemical signals that natural protein and polysaccharide gels provide. To address this, these systems are typically functionalised by adding bioactive sequences as pendant groups.[79] However, SAPs can also be formed from short biologically relevant sequences, thereby incorporating a biochemical cue directly into the self-assembled fibril structures.[8,9] Those long sequence peptides are designed specifically to undergo self-assembly, with correspondingly attracted regions to encourage the formation of β-sheets. When the peptide sequence is instead chosen for its biological significance, and too short to naturally fold into sheets, additional self-assembling motifs are used to drive the formation of the nanofibrillar structures. The bioactive peptide sequence can be capped with aromatic groups, such as naphthalene or fluorenylmethyloxycarbonyl chloride (Fmoc). These groups encourage the self-assembly of the supramolecular fibrils though π-π stacking of aromatic groups in addition to the β-sheet formation between the short peptide chains (Figure 2.5).[7,9] Additional aromatic peptide residues can be used to further enhance self-assembly through additional π-π stacking interactions[78] while acidic or basic residues can be added to shift the pH at which the net molecular charges favour self-assembly, ensuring self-assembly at physiological pH.[9]

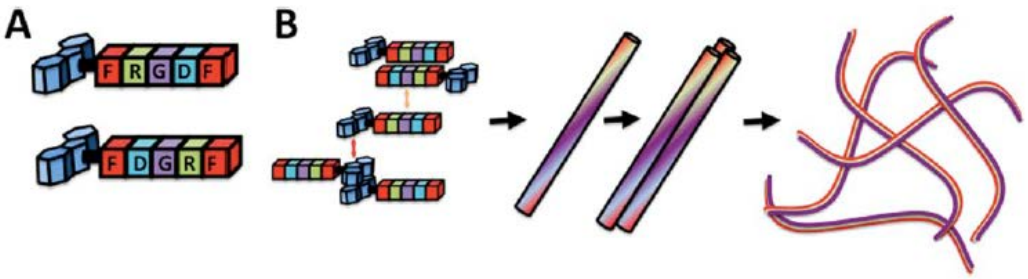

Figure 2.5: Self-assembling peptide fibril formation.[78] A: Fmoc peptide sequences. B: Fmoc groups engage in aromatic π-π stacking with peptide chains in alternating directions. The peptide chains interleave forming β-sheets between lines of stacked Fmoc moieties. The resulting sheets roll into hollow fibrils, which interact most strongly longitudinally, forming bundles of fibrils which then form the nanofibrous hydrogel network. (Reproduced with permission from John Wiley and Sons)

The arginine-glycine-aspartate (RGD) peptide is a bioactive sequence presented by the ubiquitous ECM protein fibronectin that encourages integrin activation and cell attachment. In a short sequence Fmoc-SAP, such as the RGD containing Fmoc-FRGDF, the biological cues (i.e.: the bioactive peptide sequence) are presented at a high density on the surface of the fibrils, and thereby throughout the hydrogel, improving the biological environment of the otherwise structurally biomimetic, but biologically inert material. The effectiveness of this presentation was demonstrated by the 3D culture of human mammary fibroblast cells (hMFCs), where the RGD SAPs showed significantly improved viability over a scaffold that was identical in bulk physical and chemical properties, but displayed a biologically inactive sequence, DGR.[78]

The incorporation of bioactive sequences into the hydrogel structure mimics the static presentation of biological molecules. To provide dynamic control of drug release from a SAP hydrogel, methods like those described above for traditional hydrogels may be used. For example, including enzyme sensitive moieties within long chain SAPs, as well as SAP-drug complexes, results in fibrils that gradually degrade as the chains are broken down, providing a sustained release of the drug.[80] However, when the intrinsic hydrogel matrix plays an active role in the drug release mechanism, it affects the gel properties and the static support

environment over time, especially in this case where the material must degrade to provide controlled drug delivery. Ideal tissue engineering materials must be designed with both drug delivery and material properties in mind. For more information regarding the cellular response to SAP scaffolds, the interested reader is directed to our previous review.[8]

2.5.5 Responsive Hydrogels

As long as stimuli can reach the material, then *in situ* modulation of gel properties is possible, allowing for the engineering of stimuli-responsive hydrogel materials. Hydrogels can be engineered to respond to external stimuli such as changes in temperature, pH, electric fields, light, and enzymes.[81,82] Photodegradable hydrogels offer easy external control, such as poly(ethylene glycol)-tetrathiol (PEG4SH) hydrogels, which can be degraded with only 120 seconds of low intensity UV light exposure (10 mW/cm^2, 365 nm).[82] Here the hydrogel degradation is irreversible, meaning that once the material is degraded to release any loaded drugs it can no longer offer the same structural support.

Perhaps the most promising stimuli-responsive mechanisms for targeted drug delivery are the antigen responsive hydrogels. These can be tailored to respond to stimuli found at the site of therapeutic need; for example, hydrogels that swell in the presence of a specific disease associated antigen can be created by modifying the polymer chains with paired antibodies and antigens (Figure 2.6).[83] In the absence of free antigen, the bound antibodies and antigens interact, creating more crosslinking points in the gel and essentially keeping the matrix very tight. When free antigen is present, some of the antibody-antigen interactions within the hydrogel are disrupted in favour of interactions with the free antigen, which lowers the degree of crosslinking and essentially loosens the gel. This process is reversible[83] and since the degree of crosslinking in a hydrogel is directly linked to its permeability[84] this system can provide pulsatile release of active agents responding to changing free concentrations of the antigen.[83]

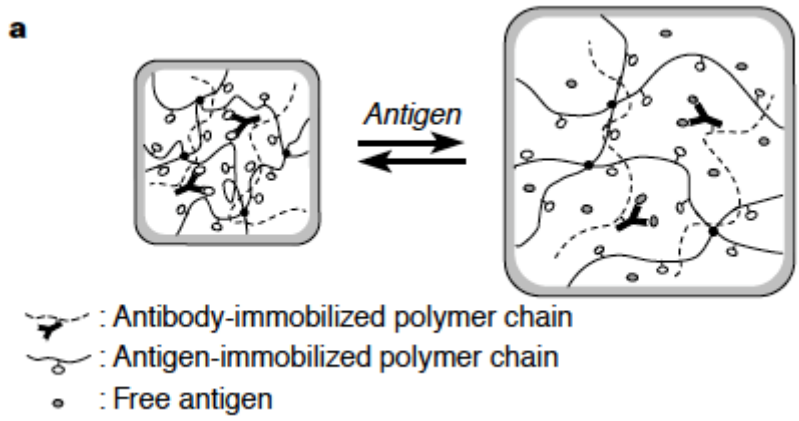

Figure 2.6: Antigen responsive hydrogel.[83] Antibodies and corresponding antigens are bound to the hydrogel chains, and increase the interconnectivity of the hydrogel network when they pair. Free antigen in the surrounding environment reduces the number of bound antibody-antigen pairs and decreases the interconnectivity of the hydrogel. (Reproduced with permission from Nature Publishing Group)

Interestingly, this approach can be used to respond to externally controlled signals, or to automatically react to naturally arising cues. When foreign antigens, such as fluorescein isothiocyanate (FITC),[85] or rabbit IgG,[83] are used as trigger molecules, the release profile can be controlled independently of any ongoing biological processes. These materials are not naturally occurring in the body, so drug release can only be triggered by the controlled introduction (such as via injection) of the foreign antigen. The highly specific nature of antibody interactions means that even very similar antigens will not trigger release[83] so complete and independent control of the release profile is retained. Alternatively, hydrogels can be designed to respond to predefined natural cues and automatically release the appropriate therapeutic agent. This approach also offers a potential way around the issues involved with the large size of protein growth factors, such as bypassing the blood brain barrier. A molecule that can cross the BBB can be selected as the trigger, such that systemic delivery can be used to trigger release of growth factors if not to deliver them.

Glucose responsive hydrogels have been engineered to act as an artificial pancreas to provide automatic pulsatile release of insulin as needed.[86] Several systems have been explored for glucose responsive insulin delivery. Lectin proteins that bind to carbohydrates have been

used in a similar system to the antigen-antibody interactions described above.[87] Other systems incorporate reactive agents into the hydrogel mesh that affect charge changes in the presence of glucose and swell the gel via increased electrostatic repulsion between polymer chains.[86] Glucose oxidase immobilised onto the polymer chains converts glucose to gluconic acid, which can in turn protonate tertiary amines on appropriate hydrogelating polymers, such as dimethylaminoethyl methacrylate (DMA), thereby swelling the hydrogel via electrostatic repulsion between chains.[86] A non-enzymatic system based on phenylboronic acid (PBA) complexes with glucose and other 1,2 or 1,3-cis-diols to form an anionic group.[81,87] The PBA approach is less specific, but offers improved longevity over systems dependant on proteins that degrade over time.[87]

Responsive swelling gels are only applicable for the release of entrapped large molecules, such as proteins, whose transport depends on the hydrogel mesh size and permeability.[85] The approach can be adapted for smaller drugs by covalently attaching the small drug molecule to larger gelling molecules by a cleavable linker.[88] This also adds a second stage to the mediation of the drug release, as linkers can be selected that are susceptible to proteases expressed by disease cells to increase targeting efficiency.[88] A common theme among stimuli-responsive hydrogels is the alteration of gel properties to facilitate release. Even if temporary, this is still undesirable in tissue engineering materials where the hydrogel properties have been optimised to provide optimal static cues to the surrounding cells. Ideal tissue engineering materials must be designed to concurrently provide a static structurally supportive environment and provide controlled drug delivery.

2.6 Independent Drug Delivery Vehicles

A common theme in the dynamic control of drug delivery from tissue engineering materials is to use material degradation or alteration, which inherently requires the static material environment to change. This makes independent control of both the static

environment and drug delivery impossible. A combination of dynamically controlled drug release and static biomimetic tissue engineering materials will be required for optimised regenerative medicine strategies. Combining these two features, without compromise, is the goal, and perhaps the best strategy to achieving this independent control is to focus temporal control mechanisms on the drug-end rather than within material modifications. Modifying the tissue engineering material not only disrupts its (carefully) optimised properties, but also hinders independent control of multiple releases since changes to the scaffold material will affect all incorporated agents. Sophisticated techniques exist to control the targeting and release of drugs introduced systemically, most notably in the form of functionalised nanoparticle delivery vehicles, which can be incorporated directly into tissue engineering materials in the same way as soluble drugs.

2.6.1 Nanoparticles in Tissue Engineering Materials

Drug encapsulation in nanoparticles is a simple shielding procedure that allows for diverse functionalisation. Polymer materials with excellent biocompatibility and biodegradability can be used to create the nanoparticles, which can then be made to incorporate fluorescent or radioactive tags for diagnostic imaging, targeting moieties for location specific delivery, and delayed or stimuli-responsive release mechanisms.[89] Once encapsulated, drugs can be incorporated directly into hydrogels[22] or electrospinning solutions.[90] Encapsulation also provides shielding to protect the drug from interactions with solvents used in electrospinning and harsh chemicals such as acids and bases used to induce gelation, making nanoparticles attractive for delivery of sensitive or reactive drugs.

Using this approach, epidermal growth factor (EGF) and erythropoietin (EPO) have been presented sequentially to stimulate endogenous NSPCs to heal after stroke.[22] EGF encapsulated in polylactic-co-glycolic acid (PLGA) nanoparticles and EPO encapsulated in PLGA and further coated in polysebacic acid (PSA) were incorporated in a hyaluronan methylcellulose (HAMC) hydrogel to provide sequential delayed release.[22] EGF release was

observed from days 4-11, while EPO release was observed from days 11-25.[22] When tested *in vivo* with mice, this functionalised nanoparticle and hydrogel system showed similar results in terms of cell differentiation and proliferation when compared to a standard mechanical pump system used to control drug delivery from implanted reservoirs, demonstrating state of the art drug delivery control from a minimally invasive and biodegradable material.[22] Similarly, nanoparticle loaded growth factors can also be loaded into electrospun materials to provide sequential delivery, with the nanoparticle loaded growth factor being delayed. Wound dressings have been prepared by electrospinning a chitosan/PEO blend loaded with free VEGF, which showed a burst release, and PLGA nanoparticles loaded with PDGF-BB, which showed a sustained ongoing release.[91]

There is a vast array of stimuli responsive nanoparticle drug delivery vehicles[92] and often these can be incorporated into tissue engineering materials to essentially achieve the same stimuli-responsive control of drug delivery discussed above without disrupting material properties. Silica nanoparticles have been modified with photo-sensitive attachment of small molecules drugs and then mixed into a PEG hydrogel to demonstrate photo-triggered drug release from a hydrogel.[93] Nanoparticle systems also offer stimuli responsive behaviour not available otherwise, such as magnetically controlled delivery. Superparamagnetic Fe_3O_4 nanoparticles have been incorporated into a poly(N-isopropylacrylamide) (PNIPAAm) hydrogel, which is reverse temperature responsive, to provide remote triggered drug delivery[94] and pulsatile on-off delivery[95] upon application of an alternating magnetic field. However, in this system the drug was loaded into the hydrogel, and once again the control of delivery depended on altering the material properties of the hydrogel, in this case by using the magnetically responsive nanoparticles to increase the temperature in the thermally responsive hydrogel,[94,95] making it useful as a controllable drug reservoir but not as a general method for drug delivery from tissue engineering materials.

2.7 Conclusion

Many techniques used to provide drug delivery systems from tissue engineering materials use the material as a biodegradable depot, which is definitely preferable to invasive micropumps,[22] but is not achieving the full potential of drug delivery tissue engineering materials. Both the static environment, the physical, chemical, and biological cues mimicking a healthy ECM, and dynamic temporally controlled drug/growth factor delivery are important considerations in tissue engineering and they affect each other. Truly optimised tissue engineering systems need to consider both of these topics in their design. A common limitation with these current methods is incompatibility with multiple delivery profiles simultaneously. While many adaptable methods exist that could be used for a variety of drugs or growth factors, when the delivery method relies on adjusting properties of the tissue engineering material itself it can only be adjusted for a single delivery profile. There is also a tendency, especially with passive diffusion, affinity controlled release, and immobilisation delivery strategies, to adjust delivery timing only in terms of the duration of delivery but not delays to the start time. This is a vital consideration for achieving sequential delivery.

The broad nature of research in this field, investigating individual aspects of tissue engineering material properties and diverse drug delivery systems, presents many options for potentially synergistic combination. Indeed, while one single universally controllable delivery system has not been established, the broad selection and adaptability of current methods may solve that problem. This thesis provides a collection of distinct delivery systems, each controllable within a different temporal range, working with the same tissue engineering material. These novel systems are based on the existing methods and materials described here, designed with both material properties and drug delivery in mind to provide optimal therapeutic performance.

Chapter Three

Methods

3.1 Materials

Fmoc protected amino acids, Hydroxybenzotriazole (HOBt), O-Benzotriazole-N,N,N',N'-tetramethyl-uronium-hexafluoro-phosphate (HBTU) and Wang resins were purchased from GL Biochem (China). Dimethylformamide (DMF) was dried using 4 Å molecular sieves for a minimum of 2 hr prior to use. Custom Fmoc capped and desalted peptides were purchased from Pepmic (China) for work done in Chapter Eight-Chapter Nine. BDNF and GDNF proteins, ELISA supplies (capture, primary and secondary antibodies; and the color reagent pack) and DuoSet GDNF ELISA Kits were purchased from R&D Systems (USA). Poly(lactic acid) (PLA) a.k.a. Poly(L-lactic acid) (PLLA) was purchased from Absorbable Polymers, Inc (AL, USA). All other chemicals were purchased from Sigma-Aldrich unless otherwise stated. Dialysis membranes were purchased from Spectra/Por (USA).

3.2 Material Preparation

3.2.1 Solid Phase Peptide Synthesis (SPPS)

Peptides were manually synthesised for the work in Chapter Four-Chapter Six as previously described.[9] The N-terminus Fmoc-capped peptides were synthesised by addition of individual Fmoc-capped amino acids one at a time, synthesising from the C-terminus to the N-terminus, starting with the C-terminal amino acid in resin bound form (with an N-terminus Fmoc cap and linked to a resin bead at the C-terminus). All reactions were conducted in a rotating reaction vessel. 0.4 mmol of resin was swelled in 8 mL DMF for 15 min. In series, the protecting Fmoc groups were removed by reaction with 5 mL of 20% piperidine in DMF for 20 minutes, and the next amino acid in the sequence coupled by reaction with a 2 mmol solution of the amino acid in 8 mL of DMF with HOBt (2 mmol), HBTU (1.92 mmol), and DIPEA (0.8 mL) for 60 minutes. In between each reaction the resin was washed with DMF to remove the reaction solution and then with dichloromethane (DCM) to perform a Kaiser test/ninhydrin reaction to confirm reaction progress based on the presence or absence of free amine groups before washing again with DMF. The final peptide resin was washed with ethanol and stored under vacuum for at least 2 days before cleaving the peptide from the resin in trifluoroacetic acid (TFA) containing 2.5% (v/v) triethylsilane (TES) and 2.5% (v/v) deionised water. The peptide was recovered by filtration through glass wool, and excess TFA was removed under gently flowing nitrogen gas. The remaining solution was precipitated and washed in dry ice-cooled ether and separated by centrifugation. This product was dried under vacuum for at least 2 days before being ground into a fine white powder and dried for a further 7 days before use.

3.2.2 Self-Assembled Peptide (SAP) Hydrogel Preparation and Loading

The SAP hydrogels were prepared as previously described[9]. Briefly, peptide powder was suspended in deionised water (DI H_2O) and dissolved by minimal addition of 0.5 – 1 M sodium hydroxide (NaOH). The self-assembly was induced by a pH switch caused by the

dropwise addition of 0.1 – 0.2 M hydrochloric acid (HCl), then made up to volume with PBS. Hydrogels were prepared at a peptide concentration of 20 mg/mL (Chapter Four-Chapter Six) or 15 mg/mL (Chapter Eight-Chapter Nine). Hydrogels used in biological testing were made up to volume using Hank's buffered saline solution (HBSS) (Gibco) instead of PBS and diluted 1:1 with cell media/suspension when used in biological testing. Loading with growth factor materials was done immediately before the commencement of release profile experiments to minimise degradation. Loading was performed by adding growth factor/short fibre solution via micropipette directly to the hydrogel and vortexing to mix.

3.2.2.1 Growth Factor Loading (Chapter Six)

After formation, hydrogels were loaded with BDNF or modified BDNF-Chitosan at a concentration of 865 ng/mL. GDNF was loaded at a concentration of 1000 ng/mL.

3.2.2.2 Growth Factor Loading (Chapter Eight)

After formation, hydrogels were loaded with short fibres and/or growth factor solutions as required. GDNF solution was loaded at a final concentration in the hydrogel of 1000 ng/mL. Short fibres were loaded for final concentrations in the gel of 0.2 – 5 mg/mL, using 5 mg/mL in release profiles (resulting in a final concentration in the hydrogel of 806 ng/mL GDNF from 0.0156% (w/w) loaded mGDNF short fibres).

3.2.2.3 Growth Factor Loading (Chapter Nine)

After formation, hydrogels were loaded with nanoparticles and growth factors as required. Nanoparticles were loaded at a final concentration in the hydrogel of 0.085 mg/mL. GDNF was loaded at a final concentration in the hydrogel of 1000 ng/mL. All nanoparticle containing gel containers were wrapped in aluminium foil to minimise light exposure.

3.2.3 Xyloglucan-PDL Hydrogel Preparation and Loading

For *in vitro* application, xyloglucan (3% (w/v)) was dissolved in PBS and stored below 4 °C to prevent gelation. Composite scaffolds were generated by mixing PLLA short fibres

(SF, 0.25% (w/v)) into xyloglucan (at 4 °C) prior to its gelation. For cell culturing, 100 μL of xyloglucan (± SF) was used to coat glass coverslips, placed into the bottom of the culture wells (24-well plate). The plate was stored at 37 °C for 30 min prior to seeding of cells, and maintained at 37 °C for the duration of the study to ensure preservation of the integrity of the gel. For *in vivo* application, the xyloglucan was prepared at 4.5% (w/v) in Hanks Buffered Saline Solution (HBSS, Gibco), and subsequently diluted with cells at a ratio of 2:1 (i.e. final concentration of 3% (w/v)) at the time of implantation. All gels for *in vivo* delivery were stored on ice to prevent gelation prior to implantation.

3.2.4 SMCC Crosslinking – Covalent Attachment to Growth Factor

The SMCC crosslinker used here for covalent attachment to growth factors refers to sulfo-SMCC (the water soluble form): 4-(N-maleimidomethyl)cyclohexane-1-carboxylic acid 3-sulfo-N-hydroxysuccinimide ester sodium salt. The SMCC solution used in all attachments was prepared at 2.5 mg/mL in PBS, and mixed for 1 hr with gentle oscillation on an oscillating rocker table, and then filtered through a 0.2 μm filter. In all cases this SMCC solution was reacted with the amine moiety only for 2 hours with gentle oscillation, washed if applicable, then reacted overnight at 4 °C with the growth factor at ≥ 4 μg/mL. Both the BDNF and GDNF growth factors, as well as other members of the NGF and GDNF families, contain the cystine knot motif,[96,97] a cysteine rich structure that has been shown to include the free unpaired cysteine residues necessary for SMCC crosslinking.[98]

3.2.4.1 Chitosan-Growth Factor Attachment

3.5 mL of filtered SMCC solution was reacted with 26 mg methacrylated chitosan for 2 hr at room temperature on an oscillating rocker table. BDNF protein (in 25 μg/mL solution) was added to the SMCC-chitosan solution at a 35:100 volume ratio of BDNF to SMCC-Chitosan and allowed to react overnight at 4 °C before being transferred to −20 °C for storage.

3.2.4.2 Electrospun Fibre-Growth Factor Attachment

Intact scaffolds or short fibres were first aminolyzed in 0.5% (v/v) ethylenediamine (ED) in isopropanol (IPA) (Caledon Laboratories, Canada) for 15 min to provide amine groups on the fibre surface. For biological testing in Chapter Seven the materials were sterilised with 70% (v/v) ethanol. All materials were washed in sterile deionised water. The materials were immersed in the filtered SMCC solution for 2 hours at room temperature, prior to being transferred to a solution containing growth factor at 4 μg/mL overnight at 4 °C. The vortexed scaffolds described in section 7.4 were vortexed for several minutes after this procedure.

3.2.4.3 Nanoparticle-Growth Factor Attachment

Amine coated TiO_2 nanoparticles prepared as previously described, with predominant (87%) anatase phase and a smaller component of rutile phase(13%),[99] were obtained. 1.5 mL of filtered SMCC was reacted with 17 mg of amine coated TiO_2 nanoparticles for 2 hr at room temperature on an oscillating rocker table, then washed 3 times in ~45 mL DI H_2O mixed using a vortex mixer and separated by centrifugation for 30 min at 4000 rpm. 1.5 mL of 4 μg/mL BDNF protein solution was added to the SMCC-nanoparticle solution and allowed to react overnight at 4 °C before using centrifugation to remove the BDNF solution from the nanoparticles and immediately commencing the UV exposure and washing experimentation. All nanoparticle reaction containers were wrapped in aluminium foil to minimise light exposure.

3.2.5 Chitosan Methacrylation for Water Solubility

Chitosan was treated to become water soluble using previously published methods[100]. Briefly, 3% (w/v) chitosan (190,000-310,000 Da) was dissolved in 2% (v/v) acetic acid overnight then reacted with 7.45 mmol methacrylic anhydride for 3 h. The solution was dialyzed using 12-14 kDa molecular weight cut-off (MWCO) membranes and lyophilised to recover the methacrylated chitosan. This product was subsequently re-dissolved in water,

with all insoluble material removed, leaving only the demonstrably water soluble chitosan to be re-lyophilised and used in the attachment.

3.2.6 Xyloglucan-PDL Preparation and Gelation

Poly-D-Lysine (PDL) was coupled to xyloglucan as previously described.[101] Briefly, 54 mg poly-D-lysine (PDL) and 58 mg 4-azidoaniline were covalently bound using 155 mg N-(3-dimethylaminopropyl)-N'-ethylcarbodiimide hydrochloride (EDAC) in 140 mL DI H_2O in an ice bath for 4 hr without light exposure. The solution was dialyzed in DI H_2O through a 500 Da MWCO cellulose ester membrane for 48 hr and lyophilised. 110 mg of this photosensitive intermediate product was recovered and reacted with 201 mg xyloglucan (Dainippon Sumitomo Pharma, Japan) in 6 mL PBS under 100 W 365 nm UV light (Spectroline SB-100P/FA) for 150 s at 5 cm from the source and the product was lyophilised.

3.2.7 Electrospinning

A custom built electrospinning setup was used consisting of a syringe pump (KD-100, KD Scientific, Holliston, USA) and an adjustable DC voltage power supply (Model RR 50-1.25R/230/DDPM, Gamma High Voltage Research, Ormond Beach, FL, USA) and a 13 cm diameter grounded metal rotating mandrel to collect the fibres. A solution of 0.1 g/mL PLA (a.k.a. PLLA) in 3:1 chloroform to acetone was stirred to dissolution. For growth factor loaded fibres GDNF was mixed with the PLA solution at a ratio of 135 μL GDNF stock solution (at 100 μg/mL) added to 865 μL PLA solution (at 0.1 g/mL) for a theoretical concentration of 0.0156% (w/w) GDNF. The solution was loaded into a syringe fitted with a metal drawing up needle, and dispensed at a rate of 2 mL/h while charged to 7.5 kV at a working distance of 5 cm. Unmodified PLA was charged to 20 kV at a 12 cm working distance onto a rotating collector (1000 rpm).

For Chapter Seven, The PLLA solution used the solution also contained 1 mM Dodeoyltrimethyl-ammonium bromide (DTAB), and was spun using a 21 G needle, 22 kV,

1.0 mL/h, 10 cm working distance with a rotating collector (2000 rpm). Polycaprolactone (PCL) scaffolds were prepared similarly in a 3:1 solution of chloroform to methanol, using a 21 G needle, 20 kV, 2 mL/h, 13 cm working distance onto a rotating collector The collected scaffolds were dried in a vacuum oven (Labec) overnight at 30 °C.

3.2.8 Short Fibre Cutting

Short fibres were cut on a Leica microtome, using dry ice to freeze small pieces of the intact scaffolds in an upright position embedded in cryo-mounting media (TissueTek OCT, Fisher Scientific, USA). Short fibres were cut and using an appropriate step size 2 – 10 μm (Chapter Seven) or 20 μm (Chapter Eight) and collected in DI H_2O. After cutting, short fibres were washed with DI water 3 times to remove the tissue mounting media, recovering the short fibres by centrifugation at for 30 min at 4000 rpm (Chapter Eight). For Chapter Seven the short fibres were 5 times by centrifugation and also washed in an ultrasonic bath.

3.2.9 Nanoparticle Preparation

37 mg of TiO_2 nanoparticles (Degussa P25) were added to 90 mL of 0.1 M HCl and then ultrasonicated for 3 min. 7.5 mg of L-lysine was dissolved in 10 mL of 0.1 M HCl and added to the nanoparticle suspension. The reaction mixture was stirred continuously over 24 hr at room temperature in dark conditions, then washed 3 times in ~ 40 mL DI H_2O using centrifugation for 40 min at 4000 rpm followed by sonication for 3 min.

3.3 Material Characterisation

3.3.1 Transmission Electron Microscopy (TEM)

Transmission electron microscopy (TEM) was performed on a Hitachi H7100FA electron microscope using a 100 kV beam with a LaB_6 cathode. Formvar coated copper grids were glow-discharged for 30 s at 15 mA. Hydrogel samples were negatively stained with 0.75% (w/v) uranyl formate (UF): after glow discharge the grids were gently immersed in the sample for 30 s, then briefly immersed in two consecutive drops of deionised water, then two drops

of the UF negative stain solution staying in the second drop for 20 s. The grids were gently blotted dry between immersions. Nanoparticle samples were imaged without staining: drops of nanoparticle solutions in DI water were air dried on glow discharged grids.

3.3.2 Scanning Electron Microscopy (SEM)

Scanning electron microscopy (SEM) was performed on a Zeiss UltraPlus electron microscope using a 3.0 kV beam, 7.5 μm aperture, and an in lens detector. Samples were affixed to double sided carbon tape before being sputter coated with platinum for 20 – 60 s at 20 mA. Hydrogel samples first were snap frozen in liquid nitrogen and lyophilised for at least 24 hours before being affixed to the carbon tape. Short fibre solution droplets were allowed to air dry on the carbon tape before being platinum coated.

3.3.3 Rheology

Rheological analysis was performed using a Kinexus Pro+ Rehometer (Malvern) using flat plate geometries with a solvent trap (Upper Geometry: PU20 SR1351 SS, Lower Geometry: PLS55 C0177 SS). A gap of 0.2 mm was used, with temperature maintained at 37 °C and frequency sweeps were performed from 0.1 – 30 Hz at 0.1 or 0.5% strain. Isothermal rheology (Chapter Seven) was performed at 37 °C and 0.1 Hz on samples initially loaded at 4 °C to determine the induction time of gelation.

3.3.4 Spectroscopy

Fourier Transform Infrared (FTIR) spectroscopy was conducted with an Alpha Platinum ATR FTIR (Bruker Optics) on 10 μL hydrogel samples, collecting up to 200 scans of each. The samples were allowed to dehydrate for 20-30 min to distinguish the SAP spectra from that of water, or else allowed to sit for 5 min using a background scan of DI H_2O to distinguish the spectra.

Circular dichroism (CD) was conducted with a Chirascan CD Spectrometer (Applied Photophysics Limited), scanning from 350 to 170 nm at a step size of 1 and 1 nm bandwidth

using a deionised water background scan. SAP hydrogels were diluted at 1:200 in deionised water, or 1:21 in Chapter Six.

X-ray photochemical spectroscopy (XPS) analysis and peak assignment, used to confirm the presentation of PDL on the xyloglucan in Chapter Seven, was performed externally at CSIRO. The high-resolution spectra obtained were curve fitted to determine the contributions from chemically different C and N species (C1 – C4, N1 - N2).

3.3.5 Surface Area Analysis

Brunauer-Emmett-Teller (BET) surface area analysis was performed using a micromeritics TriStar II surface area and porosity instrument to determine the surface area of the scaffolds, and subsequently the amount of GDNF tethered onto the PCL surface. 45 mg of untreated polymer scaffold was loaded into a dry 0.95 cm diameter sample tube and degassed under vacuum (0.15–0.3 mbar) at room temperature for 7 days on a micromeritics VacPrep 061 sample degas system. The degassed sample mass was determined to be 43 mg. The sample tube was then loaded into the instrument for adsorption analysis of nitrogen gas in a liquid nitrogen bath. The specific surface area was determined to be 3.0050 m^2/g. The weight of the punch biopsies (0.6 cm in diameter) on which GDNF was attached, and cells cultured, was 0.80 mg so the absolute surface area was 0.0008 g × 3.0050 m^2/g = 0.0024 m^2 = 24 cm^2.

3.4 Release Profiles

3.4.1 Degradation and Release Profiles

For BDNF degradation triplicate 200 μL samples of 1000 ng/mL solution of BDNF in PBS were added to wells of a 96-well plate for each time point. For the release profiles, 100 μL samples of growth factor loaded hydrogel were added to 3 wells (Chapter Six) or 4 wells (Chapter Eight-Chapter Nine) each in 96-well plates. Dually loaded gels were loaded into double the number of wells to allow samples to be collected and tested for each growth

factor. Intact scaffold pieces ~7 mm^2 (average 1.3 mg/piece for mGDNF, 6.6 mg/piece for iBDNF) were added to 5 wells each. The hydrogel was allowed to settle for ~5 min to reform into a gel before 200 μL of PBS was gently added on top of the hydrogels and/or scaffold pieces, marking the start point of the release profile. The sample plates were incubated at 37 °C at 5% CO_2. 150 μL samples were taken at appropriate time points and 150 μL of replacement PBS was added after removing each sample. The collected samples were stored at −20 °C (Chapter Six) or −80 °C (Chapter Eight-Chapter Nine).

Nanoparticle loaded hydrogel plates were wrapped in aluminium foil to minimise light exposure. The "initial UV" plate was exposed before adding the first 200 μL of PBS, the "midway UV" plate was treated after 6 hr, after removing the 6 hr time point samples and before adding the replacement PBS.

3.4.2 Lentiviral Release Profile and ELISA

To determine successful immobilisation of the mCherry lentivirus, release of mCherry lentivirus from the two Fmoc-SAP hydrogels was compared. 100 μL samples of Fmoc-SAP hydrogels at 20 mg/mL were mixed with 1 μL of mCherry lentivirus (titre at 9.28 x 1010 copies/mL; GeneCopoeia) and placed in a 96 well plate. 200 μL of PBS was placed on top of the gel and the plate placed in an incubator (37 °C, 5 % CO2). The PBS was then collected and replaced with fresh PBS every 24 hours for 5 days. The PBS supernatant was stored in a freezer until ready for analysis by an enzyme linked immunosorbent assay (ELISA). A HIV Type 1 p24 Antigen ELISA 2.0 kit (ZeptoMetrix) was used to measure the amount of mCherry released. The ELISA was performed as per the manufacturer's instructions.

3.4.3 Enzyme Linked Immunosorbent Assay (ELISA)

Enzyme linked immunosorbent assay (ELISA) was used to quantify the protein present in degradation and release profile samples, as well as the growth factor bound nanoparticle suspension and supernatant samples. GDNF was quantified using a DuoSet ELISA kit

(R&D Systems) following the manufacturer's instructions as well as our previously described ELISA method also used for BDNF.[102] 96-well plates were incubated with 100 μL/well capture antibody (R&D Systems: MAB848 for BDNF, MAB212 for GDNF) solution at 4.0 μg/mL in PBS at room temperature overnight, then incubated for 1 hr at 37 °C with 200 μL/well 2.5% (w/v) gelatin blocking solution. 100 μL/well samples and standard solutions (0.1-200 ng/mL) were incubated for 2 hr at room temperature, followed by 100 μL/well of primary antibody (R&D Systems: BAM648 for BDNF, AF-212-NA for GDNF) solution at 1.0 μg/mL in 5% (v/v) donkey serum for 2 hr at 37 °C, then 100 μL/well secondary antibody (R&D Systems: HAF018 for BDNF, HAF109 for GDNF) solution diluted 1:40000 for BDNF or 1:20000 for GDNF in 2% (v/v) donkey serum for 1 hr at 37 °C. 100 μL/well of color reagent (R&D Systems: DY999) solution was allowed to react for 20 min at room temperature before being stopped by the addition of 30 μL/well 1 M HCl. Absorbance at 450 nm was measured by a Tecan plate reader spectrophotometer and a calibration curve of standard solutions used to quantify protein present. The plate was washed 3 times by addition of a solution of 0.05% (v/v) Tween20 in PBS and 10 min of gentle oscillation after each incubation period, and this solution was used as the diluent for the gelatin, primary antibody, and secondary antibody solutions. The plates were wrapped in aluminium to minimise light exposure after the introduction of the secondary antibody solution until the end of the procedure.

ELISAs on scaffold materials were performed on cut pieces of scaffold incubating in solutions in the 96-well plates. In these cases, the procedure started with the primary antibody incubation, and washing steps were done using vortexing of the scaffolds in the wash solution in separate vials. The scaffolds were removed from the 96-well plates after the colour change reactions were completed, leaving only the coloured solution in the well plates to be measured.

3.4.4 Hydrogel Washing (Chapter Five and Chapter Eight)

100 μL portions of the different short fibre loaded DDIKVAV hydrogels, or fucoidan-GNP loaded FRGDF hydrogels, were added to wells of a 96-well plate and 200 μL of DI H_2O was gently added on top after letting the gels settle and reform ~5 min. The plate was placed on an oscillating rocker table to gently rinse the hydrogels, and the water was changed (175 μL removed, 175 μL fresh water added) at 1, 3.25, 5.5, and 7.5-hour time points ±10 min, with no fresh water added at the final time point.

3.4.5 Nanoparticle UV Exposure and Washing

40 mL of DI H_2O was added to the nanoparticles, followed by vortex mixing, making them up to a 0.425 mg/mL suspension. Triplicate 1 mL samples were taken for UV exposure, and another triplicate for untreated control samples. The UV exposure samples were treated, then 100 μL portions of all six nanoparticle suspension samples were taken. Then the suspension samples were centrifuged for 30 min at 4000 rpm and 200 μL portions of all six supernatants were taken. These portions were immediately stored at −80 °C until later analysis. Meanwhile, the original nanoparticle suspension was also centrifuged to separate the now once washed nanoparticles and refilled with DI H_2O to 34 mL to maintain the nanoparticle concentration in the suspension. This process was repeated for 5 washed. All nanoparticle containers and samples were covered with aluminium foil to minimise light exposure. UV exposure was performed under 100 W 365 nm UV light (Spectroline SB-100P/FA) for 2 min at a distance of 7 cm from the source.

3.5 Biological Testing

3.5.1 Animal and Cell Culture Conditions

3.5.1.1 Animal Ethics

All procedures were conducted in accordance with the Australian National Health and Medical Research Council's published Code of Practice for the Use of Animals in Research,

and approved by the Florey Neuroscience Institute animal ethics committee or the ANU Animal Care and Use Committee. Mice and athymic nude rats were housed on a 12 hr light/dark cycle with ad libitum access to food and water. Cells used for *in vitro* culturing and transplantation were obtained from mice that were time mated overnight, with visualization of a vaginal plug on the following morning taken as embryonic day (E) 0.5.

3.5.1.2 Ventral Midbrain (VM) Primary Cell Culture (Chapter Seven)

Except for Section 7.4, Ventral midbrain (VM) tissue was isolated from Swiss mice at E12.5 as previously described.[103,104] Cells were seeded at a density of 350,000 cells/well (37 °C, 5% CO_2) for 72 hours prior to fixation with 4% (v/v) paraformaldehyde. Culture substrates included: PDL-coated coverslips (PDL), xyloglucan coated coverslips (XYLO), xyloglucan + short fibres (XYLO+SF), xyloglucan + soluble GDNF (XYLO+sGDNF), xyloglucan + blended GDNF (XYLO+bGDNF), xyloglucan + short fibres with immobilised GDNF (XYLO+SF-iGDNF).

In Section 7.4, VM tissue was isolated from C57BL/6 mice. Pregnant mice (E11.5) were anesthetised with isoflurane prior to cervical dislocation. The collected embryos were immersed in chilled L15 medium (Invitrogen), the brains removed and ventral midbrain microdissected. Subsequently, the tissue fragments were incubated in 0.1% (v/v) DNase and 0.05% (v/v) trypsin (in magnesium and calcium free Hank's buffered saline solution (HBSS)) for 15 min followed by three gentle washes in HBSS. Finally, the tissue fragments were dissociated in N2 media consisting of a 1:1 mixture of F12 (Invitrogen) and MEM (Invitrogen) supplemented with 15 mM HEPES buffer (Invitrogen), 1 mM glutamine (Invitrogen), 6 mg/ml glucose (Sigma-Aldrich), 1.5 mg/ml bovine serum albumin (Invitrogen), and 1% (v/v) N2 supplement (Invitrogen). Cells were seeded at a density of 175,000 cells/cm^2 onto either PDL-coated coverslips (in the presence or absence of soluble GDNF, 30 ng/ml) or PCL scaffolds (± immobilised GDNF) and incubated at 37 °C in 5% CO_2 for 3 and 7 days. After 3 days and 7 days, the cells were fixed with 4% (v/v)

paraformaldehyde for 20 min, washed, and stored in PBS containing 0.025% (v/v) sodium azide until the time of immunocytochemistry.

3.5.1.3 Neuron Primary Cell Culture (Chapter Eight)

Isolation and culture of primary cells was performed as previously described[105] unless otherwise noted. Briefly, mice were obtained from the Australian Phenomics Facility (APF) having been time- At E14.5 the pregnant mouse was sacrificed by cervical dislocation (CD) to collect the fetuses for cortical dissection for cortices without hindbrain, olfactory bulb, and meninges under sterile conditions. The cortices were trypsinised by 1x 0.25% (v/v) trypsin (Gibco), 1x DNAase (Gibco) in Hank's balanced salt solution (HBSS) (Invitrogen) for 20 min in the incubator at 37 °C, 5% CO_2. After digestion, cells were washed with HBSS three times. MEM solution with 10% (v/v) FBS was added to dissociate tissue into dispersed cells, which were counted with a haemocytometer and trypan blue.

Cortical neurones were seeded at 2.5×10^5 cell/mL in 0.1 mL of MEM with 10% (v/v) FBS in 96-well plate wells. After 2 hours for attachment, the media was changed to primary culture media containing Neurobasal medium (Gibco), 1% (v/v) B27 serum-free Supplement (Gibco), 5 mM glutamine (Gibco) and 10 μg/mL gentamicin (Sigma) and cells were maintained for 3-5 days.

The 96-well plates were prepared in advance with a poly-D-Lysine (PDL) coating. 10ug/mL PDL was added into the wells to cover the surfaces of wells and stored in an incubator overnight. The next day the excess PDL removed by washing with PBS 3 times and the plates were returned to the incubator.

3.5.1.4 Preparation of Primary Cortical Cells for Transplantation (Chapter Four)

Adult female C57BL/6 mice were used as graft recipients while donor tissue for transplantation was obtained from time mated mice expressing green fluorescent protein (GFP) under the β-actin promoter. Embryos at E14.5 were collected in chilled L15 media. GFP+ embryos were selected, their brains removed and the cortices dissected to isolate

GFP+ cortical primary tissue. The cortices were incubated for 20 minutes in 0.1% (v/v) DNase and 0.05% (v/v) trypsin in magnesium and calcium HBSS. The tissue was then washed gently 3 times with HBSS. The tissue was then dissociated and the cells re-suspended in HBSS with 0.1% (v/v) DNAse at 200,000 cells/mL.

3.5.1.5 Differentiation of Human Embryonic Stem Cells (hESCs)

The human ESC line, HES3-ENVY, that constitutively expresses GFP under the human β-actin promoter,[106] was cultured and differentiated using the dual Smad, dorsal forebrain differentiation protocol, as previously described.[107] In brief, day 7 hESC colonies were manually dissected and transferred to organ culture dishes coated with 1 mg/mL laminin and grown in neural basal media (NBM: Neurobasal Media with 1% (v/v) N2 supplement, 1% (v/v) ITS-A, 2% (v/v) B27 without vitamin A, 0.5% (v/v) penicillin-streptomycin, 1% (v/v) Glutamax). Neural induction (day 0-4) was achieved by dual SMAD-inhibition using 500 ng/mL human recombinant noggin (PeproTech) and 10uM SB-431542. From day 4, media was supplemented with 20 ng/mL FGFb and EGF (R&D Systems), to promote neural precursor proliferation and maintenance. At day 10 thick central cores of neural precursor colonies were manually isolated and pieces transferred to low attachment 96-well plates to generate neurospheres for a further 7days. Spheres were either cryopreserved (4% (v/v) paraformaldehyde, 7min; followed by 20% (w/v) sucrose in PBS) and sectioned for immunohistochemical analysis or dissociated (Accutase, Invitrogen; 37°C for 10 minutes,) to provide a single cell suspension (100,000 cells/μL) for the purpose of transplantation. At the time of implantation, cells were diluted 1:1 in SAP gels or HBSS media.

3.5.1.6 Cell Lines and Culture Conditions (Section 5.3)

The human tongue squamous cell carcinoma cell line (SCC25) cultures were obtained verified from ATCC and were maintained in DMEM-F12 complete medium containing 10% (v/v) FBS and 400 ng/mL hydrocortisone and penicillin/streptomycin. The human

mammary fibroblast cell line (hMFC) cultures were maintained as described previously.[78] Cell line cultures were maintained at 37 °C with 5% CO_2.

3.5.1.7 Endothelin-1 Lesioning and Transplantation in Rats

Surgeries were performed under general anaesthetic using 2% isoflurane inhalation (Baxter; Deerfield, IL, USA). To model focal ischemia, 81 rats received unilateral injections (2 × 1 μL) of the vasoconstrictor endothelin-1 (400 pmol/μL) into the sensorimotor cortex at the following co-ordinates: 0.5 and 2.0 mm anterior, 2.5 mm lateral relative to bregma, and at depths of 0.0 and 2.0 mm below the dural surface. An additional 12 rats were used as unlesioned controls. At 6 days or 3 weeks after lesioning, animals received two intracortical injections (1 μL/injection) of hESC-derived cortical progenitor and/or SAP gels into the lesion site (0.5 and 2.0 mm anterior, 2.5 mm lateral relative to bregma, and at depths of 1.5 mm below the dural surface). Where relevant, the final concentration of implanted SAP gels was 10 mg/mL and the total number of transplanted cells was 100,000/animal.

3.5.1.8 6-Hydroxydopamine Lesions and Transplantation (Chapter Seven)

For *in vivo* studies, adult female Swiss mice were used as graft recipients while tyrosine hydroxylase-green fluorescent protein (TH-GFP) mice [108] were used to generate embryos as a source of donor tissue for transplantation. The use of TH-GFP donor tissue enabled identification of graft (GFP+) verses host (GFP-) derived TH+ dopamine neurons *in vivo*.

All surgeries were performed under general anaesthetic using 2% isoflurane inhalation (Baxter; Deerfield, IL, USA). To model Parkinson's disease, mice received partial lesions of the VM DA neurons by unilateral injection of the selective catecholamine neurotoxin 6-hydroxydopamine (6-OHDA, 3.2 μg) into the SNpc, as previously described.[109] Using previously described methods, 3 weeks after lesioning, host animals received ectopic intrastriatal grafts of a single cell VM suspension.[103] The cell suspension (150,000 cells/μL) was diluted 1:2 in either: HBSS, xyloglucan (±GDNF), or xyloglucan+PLLA short fibres (±GDNF) to give a final concentration of 50,000 cells/μL. The various cell suspensions

were stereotaxically injected (2 μL, i.e. 100,000 cells) into the denervated host striatum at the following co-ordinates relative to bregma: anterior 1.0 mm, lateral 2.3 mm, and 3.1 mm below the dural surface. Ten weeks after transplantation animals were killed by an overdose of sodium pentobarbitone (100 mg/kg) and their brain processed as previously described.[19]

3.5.1.9 Implantation (Chapter Four)

Mice received implants of cells in the presence or absence of Fmoc-SAPs (Fmoc-DIKVAV; Fmoc-FRGDF; Fmoc-DYIGSRF), n = 6 per group. Mice were anaesthetised with 5% isoflurane, and the level of anesthesia maintained at 2% for the duration of the surgery. Mice were placed in a stereotaxic frame, midline incisions were made in the scalp and craniotomies were performed overlying the striatum. Cells were mixed at a 1:1 ratio with HBSS or Fmoc-SAP prior to implantation into the striatum. A total of 2 mL (200,000 cells) were injected, using a fine glass capillary, at the following co-ordinates: 1.0 mm anterior and 2.5 mm lateral relative to bregma, and at a depth of 3.2 mm below the dural surface. After 28 days, mice were delivered a terminal dose of barbiturate and were transcardially perfused with warm saline followed by 4% (v/v) paraformaldehyde (PFA). Brains were removed and post-fixed for 2 hours in 4% (v/v) PFA before overnight cryo-preservation in 30% (w/v) sucrose solution. The brains were then coronally sectioned at 40 mM in 12 series before free-floating immunohistochemistry was performed.

3.5.1.10 Implantation of m-Cherry virus

Adult Swiss mice received stereotaxic implants of mCherry lentivirus alone (n = 6) or mCherry virus in the presence of Fmoc-DDIKVAV (n = 6) or Fmoc-DDIKVAVK (n = 6). 5% isoflurane was used to induce anaesthesia. 2% isoflurane was maintained for the duration of surgery. Mice were placed into a stereotaxic frame and a craniotomy performed for microinjections into the underlying striatum (co-ordinates: anterior +1.0 mm and lateral -2.3 mm, relative to Bregma). A fine pulled micropipette coupled to a Hamilton syringe was used to inject virus or virus with Fmoc-SAP at a depth of 3.2 mm below the dura surface. For

control animals, 1 µL of mCherry (10^9 UI/mL) was diluted in 1 µL sterile PBS and the total 2 µL suspension implanted. Alternatively, the virus was mixed at a 1:1 ratio with the Fmoc-SAP.

3.5.1.11 Sample Preparation (Chapter Seven)

For *in vitro* culturing, GDNF was delivered: (i) directly into the culture media (soluble GDNF, sGDNF; 30 ng/mL), (ii) blended into xyloglucan gels prior to casting into culture plates (blended GDNF, bGDNF, 150 ng/mL gel, 100 µL gel per coverslip/well) or alternatively (iii) covalently immobilised onto PLLA short fibres that were delivered in xyloglucan gel (immobilised GDNF, iGDNF, with 100µl of gel including PLLA short fibres per coverslip/well). All conditions were cultured in 24-well culture plates in the presence of 0.5 mL of media—hence the total dose of sGDNF and bGDNF was 15 ng/well.

For *in vivo* delivery, GDNF was delivered within the cell preparation (Cell + sGDNF, 1 µg/injection), blended into the xyloglucan at the time of delivery with cells (Cells + XYLO-bGDNF, 1 µg/injection), delivered by immobilization of short fibres (Cells + XYLO + SF-iGDNF) or a combination of blended and immobilised (Cells + XYLO-bGDNF +SF-iGDNF).

3.5.2 Biological Assessment

3.5.2.1 Assessment of Grafts in Rats (Chapter Four)

Atrophy and neuronal cell loss within the host cortex were quantified in ET1 lesioned rats, immuno-labelled with NeuN, at 36 weeks after cell and/or SAP implants. Six sections from a 1:12 series, spanning from bregma to 2.5 mm rostral, were analysed. Cortical area, ipsilateral to the infarct, was delineated based on anatomical landmarks and expressed as a percentage of the intact (saline-injected) brain. The cortical area boundaries were established via the corpus collosum and limited ventrally by the piriform cortex. Volumetric assessment across the rostro-caudal axis was performed according to Cavalieri's principle using StereoInvestigator Software (MicroBrightfields, USA).

NeuN cell loss within the cortex was estimated from the two sections adjacent to the lesion core. The atrophied area delineated, was used to estimate NeuN cell density from lesioned and intact animals. Stereological counts within the area were made at regular pre-determined intervals (200 × 200 μm) within a defined counting frame (40 × 40 μm), according the optical fractionator principles[110] and previously described methods,[109] and density determined according to the volume sampled.

Human ESC-derived grafts were identified by GFP-labelling within the cortex, with volumetric assessments, cell counts (DAPI, NeuN and TBR1) and cell densities, performed stereologically. Counts were made at the following pre-determined intervals (DAPI: 500 × 500 μm; NeuN: 400 x 400um; TBR1 & BRN2: 280 x 280um) using unbiased counting frames of known areas (DAPI: 10 × 10 μm; NeuN: 20 × 20 μm; TBR1 & BRN2: 30 x 30um). For all counts, the co-efficient of error (CE) coefficient of variance (CV) were calculated as estimates of precision, and values of less than 0.1 were accepted.[111]

3.5.2.2 Assessment of Grafts in Mice (Chapter Four)

Grafted cells, and the extent of their innervation were discernible by the presence of GFP+ staining. For all animals, total number of GFP+ cells, density (GFP+ cells/mm^3) and volume of innervation (mm^3) were quantified. Optical intensity was measured at two fields of view (FOV) for comparison of innervation between each group. This technique was also used for assessment of inflammation. ImageJ was used to determine the optical intensity of the fluorophore (488 for GFP; 550 for GFAP and 649 for CD11b) in each image at each FOV. This provides a relative comparison for the extent of innervation or elicited inflammatory response induced in each group.

3.5.2.3 Cell Counting and Assessment of Neurite Growth (Chapter Seven)

For *in vitro* assessment, neuronal differentiation and neurite morphology were analysed from cultures using previously described methods.[104] In brief, TH+, TUJ+ and DAPI labelled cells were quantified from 10 sampling sites/well and 3 technical replicates (i.e. wells)

performed per experimental condition. For assessment of neurite morphology, 30 TH+ cells were quantified. Photomicrographs of each DA neuron (identified by TH+) were taken using a 20x objective (Olympus IX71) and measurements of total neurite length obtained using NeuronJ software (ImageJ, NeuronJ plugin, NIH).

The inflammatory response of the host brain to the implants was assessed at predetermined sites adjacent to the graft core for each graft (Figure 7.7C). Leica LAS Image Analysis LAS Software (Leica) was used to estimate GFAP and CD11b density from images captured at 20x on a Leica 6000 microscope. The area covered by GFAP+ fibres or CD11b+ cells was expressed as a percentage of total area.

For *in vivo* assessment of the graft, the number of grafted dopamine (DA) neurons within each animal was quantified based upon GFP+ labelling.[112] The volume of the graft core (area delineated exclusively around the grafted GFP+ cell bodies) was used to estimate cell density within the grafts and total volume on GFP+ innervation was assessed by delineation of densely stained GFP+ fibre innervation of the striatum. Density of innervation within the striatum was examined at a predetermined location, directly adjacent to the graft core.[19] Leica LAS Image Analysis Software was used to estimate fibre density from images captured at 40x magnification on a Leica 6000 microscope.

3.5.2.4 Immunoblotting

The dopaminergic (DA) neural stem cell line, SN4741, was cultured in DMEM, 10% (v/v) FBS, L-glutamine (2 mM), penicillin/streptomycin (50 units/mL), and glucose (0.6% (w/v)). For analysis of intracellular GDNF signalling, 100,000 cells were seeded onto 12-well plates or PCL scaffolds. At 70% confluency the cells were changed into serum-free media with or without GDNF (soluble or immobilised). A standard curve of GDNF treatment (0, 3, 10, 30, 100 ng/ml), using the same cell line, was performed in parallel to quantify the levels of GDNF activity. Cells were stimulated with soluble GDNF (sGDNF, 30 ng/ml) for 60 min or 3 days, and tethered GDNF (iGDNF) for 1 day or 3 days prior to being lysed in ice-cold

buffer containing 20 mM Tris-Cl, pH 7.5, 150 mM NaCl, 1% (v/v) Triton X-100, 1% (v/v) protease inhibitor mixture, 50mM NaF, and 0.2mM Na3VO4 for 20 min. Lysates were centrifuged at 14,000 rpm for 20 min at 4 °C to collect supernatants. Protein was quantified using the bicinchoninic acid assay kit (Pierce) using bovine serum albumin standards.

Protein (50 μg) was electrophoresed through 12.5% SDS-polyacrylamide gels and transferred to Immobilon PVDF-FL membrane (Millipore). Membranes were blocked with 5% (v/v) skim milk in Tris-buffered saline with Tween-20 (TBST), pH 8.0, for 30 min and incubated with mouse pErk1,2 (1:2000, #9106, Cell Signaling Technology) and rabbit total Erk1,2 (1:1000, #9102, Cell Signaling Technology) antibodies in 3% (w/v) BSA in TBST overnight at 4 °C. Blots were washed 3x in TBST for 10 min and incubated with IRDYe 680 and 800CW-conjugated secondary antibodies (1:10000) followed by 3 washes in TBST for 10 min and detected using the Odyssey Classic infrared imaging system. Membranes were then stripped and re-probed with mouse anti β-actin (1:5000, Sigma). Blots were quantified by taking the ratio of pErk/Erk bands and subtracting background intensity

intensity.

3.5.2.5 Immunocytochemistry and Immunohistochemistry

Procedures were performed as previously described.[112] Primary antibodies and dilution factors used were: mouse anti-βIII-tubulin (TUJ1, 1:1500, Promega), rabbit anti-tyrosine hydroxylase (TH, 1:800; PelFreez), chicken anti-GFP (GFP, 1:1000, Abcam), rabbit anti-GFP (1:20000; Abcam), rabbit anti-GFAP (GFAP, 1:800, DAKO), and mouse anti-CD11b (1:100, Serotec). The secondary antibodies used for direct detection were DyLight 488 donkey anti-mouse, DyLight 549 anti-chicken, DyLight 649 anti-rabbit, DyLight 550 donkey anti-rabbit, and DyLight 649 donkey anti-mouse (Jackson ImmunoResearch) used at dilution of 1:200 for immunohistochemistry; and Dylight 488 donkey anti-rabbit and Dylight 549 donkey anti-mouse (Jackson ImmunoResearch) used at a dilution of 1:300 for immunocytochemistry. The secondary antibodies used for indirect detection were biotin

conjugated donkey anti-rabbit (1:500; Jackson ImmunoResearch) followed by peroxidase conjugated streptavidin (Vectastain ABC kit, Vector laboratories) or 649 conjugated streptavidin (1:200; Jackson ImmunoResearch). All *in vitro* cultures were additionally counterstained with Hoechst (Life Technologies) at 1:5000 for immunohistochemistry and 1:1000 for immunocytochemistry. All fluorescent images were captured using a Zeiss Axio Observer.Z1 or Leica CTR6000 microscope whilst bright and dark-field images were obtained using a Leica DM6000 upright microscope. For the long-term study in Chapter Four, at 36 weeks post-implantation (gels and/or cells) animals were killed by an overdose of sodium pentobarbitone (100 mg/kg) and their brain processed for immunohistochemistry as previously described.[112]

3.5.2.5.1 mCherry Staining (Section 5.4)

After 21 days, mice were killed by an overdose of sodium pentobarbitone (100 mg/kg) and transcardially perfused with warm saline followed by 4% (v/v) paraformaldehyde (PFA). After removal, mouse brains were post-fixed for 2 hours in 4% (v/v) PFA. Following fixation, brains were cryo-preserved in a 30% (w/v) sucrose solution overnight. The brains were coronally sectioned (40 μm at a 1:12 series) and immunohistochemistry against red fluorescent protein (rabbit anti-RFP, 1:1000, Rockland, USA) was performed to amplify the mCherry signal, using previously described methods.[112] Cell counts for mCherry virally infected cells (mCherry+), transduction volume and density measurements were carried out on a Leica CTR6000 microscope using LAS software.

3.5.2.5.2 NFκB and CEP55 Staining (Section 5.3)

SCC25 cells were treated without and with fucoidan (2 mg/mL) for 48 h. Cells were fixed with paraformaldehyde and permeabilised with 0.1% (v/v) triton-X-100. For Annexin V cells were stained with the Alexa Fluor® 488 annexin V/Dead Cell ApoptosisKit (Life Technologies) and counter-stained with Hoechst dye to stain the live cells. For NFκB and CEP55 cells were blocked with 1% (w/v) bovine serum albumin (BSA) in PBS for 1 hr at

room temperature and further treated with primary antibody rabbit polyclonal NFκB p65 (Abcam) or rabbit monoclonal CEP55 antibody (Abcam) overnight at 4 °C. Cells were further incubated with anti-rabbit Alexa Fluor 488 secondary conjugates for 1 hr at room temperature. Following several washes cells were visualised under fluorescence microscope (Nikon Eclipse Ti-S).

3.5.2.6 Reverse Transcription and Quantitative Polymerase Chain Reaction (QPCR)

Total RNA was reverse-transcribed to generate complimentary DNA using Superscript III (Invitrogen) following the manufacturer's protocol. To challenge fucoidan, cells were stimulated with LPS at a concentration of 10 μg/mL in the complete media. cDNA of 30 ng was used to perform quantitative real time PCR in a 20 μL reaction using SYBR Green (Biorad) on a CFX connectTM Real Time PCR detection system (Biorad). Primer oligosequences were designed using Primer3 PCR prime design tool (Whitehead Institute for Biomedical Research, Cambridge, MA, USA) and the gene specificity was checked using the National Center for Biotechnology Information nucleotide database. Steps followed during QPCR to generate amplification curves included an initial denaturing step for 3 min at 95 °C, followed by 40 cycles of 95 °C for 10 s, 60 °C for 30 s, and 72 °C for 30 s. The expression of each gene in terms of fold change was normalised to the housekeeping gene ACTB.

3.5.2.7 Functional Recovery/Behavioural Testing

The staircase test was performed as previously described,[113] using 1 week post-lesioning as the untreated starting point and additional tests after treatment implants at 4, 8, 16, 24, and 36 weeks post-lesioning. Briefly, animals were placed on a food-restricted diet (maintained at 85% of pre-test free-feed weight) for the duration of the 7-day test period. Each day rats were placed in the staircase apparatus where each forepaw had unilateral access to sugar pellets positioned on ascending steps. The total number of pellets (maximum 50) retrieved and eaten for each forelimb was reordered in a 20 min test period. The number of

pellets eaten was recorded and averaged for the last 3 days of the test period Retrievals made with the impaired paw (left) were expressed as a percentage of total retrievals, (%L/L+R).

The cylinder test was performed at 36 weeks post implantation as previously described.[114] Animals were placed in a glass cylinder (20 cm diameter) and weight-bearing forepaw contacts with the glass wall in response to exploratory behaviour were recorded. A total of 20 paw contacts were recorded per animal and expressed as a percentage of left (impaired paw) touches/total touches.

The stepping test was performed as previously described.[115] Rats were restrained by the experimenter and allowed to make unilateral forepaw weight-bearing contact with the bench. Rats were assessed for their ability to make stepping adjustments with their weight-bearing forepaw when moved laterally over a distance of 1 m. The number of steps made by the paw was recorded in both the forehand and backhand direction with testing repeated 3 times/day over 5 consecutive days.

The rotarod performance test was conducted in rats at 36 weeks following treatment implantation. Animals were placed on a horizontally suspended rotating rod and the time on the rod before falling (maximum 300s) was recorded. Each animal received 3 consecutive trials.

3.5.2.8 MTT Assays

Primary cells were incubated overnight to adhere before commencing. Cell media was removed and cells were replaced with 100 μL of fresh media containing growth factor samples, including: growth factor solution at a final concentration in the media of 1000 ng/mL, scaffold segments approximately 4 mm square with average masses of 1.4 mg for the iBDNF scaffolds and 1.6 mg for the mGDNF scaffolds submerged in media, and short fibres solutions at 9.1 mg/mL in media (for a theoretical maximum concentration of 1.4 μg/mL GDNF from 0.0156% (w/w) loaded mGDNF short fibres, noting that release data suggests this would not be completely released over the 3-day incubation). Samples were

incubated with the cells for 3 days, after which the samples were removed, the cells washed with PBS, and the MTT assay conducted. MTT Assays were performed using a Vybrant MTT Cell Proliferation Assay Kit (V-13154) following the manufacturer's instructions using the DMSO quick method. Cells were visually assessed by light microscopy before and after the MTT assay to confirm healthy neuron growth.

3.5.2.9 Statistical Analysis

One-way ANOVAs with Tukey post-hoc tests were used to identify statistically significant changes between groups. Statistical significance was set at a level of $P < 0.05$. Data represents mean ± standard error of the mean (SEM), or data ± standard deviation (SD) in Section 7.4. For the intact brain biocompatibility studies in Chapter Four the data was also transformed in order to obtain equal variance and the tests repeated, however, this had no effect on the statistical information obtained. For Chapter Seven, all *in vitro* studies were performed on 3 technical replicates per condition per experiment and repeated on 3-5 independent VM primary cultures. A total of 74 animals received cell transplants ± scaffolds, with 9-11 animals assigned per treatment group. For assessments of cell viability and differentiation, 10 fields of view per coverslip or scaffold were imaged using a Zeiss200 inverted microscope (images captured at 20x magnification).

Chapter Four

SAP Hydrogels *in vivo*

4.1 Chapter Details

The work in this thesis was aimed at achieving temporal control of the delivery of growth factors from self-assembling peptide (SAP) hydrogels, making SAP hydrogels a critical component. This chapter briefly discusses work to which I have contributed to confirm the biocompatibility of the SAP hydrogels used before moving on to the incorporation of growth factor delivery into the materials. The work includes the primary SAP sequences used throughout this thesis (FRGDF, DDIKVAV, and DIKVAV) as well as another neurologically relevant sequence (DYIGSRF). All sequences were tested *in vivo*, with the FRGDF, DIKVAV, and DYIGSRF sequence hydrogels tested for their biocompatibility with cell grafts in an intact brain in mice and the DDIKVAV assessed separately in a more extensive long-term study for their ability to provide cell graft support to aid recovery in an ischemic (stroke) brain injury in rats.

The biocompatibility testing in intact brains section of this chapter briefly describes work published in the research article listed below, and included in full in Appendix B:

A. Rodriguez, T. Wang, K. Bruggeman, C. Horgan, R. Li, R. Williams, C. Parish, D. Nisbet, "*in vivo* assessment of grafted cortical neural progenitor cells and host response to functionalised self-assembling peptide hydrogels and the implications for tissue repair", *Journal of Materials Chemistry B*, 2014, vol. 2, pp. 7771-7778 - Reproduced by permission of The Royal Society of Chemistry (http://www.rsc.org/)

The ischemic brain study section of this chapter briefly describes work from a manuscript in preparation.

4.2 Abstract

Tissue engineering materials that can mimic the physical, chemical, and biological properties of the natural extracellular matrix (ECM) are of great interest in regenerative medicine. Self-assembling peptide (SAP) hydrogel materials are of particular interest for their inherent biocompatibility and ability to be engineered with biologically relevant and tissue-specific sequences, which are then presented at a high density in a nanofibrous environment structurally mimetic of the ECM. Here SAP hydrogels designed from a range of biological peptide sequences were tested *in vivo* for their biocompatibility delivered with cell grafts into an intact brain (in mice). Additionally, a brain tissue specific hydrogel, designed from the common brain ECM protein laminin, was tested for its efficacy in supporting cell grafts in treatment of ischemic brain injury (stroke) in a protected 9-month study (in rats). All hydrogels tested show non-cytotoxicity, and the tissue-specific hydrogel significantly improved the cell graft results in treating the ischemic brain, showing improvements in sensorimotor behavioural analysis, specific neuronal differentiation, and reduction in secondary degeneration/cortical atrophy of the host tissue.

4.3 Introduction

Three-dimensional (3D) ECM mimicking materials have demonstrated their potential to provide cellular support *in vitro* and *in vivo*.[116] Materials designed with a "bottom up" approach, particularly nanofibrous SAP materials, are gaining interest[62,117] and being

investigated for their ability to promote endogenous repair of support cell transplantation.[8] The ECM itself includes tissue-specific proteins that initiate cell pathways via integrin activation,[9] and specific sequences within these proteins are known to influence intracellular processes including adhesion, proliferation, differentiation, and migration.[118] Research has shown that incorporating these peptide sequences into multicomponent materials can direct intracellular signalling and control cell fate.[119,120] Commercial SAPs consist of long sequences engineered for self-assembly and inherent biocompatibility, and these have been additionally modified to include biologically relevant peptide sequences as pendant groups to add an element of biological signalling/mimicry to the materials.[79] The design of Fmoc-capped minimalist SAP materials simplifies the process by using the bioactive sequence directly as the SAP, engineered with small additions to the sequence in order to ensure self-assembly under physiological conditions.[9] In addition to the inherent biocompatibility of a peptide material, the use of peptide self-assembly to incorporate biological cues means that those biochemical and biomechanical cues are presented to cells in a manner similar to that of natural cues from the natural ECM,[121] increasing the biomimicry of the material.

Biological testing of these minimalist Fmoc-capped SAPs has focused on the *in vitro* cell culture using short di- or tri-peptide or the arginine-glycine-aspartic acid (RGD) sequence from fibronectin.[7,122-124] The specific design of the peptide sequence to allow the inclusion of larger 5-amino acid sequences is relatively new,[9] and these materials have not been fully investigated *in vivo*. Here we focus on *in vivo* investigation of laminin derived SAPs, designed for tissue-specific application in the brain by using the sequences from the ECM protein common in brain tissue. Both isoleucine-lysine-valine-alanine-valine (IKVAV) and tyrosine-isoleucine-glycine-serine-arginine (YIGSR) sequences from laminin have been incorporated into minimalist Fmoc-SAPs, and are tested for biocompatibility as a cell graft support material in an intact brain in mice along with an RGD derived sequence for comparison and confirmation of the benefit of tissue-specific materials. The IKVAV sequence is further

investigated as a cell graft support material in repairing brain tissue in an ischemic brain injury model in rats.

Biomaterials have been shown to be very useful in regenerative medicine[125] including supporting neural cells for central nervous system (CNS) repair.[23] In the case of stroke or ischemic brain injury, much of the dysfunction is caused by the loss of neurons in the cerebral cortex as well as secondary degeneration in the surrounding penumbra.[126,127] However, clinical trials in cell transplantation for stroke have not focused on neuron replacement, but rather on penumbral protection or controlling angiogenesis or inflammation.[128-132] Studies have shown that pluripotent stem cells (PSCs) survive when transplanted into an ischemic brain, and increase neuron numbers and partially alleviate functional deficits.[133-141] However, cells injected alone into ischemic brain lesion cavities have poor survival rates as they migrate from that hostile host environment to the adjacent parenchyma, indicating the need for adjuvant scaffolds to provide a supportive environment at the lesion site to improve the effectiveness of cell transplantation treatments. These tissue engineering materials could essentially bridge the cavity and provide a substratum for the grafted cells and their axons. Polymer-based tissue engineering materials have been well explored in this supportive role for cell grafts into ischemic brains,[142-149] and the work described here represents the first protracted (~9 months) assessment of human stem cell-derived neural progenitor cell grafts with SAP hydrogels.

4.4 Results and Discussion

The π-β self-assembly mechanism of Fmoc-SAPs has been previously investigated and explained.[7] π-π stacking of the aromatic Fmoc groups and formation of β-sheet structures between peptide sequences together form slightly twisted sheets that create a cylindrical structure.[7] Following this assembly mechanism (Figure 4.1A-G), the minimalist Fmoc-capped self-assembling peptide (SAP) sequences used here have several important features. The aromatic Fmoc capping groups engage in π-π stacking (Figure 4.1B), one of the driving

forces of the self-assembly process. The self-assembly also involves hydrogen bonding and charge-charge interactions between the peptide sequences themselves, forming β-sheet structures (Figure 4.1C). Because these interactions depend on charges, and the charges present in peptide molecules are dependent on pH, the self-assembly process is pH driven. This has been considered in the peptide sequence design.

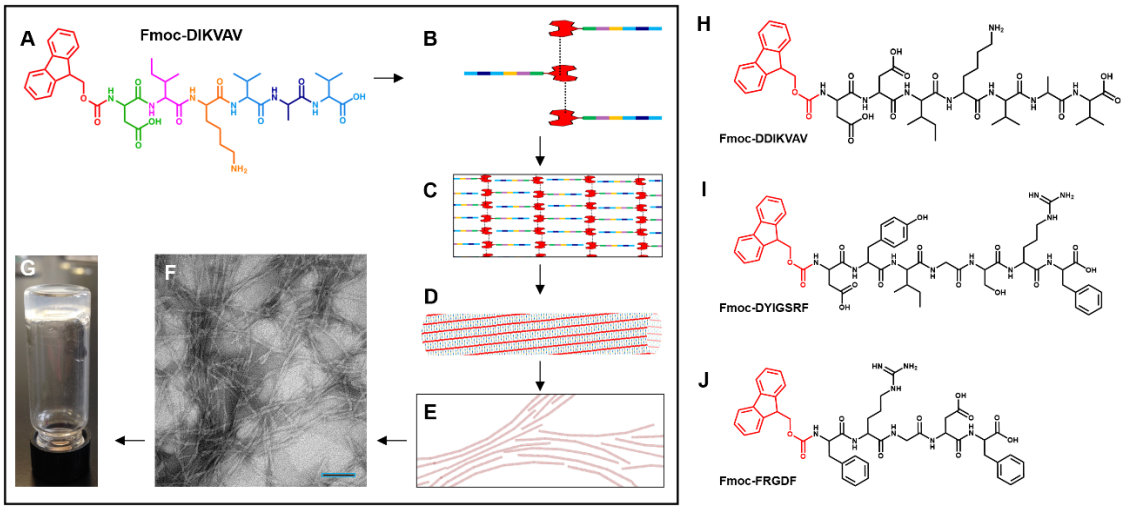

Figure 4.1: Self-assembling peptides. A-G: Self-assembly mechanism: molecular structure of Fmoc-DIKVAV (A), π-π stacking between aromatic Fmoc groups (B), additional anti-parallel β-sheet interactions between peptide sequences resulting in sheets (C) that wrap around into hollow nanofibres (D) and associate longitudinally in bundles (E), and TEM micrograph (F) and photo (G) of resulting nanofibrous hydrogel. Scale bar represents 100 nm. H-J: Molecular structures of other self-assembling peptide sequences: Fmoc-DDIKVAV (H), Fmoc-DYIGSRF (I), and Fmoc-FRGDF (J).

All the sequences studied here include biologically recognisable epitopes (Figure 4.1A,H-J), IKVAV or YIGSR from laminin, or RGD from fibronectin, both ECM proteins. The sequences also contain additional amino acid residues to engineering the molecules to allow self-assembly under physiological conditions. The additional aspartic acid (D) residues shift the pKa of the overall molecule, affecting the charges on the sequence such that self-assembly occurs at a lower pH (as the IKVAV sequence alone self-assembled under very basic conditions).[9] The additional aromatic phenylalanine (F) residues aid the self-assembly by engaging in additional π-π stacking.[78] All the sequences studied here do self-assemble at physiological pH, forming nanofibres that physically associate longitudinally with each other

due to surface interactions, and form into bundles of nanofibres and a nanofibrous hydrogel network (Figure 4.1D-F). Unlike some commercial SAP sequences, the minimalist Fmoc SAPs used here all present a high density of biologically relevant cues on the surface of the nanofibres.

Working first with the DIKVAV, DYIGSRF, and FRGDF sequences the material properties of the hydrogels were assessed. The TEM micrographs showed nanofibrous networks for all hydrogels (Figure 4.2A-C). Rheological analysis confirmed the viscoelastic properties of a hydrogel in all cases, with the storage modulus (G') greater than the loss modulus (G") and both mostly independent of frequency (Figure 4.2D-F).[9] The DIKVAV sequence was stiffer than the other two, with G' ~ 30 kPa, compared to ~100 Pa and ~200 Pa for the FRGDF and DYIGSRF sequences. These values all fall in the range appropriate to various soft tissues (0.1 – 40 kPa),[2] and while the ideal range for brain tissue is 0.1 – 1 kPa,[2] the exact stiffness for each sequence can be adjusted by changing the peptide concentration in the hydrogel. The spectroscopic analysis confirmed the intermolecular interactions, with FTIR major and minor peaks around 1630 cm^{-1} and 1690 cm^{-1} respectively indicative of β-sheets (Figure 4.2G).[9] The CD spectroscopy showed transitions in the in the 180-220 nm range indicative of anti-parallel β-sheets, and another in the 230-270 nm range, indicative of supramolecular ordering (Figure 4.2H).[9]

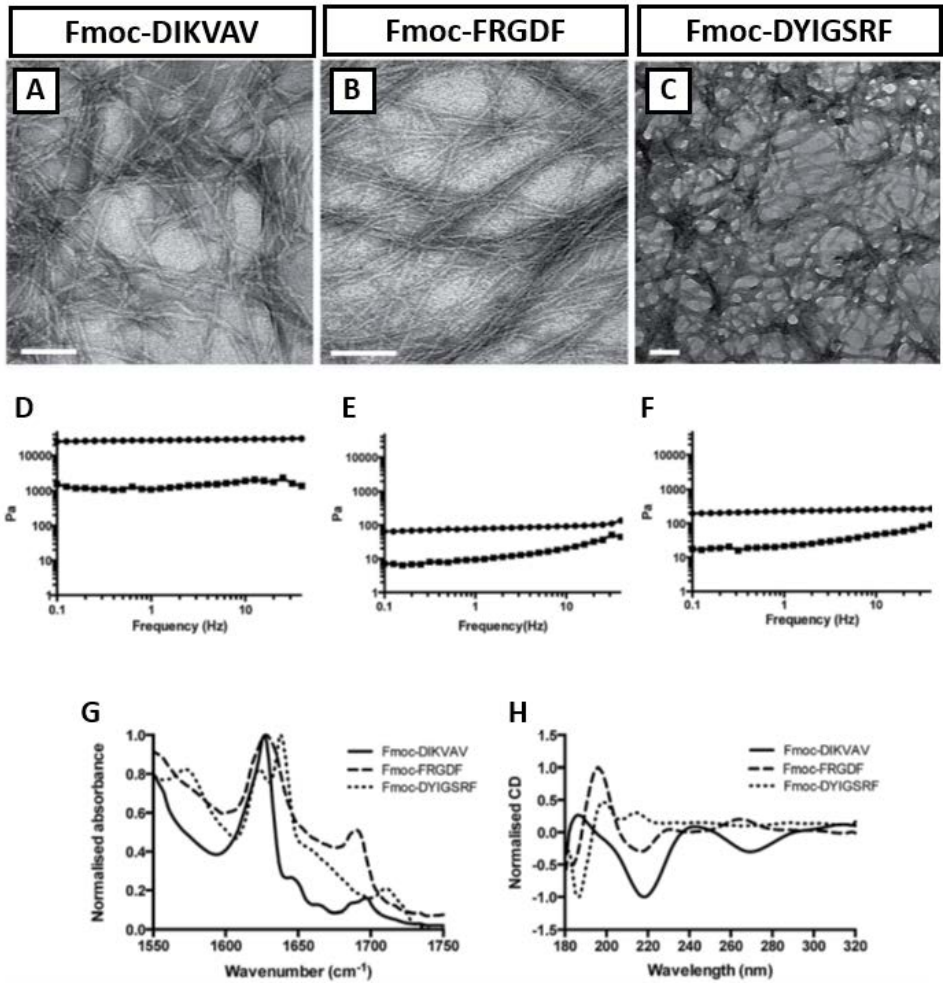

Figure 4.2: Material properties of SAP hydrogels. A-C: TEM micrographs of the SAP nanofibres. Scale bars represent 100 nm. D-F: Rheological analysis of SAP hydrogels showing storage modulus (G') (black circles) and loss modulus (G") (black squares). G-H: Spectroscopic FTIR (G) and CD (H) analysis of the SAP hydrogels. Fmoc-DIKVAV (A, D, solid line), Fmoc-FRGDF (B, E, dashed line), and Fmoc-DYIGSRF (C, F, dotted line).

The SAP hydrogels were tested biologically as carriers for use in cell replacement therapy (CRT), injected with GFP+ neural progenitor cells from embryonic mice (Section 3.5.1.4, 3.5.1.9). After 28 days, we assessed the graft (Section 3.5.2.2), looking at the overall graft region, the region permeated by GFT+ cells, as well as the graft core, with the highest density of implanted GFP+ cells (respectively, the brown and dark/black regions seen in the brain hemisphere (Figure 4.3D)). The overall graft innervation volume, as well as the number of GFP+ cells and GFP+ cell density in the core of the graft (Figure 4.3A-C), all showed no statistically significant difference between any of the hydrogels or the cell graft alone,

indicating that the materials are non-cytotoxic. Although not statistically significant, the FRGDF sequence did show lower GFP+ cell number, volume, and density. This supports the idea of designing tissue-specific SAP hydrogels, as the bioactive RGD portion of the sequence is from fibronectin rather than laminin. Laminin is a major constituent of the ECM of the brain and is known to modulate neural differentiation and neurite extension.[150] Fibre innervation specifically was assessed at 2 pre-determined locations starting at the edge of the graft and moving outward (Figure 4.3D-J). Again, there was no statistically significant difference between the groups, indicating that neurite outgrowth from the grafted cells was not impeded. This is particularly important as integration of transplanted cells and reinnervation of damaged tissue are key goals in cell replacement therapy required for last repair of neural circuitry.[151]

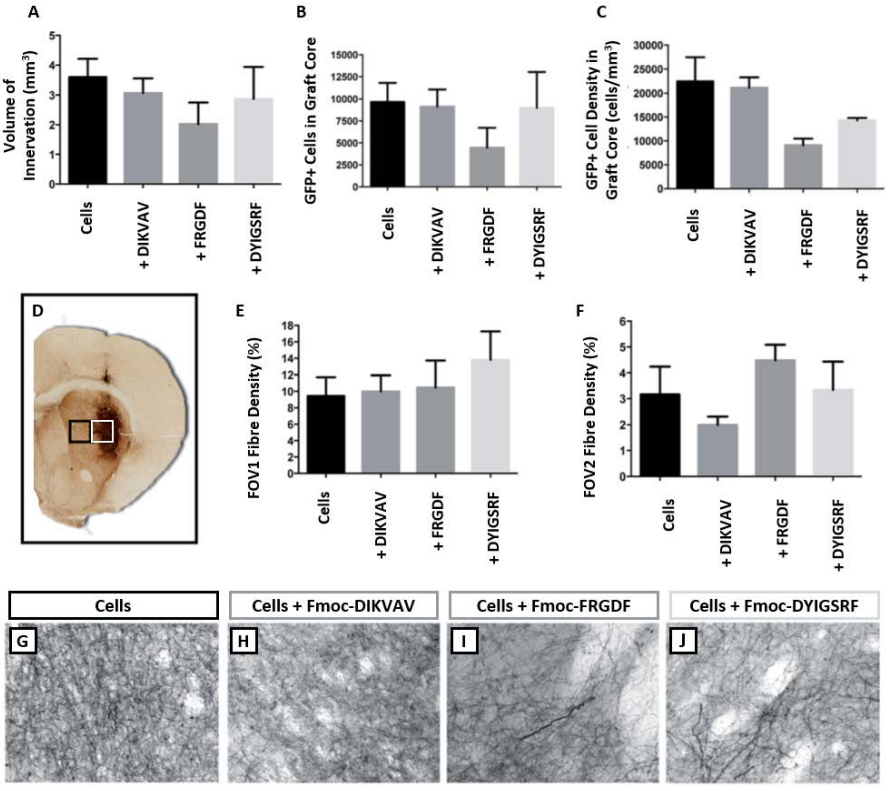

Figure 4.3: Cell grafts with SAP hydrogels. A: Total innervation volume. B-C: cell number (B) and cell density (C) of GFP+ cells in the graft core implanted into mouse brains alone and with the 3 SAP hydrogels studied. D: Locations within single brain hemisphere of field of view (FOV) 1 (white box) and FOV2 (black box), starting at the edge of the graft and moving outwards. E-F: Fibre density within FOV1 (E) and FOV2 (F). G-J: Images from FOV2 used to measure fibre density and to show innervation. Data represent mean ± SEM.

Another important concern with injuries in the CNS specifically is the formation of a glial scar, which is formed by reactive astrocyte and microglia cells forming a fibrotic scare and secreting inhibitory proteins.[152-154] For this reason, we also assessed the astrocyte and microglia response to the SAP hydrogel cell grafts among the host (GFP-) cells (Figure 4.4). Here the same trends continued, the DIKVAV was not treated as a foreign material, while the DYISRF sequence showed only minimal microglia response after 28 days. The FRGDF sequence showed significantly more microglia present as well as a non-statistically significant increase in astrocytes, indicating that although results above confirm its non-cytotoxicity, the fibronectin based sequence is not suitable for applications in the brain.

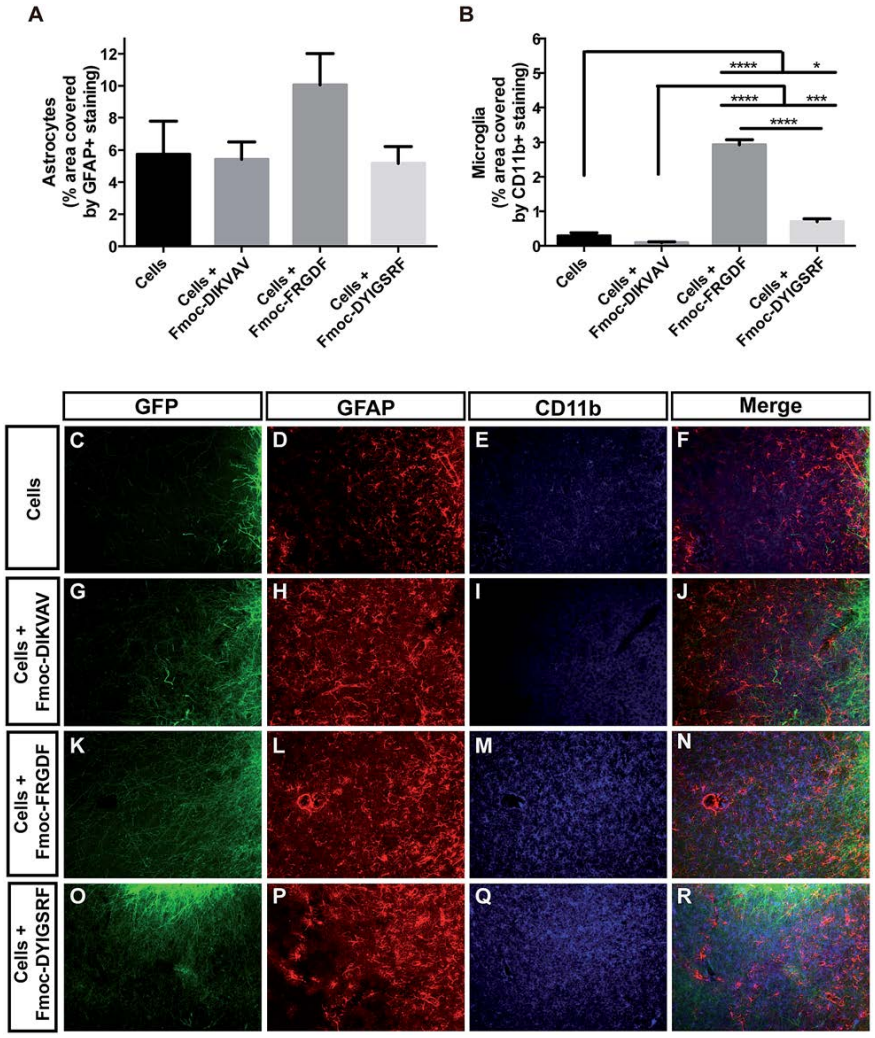

Figure 4.4: Astrocyte and microglia response to transplants. A-B: Astrocyte (A) and microglia (B) present at the edge of the grafts measured by fluorescence optical density. Data represent mean ± SEM, * $p < 0.05$, ** $p < 0.01$, ***(*) $p < 0.0001$. C-R: images of transplanted neural progenitor cells (GFP, green), astrocytes (GFAP, red), and microglia (CD11b, blue).

Fmoc-DDIKVAV was studied separately in a long-term 36-week (~9-month) study of transplantations of GFP+ human embryonic stem cells (hESCs) (Section 3.5.1.5) into a stroke model ischemic lesion (induced via injection of endothelin-1 (ET1) into the sensorimotor cortex) in rats (Section 3.5.1.7). First the material properties of this hydrogel were assessed (Figure 4.5) and found to be similar to the hydrogels studied above, concurrent with the self-assembly mechanism (Figure 4.1). Note that the hydrogel used here displayed a stiffness ~ 1000 Pa (Figure 4.5D), which is within the range of rat brain tissue stiffness of ~ 100-1000 Pa.[155] This sequence also contains the IKVAV sequence from laminin, and therefore appropriate for tissue-specific support in the brain.

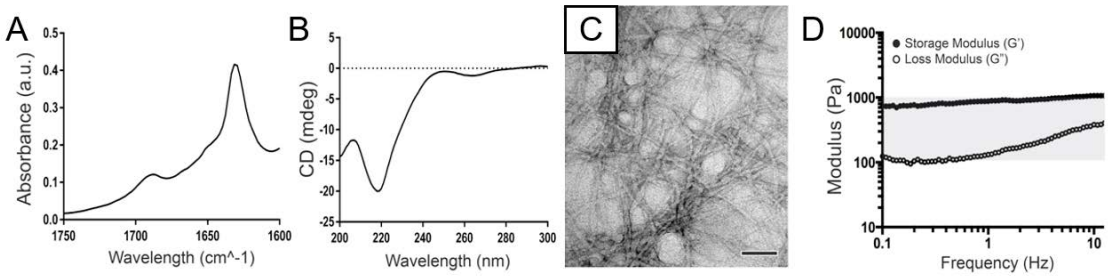

Figure 4.5: Material characterisation of Fmoc-DDIKVAV hydrogel. A-B: Spectroscopic FTIR (A) and CD (B) analysis. C: TEM micrograph. Scale bar represents 100 nm. D: Rheological analysis of viscoelastic properties showing storage modulus (G') (black circles) and loss modulus (G") (open circles). Grey region indicates stiffness range of rat brain tissue.

This more extensive study in rats allowed behavioural assessment (Section 3.5.2.7) of the treatment over 36 weeks as well as assessment of the SAP alone transplants. The staircase test was performed at several time points over 36 weeks to assess functional recovery, measuring the proportion of food pellets eaten from the stroke-affected left side (Figure 4.6A). The cell treatment alone resulted in a statistically significant improvement after 36 weeks, while the cells + SAP treatment saw significant improvement after only 16 weeks, with continual improvement out to 36 weeks surpassing that of the cells alone treatment. This shows that the SAP scaffold improves both the speed and degree of functional recovery. The cylinder (Figure 4.6B) and adjusted stepping (Figure 4.6C-D) tests showed similar results

after 36 weeks, with the cells + SAP treatment showing the most functional recovery followed by cells alone. Cells + SAP treatment showed a statistically significantly increase in the number of left (stroke-affected) paw touches in the cylinder test compared to the lesion untreated and treated with SAP alone (Figure 4.6B). In the adjusted stepping tests the cells + SAP treatment showed statistically significantly more forehand touches than all the other lesioned groups (Figure 4.6C), and was the only group with no statistically significant difference from the intact rats in backhand touches (Figure 4.6D). The Rotarod test revealed showed no statistically significant difference between any groups tested (Figure 4.6E), indicating no significant gross motor deficient impairing the rats' ability to remain on the rotating rod. These results altogether demonstrate the effectiveness of the SAP hydrogel in supporting and improving the success of transplanted cell grafts for neural recovery; while the SAPs alone treatment shows little to no positive effect on recovery, the SAP was able to significantly improve on the recovery seen with cells alone when used to support the cell graft.

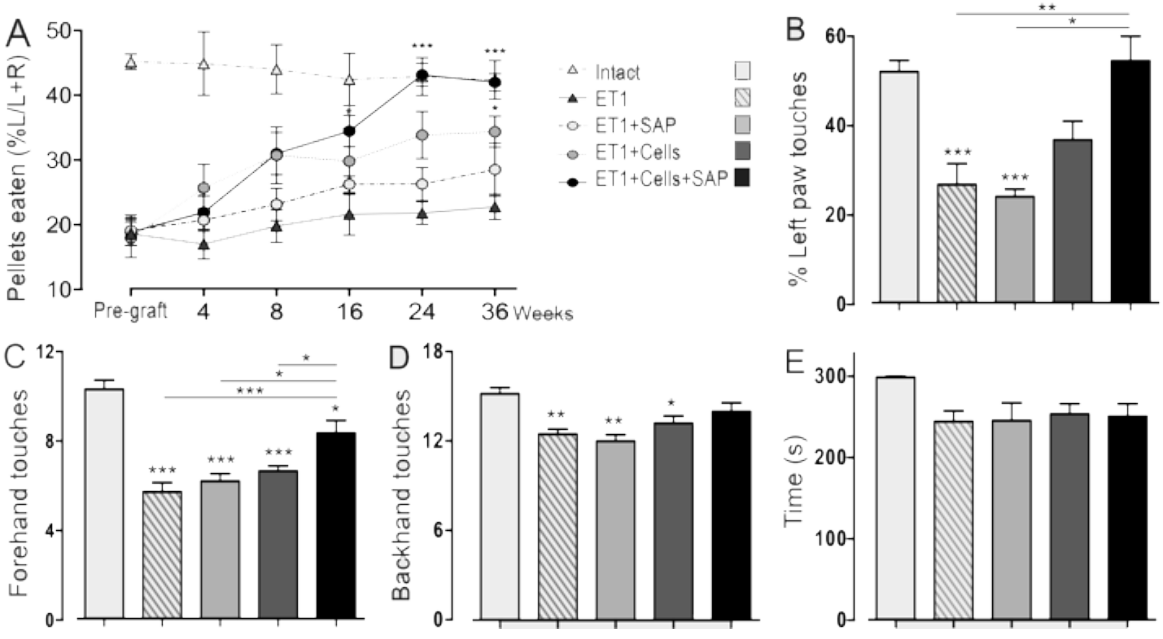

Figure 4.6: Behavioural assessment of cell and SAP transplantation. Staircase (A), cylinder (B), adjusted stepping (C-D), and rotarod (E) tests of untreated intact rats (n = 12) and right-side lesioned rats untreated (ET1) (n = 20) and treated with SAP (n = 8), cells (n = 12), and cells + SAP (n = 13). Data represent mean ± SEM, * $p < 0.05$, ** $p < 0.01$, *** $p < 0.001$.

Post-mortem analysis 36 weeks after treatment allowed detailed assessment of the cell grafts (Section 3.5.2.1). Staining of GFP+ cells highlighted the difference between cell alone and cell + SAP treatments in photomicrographs, with the cells + SAP graft being visibly larger and more integrated (Figure 4.7A-B). Quantitative assessment showed that the cells + SAP treatment resulted in significantly larger graft volume (Figure 4.7C) and cell number (Figure 4.7D) than the cells alone treatment, while the cell density was not significantly different between the two treatment groups (Figure 4.7E). Importantly, the inclusion of the SAP hydrogel within the material also resulted in an increased proportion of neurons in the graft (Figure 4.7F), indicating that not only does the SAP support graft cell survival, but also encourages neuronal differentiation.

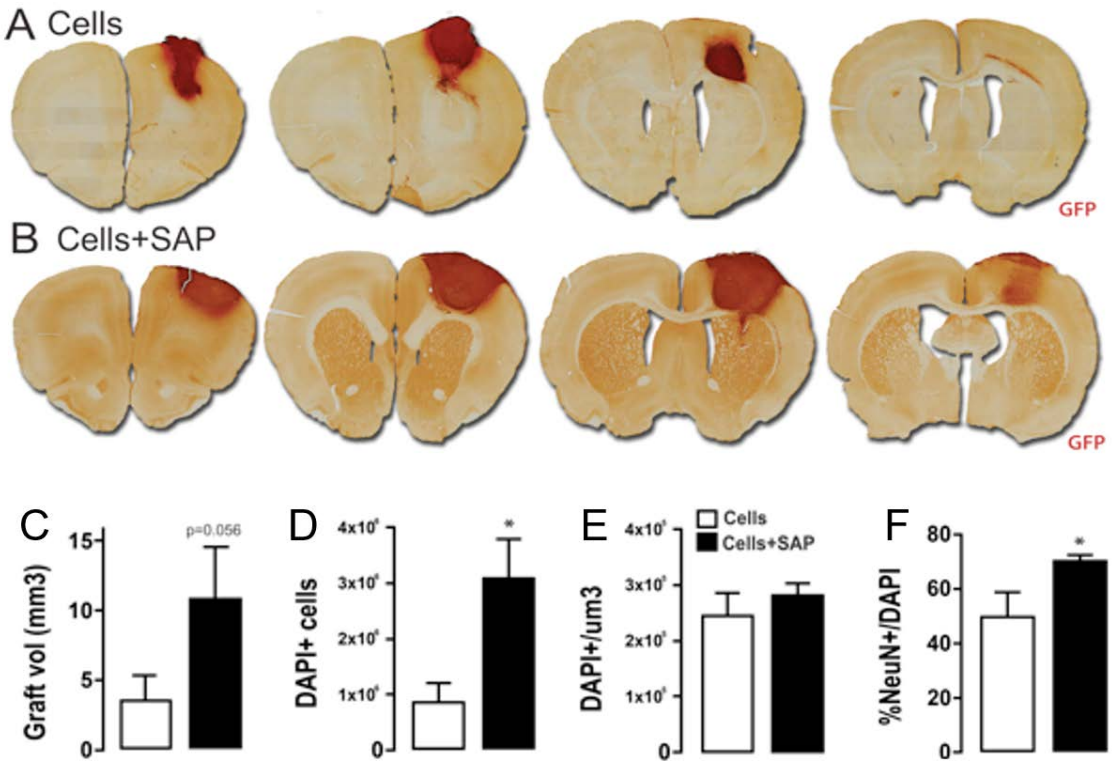

Figure 4.7: Assessment of cells alone and cells + SAP GFP+ graft transplants after 36 weeks. A-B: representative photomicrographs providing a coronal view of GFP+ (red) grafts within the cortex of cells alone (A) and cells + SAP (B) treatment of lesioned rats. C-F: Graft volume (C), cell (DAPI+) number (D), cell density (E), and proportion of neuron cells (NeuN+) after treatment with cells alone (white) and cells + SAP (black). Data represent mean ± SEM, * $p < 0.05$, ** $p < 0.01$, *** $p < 0.001$.

Cortical atrophy (determined as decrease in cortical volume) was also assessed, in animals who received acute treatment 6 days after the lesion and those who received delayed treatment 3 weeks after the lesion, to determine if the transplants would protect against secondary degeneration of the host tissue (Figure 4.8A). The untreated lesion appears as a large necrotic cavity after 1 week (Figure 4.8E) and without treatment resulted in a high degree of cortical atrophy (Figure 4.8A, F). Treatment with cells alone or cells + SAP significantly decreased the amount of cortical atrophy observed, consistent with results above of graft assessment. Regression shows a strong ($r^2 = 0.858$) inverse linear correlation between cortical atrophy and sensorimotor function as measured by the staircase test above, showing the incremental improvements from cells alone, then cells + SAP approaching the non-lesioned state (Figure 4.8B). Assessment of cortical atrophy also highlights the effect of acute vs. delayed treatment. While all treatment groups showed a trend for reduced atrophy with the acute treatment, the effect was most pronounced and only statistically significant for the cell + SAP treatment (Figure 4.8A, I, L), indicating that SAP supported cell grafts in particular should be administered early for the best results. The neuron (NeuN+) density was not affected by treatment timing, although it was affected by the treatment group, with cells and cells + SAP being the only groups to show a statistically significant increase in neuron density (Figure 4.8C). The lesion itself did not affect neurons disproportionately, so did not affect the neuron density compared to non-lesioned rats. The photomicrographs of NeuN+ staining for neurons show the degree of atrophy 36 weeks after treatment (Figure 4.8G-L) compared to intact (Figure 4.8D) and untreated lesioned (Figure 4.8F) brains, with the acute cells + SAP treatment showing the least atrophy and therefore the best ability to protect against secondary degeneration of host tissue.

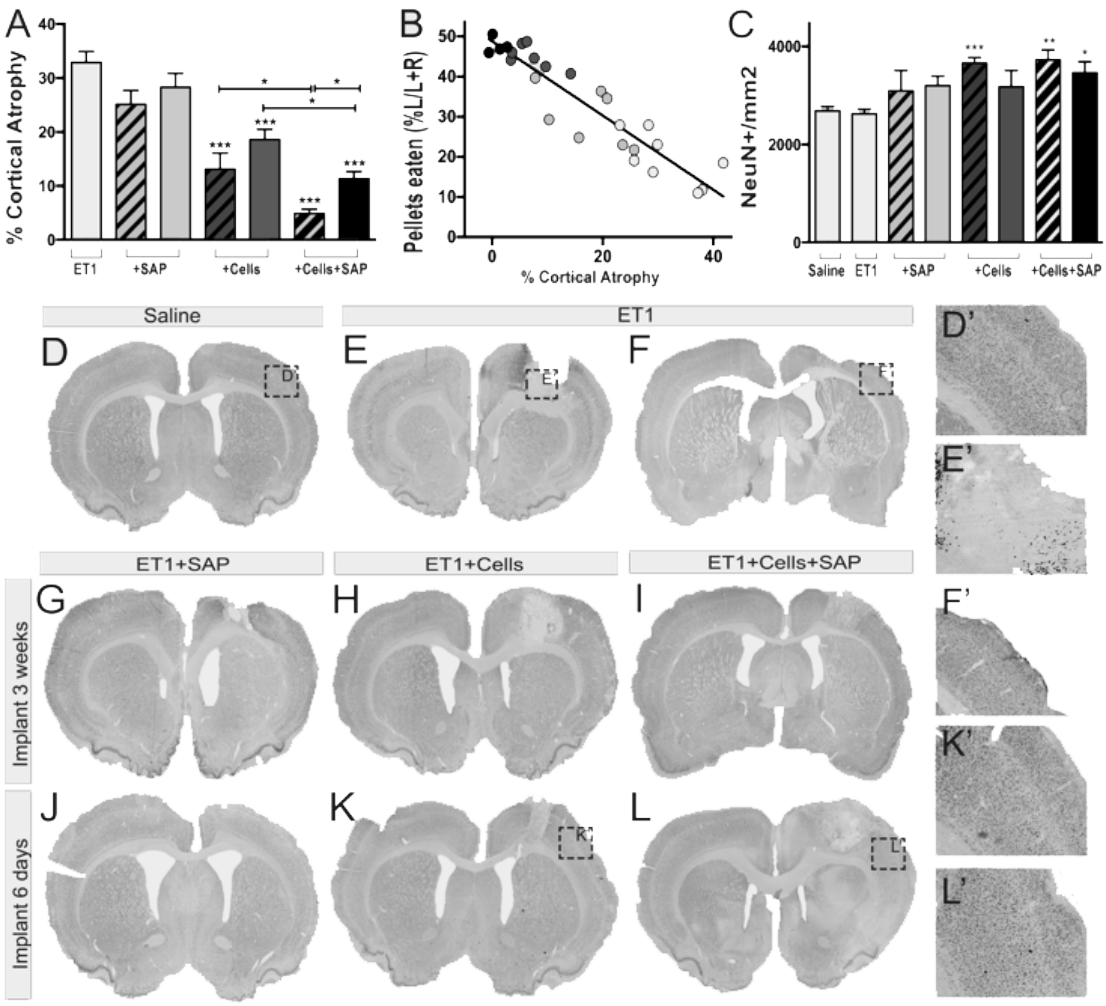

Figure 4.8: Acute implantation improves graft performance. A: Cortical atrophy of lesioned rats. B: Regression analysis of cortical atrophy and staircase test behavioural assessment for lesions alone (white) and treated with cells alone (light grey) or cells + SAP (dark grey), and non-lesioned/intact brain (black) rats. C: Neuron density in non-lesioned and lesioned rats. Results for treatments performed at 6 days (striped) and 3 weeks (solid) after lesion. Data represent mean ± SEM, * $p < 0.05$, ** $p < 0.01$, *** $p < 0.001$. D-L: Photomicrographs of NeuN+ staining for neurons 36 weeks after SAP (G, J), cells (H, K), and cells + SAP (I, L) treatments injected 3 weeks (G-I) and 6 days (J-L) after lesion. Comparative images of non-lesioned brain (D) and lesioned (ET1) brain after 1 week (E) and 36 weeks (F).

4.5 Conclusion

The work done here confirms the biocompatibility of the FRGDF, DYIGSRF, DIKVAV, and DDIKVAV sequence SAP hydrogels *in vivo*, as well as confirming the effectiveness of the DDIKVAV sequence in particular as a cell support material in cell graft treatment of ischemic brain injury. The work also confirms the validity of the tissue-specific design approach, engineering SAP hydrogels with peptide sequences relevant to the specific

tissue environment to achieve the best biological response. With this new evidence supporting previous *in vitro* studies, the potential of these minimalist and tissue-specific Fmoc SAP hydrogels as a supportive tissue engineering material is clear. While the materials did significantly improve the efficacy of cell transplantation treatment, they did not provide total recovery and so there is need to further improve these materials. The next step in their material development is the incorporation of additional therapeutic agents such as growth factors to improve the dynamic, trophic environment the materials provide.

Chapter Five

Non-Growth Factor Delivery

5.1 Chapter Details

Having established the biocompatibility of our minimalist SAP hydrogel materials, the next step in material development was to incorporate drug delivery. While this thesis focuses on providing temporally controlled delivery of growth factors from the SAP hydrogels, there are many non-growth factor therapeutic agents that can be beneficial to incorporate. As previously discussed in Chapter Two, a broad system-wide view of tissue engineering materials is required for maximum therapeutic advantage. Additionally, engineering SAP hydrogels for the presentation of non-growth factor therapeutic agents can provide both delivery strategies adaptable to growth factors and insights about the material potentially applicable to growth factor delivery systems. This chapter describes work done on projects for delivery of two distinct non-growth factor therapeutics, viral vectors and an anti-inflammatory polysaccharide, and their applicability to growth factor delivery.

The fucoidan section of this chapter briefly describes work published in the research article listed below, and included in full in Appendix C:

Rui Li, Sivapriya Pavuluri, Kiara Bruggeman, Benjamin M. Long, Andrew J. Parnell, Anne Martel, Steven R. Parnell, Frederick M. Pfeffer, Andrew J.C. Dennison, Kevin R. Nicholas, Colin J. Barrow, David R. Nisbet, Richard J. Williams, "Coassembled nanostructured bioscaffold reduces the expression of proinflammatory cytokines to induce apoptosis in epithelial cancer cells", *Nanomedicine: Nanotechnology, Biology and Medicine*, 2016, vol. 12, pp. 1397-1407 – Reproduced with permission from Elsevier

The viral particle section of this chapter describes work published in the research article listed below, and included in full in Appendix D:

Alexandra L. Rodriguez, Ting-Yi Wang, Kiara F. Bruggeman, Rui Li, Richard J. Williams, Clare L. Parish, David R. Nisbet, "Tailoring minimalist self-assembling peptides for localised viral vector gene delivery", *Nano Research*, 2016, vol. 9, pp. 674-684 – Reproduced with permission from Springer

5.2 Abstract

Two distinct therapeutic agents, the polysaccharide fucoidan and viral vectors, were incorporated into SAP hydrogels to provide sustained presentation. In both cases the physical interactions with the peptide nanofibres were fundamental to successful presentation of the therapeutic. While working with fucoidan, a novel gold nanoparticle tagging method was developed to allow visualisation via electron microscopy of the interactions with the nanofibres. Experiments confirmed that fucoidan formed strong physical associations with the nanofibres, keeping it immobilised in the hydrogel while maintaining anti-cancer bioactivity demonstrated by selective inhibition of cancer cells *in vitro*. To immobilise viral vectors to the peptide nanofibres, the peptide sequence itself was re-engineered with a terminal lysine residue to provide free positive charges for electrostatic interactions with the negatively charge surface of viral capsids, and this immobilisation was used to successfully localise virus transfection *in vivo*. Both cases have parallels with growth

factor delivery and highlight interactions with the peptide nanofibres that can be used to further develop delivery systems from SAP hydrogels.

5.3 Fucoidan

5.3.1 Background

Fucoidan refers to any of a group of a sulphated polysaccharides found in seaweed, and they are currently being explored as non-steroidal therapeutics in cancer treatment for their anti-inflammatory and anti-mitogenic properties in addition to biocompatibility.[156-159] This is particularly applicable to endothelial cancers (e.g.: oral, pancreatic, and colon), where epidemiological studies have shown chronic inflammation to be a causative factor for cancer.[160-162] Studies have also shown fucoidan's ability to halt cell progression and induce apoptosis in cancer cell lines.[163] One of the major obstacles to fucoidan treatment is its high solubility, which effectively prevents sustained presentation *in vivo*.[164,165] In this way fucoidan is very similar to growth factors, although with growth factors it is enzymatic degradation that limits the sustained presentation of soluble factors.

Here we aimed to provide sustained presentation of fucoidan via incorporation with a SAP hydrogel, which would itself provide a stable microenvironment to promote healthy tissue following surgical excision.[166] To do this, we first investigated the interactions between the polysaccharide fucoidan and the SAP nanofibre structures. While SAP nanofibre visualisation via electron microscopy is established, single molecule solubilised fucoidan is too small and too atomically lightweight to be observed alone or using staining. To visualise their interactions, we adapted a method of gold nanoparticle synthesis to create gold nanoparticle tagged fucoidan, to provide a discrete and electron dense location indicator for fucoidan as it interacted with SAP nanofibres. This allowed the investigation of interactions between SAP nanofibres and the polysaccharide fucoidan, as well as with inorganic nanoparticles.

5.3.2 Results and Discussion

Gold nanoparticles are commonly produced from solution via reduction under reflux.[167] An aqueous solution of gold from hydrogen tetrachloroaurate (III) under reflux with a reducing agent yields solid gold according to the chemical half reaction described in Figure 5.1A. Maintaining dispersed nanoparticles, as opposed to large agglomerations, requires a stabilising agent. The surfaces of the solid metal nanoparticles have some inherent solubility, resulting in a layer of positive charge around the nanoparticles. A stabilising agent with negative charge forms a layer on the surface of the particles, creating a negative zeta potential and preventing their agglomeration. Often the reducing agent itself can act as a stabiliser, as is the case with the most common citrate reduced method,[168] and fucoidan can also be used as a reducing and stabilising agent.[167] Here, using fucoidan, the sulphate groups on the long polysaccharide fucoidan from *Undaria pinnatifida* (Figure 5.1B) act as a reducing agent and provide the opposing negative charge layer as they electrostatically bind to the gold nanoparticles (Figure 5.1C), essentially providing gold nanoparticle (GNP) labelled fucoidan.

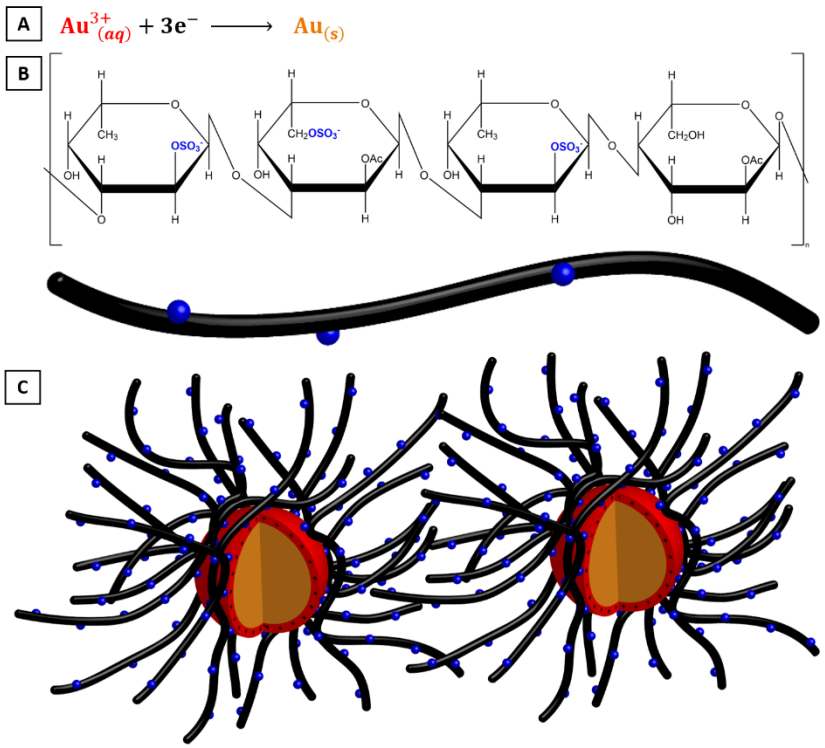

Figure 5.1: Fucoidan stabilised gold nanoparticle synthesis. A: Half reaction of the reduction of gold from solution to solid. B: Chemical structure of fucoidan polysaccharide and diagrammatic representation of main

chain (black) and negatively charged sulphate groups (blue). C: Diagrammatic representation of fucoidan stabilised gold nanoparticles, cutaway shows the solid gold interior of the nanoparticles and charged layer of positive ions (to demonstrate the nature of interaction only, not to scale).

In this work the minimalist Fmoc peptide sequence FRGDF, containing RGD from the common ECM protein fibronectin, was used. The fucoidan was mixed with the dry peptide powder and co-assembled into the nanofibrous SAP hydrogel. The GNP labelled fucoidan was used to visualise the interactions between the SAP nanofibres and fucoidan via TEM. To avoid potential ambiguity, samples were observed without the use of the normal uranyl formate negative stain. This limited image quality, as organic peptide molecules are not electron rich, but ensured that the gold nanoparticles were the only source of electron dense material present in the samples, allowing black dots to be identified confidently as gold nanoparticles. Under these conditions, the GNP labelled fucoidan was observed to closely associate with the SAP nanofibres (Figure 5.2A). The nanoparticles visible on the nanofibre surface indicate that the fucoidan is associating closely with the peptide. To test the strength of this association, we subjected the gel to gentle washing in water (Section 3.4.4) and the GNP labelled fucoidan retained its association with the peptide nanofibres (Figure 5.2B-C), indicating a strong association between the fucoidan and the peptide nanofibres. This strength of association was not observed after washing SAP hydrogels prepared with separate GNP and unlabelled fucoidan (Figure 5.2E), nor those prepared with independent GNP alone (Figure 5.2F), indicating that the association is caused by interactions with the fucoidan not the GNP.

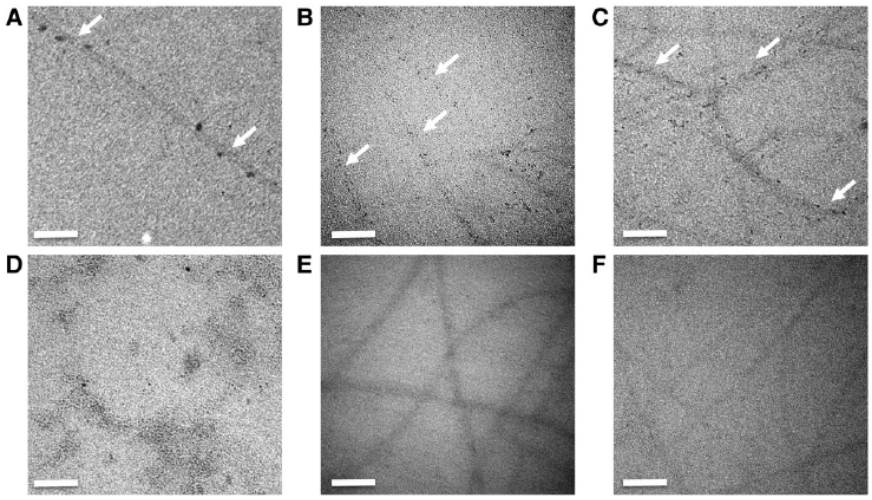

Figure 5.2: TEM micrographs of GNP labelled fucoidan and SAP nanofibres. A-C: GNP labelled fucoidan shows co-localization along peptide fibrils before (A) and after (B-C) washing of the hydrogel. D: GNP labelled fucoidan alone. E: Hydrogel co-assembled with unlabelled fucoidan and independent GNP shows no residual GNP post-washing. F: Hydrogel co-assembled only with independent GNP shows no residual GNP post-washing. Scale bars represents 100 nm.

This strong association can be explained by the similar chemical structures of the peptide and fucoidan materials, with the charged sulphate groups interacting with charged amine groups present in the peptide sequence (from the arginine (R) residues). These results also suggest that similar materials (i.e. polysaccharide chains with charged groups) might associated with the peptide nanofibres as well, a relationship that will be explored and exploited in the next chapter. In this work, the fucoidan material was further characterised and the biological effectiveness was assessed. The key results are discussed below, and the full work is included in Appendix C.

The SAP gels were tested with and without fucoidan with both healthy and cancerous cell lines, human mammary fibroblast cells (hMFCs) and human tongue squamous cell carcinoma cell line SCC25 respectively (Section 3.5.2.5.2). Testing cell viability over 3 days the healthy cells remained highly viable on both materials while the fucoidan loaded material resulted in significant decrease in viability of the cancer cells only (Figure 5.3A). The different responses from the two cell lines demonstrate the specific anti-cancer effect of fucoidan, as opposed to general cytotoxicity. Specifically, the fucoidan was found to have anti-inflammatory and

anti-mitogenic effects on the cancer cell line. Fucoidan loaded materials induced significant downregulation of genes involved in the NFκβ pro-inflammatory pathway (interleukins: IL-1α, IL-1β; and tissue necrotic factor (TNF))[169] and CEP55, a cytokinesis promoter and marker for the uncontrolled C2 to M cell cycle progression seen in oral cancer[169] (Figure 5.3C, Section 3.5.2.5.2, 3.5.2.6). Lipopolysaccharide (LPS), known to induce inflammation, was used to challenge the cells and while that did cause upregulation of all tested genes on the unloaded control hydrogel, the fucoidan loaded hydrogel negated the effect of LPS, resulting in little to no upregulation of the pro-inflammatory cytokine genes studied.

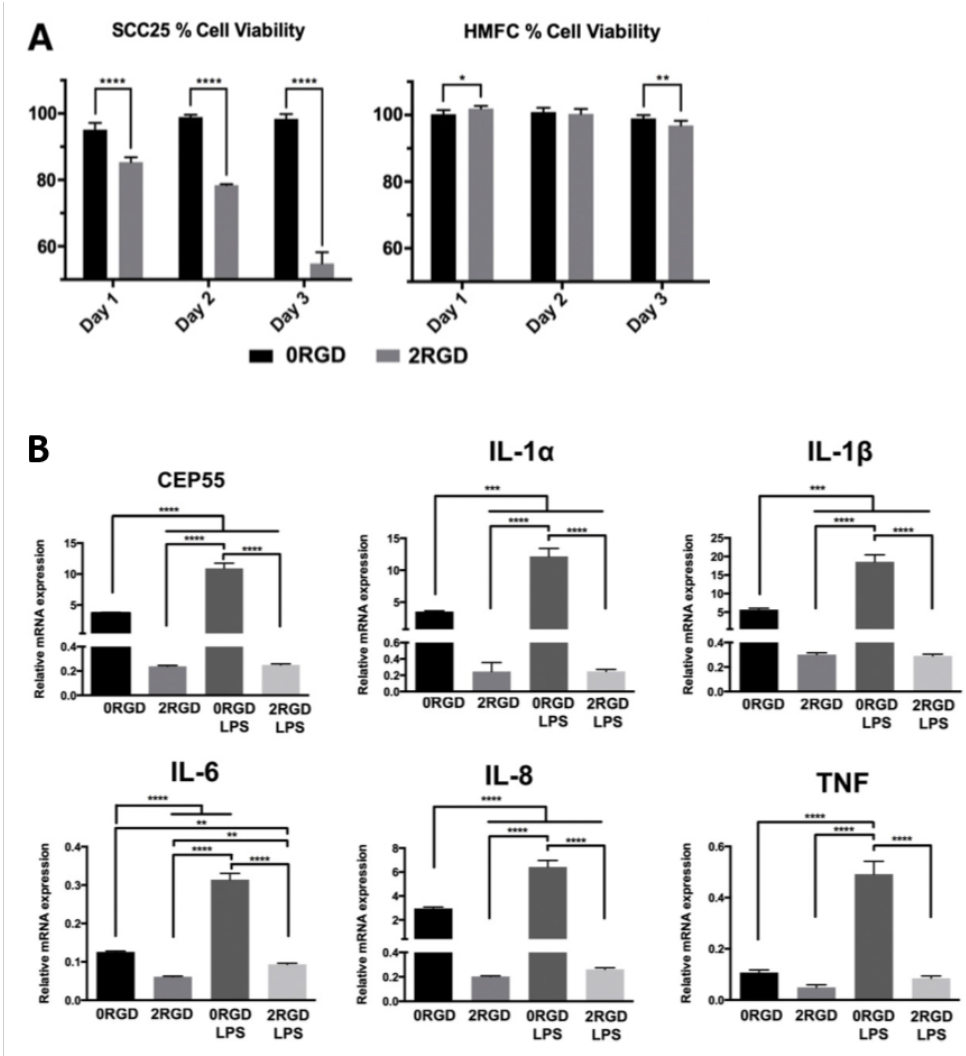

Figure 5.3: Confirmed biological effectiveness of fucoidan loaded in SAP hydrogel. A: Cell viability of cancer (SCC25) and healthy (hMFC) cell lines grown on fucoidan loaded (2RGD) and control SAP hydrogel. B: Mitogenic and pro-inflammatory gene expression profiles in LPS stimulated and non-stimulated cancer (SCC25) cells as determined by qPCR. *P = 0.05, **P = 0.01, ***P = 0.001, ****P = 0.0001.

5.4 Viral Vectors

5.4.1 Background

Viral vectors are another therapeutic agent with great potential. They are used for gene delivery in treatments being developed for cancer, autoimmune diseases, and neurodegenerative diseases.[170,171] They are particularly interesting in a drug delivery context because they allow decoupling between the agent being delivered and the drug being received. For growth factor delivery, specifically, instead of delivering the protein directly a virus is delivered to transfect local cells with the genetic material required to produce the desired protein.[172-176] This removes the need for high concentrations required for growth factors to achieve therapeutic benefit because it bypasses many of the obstacles inherent to the growth factors, such short half-lives, susceptibility to enzyme degradation, and inability to permeate selective barriers like the blood brain barrier.[177] Additionally, many growth factor delivery strategies are limited to a subset of growth factors based on their specific binding sites[66] or charge,[178] and different electrostatic and material properties between growth factors can effect individual delivery characteristics,[65] making the delivery systems inconsistent between different growth factors. Using viral vectors eliminates that variation, as the same viral vector can be used to deliver genetic material for different growth factors.

The use of viral vectors does have its own challenges and limitations. Currently viral vector therapies can experience spreading of the virus to non-target locations, neutralisation by the host immune system, and low transduction efficiencies.[170] Research is being done using biomaterials to deliver viral vectors in order to alleviate these problems using strategies common in drug delivery, including encapsulation in nanoparticles and microspheres,[179,180] incorporation into biocompatible hydrogels,[181,182] and immobilisation.[183-185] Tissue engineering biomaterials designed for biocompatibility provide some protection from the host immune response while also potentially improving the localisation of the delivery.

Here, once again using SAP hydrogels, we aimed to mix viral vectors with the hydrogel to provide localised delivery based on electrostatic interactions with the peptide nanofibres. Recently, non-minimalist SAPs have been demonstrated to effectively deliver genetic material to human mesenchymal stem cells in culture via recombinant adeno-associated virus.[186] Research has also been done using amine moieties, which exist physiologically as positively charged groups (NH3+), to immobilise viral vectors, which have a negatively charged viral capsid to a surface and found improved transduction efficiency.[187] Here we combine these findings, engineering a minimalist SAP hydrogel to provide increased localisation of viral vector delivery.

5.4.2 Results and Discussion

To optimise the peptide for viral vector immobilisation we adjusted an established peptide sequence with the addition of a terminal lysine (K) residue to provide available amine groups, and therefore positive charge, to immobilise the viral particles (Figure 5.4). The minimalist peptide Fmoc-DDIKVAV has previously been established as an appropriately biocompatible sequence for neural tissue application and was developed around the IKVAV sequence found in the ECM protein laminin, which is common in the brain.[9] The additional aspartic acid (D) residues were included in the rational design of the peptide to tune the pK_a properties of the molecule to ensure that the pH driven self-assembly occurred under physiological conditions.[9] Here we synthesised the new sequence Fmoc-DDIKVAVK. Since the Fmoc is an N-terminal group, the amine groups of the amino acid backbones are unavailable. Additionally, while the IKVAV sequence itself does include a K residue, this is not true for all minimalist SAP sequences, and in any case, the C-terminal position was selected as the ideal location for the viral immobilising K as it would be less restricted and more able to interact with the viral capsids.

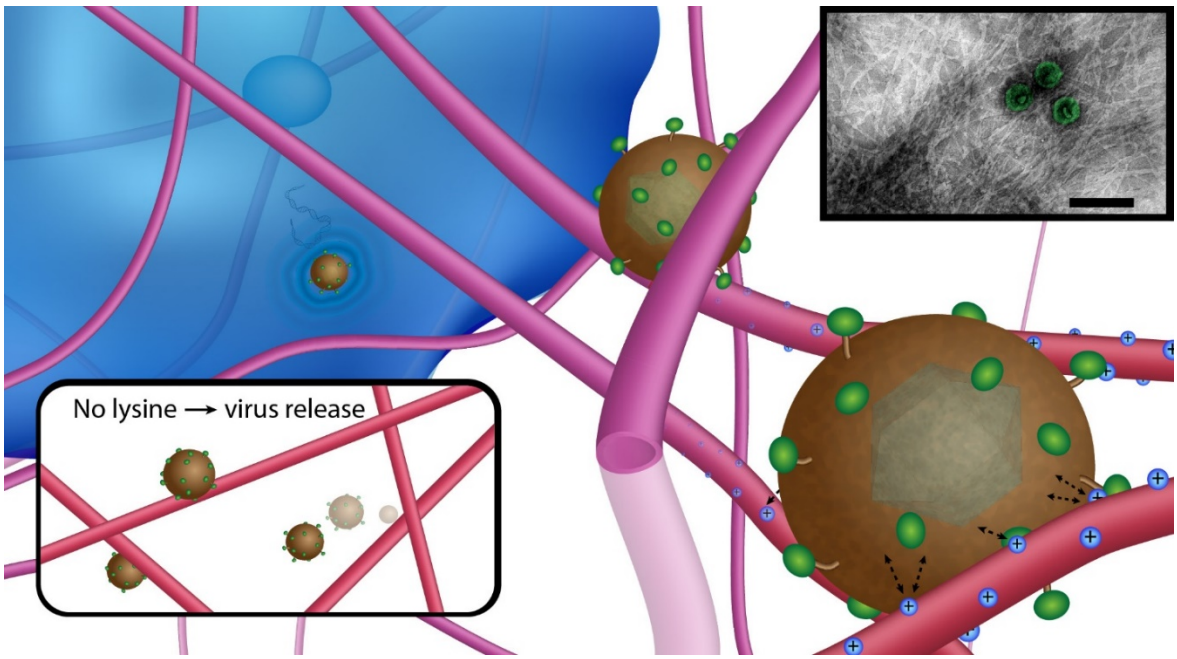

Figure 5.4: Schematic of terminal lysine driven viral vector immobilisation. Terminal lysine residues provide positive charges on the peptide nanofibre surface, which interact with negatively charged viral capsids, immobilising them to the fibres. Inserts show the proposed diffusive release from unmodified peptide nanofibres and TEM micrograph of viral capsids within the peptide nanofibre network (viral capsids false coloured for identification, scale bar represents 200 nm).

The modified peptide sequence was tested to ensure that it still underwent self-assembly into a nanofibrous hydrogel and that the material properties were maintained. The DDIKVAVK sequence did form a hydrogel visually comparable to that of DDIKVAV (Figure 5.5A) and rheological analysis confirmed no change in the hydrogel stiffness (Figure 5.5B-C). Titration was performed to investigate the pK_a properties of the two sequences, and the addition of the basic lysine group did slightly increase the gelation point, the effective pK_a observed as a plateau in the titration curve, from ~7.0 to ~7.8 (Figure 5.5). This was expected based on previous work using acidic D groups to decrease it.[9] The shift was minimal however, and the peptide was able to form a gel at physiological pH. Spectroscopic analysis confirmed the self-assembly mechanism via FTIR (Figure 5.5E) and CD (Figure 5.5F). The FTIR spectra show that the large and small peaks at 1630 cm^{-1} and 1690 cm^{-1} respectively are maintained, indicative of β-sheets.[61] The large dip in the CD spectra is also maintained and indicative of β-sheets.[61] Together these results confirm that the addition of a terminal K

residue does not interfere with the formation of a hydrogel and has only a minor effect the hydrogel's pH-responsive properties.

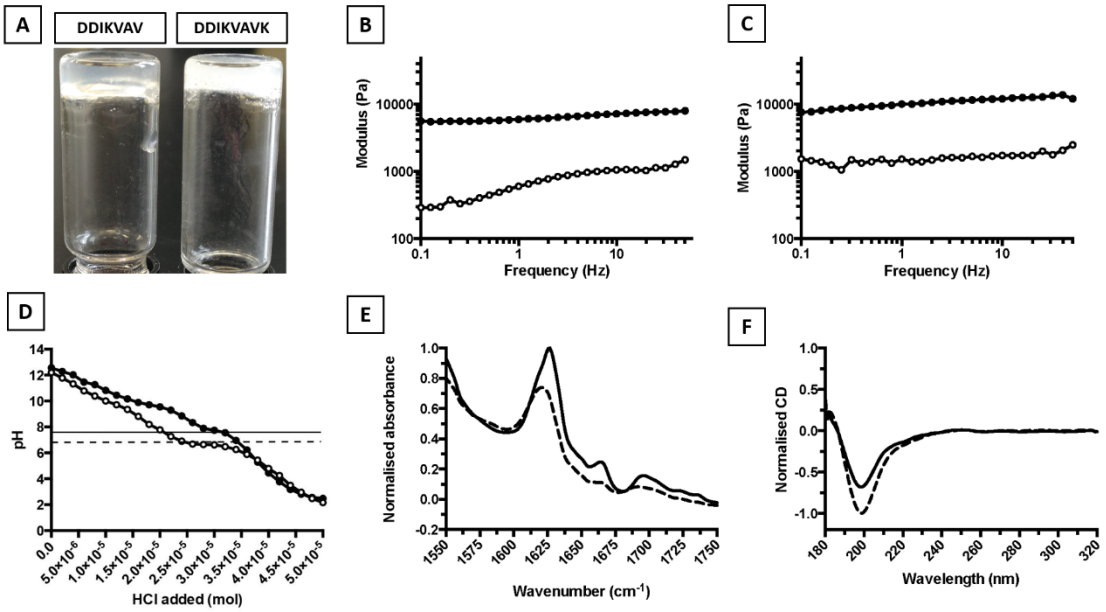

Figure 5.5: Material properties of SAP hydrogel with and without terminal lysine. A: Photos of inverted hydrogels from DDIKVAV and DDIKVAVK peptides. B-C: Rheological analysis of DDIKVAV (B) and DDIKVAVK (C) hydrogels, showing storage moduli G' (closed circles) and loss moduli G" (open circles). D: Titration curve for DDIKVAV (open circles) and DDIKVAVK (closed circles) showing a slight shift in pK_a (DDIKVAV – dashed line; DDIKVAVK – solid line). E-F: FTIR (E) and CD (F) spectroscopic analysis of DDIKVAV (solid line) and DDIKVAVK (dashed line).

AFM and TEM imaging confirm the presence of nanofibres in both hydrogels formed (Figure 5.6A-B, E-F), although the additional K residue did result in increased bundling of fibres. This increased bundling, increased supramolecular ordering, also explains the slightly larger dip observed for the DDIKVAVK sequence in the CD spectroscopy above (Figure 5.5F). Lentivirus particles loaded into both hydrogels (Figure 5.6C, G) appear embedded in the nanofibrous network, so to determine the ability of each hydrogel to immobilise and retain the viral particles the loaded hydrogels were incubated in PBS over 5 days to allow non-immobilised viral particle to diffuse out (Section 3.4.2). The unmodified DDIKVAV hydrogel showed substantial and ongoing release of the viral particles, while the DDIKVAVK hydrogel retained the viral particles within the hydrogel, with minimal

amounts detectable in the PBS (Figure 5.6D). This result is key to the project and demonstrates the success of the terminal K in viral particle immobilisation within the hydrogel.

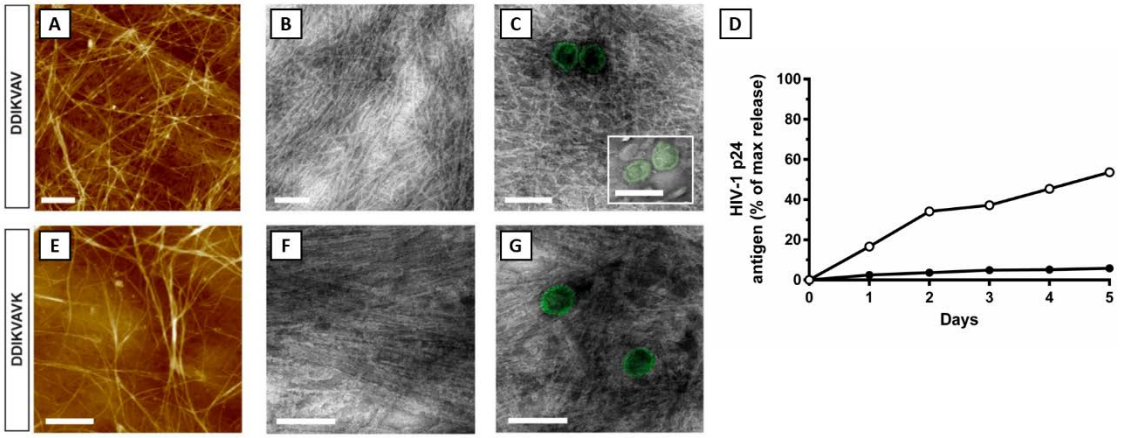

Figure 5.6: Virus loading in SAP hydrogels. AFM (A, E) and TEM (B, F) micrographs of DDIKVAV (A-C) and DDIKVAVK (E-G), including TEM micrographs of virus loaded hydrogels (C, G). Insert shows viral particles alone. Scale bars represent 1 μm for AFM and 200 nm for TEM. Viral vectors false coloured for identification. D: Cumulative release profile of viral vectors from DDIKVAV (open circles) and DDIKVAVK (closed circles).

With the immobilisation method confirmed, and hydrogel material properties maintained, the materials were tested *in vivo* for their biological efficacy and ability to specifically transfect only a highly localised environment. mCherry lentivirus was injected into mouse brain (striatum) alone and loaded into the two hydrogels (Section 3.5.1.10), and the transfection was assessed after 3 weeks (Section 3.5.2.5.1). The mCherry infected cell number (Figure 5.7A) and striatal volume (Figure 5.7B) showed the same trend, with the most transfection achieved from the virus alone, followed by the unmodified gel, and significantly lower transfection when using the lysine modified hydrogel. These results indicate that the hydrogel material and K modification successfully localised the transfection, preventing spreading of the virus to off-target tissue. The cell densities remained similar in all groups (Figure 5.7C), indicating that neither the hydrogel nor the K modification affect the nature of the transfection, only it's localisation. Chromogenic staining mCherry+ cells gave a clear visualisation of the effective localisation achieved using the K modified hydrogel (Figure

5.7D-F). These results together confirm that the hydrogel system does not impede the bioactivity of the virus, and that the K modification method is able to highly localise transfection. This is a promising development with the potential to achieve more targeted therapeutic viral delivery and to avoid off-target side effects.

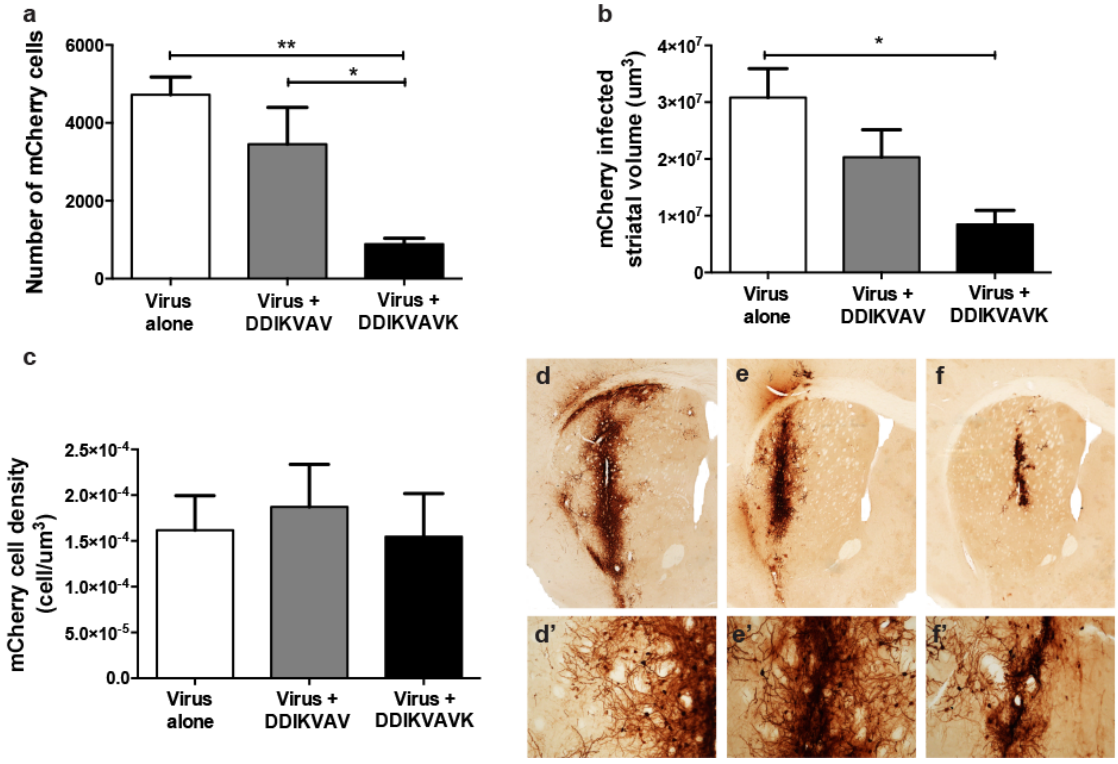

Figure 5.7: Biological efficacy and localisation of viral transfection 3 weeks post injection. mCherry+ cell number (A), infected striatal volume (B), and cell density (C). Data represent mean + SEM. *P < 0.05, **P < 0.01. Chromgoenic stain of mCherry+ cells in mouse brains treated with virus alone (D), virus in DDIKVAV hydrogel (E), and virus in DDIKVAVK hydrogel (F) at 5x (top) and 20x (bottom) magnification.

5.5 Conclusion

Working with fucoidan, the cell response confirmed the maintained presentation and bioactivity of fucoidan when loaded into the SAP hydrogel, overcoming the solubility obstacle that normally prevents sustained delivery. The specific investigation of the material component interactions suggests that the charged polysaccharide fucoidan physically associates strongly with the peptide nanofibres. Together these results indicate that simple loading could provide prolonged presentation of similar therapeutic agents, but without any temporal control.

Similarly, working with viral particles, electrostatically driven immobilisation was used to achieve highly localised presentation of viral particles, significantly reducing the infected volume relative to other delivery methods. As a means of growth factor delivery, viral vectors inherently provide a permanent or very long-term source of the protein. Again, this method would overcome the issues of short half-lives and degradation preventing sustained delivery, but again this method offers no significant temporal control.

Achieving sustained delivery is the first obstacle to overcome in achieving finer temporal control of delivery, and both systems explored here represent interesting additions to the broader field of drug delivery and tissue engineering material design. Also, both systems rely on and highlight the electrostatic interactions that occur between peptide nanofibres and other materials loaded into the hydrogel network. These specific material interactions will be explored and exploited in the next chapter to achieve the desired temporal control of delivery.

Chapter Six

Delivery System: Short (Hours) Delay

6.1 Chapter Details

Using interactions explored in Chapter Five, this chapter describes the successful development of the first temporally controlled growth factor delivery system from a tissue-specific SAP hydrogel, achieving a short delay in the release of growth factors. This chapter has been published as the research article listed below:

> Kiara F Bruggeman, Alexandra L Rodriguez, Clare L Parish, Richard J Williams, David R Nisbet, "Temporally controlled release of multiple growth factors from a self-assembling peptide hydrogel", *Nanotechnology*, 2016, 27 –

6.2 Abstract

Protein growth factors have demonstrated great potential for tissue repair, but their inherent instability and large size prevents meaningful presentation to biologically protected nervous tissue. Here, we create a nanofibrous network from a self-assembling peptide (SAP) hydrogel to carry and stabilize the growth factors. We significantly reduced growth factor degradation to increase their lifespan by over 40 times. To control the temporal release profile, we covalently attached polysaccharide chitosan molecules to the growth factor to

increase its interactions with the hydrogel nanofibres and achieved a 4-hour delay, demonstrating the potential of this method to provide temporally controlled growth factor delivery. We also describe release rate based analysis to examine the growth factor delivery in more detail than standard cumulative release profiles allow and show that the chitosan attachment method provided a more consistent release profile with a 60% reduction in fluctuations. To prove the potential of this system as a complex growth factor delivery platform we demonstrate for the first time temporally distinct release of two growth factors from a single tissue specific SAP hydrogel: a significant goal in regenerative medicine.

6.3 Introduction

Growth factors play important roles as short lived and fast acting signals, influencing cell fate and promoting survival for improved tissue repair. However, their high cost and inherent instability in physiological environments presents a challenge for long-term, sustained, therapeutic delivery.[31] Systemic growth factor delivery into the bloodstream carries overwhelming cost and risk of off-target side effects. Within the central nervous system (CNS) there are additional challenges involved in transporting such large molecules across the blood brain barrier (BBB).[20] Therefore, to ensure therapeutic benefit, growth factors must be directly introduced into the CNS. Current sustained delivery strategies involve indwelling cannulas and infusion pumps, which cause additional trauma. Thus, there is pressing need for minimally invasive strategies that can also provide sustained growth factor delivery. A significant obstacle to this goal is the short half-lives of neurotrophic growth factors. For example, brain derived neurotrophic factor (BDNF) and glial-cell derived neurotrophic factor (GDNF), have short half-lives of approximately 45 minutes *in vivo,* as they are susceptible to enzyme degradation.[14,33] To provide an ideal environment for the regeneration of CNS tissue, a delivery system is required that prevents growth factor degradation, whilst providing consistent, localised delivery over prolonged periods; all from a single injection.

Here we demonstrate an effective mechanism for improved delivery of BDNF, a growth factor that plays an important role in neuronal differentiation and proliferation, by loading it into a tissue specific self-assembling peptide (SAP) hydrogel. The CNS provides a proof of concept model for this broadly applicable growth factor delivery system that can be tailored using different tissue specific SAP hydrogels. These are sophisticated biomaterials designed with recognisable peptide sequences from tissue specific extracellular matrix (ECM) proteins to biochemically mimic the ECM while also providing nanofibrous structural support.[8,9] Importantly for a delivery vehicle, SAP hydrogels are formed via physical interactions, allowing the material to undergo reversible shear thinning. Thus, the material can flow readily when injected and will then interface with the entire surface area of irregularly shaped injury sites as it reforms into a stiffer gel,[6] providing a more customised and less invasive material than surgical implantation. Once reformed *in situ*, these hydrogels retain their mechanical properties and biomimetic nanoscale morphology.[8,9] Self-assembly of nanoscale fibres is driven by secondary bonds or physical interactions, including aromatic stacking, hydrophobicity, polarity, and charge-charge interactions between different amino acids of the SAP peptide sequence.[7,188] We have previously engineered minimalist (< 7 amino acids) N-fluorenylmethyloxycarbonyl (Fmoc) peptides that self-assemble under physiological conditions to present a high density of bioavailable and biofunctional peptide sequences to promote cell interactions.[9,78] To tailor the hydrogel to CNS tissue, we used the peptide sequence isoleucine-lysine-valine-alanine-valine (IKVAV), a recognizable peptide sequence from laminin, a protein abundant in the ECM of the brain where it is involved in neural adhesion, migration, proliferation, and differentiation.[150] To tailor material properties of the hydrogel, we used aspartic acid (D) residues to alter the pKa of the peptide molecule and therefore pH of self-assembly. The minimalist SAP Fmoc-DDIKVAV forms a hydrogel under physiological conditions with the shortest possible peptide sequence, and we have shown these peptides to be biocompatible *in vivo*.[31]

A key aspect of the hydrogel formation is the longitudinal alignment of individual fibrils through surface mediated supramolecular associations to form intertwined bundles that form the interconnected nanofibrous network.[57,62] We predicted that such interactions would occur between the peptide chains on the nanofibre surface and the peptide chains of protein growth factors. We have shown that permanent immobilisation of growth factors to a scaffold stabilised growth factors for prolonged presentation and bioactivity,[31] and hypothesised that this temporary immobilisation through reversible adsorption of growth factors to the SAP nanofibres would also stabilise them for prolonged delivery. This system presents an option for prolonged but non-permanent growth factor delivery with potential to control the delivery profile by adjusting the increasing or decreasing the fibre-growth factor interactions. This method also provides inherent control over the localisation of delivery, because growth factors are only stabilised in the presence of the stationary SAP hydrogel, unlike nanoparticle delivery systems, in which the stabilising nanoparticle carrier can diffuse away.

6.4 Results and Discussion

To test the ability of SAPs to provide prolonged growth factor delivery, we loaded Fmoc-DDIKVAV hydrogel with BDNF and examined its release into surrounding phosphate buffered saline (PBS). In PBS alone, free BDNF quickly degraded, with an approximate half-life of 5 hours (Figure 6.1 (a)) and no detectable BDNF after 24 hours. In stark contrast, BDNF loaded into the SAP hydrogel (Section 3.2.2.1, 3.4.1) showed continued delivery of stabilised BDNF into the surrounding solution all the way to the 6-week time point (Figure 6.1 (b)), representing an increase in BDNF lifespan of over 40 times compared to the degradation profile in PBS alone. These data show a distinct improvement in the longevity of BDNF within a SAP. Next we investigated growth factor release rates using daily and hourly sampling intervals, as growth factor concentration in the surrounding solution affects its diffusion from the gel (Figure 6.1 (c)). Because growth factors exhibit such short half-lives of minutes to hours *in vivo*,[14,31,33] an hourly sampling interval mimics the rate at which the

growth factor would be removed from the surrounding environment *in vivo*. We also examined the changing release rate, in addition to the cumulative release profile standard in the field. This approach allowed us to better observe changes in growth factor delivery over time. Using this method, we observed that using the more frequent (daily and hourly) sampling intervals, the release of BDNF was less consistent, with the actual release rate fluctuating significantly between consecutive time points.

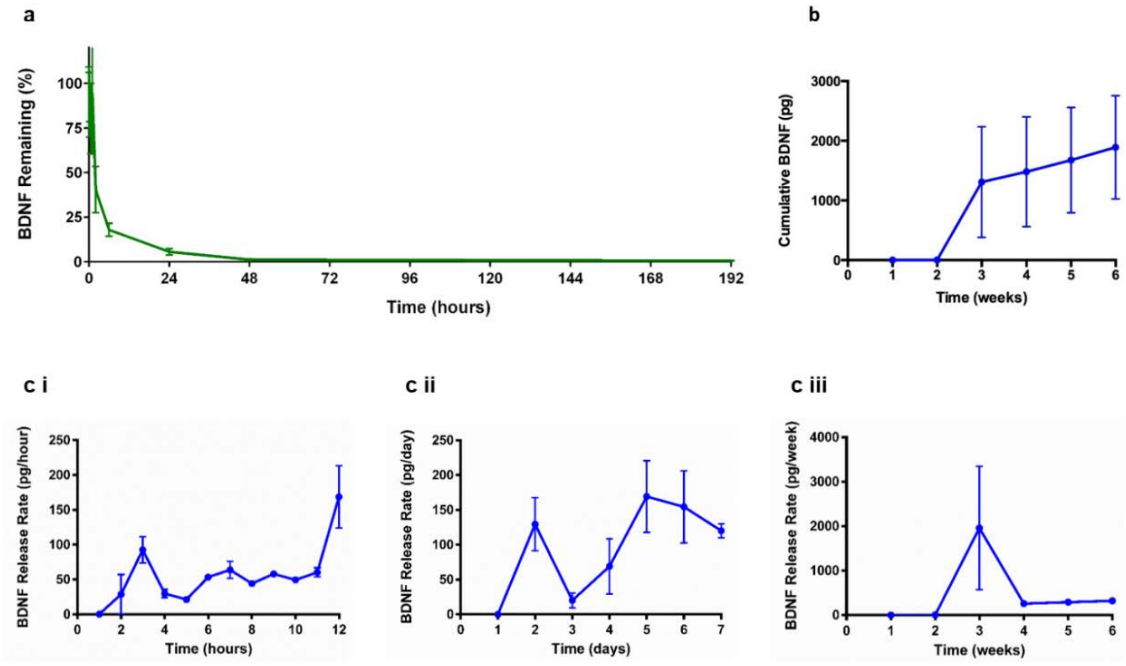

Figure 6.1: BDNF degradation and sustained release. (a) BDNF degradation profile in PBS at 37 °C. (b) Weekly cumulative release profiles from Fmoc-DDIKVAV hydrogel showing the absolute amount of BDNF released since the beginning of the experiment. (c) Hourly (i), daily (ii) and weekly (iii) release rate profiles showing the BDNF released in individual samples/intervals. Data represent mean ± standard error.

The therapeutic window is an important consideration for drug delivery. Dosage should be adequate to stimulate intracellular responses while remaining well below toxic thresholds. Burst release drug delivery can exceed the therapeutic window, resulting in toxic side effects. Preparations are usually most effective when delivered at a consistent concentration,[34] thus optimization requires minimizing bursts and fluctuations in the release. Timing is also important.[189] An ideal drug delivery system would allow temporally distinct delivery of more than one drug. From an implanted SAP hydrogel, this would mean delaying the release of some drugs.

In order to simultaneously achieve both temporal control and consistent growth factor release rate, we investigated the effects of chemical modification on interactions with the nanofibre scaffold. However, in addition to a short half-life in physiological environments, protein activity is destroyed by extremes of heat, acidity, and basicity,[190] conditions frequently employed during chemical modification. Previously, we have shown indefinitely sustained presentation of growth factors when covalently cross-linked to electrospun biocompatible polymer scaffolds via a succinimidyl 4-(N-maleimidomethyl)cyclohexane-1-carboxylate) (SMCC) crosslinking molecule.[31,55] SMCC includes N-hydroxysuccinimide (NHS) ester and maleimide moieties that, at neutral pH in an aqueous environment, react with amine and sulfhydryl groups respectively. To minimize protein denaturation, the sulfhydryl containing protein is not reacted until the final step of the cross-linking process, after the amine containing attachment material has been functionalised with SMCC.[31,36] We have previously demonstrated that SMCC attachment does not impede growth factor bioactivity, confirming bioactivity *in vitro* with BDNF,[36] and *in vivo* with GDNF,[31,191] and Interleukin-10 (IL-10).[192] In the current study, we adapted this immobilization method (Figure 6.2 (a), Section 3.2.5, 3.2.4.1) to investigate a more tuneable approach that can provide both sustained and delayed growth factor delivery. We attached the polysaccharide chain chitosan, which has D-glucosamine and N-acetyl-D-glucosamine repeating units suitable for crosslinking with SMCC. Chitosan is also biocompatible, and is used extensively in tissue engineering.[193]

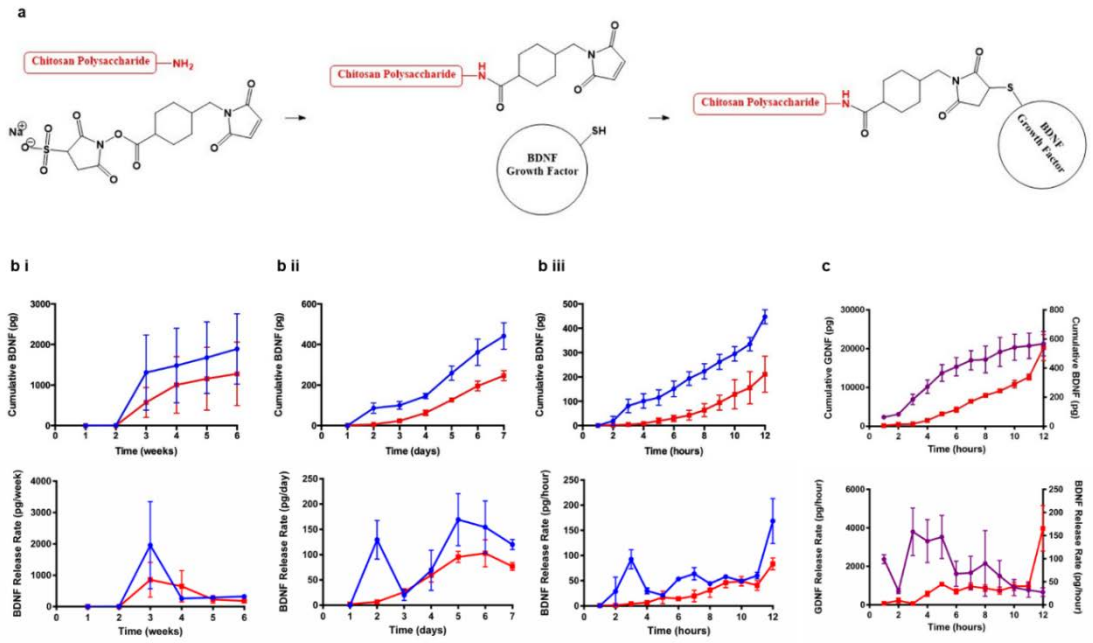

Figure 6.2: BDNF modification and temporally controlled release profiles. (a) SMCC crosslinking between chitosan polysaccharide amine group and BDNF sulfhydryl group. (b) Weekly (i), daily (ii), and hourly (iii) release profiles of BDNF (blue) and modified BDNF-Chitosan (red) from Fmoc-DDIKVAV hydrogels. (c) Hourly, simultaneous release profiles of GDNF (purple) and modified BDNF-Chitosan (red) from the same Fmoc-DDIKVAV hydrogels. Cumulative release profiles (top) show the absolute amount of growth factor released since the beginning of the experiment. Release rate profiles (bottom) show the growth factor released in individual samples/time intervals. Data represents mean ± standard error.

Electrostatic interactions can delay release of proteins from a β-peptide system.[65] BDNF is positively charged[178] with a high isoelectric point (pI) of ~9-10,[194] whereas the Fmoc-DDIKVAV molecule is negatively charged with a low pI of 0.72, as calculated by Innovagen's Peptide Property Calculator.[195] We proposed that functionalizing BDNF (27 kDa) with chitosan (190 – 310 kDa) would increase its interaction with the SAP fibres, keeping the BDNF adsorbed to the material longer, and resulting in a bulkier BDNF-Chitosan molecule that is therefore slower to diffuse out of the hydrogel matrix once desorbed. The release profile for BDNF-Chitosan demonstrated that the modified growth factor retained the sustained 6-week release, but showed notably improved consistency in its release rates in terms of the delivered dose at consecutive time points (Figure 6.2 (b)). Fluctuations between consecutive time points were reduced by 65 ± 5% in the hourly profile

(see supplementary data). The underlying cause of this reduced fluctuation was not investigated. We propose that it may be the result of steric hindrance becoming a more dominant factor in determining release characteristics for the bulkier BDNF-Chitosan. It could also be that the electrostatic interactions chitosan has with the SAP nanofibres are more constant that those of the less stable BDNF molecule.

These findings also highlight the usefulness of examining the release rate vs. the standard cumulative release profile when assessing drug delivery; the cumulative profiles hide inconsistency in release rate. The modified and unmodified BDNF release rates have markedly different consistencies in the delivered dose, despite both groups displaying a smooth cumulative profile. This analytical method could be applied across the field of drug delivery to better analyse the dynamic nature of drug delivery and ensure dose remains within the therapeutic window.

Chitosan modification also delayed the release profiles compared to unmodified BDNF (Figure 6.2 (b) ii, iii). The extent of the delay was dependent on the nature of the release profile sampling, with greater effects in more dynamic release profiles. In the most dynamic (hourly) profile that most closely mimics the *in vivo* environment, the modified BDNF release was delayed by 4 hours.

Finally, for maximum therapeutic benefit, an ideal delivery system would accommodate more than one drug.[196] Here, we evaluated the temporal release characteristics of a dual system by simultaneously loading hydrogel with BDNF-Chitosan and unmodified GDNF, a growth factor that promotes neuronal survival and neurite outgrowth.[55] The hourly release profile for the dual system showed more consistent release of modified BDNF than the unmodified GDNF (Figure 6.2 (c)). While release of both growth factors continued beyond 12 hours, unmodified GDNF peaked at 3-5 hours and BDNF-Chitosan at 12 hours. As expected, BDNF-Chitosan release was delayed, with no significant levels detected in the first 3 hours. Importantly, profiles from dually loaded material were similar as expected to those

of modified and unmodified BDNF alone. This demonstrates independent control of the delivery of more than one growth factor without affecting the release of others. The temporal distinction in delivery means that this system could be employed to deliver multiple factors each at their own most beneficial time. For example, BDNF could be delivered initially to promote neural progenitor proliferation and/or survival, whilst delayed GDNF release would enhance survival and promote neurite growth in regenerating tissue.

To ensure loading with a growth factor does not alter the established optimised properties of SAP hydrogels, we characterised unloaded, BDNF loaded, and BDNF-Chitosan loaded hydrogels. Transmission electron microscopy (TEM) micrographs showed consistent SAP fibre structure in all cases. As expected, there were more bundles and inter-fibre interactions in BDNF-Chitosan loaded SAP hydrogels (Figure 6.3 (a-c)). In all cases, the images show tubular fibrils approximately 10-20 nm in diameter, consistent with morphology expected of this SAP class. Matrix stiffness has been shown to have a major effect on stem cell differentiation, with differentiation promoted towards tissues of matching stiffness.[2] SAP hydrogels change mechanically with rate of assembly, concentration of SAP, and the presence of macromolecules.[61,62] Rheological analysis showed that growth factor loading did not disrupt the hydrogel nature; in all cases the elastic component of the storage modulus (G'), exceeded the loss modulus (G"), and the moduli were mostly independent of frequency (Figure 6.3 (d-f)), displaying the standard SAP rheological properties.[9,61] Importantly, all hydrogels exhibited similar stiffness, in the range of 1-6 kPa, within the range relevant for soft tissue applications.[2] Spectroscopic analysis confirmed the π-β mode of assembly[9] was conserved in all samples (Figure 6.3 (g-h)). Fourier transform infrared spectroscopy (FTIR) analysis showed the distinct anti-parallel β-sheet signal (a major peak at ~1630 cm^{-1} and minor peak at ~1690 cm^{-1}).[9] CD analysis also confirmed supramolecular ordering and the presence of β-sheets. These spectra all presented a chirality transition between small peaks of opposite orientation around 275 nm, indicative of supramolecular ordering, and a large peak around 220 nm, indicative of β-sheets.[9] Overall, the data confirm neither BDNF

loading nor chitosan attachment disrupt the optimal morphology or mechanical properties of the resultant hydrogels.

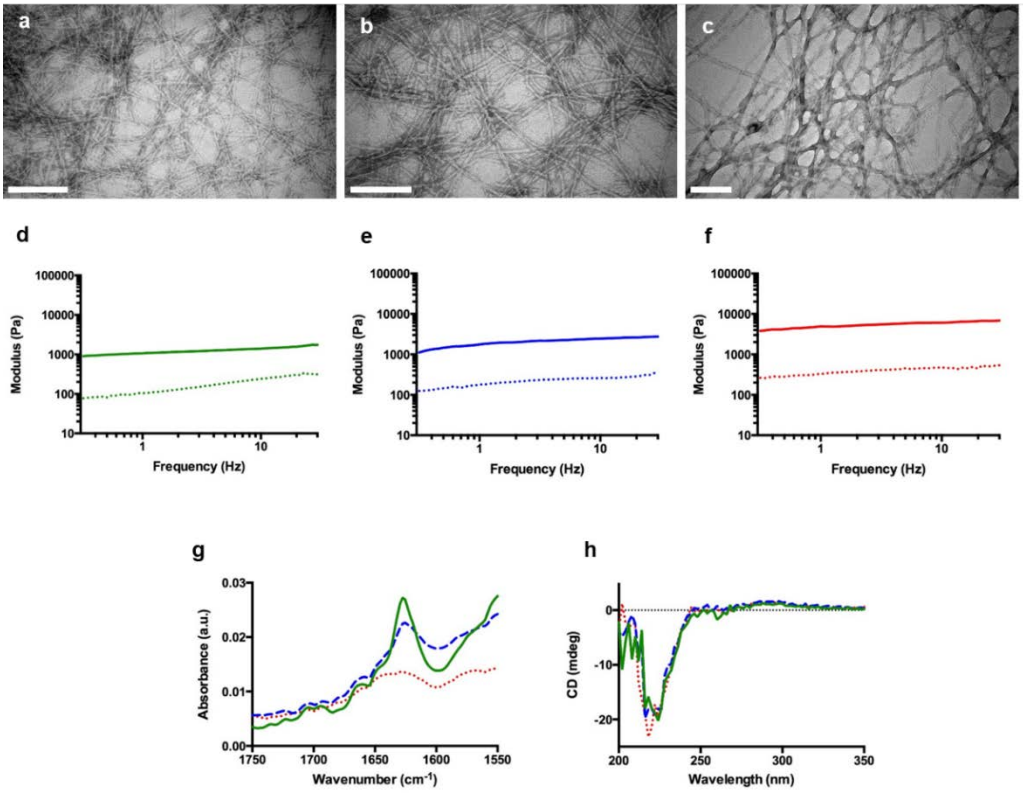

Figure 6.3: Hydrogel characterisation. Characterisation of Fmoc-DDIKVAV SAP hydrogels alone (a,d), loaded with BDNF (b, e) and loaded with modified BDNF-Chitosan (c, f). (a-c) TEM images with 200 nm scale bar. (d-f) Rheological analysis showing storage modulus (G') (solid line) and loss modulus (G'') (dotted line). (g-h) FTIR (g) and CD (h) spectroscopic analysis of hydrogel alone (solid green line), loaded with BDNF (dashed blue line), and loaded with modified BDNF-chitosan (dotted red line).

6.5 Conclusion

In summary, here we demonstrate a new and sophisticated method for sustained, localised, consistent dose and temporally controlled delivery of multiple protein growth factors from a novel biomimetic tissue engineering material. We show independent control of the release of two growth factors from a single SAP hydrogel, while maintaining the previously optimised mechanical properties of the tissue specific SAP material. We also demonstrate the improved utility of release rate based analysis compared to standard cumulative release profiles. Our findings have significant implications for regenerative medicine, where long-term and controlled delivery of multiple, trophic proteins is required.

Chapter Seven

Immobilisation onto Electrospun Nanofibres

7.1 Chapter Details

As discussed in Chapter Two, electrospun materials are another very popular class of tissue engineering material. This chapter discusses work done using electrospun materials to present immobilised growth factors for neural regeneration applications. The chapter encompasses the work of two projects, first testing the bio-functionality of growth factors immobilised to electrospun materials *in vivo*, then adapting those materials for incorporation into a non-SAP hydrogel material and testing *in vivo* in a Parkinson's disease model. The techniques used here represent important progress for the combination of growth factors and tissue engineering materials, while also providing the framework for the temporally controlled delivery mechanism from SAP hydrogels discussed in the next chapter.

This chapter has been published as the research article listed below:

> Ting-Yi Wang*, Kiara F Bruggeman* (co first author), Jessica A Kauhausen, Alexandra L Rodriguez, David R Nisbet, Clare L Parish, "Functionalized composite scaffolds improve the engraftment of transplanted dopaminergic progenitors in a mouse model of Parkinson's disease", Biomaterials, 2016, vol. 74, pp. 89-98 – Reproduced with permission from Elsevier

This chapter also contains an excerpt (Section 7.4), briefly describing work published in the research article listed below and included in full in Appendix E:

> Ting-Yi Wang, Kiara AF Bruggeman, Rebecca K Sheean, Bradley J Turner, David R Nisbet, Clare L Parish, "Characterization of the Stability and Bio-functionality of Tethered Proteins on Bioengineered Scaffolds IMPLICATIONS FOR STEM CELL BIOLOGY AND TISSUE REPAIR", *Journal of Biological Chemistry*, 2014, vol. 289, pp. 15044-15051 – Reproduced with permission from Elsevier

7.2 Abstract

With the brain's limited capacity for repair there is a need for new and innovative therapies to promote regeneration. Stem/progenitor cell transplantation has received increasing attention, and whilst clinical trials demonstrating functional integration exist, inherent variability between patients has hindered development of this therapy. Variable outcomes have largely been attributed to poor survival and insufficient reinnervation of target tissues due in part to the suboptimal host environment. Here we examined whether improving the physical properties of the host milieu, by way of bioengineered scaffolds, may enhance engraftment. We developed a composite scaffold, incorporating electrospun poly(L-lactic acid) short nanofibres embedded within a thermo-responsive xyloglucan hydrogel, which could be easily injected into the injured brain. Furthermore, to improve the trophic properties of the host brain, glial derived neurotrophic factor (GDNF), a protein known to promote cell survival and axonal growth, was blended into and/or covalently attached onto the composite scaffolds to provide controlled delivery. *in vitro* we confirmed the ability of the scaffolds to support ventral midbrain (VM) dopamine progenitors, and provide sustained delivery of GDNF - capable of eliciting effects on cell survival and dopaminergic axon growth. In Parkinsonian mice, we show that these composite scaffolds, whilst having no deleterious impact on the host immune response, enhanced the survival of VM grafts and reinnervation of the striatum, an effect that was augmented through the scaffold delivery of

GDNF. Taken together, these functionalised composite scaffolds provide a means to significantly improve the milieu of the injured brain, enabling enhanced survival and integration of grafted neurons.

7.3 Introduction

Damage to the central nervous system (CNS), as a consequence of disease or trauma, can have devastating consequences due to its limited capacity for repair. With a notable lack of therapies, the transplantation of stem cells and neural progenitors has received increasing attention. Proof of principle studies in animals and clinical trials have demonstrated that new neurons are capable of functionally integrating into the injured brain; however, hindering the development of these therapies has been the inherent variability in treatment outcomes. Key challenges facing neural transplants in the CNS have been variable graft survival, as well as inadequate integration and reinnervation of the host tissue.[197,198] In part, this has been attributed to the non-conducive environment of the adult brain – failing to provide adequate physical and trophic support for the graft, and highlighting the need for strategies to improve the host milieu.

Several lines of evidence support the importance of physical scaffolding for the growth and connectivity of new axons. In neural development, 'pioneer axons' have been observed to establish precise targeting and establish scaffolds along which later-developing axons grow.[199,200] Additionally, the presence of a number of extracellular matrix (ECM) and associated adhesion molecules in the developing brain provide critical anchoring to cells within their appropriate location and support axonal extension.[201,202] Within the injured brain, founding work by Aguayo and colleagues demonstrated that CNS axons were capable of growing over distances in the adult brain when they were placed into the permissive environment of a peripheral nerve graft,[203,204] work that was also demonstrated in the support of dopaminergic neural grafts,[205] and complimented by studies using alternate support cells such as Schwann and olfactory ensheathing cells to enhance graft integration.[206] Furthermore,

in more recent years, grafted neurons have been demonstrated to grow their axons along residual host axons within the designated pathway, or alternate axonal tracts, using these host axons as natural scaffolds.[19,207] Combined, this knowledge suggests that efforts to improve the physical support of grafted neurons could enhance integration.

One such strategy to optimize graft support is to engineer biomaterials for implantation.[208] In this regard, electrospun nanofibres provide some of the best examples of simulation of the brain's 3-dimensional (3D) *in vivo* environment—whereby scaffold fibres can support cell adhesion and axon extension. A number of our previous studies have demonstrated that electrospun scaffolds can influence cell proliferation, neural differentiation and axon extension *in vitro*, whilst also influencing survival and plasticity of both host- and grafted-derived neurons in the intact brain.[36,55,105,209-211] Despite these encouraging findings, the bulkiness of electrospun scaffolds renders them less attractive for repair of the brain and more appropriate for spinal cord or peripheral nerve injury where they can be functionalised and used to ensheath axon bundles. Consequently, increasing attention has been paid to the potential of hydrogels—particularly thermo-responsive gels that can be designed to (i) be liquid at 4°C (enabling easy injection) yet rapidly form gels *in situ* at 37°C and (ii) match the modulus of the host tissue.[40,212,213] This is appealing in the current context as cells can be mixed into the liquid prior to implantation. We have previously demonstrated that xyloglucan (polysaccharide) hydrogels can support the survival of neural cells *in vitro*, promote neurite growth of host neurons following implantation into the intact brain, and additionally suppress local reactive astrocytes[101,214]—all critical attributes for cell transplantation.

In addition to the physical support necessary for transplanted neurons, numerous studies have highlighted the capacity of trophic proteins and guidance cues to enhance graft survival and integration.[19,207,215-217] During embryonic development, establishment of neural circuits relies on the precise temporal and spatial expression of axonal growth and guidance cues. Following establishment of circuitry many of these cues are down regulated, with this loss of

expression believed to be one of the major contributors to the adult brain's poor regenerative capacity. Re-expression of these trophic cues can greatly increase the survival and integration of residual host and newly transplanted neurons. This has been most notably demonstrated through the delivery of various neurotrophins known to promote neuronal survival and axonal plasticity.[215,218] However, to date, delivery of trophic proteins into the brain relies on implantation of cells that over-express the protein, invasive pumps for protein infusion *in situ*, or injection of viral constructs to induce local cells to produce proteins. Each of these approaches is clinically problematic and new efforts for providing a prolonged, yet controllable, trophic environment to promote the integration of grafted cells is required. Using biomaterials, we have recently developed methods to prolong the presentation of proteins *in vitro* and in the intact brain.[31,36,55] Covalent tethering of proteins onto biomaterials prolongs their presentation by preventing endocytosis. Previously we have demonstrated that prolonged presentation of brain derived neurotrophic factor (BDNF) or GDNF onto electrospun fibres resulted in improved survival, proliferation, differentiation, and neurite growth of cells *in vitro* and *in vivo* following implantation into the uninjured brain.[31,36,55]

In recent years, several studies have examined the potential of biomaterials to deliver GDNF and/or cells in an effort to improve graft integration. This has included the use of various hydrogels to deliver stem cells including those over-expressing GDNF,[219,220] as well as microcarriers/spheres to deliver GDNF with and without foetal progenitors.[221,222] Unfortunately, the success of these approaches have been largely suboptimal due to the bulkiness of the biomaterials together with cells, and duration of peak GDNF dose delivery. Resultant outcomes have positively described no change or reduced host inflammatory responses yet only modest increase in graft survival, and little to no improvement in graft plasticity.

In the present study, we sought to develop a more sophisticated composite scaffold, demonstrating the benefits of electrospun scaffolds delivered as short nanofibres within a

thermo-sensitive xyloglucan hydrogel. These composite scaffolds were further functionalised to prolong the delivery of the GDNF, thereby providing an improved physical and trophic niche environment for the survival and engraftment of new neurons. As a feasibility and efficacy study, we elected to examine the potential of these biomaterials in a rodent model of Parkinson's disease, a neurodegenerative disorder characterised by the loss of dopamine neurons, that has shown the greatest progress in the field of neural transplantation.[197,198] The goal is to reverse the progression of the disease by promoting the growth of new dopaminergic neurons. The use of biodegradable tissue engineering materials means that no additional surgery is required to remove the implanted materials.

7.4 Results from Previous Material Development

While testing the stability and bio-functionality of growth factors chemically immobilised to electrospun scaffolds via SMCC, polycaprolactone (PCL) scaffolds were used with immobilised GDNF. To confirm the growth factor immobilisation technique PCL scaffolds were prepared alone (PCL), immersed in the growth factor solution to allow adsorption of soluble growth factor only (PCL_sGDNF), with immobilised growth factor via SMCC (PCL_iGDNF), and with immobilised growth factor and extensive washing in a vortex mixer to remove non-immobilised growth factor (PCL_iGDNF(v)). The vortex mixing provides significant mechanical Quantification of the growth factor present on the scaffolds by ELISA (Figure 7.1A) showed significantly more growth factor on the immobilised scaffolds, with only a slight decrease and no statistically significant change after vortexing. The very large difference between the amount of growth factor attached through adsorption (PCL_sGDNF) and via immobilisation indicates that the SMCC method is effective at tethering growth factor to the scaffold, while the relatively small decrease observed after vortexing indicates that the majority of growth factor present on the immobilised scaffolds is strongly chemically attached. BET analysis was used to determine the available surface area within the nanofibrous electrospun scaffold, and this area combined with quantification of

growth factor from ELISA was used to calculate the density of growth factor presentation as 41 pg/cm^2 (Section 3.3.5).

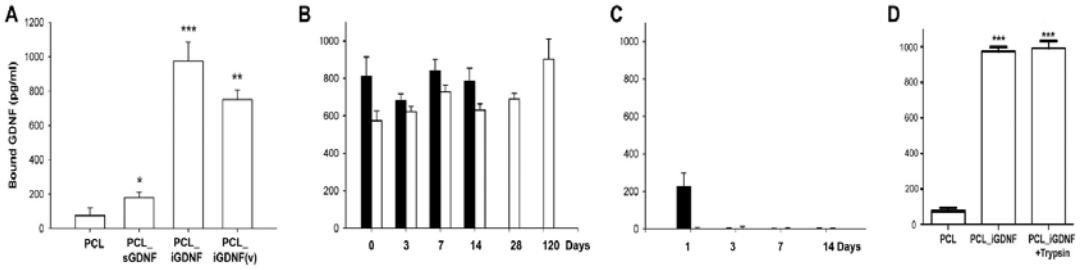

Figure 7.1: Growth factor attachment and stabilisation on electrospun scaffolds. A: GDNF on PCL scaffolds alone, with absorbed GDNF, and with immobilised GDNF with and without vortex washing. B-C: GDNF on immobilised scaffolds (B) without vortexing (black bars) and with vortexing (white bars) after incubation in PBS and in the corresponding incubation supernatant (C) D: GDNF on scaffolds with and without proteolytic trypsin treatment. All GDNF quantified by ELISA. Data represent mean ± SEM, * $p < 0.05$, ** $p < 0.01$, *** $p < 0.001$, one-way ANOVA with Tukey post-hoc test.

Immobilised scaffolds with and without vortexing were incubated in PBS over 120 and 14 days respectively to test the long-term stability of the immobilisation, and no significant change in detectable growth factor was found (Figure 7.1B). The undiminished presence of growth factor at all time points tested suggests that growth factor presentation timeframe will be limited by the scaffold material degradation and should therefore remain present in culture for over 12 months.[223] The PBS incubation supernatants were also tested (Figure 7.1C) and the results corroborate the strength of the SMCC attachment. Some growth factor was found released from the non-vortexed scaffolds after 24 hours, comparable to the difference between vortexed and non-vortexed scaffolds, meaning that the scaffold preparation results in some loosely adsorbed growth factor that can be removed with washing or over time in solution. The vortexed scaffolds did not release any detectable growth factor into the solution, indicating that the remaining growth factor was strongly bound so the scaffold. No supernatants held any growth factor after 24 hours, indicating the unattached growth factor was fully removed after 24 hours, and that that released growth factor had fully degraded by 3 days. The immobilised growth factor on the scaffolds did not

experience that degradation, and neither was it susceptible to proteolysis, as indicated by a lack of effect of trypsin treatment on the immobilised scaffold (Figure 7.1D), indicating increased growth factor stability after attachment.

To confirm the bioactivity of the immobilised growth factor immunoblotting was performed focusing on the GDNF-ErK signalling pathway, specifically the phosphorylation of ErK1 and ErK2. Testing was done with SN4741 cells were used as they are known to express the GDNF receptors c-ret and GFRa1. Non-phosphorylated ErK was found in comparable levels on both the control PCL scaffold and the immobilised scaffold (PCL + iGDNF), but the phosphorylated counterparts (pErK1 and pErK2) were significantly increased with the immobilised scaffold, showing a 4.4 times increase in the ratio of phosphorylated to total ErK (Figure 7.2A-B). This confirms that the immobilised GDNF retained its bioactivity, as it was still capable of mediating intracellular signalling. The motivation behind growth factor immobilisation is to sustain presentation beyond the normally very short active lifespan of the soluble factor. To confirm this, further immunoblotting was performed comparing the immobilised GDNF to a GDNF solution (at 30 ng/mL) over 3 days (Figure 7.2C-D). Both the GDNF solution and immobilised scaffold demonstrated bioactivity initially via increased ErK phosphorylation, only the immobilised scaffold showed continued bioactivity after 3 days. 3 days after treatment with GDNF solution the cells had returned to phosphorylation levels comparable to the basal levels of the control group. These results confirm not only that the immobilisation method retains bioactivity, but that it is successfully achieves a prolonged lifespan of growth factor efficacy.

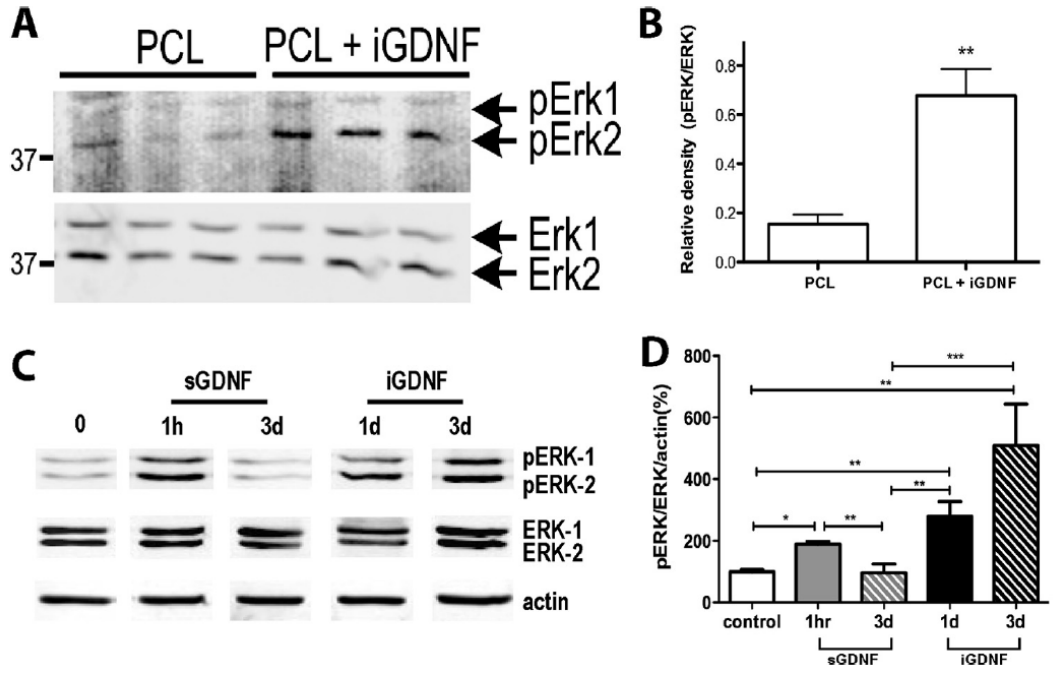

Figure 7.2: Long-term biofunctionality of immobilised GDNF confirmed based on phosphorylation of intracellular ErK. Immunoblotting (A, C) and band densities (B, D) of the ErK and phosphorylated pErK from SN4741 neural cells. A-B: Comparison of PCL scaffold alone and with immobilised GDNF. C-D: Comparison of GDNF solution and immobilised GDNF over time. Data represent mean ± SEM, * $p < 0.05$, ** $p < 0.01$, *** $p < 0.001$, student's t test and one-way ANOVA.

The bioactivity was further confirmed *in vitro* with neural progenitor cells from ventral midbrain (VM) tissue of embryonic mice. The cultures were tested at 3 and 7 days for cell viability (Figure 7.3A) and proportion of dopaminergic neurons indicated by tyrosine hydroxylase-immunoreactivity (TH+) (Figure 7.3B). Once again the PCL scaffold alone had no effect and the GDNF solution showed an initial effect only, with improved cell viability and increased dopaminergic neurons at 3 days but not at 7 days. The immobilised scaffold treatments, however, showed ongoing effect out to 7 days, confirming the long-term bioactivity of the immobilised growth factor. These results show that the immobilised GDNF, with or without vortexing, promotes cell viability and dopaminergic neuronal differentiation. This effect is also shown in the photomicrographs of the fluorescence staining for cells (Hoechst), neurons (Tuj), and dopaminergic neurons (TH) (Figure 7.3C-R).

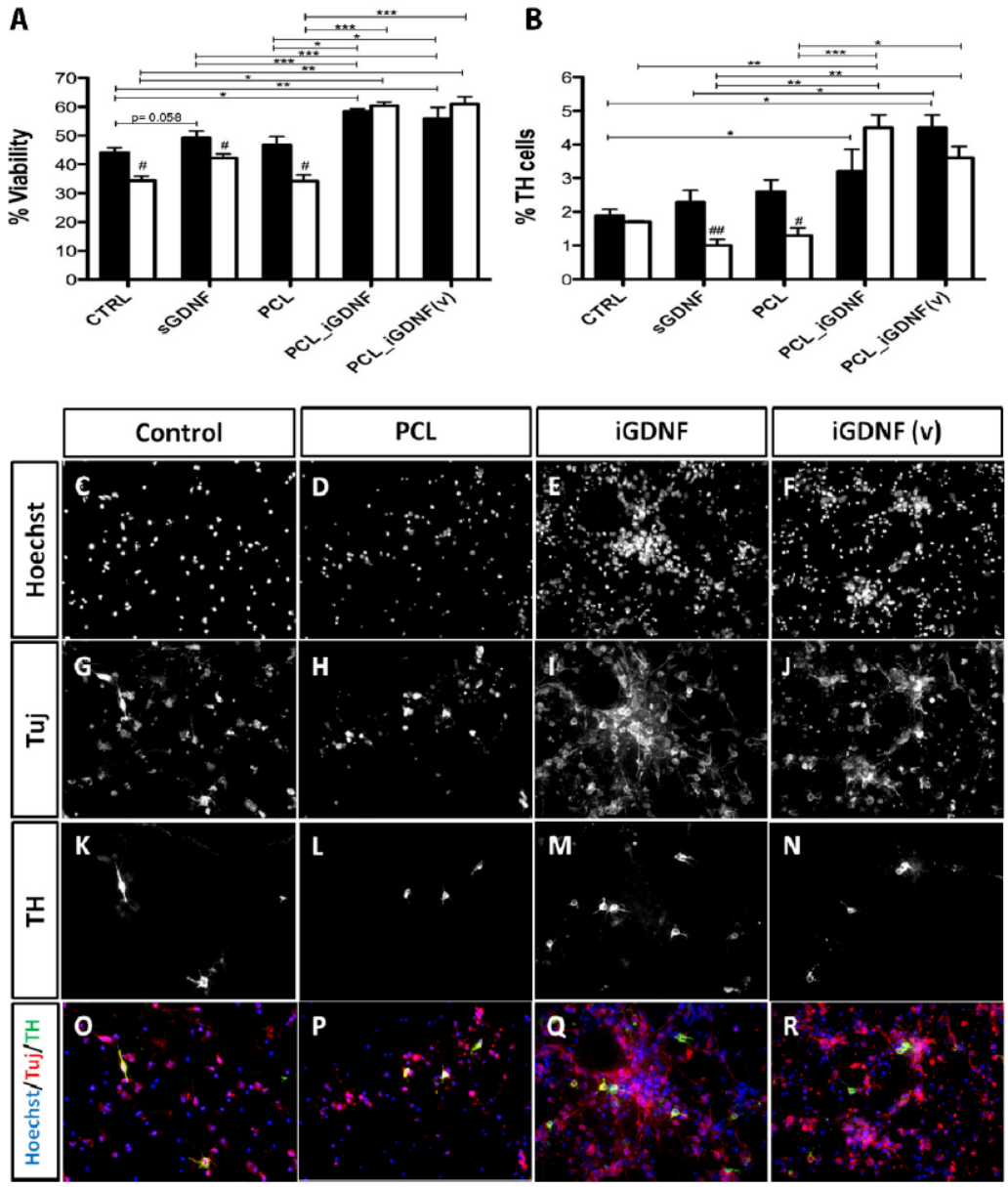

Figure 7.3: GDNF immobilisation enhances cell viability and differentiation. A-B: Cell viability (A) and proportion of tyrosine hydroxylase-immunoreactive (TH+) cells (B) in ventral midbrain cultures with control conditions (PDL-coated plastic), GDNF solution, PCL scaffold alone, and immobilised scaffolds with and without vortexing after 3 days *in vitro* (DIV) (black bars) and 7 DIV (white bars). Data represent mean ± SEM, * $p < 0.05$, ** $p < 0.01$, *** $p < 0.001$, # $p < 0.05$, ## $p < 0.01$, one-way ANOVA with Tukey post-hoc test. C–R: Representative photomicrographs of Hoechst-labelled nuclei (C-F), TUJ+ neurons (G-J), TH+ dopaminergic neurons (K-N), and merged images (O-R) of VM cells cultured on PDL-coated plastic (control), PCL, PCL with immobilised GDNF (PCL_iGDNF), and PCL with immobilised GDNF and vortexed (PCL_iGDNF(v)).

7.5 Results

7.5.1 Characterisation of Scaffolds

Desirable for bioengineered scaffolds to support neural cells *in vitro* and *in vivo* is the confirmation of their previously described physical attributes, as well as assessment of the characteristic features of the novel composite scaffold. Scanning electron micrographs confirmed the macroporous 3-dimensional structure of xyloglucan hydrogel with the inclusion of PDL (Figure 7.5A). PDL was immobilised onto xyloglucan to promote cell adhesion and neurite elongation, as previously shown (Figure 7.4, Section 3.2.6, 3.2.3).[101] In addition to SEM, the presence of PDL on xyloglucan was confirmed by XPS. The nitrogen to carbon ratio (1:0.043) indicated that there was 1.85 PDL molecules immobilised to each xyloglucan repeat unit. SEM images revealed that electrospun PLLA nanofibres showed aligned fibre orientation (Figure 7.5B), from which short fibres (Figure 7.5C) could be generated for the composite scaffold. The presence of these PLLA short fibres could be visualised within the xyloglucan gel of the composite scaffold (Figure 7.5D).

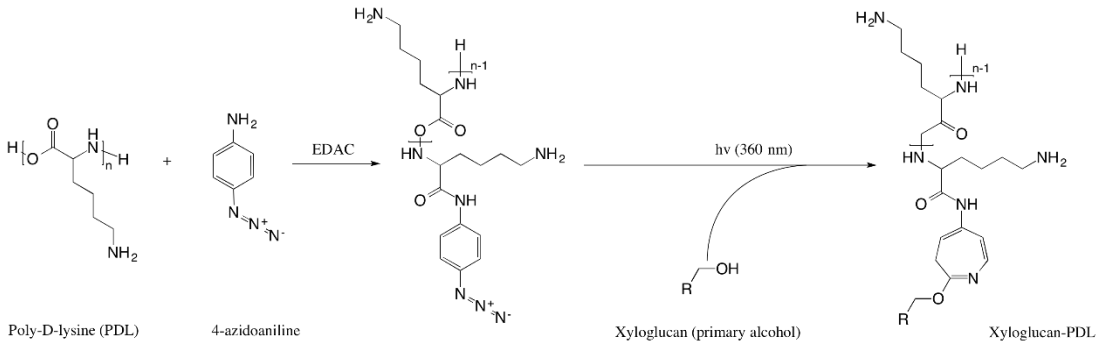

Figure 7.4: PDL xyloglucan immobilisation mechanism

Isothermal rheological experiments were conducted to determine the composition at which the elastic modulus of the xyloglucan hydrogels matched the modulus of the rodent brain (1.0-3.0 kPa[224]). At 37 °C the presence of the short fibres increased the elastic modulus of the xyloglucan-PDL (red line, Figure 7.5E) compared to xyloglucan-PDL without SF (purple line, Figure 7.5E), resulting in a biomaterial closer in shear stiffness to the host brain.

Scaffolds were functionalised with GDNF to promote cell survival and dopaminergic neurite extension. The presence of GDNF was validated using ELISA prior to *in vitro* culturing and *in vivo* implantation. In the absence of scaffolds, the presence of GDNF in the media diminished within 4 days (white bars, Figure 7.5G). The blending of GDNF into xyloglucan retarded the protein's release from the gel, resulting in maintained expression in the media for 14 days, yet undetectable by 28 days (grey bars, Figure 7.5G). The immobilization of GDNF on PLLA fibres confirmed sustained expression for 28 days (striped bars, Figure 7.5G), with little GDNF (presumably absorbed, rather than covalently attached) released from the scaffolds during this period (black bars, Figure 7.5G). These findings of immobilised GDNF are in accordance with our previous findings, that demonstrated maintained neurotrophin expression on electrospun fibres for up to 120 days.[31]

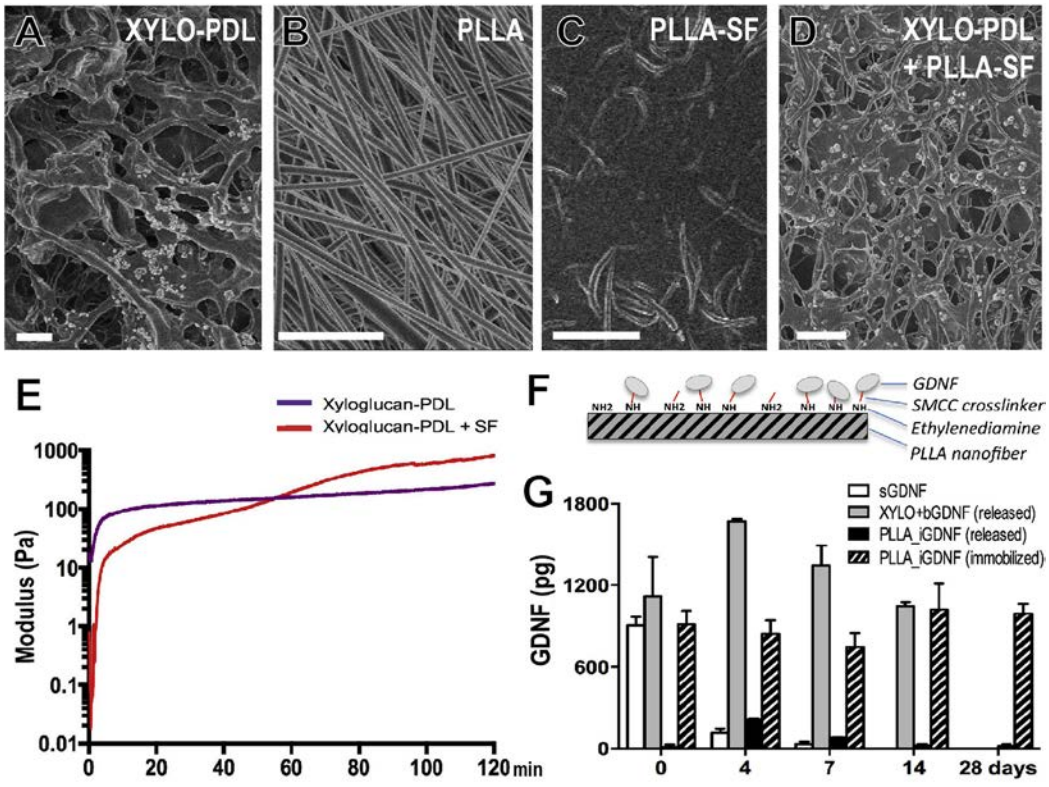

Figure 7.5: Synthesis and GDNF functionalization of bioengineered scaffolds. Scanning electron micrographs illustrating the architecture of (A) 3 wt% xyloglucan gel with photo-coupled PDL, (B) electrospun nanofibrous PLLA, (C) PLLA short fibres, and (D) the composite scaffolds, including PLLA short fibres within the xyloglucan gel. (E) Rheological measurements of the elastic (G', closed symbols) shear moduli of xyloglucan-PDL and xyloglucan-PDL + SF under isothermic (37 °C) conditions. (F) Schematic illustration of GDNF immobilization onto PLLA nanofibres. (G) GDNF ELISA showing the presence of GDNF protein

over 28 days in the media following soluble delivery (sGDNF), GDNF released from xyloglucan gels (XYLO+bGDNF), GDNF release from PLLA scaffolds immobilised with GDNF (XYLO+iGDNF (release)), and the amount of GDNF tethered onto the scaffolds (XYLO+iGDNF (immobilised)). Data represents mean + SEM. Scale bar: A-D: 5 μm.

7.5.2 Survival, Differentiation, and Plasticity of Ventral Midbrain Neurons *in vitro*

To assess the ability of the 3D bioengineered scaffold to support dopaminergic neurons and deliver functional GDNF, we cultured VM-derived cells on PDL-coated coverslips or xyloglucan (± SF ± GDNF) (Section 3.5.1.2, 3.5.1.11). Xyloglucan provided a superior substrate for the attachment and survival of VM cells compared to PDL (69.4% ± 3.2 and 53.0% ± 3.3 viability, respectively), with the presence of PLLA short fibres resulting in no further improvement in survival (71.5% ± 4.9) (Figure 7.6A). The culture substrate (PDL, XYLO or XYLO+SF) had no effect on the proportion of neurons in culture, with > 80% of viable cells expressing the neuronal marker, TUJ1, under all conditions (Figure 7.6B).

As anticipated, the presentation of GDNF in culture significantly improved cell viability to levels ≥ 83% (Figure 7.6A), as well as increasing the proportion of TH+ dopaminergic neurons in culture (Figure 7.6C) and their neurite length (Figure 7.6D). This was apparent whether GDNF was administered directly into the media (sGDNF), blended into the xyloglucan (bGDNF) or tethered onto short fibres in the gel (iGDNF). Whilst sGDNF increased the proportion of TH+ dopaminergic cells in culture compared to culturing on xyloglucan alone (3.2% ± 0.2 and 2.0% ± 0.2, respectively), the prolonged presentation of GDNF within the gel (bGDNF) resulted in a 2.5-fold increase in TH+ cells. This effect was not seen by immobilised GDNF, and is likely reflective of the amount of SF on the surface of the hydrogel and hence the subsequent amount of GDNF available to interact with the cultured neurons. Figure 7.6E-J provides representative micrographs of cells cultured on PDL, XYLO and composite scaffolds, demonstrating the benefit on viability of the enhanced 3-dimensional physical support provided by biomaterials. Figure 7.6K-N illustrates

examples of dopaminergic neurons showing increased neurite length following GDNF delivery, and confirming the ability of scaffolds to deliver functional protein.

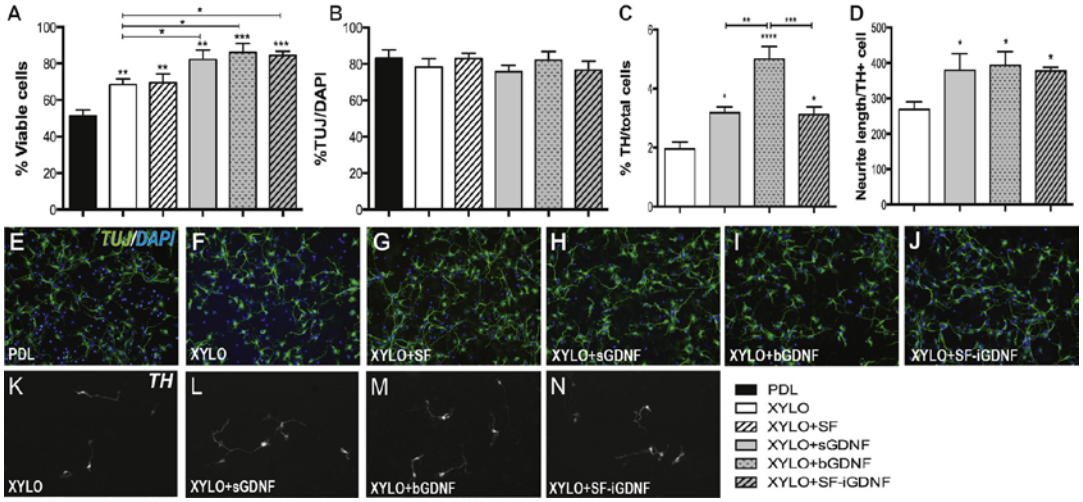

Figure 7.6: Bioengineered scaffolds, incorporating GDNF, enhance cell viability and support dopaminergic neurons *in vitro*. Quantification of (A) the number of DAPI-labeled viable cells and, (B) proportion of TUJ+ neurons in culture. (C) Assessment of the proportion of TH+ dopamine neurons and, (D) neurite length in culture following GDNF administration. Representative photomicrographs illustrating (E-J) TUJ+ neurons and total DAPI labeled nuclei, and (K-N) TH+ dopaminergic neurons. Data represents mean + SEM, * $P < 0.05$, ** $P < 0.01$, *** $P < 0.001$.

7.5.3 Biocompatibility

Given the ability of our scaffolds, including incorporated GDNF, to support VM-derived neurons *in vitro*, we next examined the potential of these scaffolds to support and promote the integration of transplanted VM progenitors in an animal model of Parkinson's disease (Section 3.5.1.8, 3.5.1.11). Paramount for the utility of bioengineered scaffolds in tissue repair is their biocompatibility and impact on the host inflammatory response. At 10 weeks post-implantation, we observed that neither xyloglucan nor the presence of PLLA short fibres at the graft site induced elevated levels of reactive astrocytes (GFAP+, Figure 7.7A,D-J) or microglia (CD11b+, Figure 7.7B,D'-J'), compared to cell implants alone.

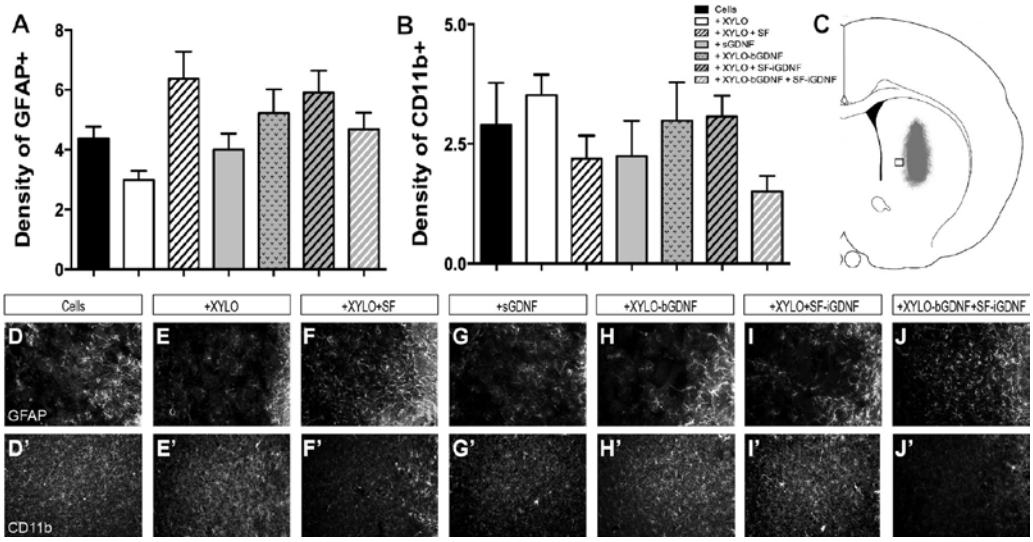

Figure 7.7: Biomaterials bear no impact of the host immune system following implantation. (A) Assessment of GFAP+ astrocyte and, (B) CD11b+ microglia density surrounding the GFP+ graft demonstrates that the employed biomaterials, nor the incorporation of GDNF protein, impacted on the host inflammatory response, as compared to cell grafts alone (black bars). (C) Schematic, illustrating the region adjacent to the graft (boxed area) used to assess GFAP and CD11b density. (D-J) Representative photomicrographs of GFAP+ and (D'-J') CD11b+ immunolabeling adjacent to the GFP+ graft core. Data represents mean + SEM.

7.5.4 Dopaminergic (DA) Neurons in VM Grafts and Reinnervation of the Striatum

The use of TH-GFP mice provided a valuable means to accurately measure graft-derived patterns of innervation of the host striatum, even in the presence of a residual level of innervation from host (GFP-) DA neurons. At the time of assessment (10 weeks post-transplantation) (Section 3.5.2.3), TH immunohistochemistry confirmed robust ablation of the host midbrain DA neurons in lesioned mice (data not shown). GFP staining verified viable grafts, confined to the striatum in 68/74 (91%) of the mice. Quantification of GFP+ cells revealed that the presence of xyloglucan, but not PLLA short fibres, significantly increased graft volume, Figure 7.8A,D-J. Assessment of the volume of the graft core highlighted a proportionate increase for cells grafted in the presence of xyloglucan Figure 7.8B, such that the overall density of cells within the graft core was not significantly different

from cell implants alone **Figure 7.8C**, and inferring that the presence of the scaffold did not retard the migration of neurons within the graft.

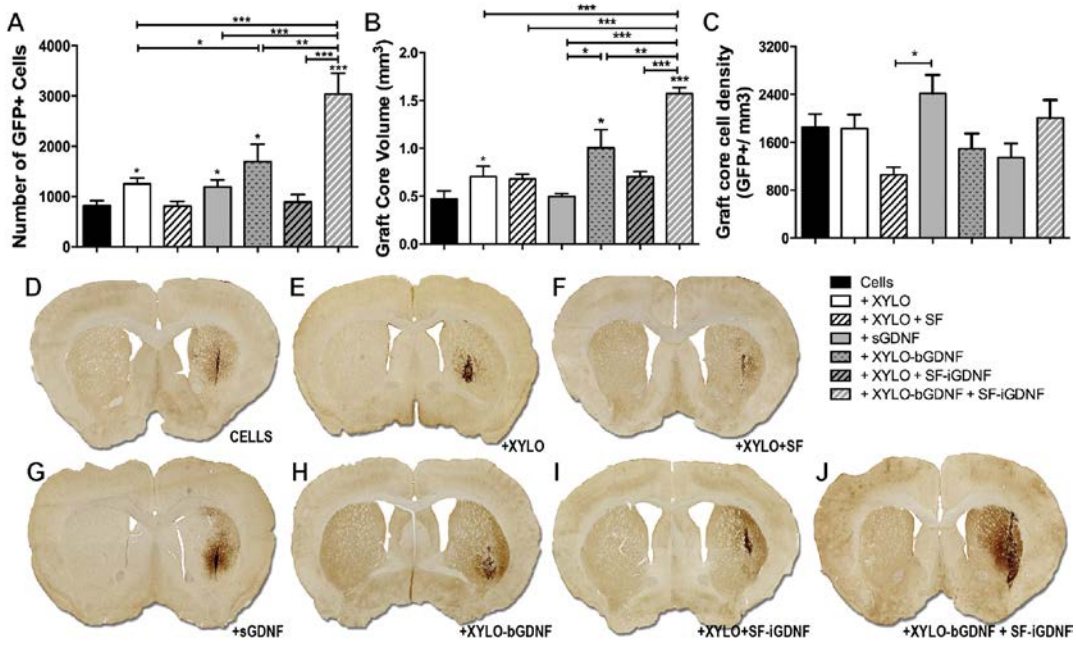

Figure 7.8: Functionalised composite scaffolds support transplanted GFP+ dopamine neurons. (A) Exposure of VM fetal grafts to xyloglucan and/or GDNF increased the number of GFP+ dopaminergic neurons following implantation. Note the synergy of the composite material and dual delivery of GDNF (blended within the gel and immobilised onto short fibres). (B) The volume of the graft core commensurately increased with increased GFP+ cell numbers, resulting in (C) no significant difference in the density of GFP+ DA neurons in the graft and importantly demonstrating that the scaffolds did not impede cell migration. (D-J) Representative photomicrographs providing a coronal view of the GFP+ grafts within the striatum. Images depict grafts of GFP+ cells alone (D), GFP+ cells in the presence of scaffolds (E-F) and GFP+ cells in the presence of GDNF ± scaffolds (G-J). Data represents mean ± SEM, * $P < 0.05$, ** $P < 0.01$, *** $P < 0.001$.

The use of TH-GFP donor tissue enabled not only improved visualization and assessment of GFP+ cells, but furthermore the extensive network of fibres emanating from these neurons. This allowed for quantitative comparisons of the total striatal area innervated by the graft (Figure 7.9A), innervation volume/grafted neuron (Figure 7.9B), and the density of grafted fibres in the striatum (Figure 7.9C). Commensurate to the increase in the number of GFP+ cells, XYLO implanted animals showed an increase in striatal innervation volume compared to cell grafts alone (2.67 mm^3 ± 0.42 and 2.04 mm^3 ± 0.36, respectively) (Figure 7.9A-B,D-E). Interestingly the presence of PLLA short fibres had a negative impact on striatal innervation and innervation/GFP+ cells (Figure 7.9A-B,F), an effect likely explained

by the preference for graft derived GFP fibres to remain within the graft core and attach to the short fibres, rather than infiltrating the host striatal tissue. Despite these differences in volume of striatal territory innervated, the overall density of fibres within the innervated areas was not significantly different from cells alone (Figure 7.9C).

7.5.5 Graft Survival and Integration

Next we examined the capacity of scaffolds to improve the delivery of GDNF, in an effort to promote graft survival and integration in Parkinsonian mice. Not surprisingly, and as previously described,[225] the inclusion of GDNF (sGDNF) within the donor cell preparation at the time of implantation significantly improved the number of GFP+ cells compared to cells alone (1188 ± 131 and 814 ± 96, respectively). Incorporation of GDNF within the gel (bGDNF) induced a 2-fold increase in GFP+ cell survival (1668 ± 343), however, presentation of GDNF on the short fibres only (iGDNF) within the gel was insufficient at boosting survival, and similar to *in vitro* findings, likely reflects the insufficient amount of GDNF presented to graft at the critical and vulnerable time of implantation. Most striking was the effect of enhanced and prolonged GDNF delivery through a combination of both blending within the xyloglucan gel and tethering onto short fibres (XYLO-bGDNF + SF-iGDNF), which resulted in a 3.7-fold increase in GFP cells (3034 ± 413), significantly greater than all other methods of GDNF presentation (Figure 7.8A,D-J). GDNF presentation to the grafted cells commensurately increased the volume of the graft core (Figure 7.8B), and hence the overall density of cells within the core was not different (Figure 7.8C) between all treatments, and again suggested that neither the physical structure of the scaffold nor the presentation of GDNF promoted or impeded cell migration.

Finally, we assessed the ability of scaffold-delivered GDNF to promote the integration of GFP+ DA grafted neurons. Only sustained GDNF delivery enhanced graft-derived striatal innervation (Figure 7.9A,D,G-J). Blending GDNF into the xyloglucan gel (+XYLO-bGDNF) resulted in a 2.1-fold increase in striatal innervation compared to cells alone (4.20

$mm^3 \pm 0.59$ and 2.04 $mm^3 \pm 0.36$, respectively) whilst blended plus immobilization GDNF (XYLO-bGDNF + SF-iGDNF) enhanced innervation by 3.1-fold ($6.34mm^3 \pm 0.82$). Furthermore, the dual presentation of GDNF not only enhanced graft-induced striatal reinnervation, but additionally the volume of innervation/GFP+ cell (Figure 7.9B) as well as the density of GFP+ fibres within the striatum compared to cells alone (7.4 ± 1.1 and 3.7 ± 0.4, respectively), and all other grafts (Figure 7.9C,D'-J'). Presentation of tethered GDNF on short fibres alone (XYLO+SF-iGDNF) had no effect on innervation (1.15 $mm^3 \pm 0.16$). The presence of short fibres significantly reduced the ability for GFP+ grafted cell to innervate the host, whilst all other grafted cells showed similar innervation capacity, as demonstrated by innervation volume/GFP+ cell (Figure 7.9B).

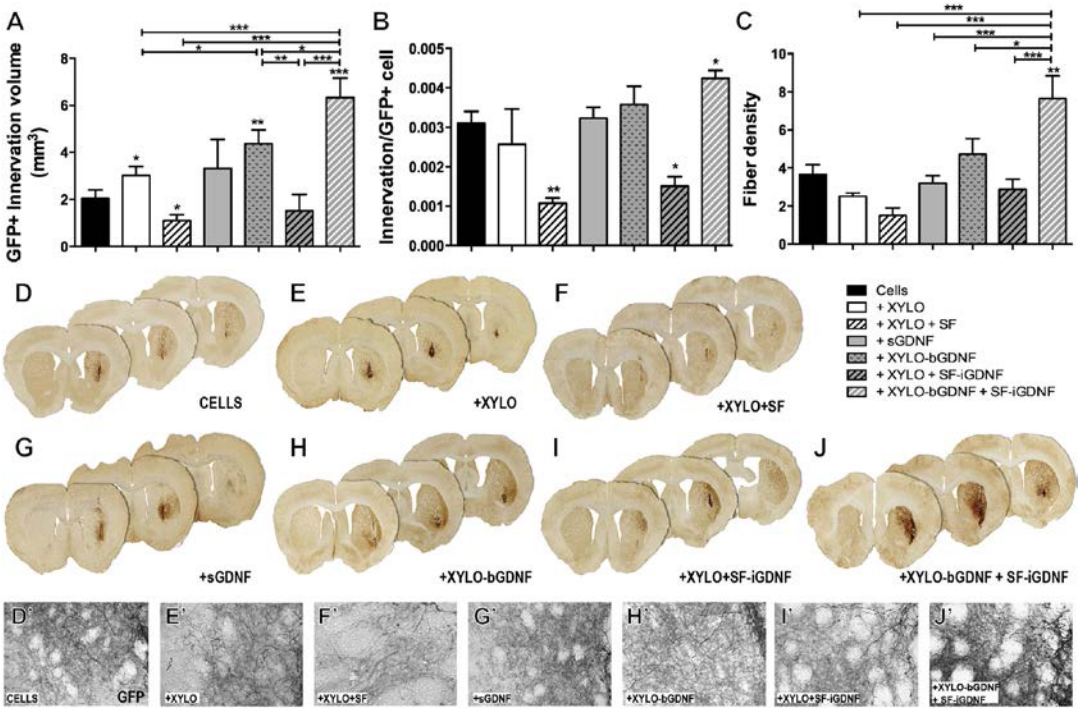

Figure 7.9: Scaffolds, incorporating GDNF, enhance innervation of grafted GFP+ neurons in the Parkinsonian brain. (A) Xyloglucan as well as the incorporation of GDNF within the gel (or composite scaffold) significantly increased the striatal volume innervated by grafted GFP+ dopaminergic neurons. (B) Innervation volume per grafted GFP+ cell remained unchanged across grafting conditions, with the exception of the presence of short fibres, which impeded fibre growth of the grafted cells. (C) Dual delivery of GDNF, via composite scaffolds, significantly increased the density of GFP+ fibres within the striatum. (D) Representative images of grafts, illustrating the extent of striatal innervation by the GFP+ grafted neurons. Note the increase in striatal innervation for grafts in the presence of xyloglucan and GDNF, most evidently GDNF delivery via composite scaffolds. (D'-J') Photomicrographs illustrating the density of GFP+ fibres

100um lateral to the graft core. Note the increased density of fibres for grafts in the presence of composite scaffolds delivering GDNF. Data represents mean + SEM, * $P < 0.05$, ** $P < 0.01$, *** $P < 0.001$.

7.6 Discussion

Whilst proof of principal exists for the success of cell replacement therapy, variability in graft integration, and consequential function, remains a stumbling block that needs to be addressed. Extensive work has been undertaken, to better understand confounding factors contributing to the variability, with the ultimate goal of developing methodologies to improve aspects related to both the donor tissue and the host environment. While these efforts have resulted in stepwise improvements in grafting outcomes, little attention has been paid to enhancing the physical support for newly implanted stem cells/neural progenitors. This study provides the first evidence of the benefits of bioengineered scaffolds to enhance the integration of dopaminergic progenitors in an animal model of Parkinson's disease. These scaffolds were demonstrated to improve both the physical and prolonged trophic support of progenitors *in vitro* and following transplantation, thereby promoting graft survival and striatal reinnervation of the injured brain.

7.6.1 Physical Properties of the Host Environment

Despite studies demonstrating the improved survival and plasticity of DA progenitors when implanted into a *partially* lesioned midbrain, where there is evidence to suggest that new grafted axons elect to follow host fibre bundles *in vivo*,[207] combined with evidence for the important role of the ECM and adhesion molecules in establishment of neural circuits during development and repair,[226,227] little effort has been made to enhance the physical support of transplanted neural progenitors within the CNS. A small number of studies have examined the potential benefits of co-grafting using, for example, olfactory ensheathing cells or bio-bridges from sciatic nerve to provide substrate support for DA-enriched grafts.[205,228-230] Additionally there have been efforts to over-express the cell adhesion molecule, L1, in the host and/or donor tissue, to enhance functional integration.[231,232] By contrast, in other

systems there has been significantly more attention focused on exploring the benefits of providing physical support for integration of grafted neurons or plasticity of host neurons following injury, for example to the peripheral nervous system and spinal cord. This includes numerous studies employing bioengineered scaffolds.[233] Here we provide the first evidence of 3D bioengineered scaffolds supporting DA progenitors *in vitro* as well as their integration following implantation in Parkinsonian mice. In particular, the support provided by the xyloglucan hydrogel resulted in increased numbers of DA neurons within grafts and re-innervation of the host striatum. Importantly, and in line with our former work,[55,210] we demonstrate that these biomaterials are biocompatible, inducing no increase in inflammation following implantation into the brain (compared to cell grafts alone) and furthermore, could be customised to match the modulus of the rodent brain. Whilst here we demonstrate the capacity of scaffolds to support the integration of ectopically grafted neurons, these findings hold implications for homotopically transplanted cells, whereby axons of neurons implanted into the midbrain need to navigate over decidedly longer distances, thereby presenting a greater need for support, to reach their forebrain targets. Further studies are required to identify optimal strategies to deliver such scaffolds along the midbrain pathways with minimal invasiveness. These findings also raise interest regarding the development of alternate scaffolds that may more closely mimic neural tissue. For example, we have recently developed self-assembling peptide hydrogels that present a laminin epitope (a major constituent of the brain ECM) and have been demonstrated to support neural grafts in the intact brain.[9,234] These newer materials may provide additional trophic benefits to the cells as well as possess the advantage of breaking down into naturally occurring amino acid subunits.

7.6.2 Delivery of GDNF to Transplanted DA Progenitors

The role of GDNF in the survival and plasticity of DA neurons is well established *in vitro*, in models of PD and following transplantation.[19,218,235] Here we developed a biomaterial capable of prolonging the presentation of the protein to DA progenitors, by way of retention

within the xyloglucan hydrogel as well as sustained delivery via covalent tethering on electrospun short fibres. Function of the scaffold-incorporated GDNF could be confirmed by its ability to enhance the proportion of TH+ DA neurons in culture and promote TH+ DA neurite extension. Most significant was the capacity for long-term presentation *in vivo* and the influence on transplanted DA progenitors. Whilst delivery of soluble GDNF was sufficient to increase DA neurons within the graft (not dissimilar to blending GDNF within the hydrogel), such acute delivery was insufficient to impact the subsequent plasticity and integration of the graft. Only presentation of GDNF within the gel, or in the composite scaffold, influenced the volume of innervation of the host tissue by grafted DA neurons. We speculate that GDNF delivery via protein tethering onto PLLA short fibres alone was incapable of promoting enhanced graft survival due to insufficient amounts of short fibres, and thereby suboptimal levels of tethered GDNF, coming into contact with grafted cells to influence their survival. Added to this is the likelihood that tethered GDNF prevented GFP+ neurites existing from the graft core, but rather staying in close association with the PLLA short fibres present. By contrast, the composite scaffold presenting sustained GDNF release over weeks from the gel was complemented by persistent tethered GDNF, such that a synergistic effect on DA neuronal numbers and innervation was observed. Hence, here we present three examples of controlling the temporal delivery of a protein *in vitro* and *in vivo*; from minutes to hours (via soluble administration), days to weeks (via retardation within the gel) and weeks to months (via tethering onto short fibres). In the future, such controlled delivery systems could be customised for specific functional requirements for providing multiple proteins over differing time frames. For example, future transplantation studies may look towards acute delivery of cell survival factors at the time of implantation, longer delivery to influence cell migration and/or differentiation and persistent protein expression to promote plasticity of newly implanted cells.

7.7 Conclusion

In summary, here we present the first evidence of bioengineered scaffolds being tailored to meet the many physical and trophic requirements of transplanted dopamine progenitors to enhance their integration into the Parkinsonian brain. Through careful selection and design of a composite scaffold, including prolonged neurotrophin presentation, we were able to improve the niche environment surrounding the implanted cells, resulting in enhanced survival and reinnervation of the host. The utility of such scaffolds, the incorporation of additional functional proteins as well as the impact on pluripotent stem cell-derived neurons, may impact on the future of cell therapy for the treatment of neurodegenerative disorders such as PD.

Chapter Eight

Delivery System: Long (Days) Delay

8.1 Chapter Details

Using materials and methods explored in Chapter Seven, this chapter describes the successful development of the second temporally controlled growth factor delivery system, achieving a long delay in the release of growth factors from the SAP hydrogel. This chapter is also a research article manuscript in preparation by Kiara F Bruggeman, Yi Wang, Francesca Maclean, Clare L Parish, Richard Williams, and David R Nisbet.

8.2 Abstract

Tissue-specific self-assembling peptide (SAP) hydrogels designed around biologically relevant peptide sequences have great potential in regenerative medicine. These materials are often compared with electrospun nanofibre scaffold sheets, which provide larger nanofibres and are known to promote cell adhesion but are limited to wrapping and bandaging applications. Here, for the first time we describe a composite scaffold from these two classes of biomaterials, explicitly engineered as a system for temporally controlled drug delivery. Short fibres, cut from electrospun scaffolds, were mixed with our tissue-specific SAP hydrogel to provide a range of nanofibre sizes mimetic of that found in the extracellular matrix (10 – 300 nm diameter). The composite material also maintained the shear-thinning

and void filling properties of SAP hydrogels that facilitate their minimally invasive injection delivery and full integration with surrounding tissue. Both components were loaded with growth factors, important signalling molecules in tissue regeneration whose rapid degradation limits their clinical efficacy. The two biomaterials provided distinct growth factor delivery profiles: the SAP hydrogel provided a burst release, with the release rate decreasing over 12 hours, and the electrospun nanofibres provided a more constant, sustained delivery. Importantly, this second release began after a 6-day delay, to potentially allow growth factor delivery after subsidence of the initial immune response common after injury. This novel composite material combines the advantages of SAP hydrogels and electrospun nanofibres while also providing a superior vehicle for the stabilisation and controlled delivery of growth factors. This is particularly relevant for neural tissue engineering applications, such as traumatic brain injury, where systemic growth factor delivery is inhibited.

8.3 Introduction

Protein growth factors are short-lived intracellular signalling molecules used in nanomedicine and tissue engineering to encourage the growth of new healthy tissue. While their usefulness is undeniable, their relatively large size compared to conventional drug molecules[20] and inherent instability[10] make their therapeutic delivery a challenge. *in vivo*, enzymatic degradation results in very short growth factor half-lives, as low as 3 min for basic fibroblast growth factor (bFGF)[13] and 45 min for nerve growth factor (NGF).[14] Growth factor delivery to the brain is particularly challenging as the blood brain barrier (BBB) inhibits systemic delivery via the bloodstream.[20] Sustained delivery can be achieved using intracerebroventricular (ICV) infusion, however, this is very invasive and causes iatrogenic injury, so much research has focused on using less invasive implantation strategies with nanoengineered biomaterials to support cells and provide growth factor delivery.[22,36,236]

These tissue engineering scaffold materials are designed to mimic the natural extracellular matrix (ECM) down to the nano-level to reduce inflammation[237] and promote repair and reconstruction. Naturally, the most abundant components of the ECM are nanofibrous

proteins and proteoglycan hydrogels,[1] and tissue engineering materials focus on mimicking these elements. Electrospun materials are popular tissue engineering scaffolds due to their nanofibrous structure, and have been shown to promote cell attachment, differentiation, and proliferation.[40,55] Growth factors have been incorporated into electrospun scaffolds both through emulsion, with the growth factor mixed into the polymer solution before electrospinning,[238] resulting in growth factors dispersed throughout the fibres, and via immobilisation, with the growth factor covalently attached to the surface of fibres after electrospinning.[31,36,192] Electrospun scaffolds have been used successfully to provide sustained delivery or presentation of growth factors. We have previously used immobilisation to provide essentially permanent presentation of growth factors, with duration dependent on the electrospun material degradation.[31,36,192] However, electrospinning forms sheets of nanofibres, which are more suited for bandaging or wrapping applications than the void filling required for a scaffold to interface with healthy tissue surrounding a 3D injury site.[40]

Self-assembling peptide (SAP) hydrogels, particularly the minimalist low molecular weight Fmoc-SAP systems, are not restricted by such limitations whilst also providing the fibrous nanoarchitecture reminiscent of the natural ECM, and hence offer the great potential as tissue engineering materials. They undergo thermodynamically controlled assembly to give 1D nanofibres, 10 – 25 nm diameter, that align longitudinally to form a reversible supramolecular hydrogel, with the peptide sequence bioavailable on the surface of the fibre.[8] As the dominant self-assembly force is non-covalent, the material flows readily under high shear stress, such as when being administered via a minimally invasive needle injection, and then reforms in situ into a stiffer hydrogel that perfectly matches any irregularly shaped 3D injury site fully interfacing with surrounding healthy tissue.[8] We have developed minimalist SAPs using recognisable peptide epitopes from biologically relevant ECM proteins to create tissue-specific SAPs that provide a high density of biomimetic cues in addition to the nanofibrous hydrogel environment.[9,234] Additionally, non-covalent binding of growth factors

via physical adsorption to the nanofibres prevents degradation of the growth factors, and we have shown that stabilisation can be achieved for at least 6 weeks.[239]

Both electrospun and SAP materials have been used to mimic the ECM and deliver growth factors and both materials have complimentary and distinct advantages. Here, we have developed a novel composite material using both SAP hydrogels and electrospun polymer nanofibres to improve ECM mimicry and move beyond simple sustained delivery to provide temporal control over the delivery of growth factors.

8.4 Results and Discussion

8.4.1 Material Development

For this work, we used the rationally designed fluorenylmethyloxycarbonyl (Fmoc) capped aspartic acid-isoleucine-lysine-valine-alanine-valine (DIKVAV). The IKVAV sequence is a biologically recognised peptide epitope from laminin, an ECM protein common particularly in the central nervous system including the brain. The N-terminal addition of the acidic D amino acid was used to adjust the apparent pK_a of the peptide molecule to ensure that the pH driven self-assembly occurs at physiological pH.[9] We have previously demonstrated the biocompatibility and utility of this SAP hydrogel *in vivo* via direct injection to the parenchyma of mouse brains.[234] The peptide forms nanofibres ~10 nm in diameter (Figure 8.1A) and presents a macroscale supramolecular hydrogel with where the assembly derived stiffness is easily tuned to match the appropriate soft tissue type, an important factor in directing endogenous cell survival, integration and differentiation.[2,240]

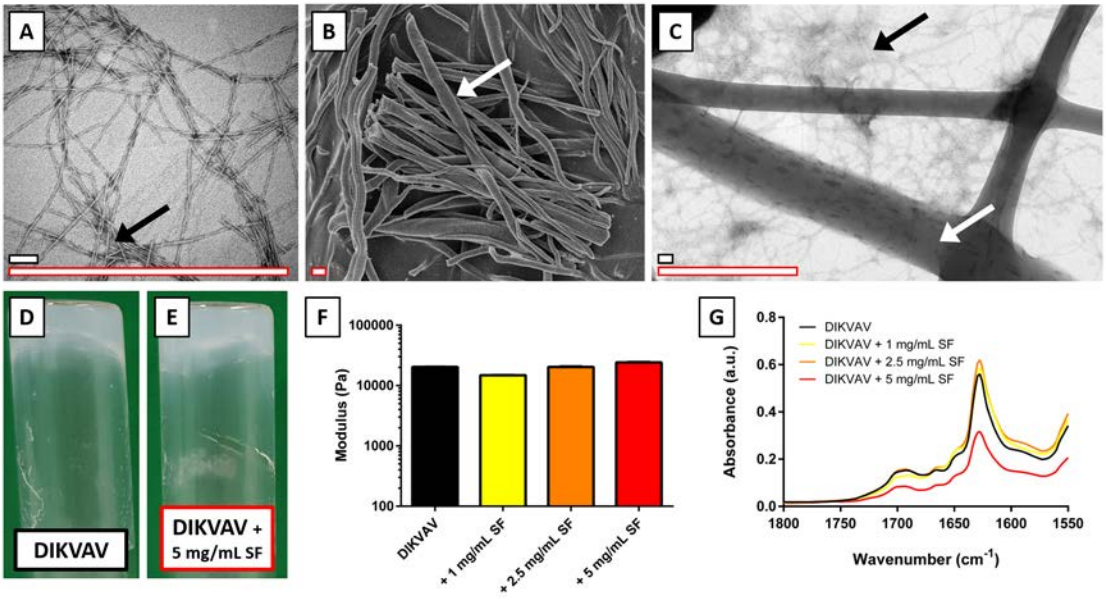

Figure 8.1: Composite self-assembling peptide (SAP) hydrogel and electrospun short fibres. A-C: TEM (A, C) and SEM (B) micrographs of nanofibres in DIKVAV self-assembling peptide hydrogel (black arrow) (A), electrospun and cut short fibres (white arrow) (B) and both features highlighted in the composite material. Scale bars show 100 nm (black) and 1 μm (red). D-E: Photographs of DIKVAV hydrogel alone (D) and loaded with short fibres (E). F-G: Rheology showing storage modulus (G') (F) and FTIR spectra (G) of DIKVAV hydrogel alone (black) and loaded with varying concentrations of short fibres (yellow, orange, red). Rheology data represent mean ± SEM (F).

The biocompatible polymer poly(lactic acid) (PLA) was electrospun into nanofibres ranging ~100-2000 nm in diameter, and the scaffold was then cut by microtome into loose short fibres ranging ~20-100 μm long (Figure 8.1B, Section 3.2.7-3.2.8). The short fibres were then mixed directly by thorough vortexing into the DIKVAV hydrogel. The resultant composite material retained the macroscopic properties of the SAP hydrogel (Figure 8.1D-E), specifically its injectable, shear-thinning property. On the nanoscale, the composite material showed the full range of nanofibres from both component materials (Figure 8.1C), which is more mimetic of the diverse range of nanofibre diameters found in the ECM.[241] The addition of short fibres to the hydrogel showed little effect on the mechanical properties of the hydrogel (Figure 8.1F), displaying a very slight increase in stiffness with increasing short fibre concentration. The stability of the peptide structures was broadly retained; the FTIR spectra (Figure 8.1G) showed major peaks at 1630 cm^{-1} and minor peaks at 1690 cm^{-1},

confirming that the dominant supramolecular structure adopted within the nanofibres was unaffected by the addition of short fibres.[61] These observations confirm the composite material, by retaining the desirable structural properties of its components, is capable of providing superior structural biomimicry than either SAP gels or electrospun scaffolds individually.

8.4.2 Growth Factor Delivery

We have previously demonstrated the ability of SAP hydrogels to stabilise and deliver multiple growth factors, specifically using the neurotrophic growth factor glial cell-line derived neurotrophic factor (GDNF) and brain derived neurotrophic factor (BDNF).[239] To develop the composite material to provide more sophisticated control over growth factor delivery we first assessed the release profiles of neurotrophic growth factors from the intact electrospun scaffold materials alone into PBS (Figure 8.2A). We tested both common methods of growth factor incorporation into electrospun scaffolds, with the growth factor emulsion mixed directly into the polymer solution used for electrospinning (emulsion (m)) (Section 3.2.7), and with the growth factor covalently attached to the fibre surface after electrospinning (immobilised (i)) (Section 3.2.4.2). The emulsion scaffold showed a burst release, decreasing steeply over 12 hours and then providing a lower sustained delivery. The covalently immobilised scaffold showed little to no delivery into the surrounding media, which was expected as the growth factor was permanently immobilised onto the scaffold surface. The negligible amount detected may have been residual unattached growth factor or material degradation.

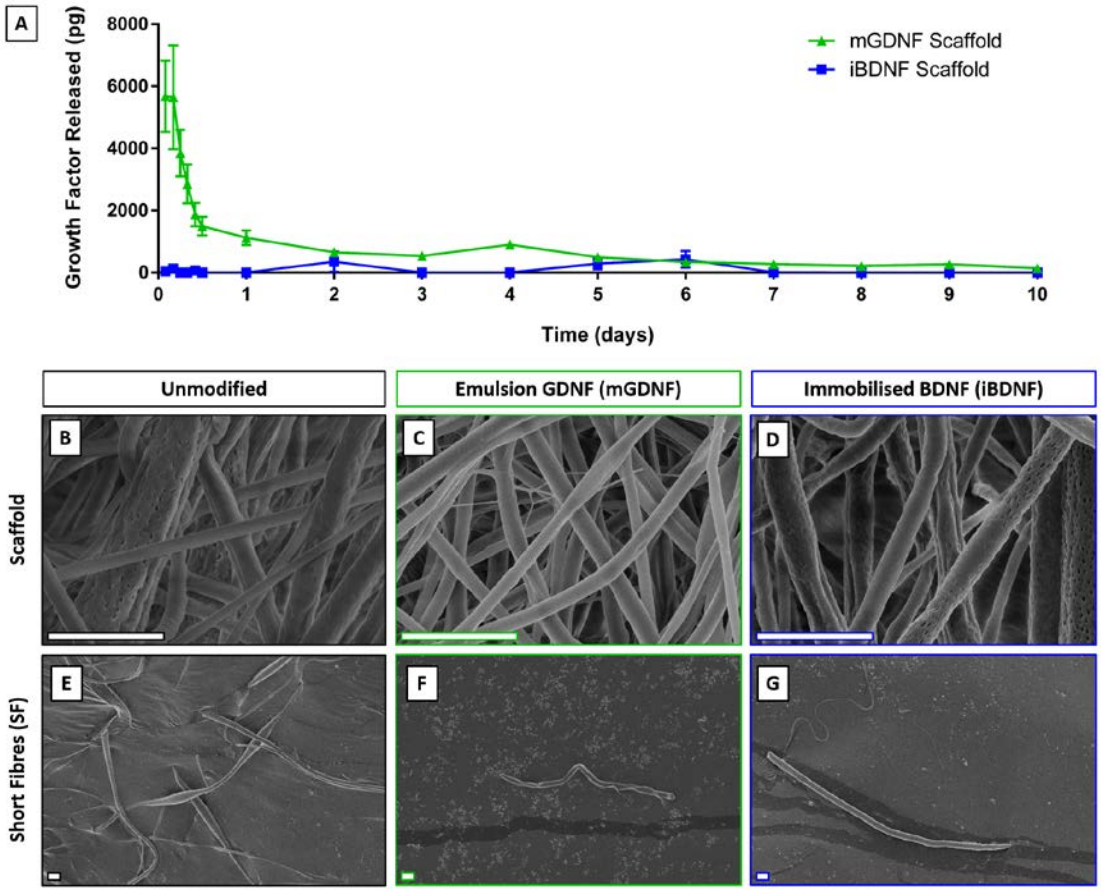

Figure 8.2: Growth factor incorporated electrospun materials. A: Release profiles from scaffolds with growth factors incorporated via emulsion (green) and immobilisation (blue) directly into PBS. Data represent mean ± SEM. B-G: SEM micrographs of intact scaffolds (B-D) and cut short fibres (E-G) from unmodified (B, E), emulsion GDNF (C, F), and immobilised BDNF (D, G). Scale bars show 2 µm.

We also confirmed that growth factor incorporation, either by emulsion or immobilisation, did not disrupt the nanofibrous structure of the scaffold or short fibres (Figure 8.2B-G). For the composite material to work as a growth factor delivery system, with the electrospun short fibres contained within the SAP hydrogel, the growth factor must be able to leave the electrospun material to reach the surrounding environment. The release data demonstrates that only the emulsion growth factor shows substantial release, and that it is therefore more suited for use in the composite material than the immobilised growth factor.

In isolation, the SAP and the emulsion electrospun materials loaded with GDNF both provided an immediate burst release diminishing over 12 hours (Figure 8.3A and Figure 8.2A respectively). This 'slow' burst delivery offered by both the SAP hydrogel alone and emulsion

scaffold alone offers an improvement over a solution of growth factors alone, which, unshielded, degrade rapidly. However, while immediate growth factor delivery can be useful in some contexts, delayed delivery is also very important. The therapeutic effects of drugs or growth factors are optimal at varied stages of the treatment; for example, epidermal growth factor (EGF), which increases proliferation of neural stem/progenitor cells (NSPs), is best delivered initially for 7 days, followed by erythroprotein (EPO) to protect and reduce apoptosis in these new cells.[22] In neural tissue regeneration the blood brain barrier (BBB) prevents systemic delivery, making controlled delivery particularly difficult to achieve in a non-invasive and non-iatrogenic way. Additional surgical disruption of the BBB can actually induce inflammation in the brain, which leads to secondary cell death.[191,242] This means that minimally invasive temporally controlled delivery should ideally come in the form of delayed release from the original implanted material. To maximise the effectiveness of an implanted treatment strategy after injury or disease, delayed release of growth factors ensures that the therapeutic value of growth factors is not compromised by the initial inflammatory reaction after BBB breach. Concomitantly, this controlled, delayed release will not disrupt the inflammatory response - which has been shown to be crucial to repair[243] – within the acute phase after brain injury, and will allow for the delivery of therapeutic factors to facilitate repair at a later time point, overcoming a potentially chronically persistent inflammatory response.

Temporally controlled, sequential growth factor delivery is an important goal in regenerative medicine and was the primary motivation for the engineering of our composite delivery system. Emulsion growth factor loaded short fibres within a SAP hydrogel essentially have two sequential diffusion steps required to reach the surrounding media. They must diffuse first from the short fibre into the hydrogel, then from the hydrogel into the surrounding media. The release profile from short fibres within the composite material (Section 3.2.2.2) shows a 6-day delay in delivery to the surrounding media, and a more sustained delivery profile compared the burst release from the intact scaffold alone (Figure

8.3A). This is an important characteristic as it offers two temporally distinct delivery profiles, which is difficult to achieve in a homogeneous tissue engineering scaffold. The material can be designed to deliver different growth factors in an initial burst or after a delay based on whether they are loaded into the SAP gel or electrospun short fibre component of the composite.

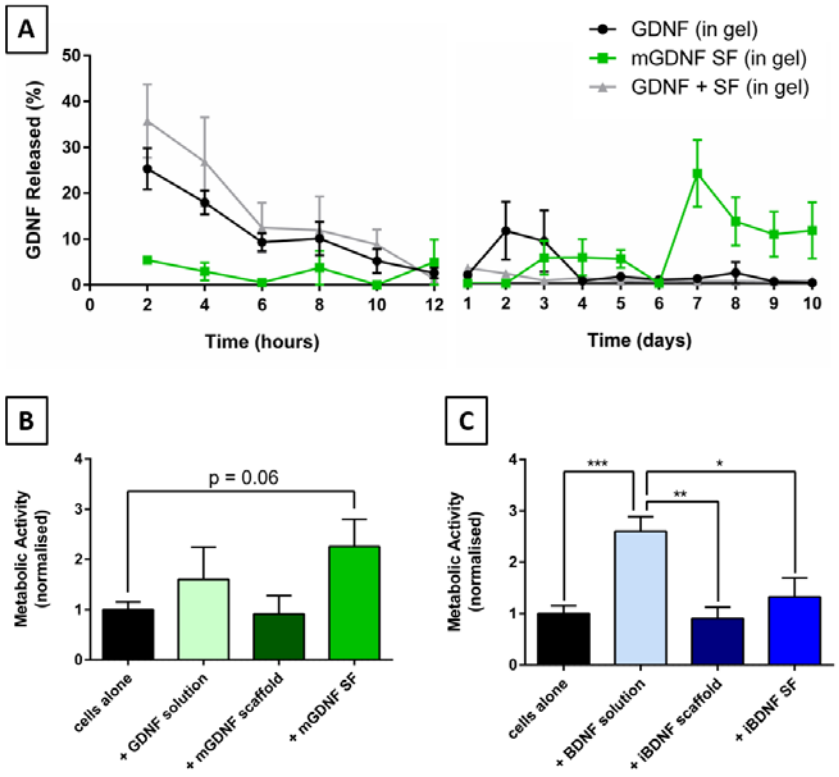

Figure 8.3: Short fibre growth factor delivery. A: Release profiles of GDNF solution (black), GDNF mixed with unmodified SF (grey), and mGDNF SF (green). Data show mean ± SEM. B-C: Metabolic activity of E14.5 murine cortical neurons after 3 days of incubation with growth factor treatments. Data show mean ± SEM. Statistical significance determined by two-way ANOVA: *** $p < 0.001$, ** $p < 0.01$, * $p < 0.05$.

We also tested the effect of the short fibres on growth factor delivery by mixing unmodified short fibres with GDNF solution before being loaded into the hydrogel (Figure 8.3A). This method has been used with polymer nanoparticles to provide encapsulation free nanoparticle style growth factor delivery based on surface charge interactions between the polymer particle and the growth factor.[178] This encapsulation free method offers simplification for single growth factor delivery, while also raising concerns about potential

interference in multiple growth factor systems using nano-carriers. Here we show that the growth factor solution exhibits the immediate slow burst profile when it is loaded into the hydrogel alone or when mixed with unmodified short fibres. It is likely that the encapsulation free effect is not observed here due to the much lower surface area to volume ratio of these relatively large short fibres compared to nanoparticles, which minimises the chance for interference from surface interactions.

The neurotrophic growth factors used, GDNF and BDNF, are known to increase neuron survival/metabolic activity as measured by MTT assay.[244-246] Here MTT assays were used to confirm the bioactivity of growth factors released from the electrospun materials with primary murine neurons (Figure 8.3B-C, Section 3.5.1.3, 3.5.2.8). The materials were incubated for 3 days before testing, allowing for degradation of free growth factor in solution. The emulsion short fibres showed the most significant effect on neuron metabolic activity, even more so than the control growth factor solution. We expect the improvement over the performance of the control was due to the prolonged delivery due to stabilisation from the short fibres. The intact emulsion scaffold showed little or no effect on the neurons, demonstrating the advantage of the short fibre form vs. the intact scaffold. Dispersed short fibres have a high surface area to volume ratio, and each fibre is able to interact with the solvent fully, whereas the intact scaffold has a higher density of hydrophobic polymer fibres to inhibit wetting of and diffusion from the interior layers of fibres. The inhomogeneous layered nature of intact scaffolds vs. the homogeneous dispersion of short fibres also contributes to the burst then sustained delivery profile observed above for the intact scaffold compared to the consistent delivery from the short fibres in the composite material. The immobilised materials, both the intact scaffold and short fibres, showed little to no effect on neuron metabolic activity, again because the growth factors were permanently immobilised to the fibres and unable to diffuse to the surrounding media and cells.

8.4.3 Resilience of Composite Structure

To ensure the resilience of the composite materials, specifically to determine if the short fibres would remain in the gels, the SAP gels were loaded with varying concentrations of short fibres were gently washed in water for 7.5 hr (Section 3.4.4) using a washing procedure we have previously used with gold nanoparticles in SAP hydrogels.[237] We found short fibres present and integrated into the hydrogel structure at all concentrations before and after washing (Figure 8.4). Importantly, we could find no visual evidence of displaced short fibres in the wash water under scanning electron microscopy (SEM). This is a significant result for a growth factor delivery vehicle in a tissue engineering material specifically, where the goal is the localised and long-term delivery to the extracellular environment. The resilience of the short fibres within the composite gel means that the growth factors will continue to be delivered from the implantation location only, thereby avoiding any off-target effects.

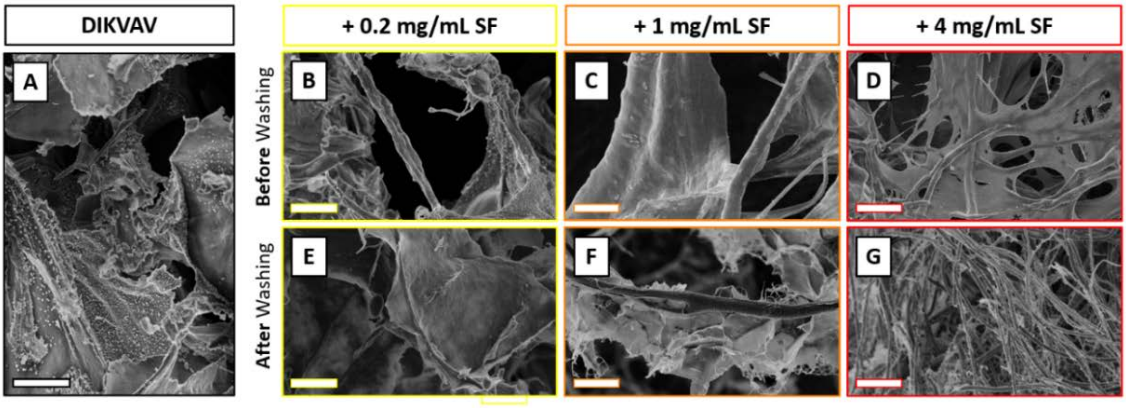

Figure 8.4: Locational resilience of short fibres in hydrogel. SEM micrographs of DIKVAV hydrogel alone (A) and loaded with varying concentrations of short fibres before (B-D) and after (E-G) washing. Scale bars show 5 μm.

We have previously tested small inorganic gold nanoparticles under the exact same washing conditions used here and found that they washed out readily from the SAP hydrogels, with complete removal of gold nanoparticles (as imaged by TEM) (Section 5.3.2).[237] The localisation of the short fibres here compares favourably to those nanoparticles. Intuitively, the smaller size of nanoparticles makes them more able to diffuse out of hydrogels. Nanoparticles in general are very popular drug delivery vehicles, as they are

versatile and easily functionalised. The very small size of nanoparticles makes them well suited for systemic and intracellular delivery systems, where small size and easy movement are required to allow the nanoparticle to reach its final target. Nanoparticles can be chemically adapted/functionalised to prevent diffusion and achieve localisation. We propose that here the localisation is more innate and achieved morphologically rather than chemically, which could be advantageous where other chemical surface modifications are required to control other properties (hydrophobicity, shielding layers, etc.).

Much work has been done incorporating nanoparticles into tissue engineering scaffolds, as has been done here with short nanofibres. However, for incorporation into tissue engineering materials, we propose that the innate locational resilience of these larger nanofibres provides a drug delivery platform with superior long-term localisation of growth factor delivery. Considered with the structural biomimicry benefits of the short fibres, and the controlled delivery profiles, we believe that these short fibres have great potential as growth factor delivery vehicles in tissue engineering materials.

8.5 Conclusion

The novel composite material described here represents a step forward for the utility of both SAP hydrogels and electrospun nanofibres as tissue engineering materials. By combining these materials, we have demonstrated improved structural biomimicry of the ECM by providing a range of nanofibre sizes. The composite material also represents a novel growth factor delivery system capable of distinct release profiles of either a slow burst or 6-day delayed and sustained delivery. This is a significant achievement applicable to neural tissue regeneration, matching the time required for the neuroinflammatory response to subside,[247] and therefore allowing controlled growth factor delivery into a non-reactive cell environment to maximise therapeutic benefit.

We propose that fine tuning of the short fibre parameters, including fibre dimensions, surface porosity, polymer composition, and growth factor loading could be used to also fine-tune the release properties. Independent control of the release dose could be achieved by

varying the fibre loading within the hydrogel. As the system's functionality is based on morphology and diffusion rather than specific chemistry, it is also inherently adaptable for use with other growth factors. Overall this system integrates beneficially with the SAP hydrogel on a material level while also providing controlled growth factor delivery.

Chapter Nine

Delivery System: Stimuli Responsive

9.1 Chapter Details

This standalone chapter describes the successful development of the third temporally controlled growth factor delivery system, achieving stimuli-responsive control of the shape of the temporal release profile of growth factor from the SAP hydrogel. This chapter is also a research article manuscript in preparation by Kiara Bruggeman, Tina Zhang, Richard Williams, Antonio Tricoli, and David Nisbet.

9.2 Abstract

Here, we utilise a novel hybrid tissue engineering scaffold to achieve temporally controlled delivery of growth factors, which are important but unstable molecules used in regenerative medicine. Growth factors were chemically crosslinked to UV-sensitive nanoparticles, which were subsequently loaded into self-assembling peptide (SAP) hydrogels. We observed stimuli controlled delivery, where UV exposure was used to release growth factors bound to the nanoparticles. When the nanoparticles were incorporated within the SAP hydrogel, this UV trigger caused a counter-intuitive decrease in growth factor released from the hydrogel. This novel observation was caused by growth factor, upon release from the rapidly diffusing nanoparticles, instead competitively adsorbing to the SAP structures. We are the first to

report three temporally distinct release profiles from a SAP hydrogel, obtained from: unmodified growth factor, nanoparticle bound growth factor, and UV controlled release of nanoparticle bound growth factor. This stimuli-based control allows the design of a specific release profile, and we used it to create a burst-free constant dose delivery profile. Significantly, we were able to use this approach to temporally distinguish the release profiles of multiple growth factors simultaneously loaded into the same hydrogel.

9.3 Introduction

Growth factors are important intracellular signalling protein molecules that have significant potential for controlling cell and tissue fate for improved regenerative medicine outcomes. However, as these molecules function as short-term soluble signalling molecules, they are rapidly secreted and consumed; their inherent instability therefore makes their controlled delivery a challenge.[31] We have previously demonstrated that brain-derived neurotrophic factor (BDNF) specifically shows near total degradation after only 1 day in PBS,[102] and growth factors are even more short-lived *in vivo* where enzymatic degradation is a factor.[10] Growth factor half-lives *in vivo* are as low as 3 minutes for basic fibroblast growth factor (bFGF)[13] and 45 minutes for nerve growth factor (NGF).[14]

This short lifespan has a detrimental effect on the use of growth factors therapeutically, where their ideal delivery timeframe can occur over weeks,[22] and their size and instability make them unsuited for systemic delivery.[10] A significant design challenge lies in preventing growth factor degradation long enough to allow the delivery of a still functional protein throughout the desired timeframe only. It is important for any drug, including growth factors, to be delivered at the appropriate time and dose. Too much can have toxic or off-target effects and too little can have no effect, hence delivery must occur within a therapeutic concentration window.[10,248] Any material strategy for controlled growth factor delivery *in vivo* must therefore ensure the long-term stabilisation of the growth factor as well as providing temporal control over the delivery profile.

Tissue engineering scaffold materials mimic the natural extracellular matrix (ECM) to promote tissue regeneration and degrade naturally as healthy tissue grows. An ideal growth factor delivery system for regenerative medicine should operate synergistically with these tissue engineering scaffold materials. Spatial control of growth factor delivery is achieved by loading them into an implanted or injected scaffold, which acts as a reservoir for diffusional delivery to the surrounding tissue. The goal is often to provide a consistent therapeutic concentration through sustained, ongoing delivery, although depending on the application many different delivery profiles can be required, such as rapid burst or pulsatile release.[22] Advancement of the field depends on building a library of control techniques so as to be able to engineer any possible combination of different release profiles of multiple drugs or growth factors into a single material.

We have previously used chemical cross-linking via 4-(N-Maleimidomethyl)cyclohexane-1-carboxylic acid 3-sulfo-N-hydroxysuccinimide ester sodium salt (SMCC) to provide a permanent ongoing presentation of growth factors by immobilising the growth factors to electrospun nanofibres in tissue engineering scaffold materials.[31,36,191,192] We have also used this SMCC attachment to temporally control their non-permanent delivery, by attaching polysaccharide chains to the growth factor to delay their release from self-assembling peptide (SAP) hydrogel tissue engineering materials.[102]

Photo triggered drug delivery from nanocarrier vehicles have been well explored, using light sensitive polymers as well as inorganic nanoparticles.[57] They are often used independently but can also be incorporated into other materials, such as the photo responsive silica nanoparticles incorporated into hydrogel materials to provide UV-triggered drug delivery in a localised environment.[93] In both cases, the majority of these studies focus on using a photo trigger to commence the release/delivery of a drug.[92] The novelty of our study is that we use SMCC attachment to create the reverse system, in which UV light triggers a reduction in drug delivery rather than an increase.

The photocatalytic properties of titanium dioxide (TiO_2) are well known, and one of the reasons TiO_2 is a popular material for nanoparticle drug delivery systems.[249] TiO_2 nanoparticles alone are acceptably biocompatible,[250] and their biocompatibility can be improved with a biocompatible coating.[251,252] We have previously demonstrated a method of creating TiO_2 nanoparticles with a UV-sensitive lysine coating,[99] which provides the necessary amine functional group required for growth factor attachment via SMCC. We have also previously explored the unique relationship between growth factors and the nanofibrous hydrogels formed from self-assembling peptides (SAPs).[102] We have shown that growth factors adsorb to the SAP nanofibres,[102] and that gold nanoparticles, inorganic nanoparticles similar to TiO_2, are able to diffuse out of the SAP hydrogel readily.[237]

Here, we use the SMCC attachment method and nanoparticle delivery to explore two new mechanisms for temporal control of delivery: attachment to a carrier nanoparticle embedded within a SAP hydrogel, and stimuli-responsive control of delivery from these nanoparticles. We report on a system in which nanoparticle bound BDNF shows greater release from the SAP hydrogel before UV treatment, at which point the unbound growth factor adsorbs to the SAP nanofibres. We also use this relationship and the UV-sensitive nanoparticles to induce a consistent release profile, using the UV response to counter the natural non-zero order delivery profile.

9.4 Results and Discussion

The growth factor brain derived neurotrophic factor (BDNF) was covalently attached to amine coated titanium dioxide (TiO_2) nanoparticles via the chemical crosslinker SMCC (Section 3.2.4.3). After SMCC attachment the BDNF coated nanoparticles were measured via enzyme linked immunosorbent assay (ELISA) after repeated washing and UV exposure (Section 3.4.5) to assess their utility alone as photo triggered growth factor delivery vehicles. Repeated washing was performed to remove unbound BDNF and to test the resilience of the bound BDNF. The nanoparticles consistently presented more BDNF before UV

treatment (Figure 9.1A), while the supernatant wash solution consistently presented more BDNF after UV treatment (Figure 9.1B). These data indicate that the nanoparticles function as expected, releasing the bound BDNF into the surrounding solution only after UV exposure. We have previously demonstrated that the amino coating around the nanoparticles can be removed by UV exposure,[99] and the attached BDNF is removed with it. Here, samples received only one UV treatment each, always performed in the last wash, to give the repeated washing as much chance as possible to remove the bound BDNF before the UV treatment. For example, the wash four samples were all washed three times without UV exposure, and in the fourth wash cycle samples were exposed to UV (or not for the control group). The high levels of BDNF in the first wash of the nanoparticles can be explained by the residual presence of the original BDNF reaction solution; reaction solution was removed via centrifugation only once before immediately commencing the washing and UV exposure testing. The lowest detectable BDNF release from unexposed particles was after three washes, which were used in further development below. The increase in BDNF detected in the supernatant of the fourth wash could be caused by breaking up nanoparticle agglomerates, or an effect of persistent mechanical washing on the bound BDNF. TEM micrographs (Figure 9.1C-E) show no change in nanoparticle size or morphology after BDNF attachment (Figure 9.1D) or UV treatment (Figure 9.1E) compared to the original amine coated nanoparticles (Figure 9.1C).

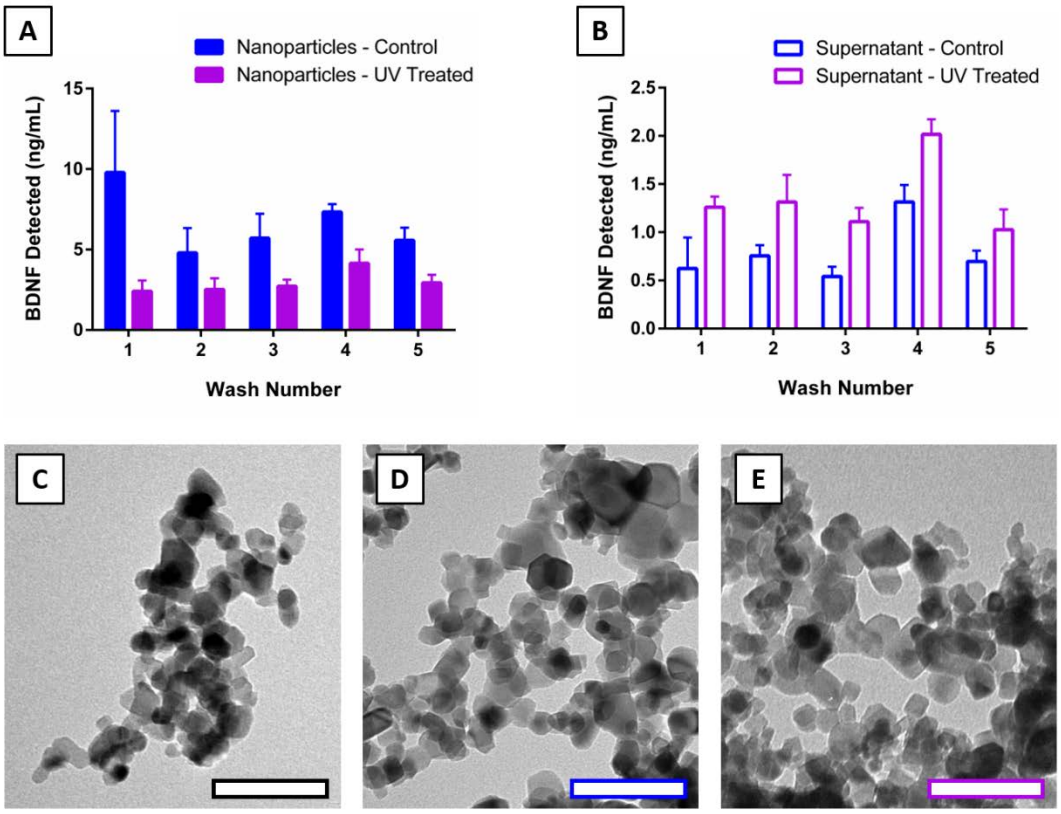

Figure 9.1: Nanoparticle growth factor attachment and UV triggered release. A-B: BDNF detected on nanoparticles (A) and in washing supernatant (B) with UV treatment (purple) and untreated (blue) after a number of washes. Each group received only one UV treatment during the latest wash (i.e.: after having already been washed n-1 times) and data represent mean ± SEM. C-E: TEM micrographs of amine coated nanoparticles (C), nanoparticle bound BDNF (D), and nanoparticle bound BDNF after UV treatment (E). Scale bars show 100 nm.

The above results demonstrate the potential for this nanoparticle system to provide UV triggered growth factor release upon UV stimulus. Next we combined this nanoparticle system with our promising novel minimalist SAP hydrogels.[9] Here we used Fmoc-DIKVAV peptide, which contains the isoleucine-lysine-valine-alanine-valine (IKVAV) sequence from the extracellular matrix protein laminin, modified with an additional N-terminal aspartic acid (D) residue to adjust the pK_a properties of the molecule such that pH-driven self-assembly occurs at pH 7.4. These hydrogel materials have a nanofibrous morphology that provides structural support on a cellular level in addition to their biocompatible aqueous environment.[61] We confirmed that incorporating nanoparticles and subsequent UV treatment did not disrupt the SAP hydrogel. The FTIR spectra of all gels (Figure 9.2A) show

a major peak at 1630 cm^{-1} and a minor peak at 1690 cm^{-1}, which confirm the supramolecular assembly mechanism of the SAP nanofibres.[9,61] Parallel plate rheology (Figure 9.2B) confirmed that the elastic modulus, an important factor in tissue-specific regeneration,[2] maintains largely unaffected by nanoparticle or UV treatment. While the addition of nanomaterial fillers often increases hydrogel stiffness, in this case it has no affect. This could be because the nanoparticles and SAP nanofibres are on the same scale, so the unloaded SAP hydrogel already has a sort of nanomaterial filler. TEM micrographs (Figure 9.2C) further confirm the nanofibrous structure was maintained across all hydrogels. These results confirm that the SAP hydrogel, a proven ECM mimetic tissue engineering material, retains its beneficial properties after incorporation of the nanoparticle bound growth factor pre and post UV treatment.

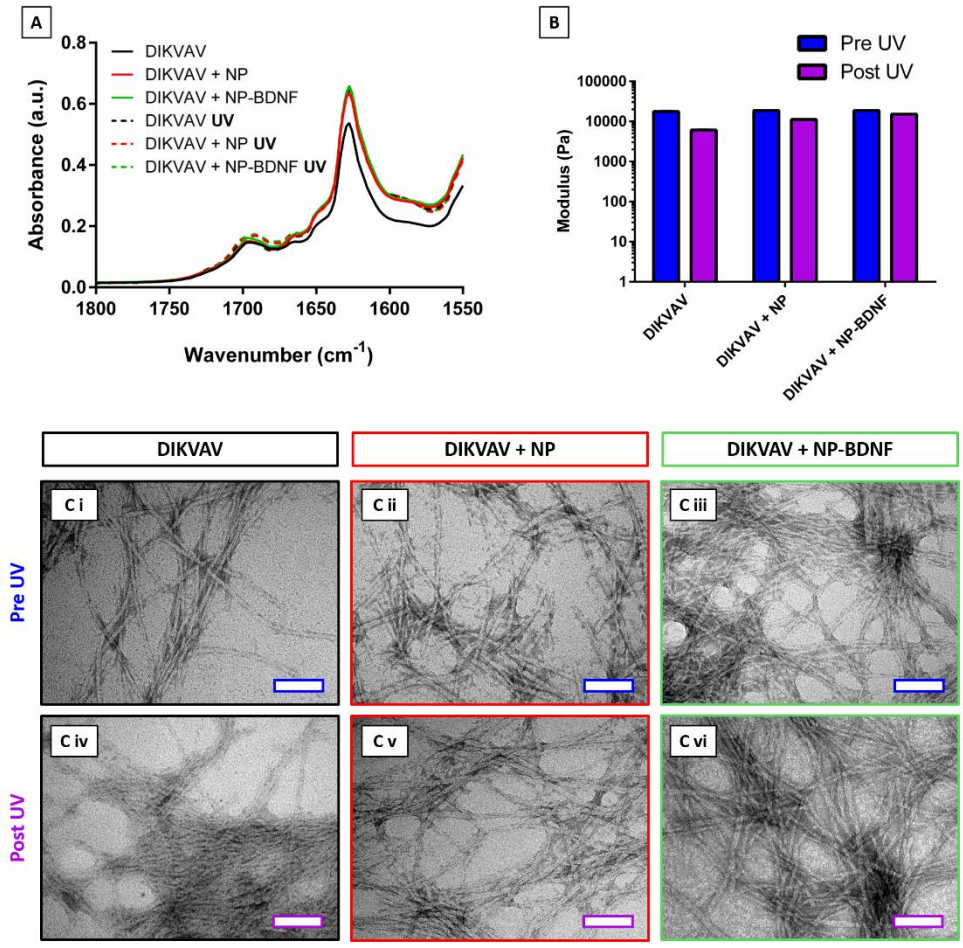

Figure 9.2: SAP hydrogel characterisation with nanoparticle incorporation and UV treatment. Characterisation of DIKVAV hydrogel alone (black), loaded with unmodified nanoparticles (red), and loaded

with nanoparticle bound BDNF (green), before (blue) and after (purple) UV treatment. A: FTIR Spectra with faded colours showing spectra after UV treatment. B: Rheological analysis showing mean storage modulus (G'). C: TEM micrographs of SAP nanofibres with scale bars showing 100 nm.

Next, to assess the effect of nanoparticle attachment on the temporally resolved delivery profile of a two-component system, the SAP gels were simultaneously loaded with nanoparticle bound BDNF (NP-BDNF) as well as unmodified GDNF (Section 3.2.2.3). The delivery profiles of each growth factor (Section 3.4.1) were then assessed without UV treatment (Figure 9.3A). As expected, the unmodified GDNF profile shows a slow burst delivery, with high initial delivery decreasing steadily to near zero over 12 hours. This matches the delivery profile we have observed from GDNF loaded alone into DIKVAV hydrogels (unpublished), indicating that the nanoparticles do not significantly interfere with other growth factors within the same system. The nanoparticle bound BDNF demonstrates a steady increase over 12 hours. These distinct delivery profiles from the same SAP gel demonstrate that the nanoparticle attachment method can be used to temporally control the release profile of two separate growth factors. We have previously demonstrated that SMCC attachment of growth factors to scaffold materials (electrospun polymer nanofibres) prevents their degradation while maintaining their bioactivity *in vitro* and *in vivo*, confirming bioactivity *in vitro* with BDNF,[36] and *in vivo* with GDNF[31,191] and Interleukin-10 (IL-10).[192] And we have also demonstrated the stabilising effect of SAP hydrogels on growth factors, with BDNF specifically showing stabilisation out to at least 6 weeks.[102] The fact that increasing amounts of BDNF were detected here out to 12 hours confirms that degradation is being halted and suggests that the nanoparticle bound BDNF would have stability similar to the nanofibre bound growth factors that we have published previously. All together this information indicates potential for nanoparticle binding as another method of temporal control of growth factor delivery from SAP hydrogels.

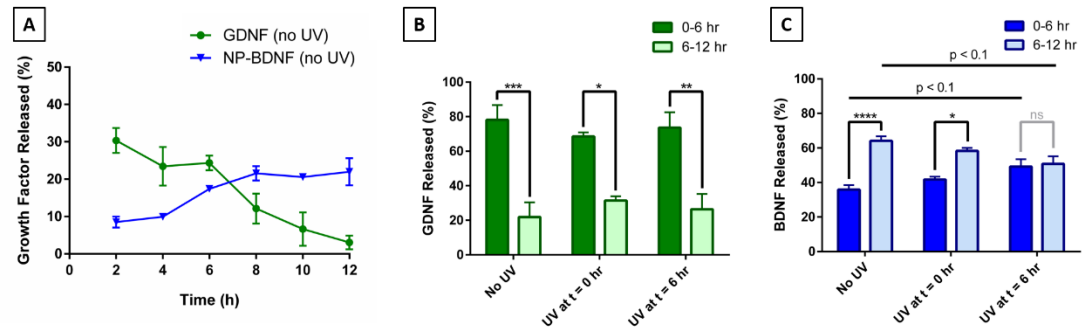

Figure 9.3: Relative release profiles of lone and nanoparticle bound growth factor. Release profiles showing the relative (percent of total) release of GDNF (green) and BDNF (blue) released at each time point from dually loaded SAP hydrogels. Data represent mean ± SEM. Statistical significance determined by two-way ANOVA: **** $p < 0.0001$, *** $p < 0.001$, ** $p < 0.01$, * $p < 0.05$, ns = no statistically significant difference. A: Full release profiles of unmodified and nanoparticle bound growth factors without UV treatment. B-C: Condensed release profiles including UV treatment groups. Note statistically significant difference was found between each GDNF "0-6 hr" group and each "6-12 hr" groups (i.e.: 9 relationships total), and no statistically significant difference was found between different GDNF "0-6 hr" groups or between different GDNF "6-12 hr" groups (B).

Next, we explored the stimuli responsive growth factor delivery from within the dually loaded SAP gel. The release profile of the unmodified GDNF was changed slightly, possibly due to the interaction of the GDNF with newly released BDNF or the surface of the nanoparticles post treatment. However, this effect was small, and the total release profiles overall were consistent with that observed without UV treatment, indicating that this stimulus did not significantly affect the properties determining unbound GDNF delivery (Figure 9.3B). However, UV treatment significantly affected the delivery of the nanoparticle bound BDNF (Figure 9.3C). Over the 12-hour release profile without UV stimulus, more BDNF is released later in the profile. Only 36% of the total BDNF release occurred in the first 6 hours, with 64% released in the second half. With initial UV stimulus (i.e. UV treatment performed at time t = 0 hr), the release profiles were similar: 42% released in the first 6 hours, and 58% in the second. When the UV stimulus was applied midway (i.e. UV treatment performed at time t = 6 hr), however, the release profile of the BDNF changed more significantly, displaying a constant release rate with near equal release in the first and second halves (49% and 51% respectively). Counter intuitively, and interestingly, this

suggests that unbound BDNF is released from the bulk material more slowly than bound BDNF on nanoparticles.

This interesting observation becomes more intuitive when considering the relationships between SAP nanofibres, growth factors, and nanoparticles, and when looking at the how UV treatment affects the absolute delivery profiles (Figure 9.4A). The absolute delivery profile (Figure 9.4A) shows the raw data, the actual amount of growth factor released (in ng) values used to calculate the relative profiles shown above (Figure 9.3C). The initial results above looking at nanoparticles alone confirm that UV treatment caused the bound BDNF to be released from the nanoparticles. Meanwhile, our previous work shows that growth factors (specifically BDNF) alone adsorb to the SAP nanofibres. We propose that the UV treatment of these particles when inside a SAP gel caused the BDNF to be released to the hydrogel, and then reversibly adsorb to the nanofibre surface, placing their release under the control of this adsorption interaction (Figure 9.4B). The general trend or temporal shape of the release observed for the untreated samples is characterised by an initial slow release, with an increase in release in the second half of the profile, presumably due to the diffusion of the nanoparticles through the system. This trend was maintained with an initial UV treatment, but at a lower magnitude, consistent with an incomplete detachment of BDNF from the nanoparticles. There may also be some photolytic degradation of the BDNF. The UV treatment did not change the release behaviour of the nanoparticles; it only reduced the amount of BDNF bound to those nanoparticles. The slight differences in the relative release profiles above (Figure 9.3C), with a slight shift towards earlier release from the UV treated gels, could be explained by factoring in a secondary release profile of unbound BDNF from the SAP gel, which we have shown is similar to that of unbound GDNF, characterised by a slow burst with more growth factor released initially.[102]

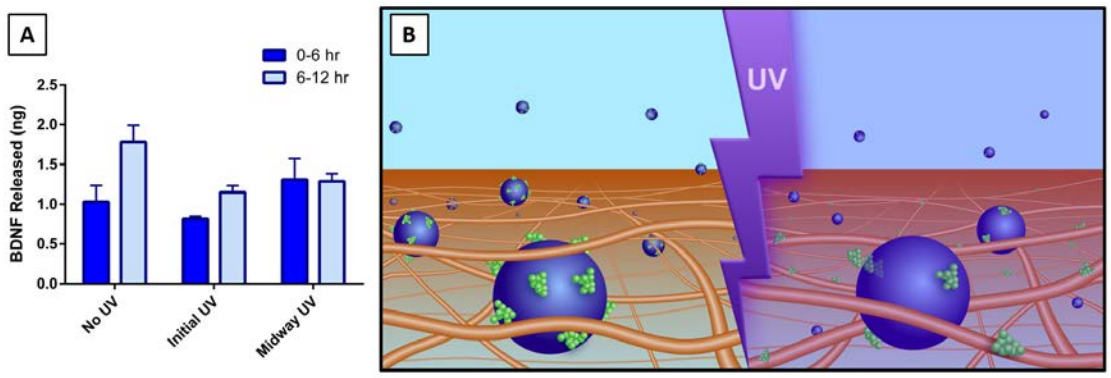

Figure 9.4: Reverse UV triggered delivery. A: Condensed release profile showing absolute amount of BDNF released in different UV treatments. Data represent mean ± SEM. B: Mechanism of growth factor interactions when bound to nanoparticles and after freed by UV treatment able to adsorb to SAP nanofibres

Applying the UV treatment midway through the release profile allowed us to change not just the dose but the temporal shape of the release profile, providing a consistent dose over the course of the release profile by combining the first half from the relatively higher release rate of the untreated group followed by the second half of the relatively lower release rate of the UV treated group. Again, the release behaviour of the nanoparticles is unchanged, but UV treatment can be used to control how much growth factor those nanoparticles carry and when. This additional consistent dose release profile allows us to selectively induce a third distinct temporal release profile offered by this nanoparticle growth factor delivery system. The results above suggest that there is an incomplete detachment of BDNF from the nanoparticles, indicating that multiple UV treatments could be used to further smooth and control the release profile over longer periods, allowing a truly constant delivery from a diffusion based system. The proposed mechanism is shown in more detail below (Figure 9.5).

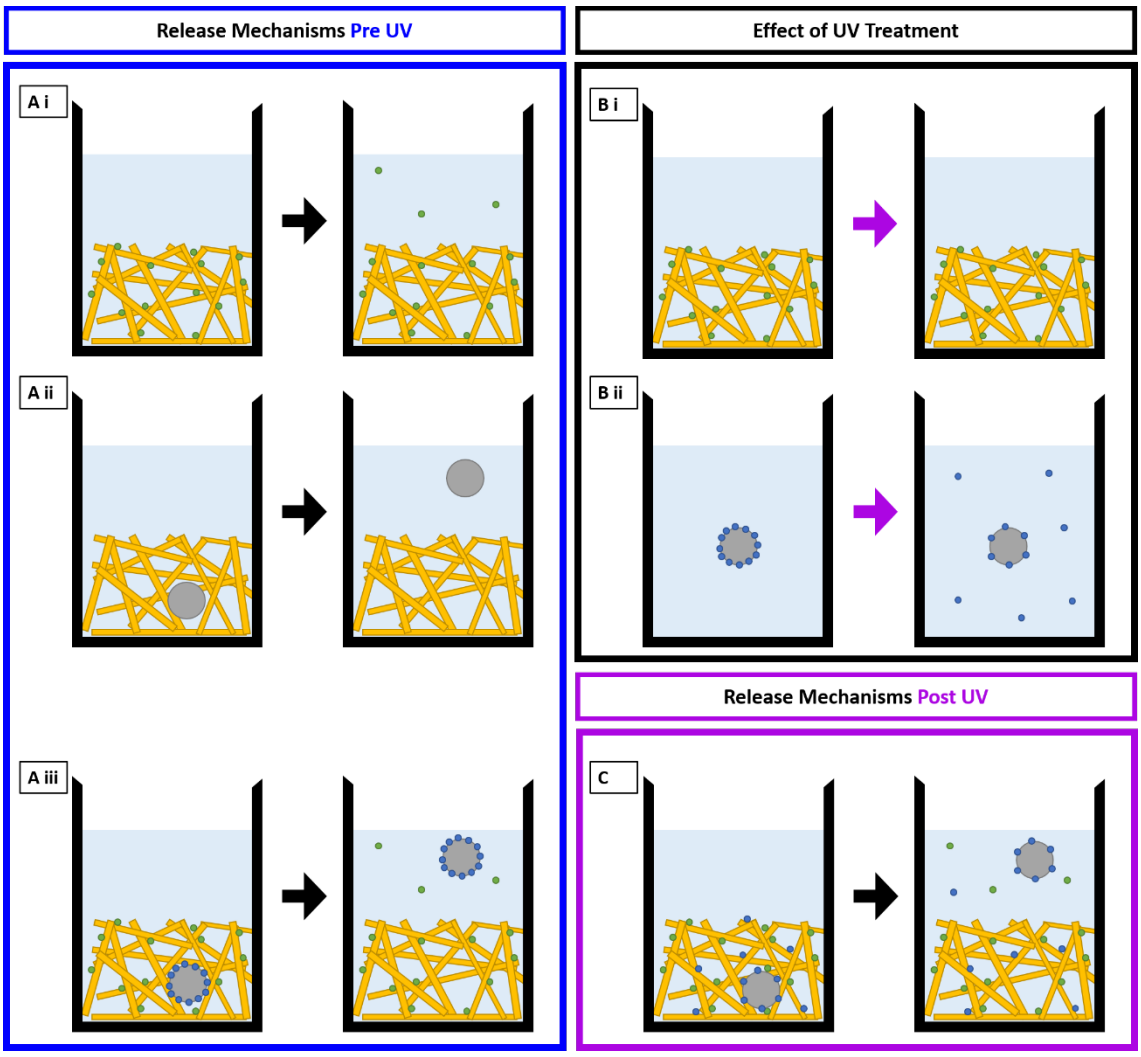

Figure 9.5: Detailed mechanism of reverse UV-triggered release. Small green and blue circles represent GDNF and BDNF respectively. Large grey circles represent nanoparticles. Orange lines/thin rectangles represent SAP nanofibres making up the SAP hydrogel. Black arrows represent time passing only. Purple arrows represent UV treatment. A i: Growth factors adsorb to SAP nanofibres and release slowly from the hydrogel. A ii: Nanoparticles diffuse readily from the hydrogel. A iii: SAP hydrogel loaded with bout free (GDNF, green) and nanoparticle bound (BDNF, blue) growth factors exhibits two distinct release mechanisms. B i: The SAP nanofibre/growth factor interaction is unaffected by UIV treatment. B ii: UV treatment causes nanoparticle bound growth factor to be released into the surrounding solution as free growth factor. This release is incomplete, with some growth factor remaining bound. C: After UV treatment, the nanoparticles continue to release readily, but with a reduced amount of bound BDNF, decreasing the amount of BDNF released. The unbound BDNF now acts as a free growth factor and adsorbs to the SAP nanofibres, from which there is a small amount of release. Meanwhile, free GDNF release from the SAP nanofibres continues unaffected.

9.5 Conclusion

In this work, we have used TiO_2 nanoparticles combined with novel SAP hydrogels to create a growth factor delivery system. Exploring both the effect of nanoparticle binding and

UV treatment we demonstrate that this system is capable of providing at least three temporally distinct release profiles: a steady increase, a steady decrease, and a consistent dose. We have demonstrated how the intuitive UV controlled growth factor release is reversed by interactions with SAP gels, and how the nanoparticles can be used to tune and tailor growth factor release profiles. We have also confirmed that neither nanoparticle incorporation nor UV treatment adversely effects the SAP gel properties. This is an important consideration when considering implementing this technology within materials with structure dependant design features. This system therefore shows great promise for a facile and non-intrusive drug delivery approach. Although UV sensitive TiO_2 nanparticles were used here, the novelty of this system, the reverse trigger effect, depends on the combination with SAP hydrogels and is independent of the stimulus used to trigger release from the nanoparticles. A variety of stimuli-responsive nanoparticle systems for triggered drug release exist currently, using stimuli including infrared (IR) light, ultrasound waves, and magnetic fields.[92] As such, there are many options for available for incorporation into this system when UV stimulus is not feasible. Incorporation of materials capable of second harmonic generation of UV light from an IR light trigger could also be used to address the issues of low penetration depth and cytotoxicity of UV light as a trigger.[253] As a proof of concept here, we demonstrate that multiple aspects of temporal control over growth factor delivery are possible, and provide the temporally distinct delivery of multiple growth factors from a single material, an important goal in regenerative medicine.

Chapter Ten

Conclusion

The work described in this thesis represents a significant contribution to the field of tissue engineering and growth factor drug delivery. While a variety of strategies exist to incorporate growth factors into tissue engineering materials, there are some common drawbacks. Most of the existing methods focus on sustained presentation of growth factors, overcoming the short lifetime of these molecules but not providing the any further temporal control. We have established that SAP hydrogels can provide that sustained delivery, and have gone further developing methods of temporally controlling when that delivery occurs and the nature of the delivery profile.

Current growth factor delivery strategies also often involve direct modification or controlled degradation of the tissue engineering material, as though the tissue engineering material can be either a supportive ECM mimic or a depot for sustained growth factor delivery, but not both. While the aim of this thesis has been to provide controlled growth factor delivery, an emphasis on ECM mimetic material properties has been maintained throughout. The materials were first investigated *in vivo* without growth factors, confirming their relevance and efficacy as a support material. The SAP material has remained a crucial consideration in the development on the delivery strategies discussed here, and we have

confirmed that none of the three modified delivery strategies developed significantly affect the important ECM mimetic characteristics of the SAP hydrogel. In fact, the composite material described in Chapter Eight adding short electrospun fibres to the SAP hydrogel to achieve a long delay represents a potential improvement to the biomimetic structural properties of the SAP hydrogel.

The three proof of concept delivery strategies developed here have all been successfully demonstrated as means of temporally controlling growth factor delivery from SAP hydrogels. The short (hours) and long (days) delay methods provided barriers to the diffusion of growth factors out of the SAP hydrogel, delaying the start time of growth factor delivery. This is particularly relevant to application in brain tissue regeneration where systemic delivery is inhibited, so control over the timing of delivery must come in the form of controlled delayed between the initial material injection/implantation and the delivery or growth factors. The stimuli responsive method provided control over the shape of the temporal delivery profile rather than the starting point. The nanoparticle binding provided a distinct profile compared to the unbound growth factor, a gradual increase in delivered dose rather than the burst and gradual decrease observed from growth factors alone. The UV stimulus was also used to effectively smooth the delivery profile to a constant delivered dose, a burst-free sustained delivery.

The short delay strategy was achieved by using electrostatic interactions between the SAP nanofibres and other materials. These interactions were first investigated with the SAP materials for delivering non-growth factor materials. Mixing the sulfonated polysaccharide, fucoidan, with the SAP hydrogel allowed its sustained presentation to cells and material characterisation revealed that the fucoidan molecules were associating closely with the SAP nanofibres. Similarly, the addition of a positively charged lysine residue into the SAP sequence was shown to increase interactions between the nanofibres and negatively charged viral particles. Based on these immobilising physical associations, growth factors were

modified by covalent attachment of the polysaccharide, chitosan, and the additional interactions between the chitosan and the SAP nanofibres cause the modified growth factors to remain in the SAP hydrogel longer. Future development of this system could focus on tuning the exact duration of the delay by changing the relative amount of bound chitosan, or by investigating other polysaccharide chains for attachment.

The long delay strategy was achieved by combined electrospun nanofibres with the SAP hydrogel, creating a composite material. The use of electrospun materials for sustained presentation of immobilised growth factors was first investigated, including cutting the scaffolds into short fibres to mix into a non-SAP gel. While the growth factors presented maintained bioactivity, the immobilised growth factors stuck to electrospun fibres within a hydrogel material were not able to reach and influence cells in the surrounding environment. This approach was adapted with emulsion electrospinning, creating short electrospun fibres to act as a depot from which growth factors could slowly diffuse out, rather than an anchor to which they were permanently attached. The bioactivity of growth factors prepared in this adapted approach was confirmed, and the method successfully achieved a 6-day delay in growth factor delivery.

Future work on this delivery system could see the development of multi-layered short fibres prepared by coaxial electrospinning to create more complex multi-component delivery profiles from the single material (Figure 10.1). Growth factors, or other drugs, loaded into the core layer could achieve a greater delay in reaching the surrounding environment, and unloaded shielding layers could be used as well to increase the duration of the delay. This approach has been demonstrated with intact electrospun scaffolds,[50] and could readily be adapted to provide multi-layered short fibres. The high length to diameter aspect ratio (~ 100x) of the fibres should minimise the effect of growth factors released from the ends of the fibres, or else post cutting treating such as layer-by-layer deposition could be used to create fully enclosed additional layers.

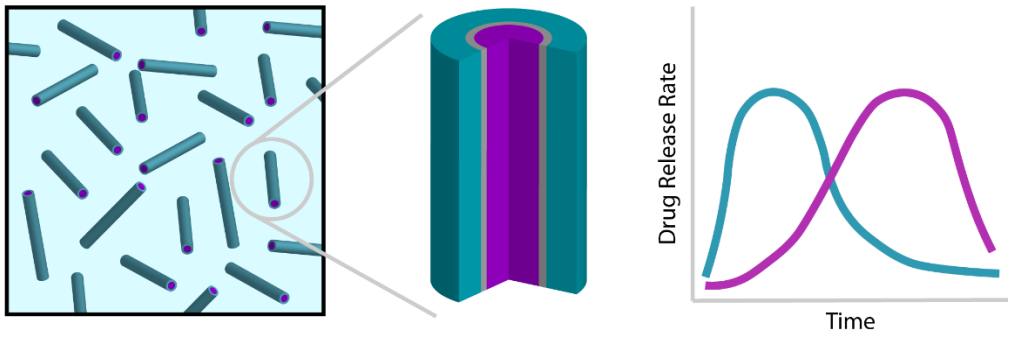

Figure 10.1: Multi-layered electrospun short fibre growth factor delivery vehicles. Proposed design approach showing (from left to right) loose short fibres, a short fibre cross section exposing the interior layers, and the hypothesised multi-component growth factor delivery profiles. Blue and purple layers contain distinct growth factors, grey layer is unloaded and provides shielding only, additionally delay the release from the core purple layer.

The stimuli responsive control was achieved using UV sensitive nanoparticles and the same covalent chemical attachment method used to achieve a short delay and used to immobilise growth factors to electrospun materials. While the growth factor bound nanoparticles allowed displayed intuitive release behaviour, with the UV stimulus resulting in growth factor being released into the surrounding solution, by loading the bound nanoparticles into the SAP gel we were able to achieve counter intuitive stimuli responsive behaviour. Upon UV exposure, the bound growth factor was still released from the nanoparticle, however, the nanoparticles diffused more readily from the SAP hydrogel than unbound growth factors alone, which adsorbed to the SAP nanofibres to remain longer within the hydrogel. Accordingly, UV exposure reduced the growth factor release to the surrounding environment rather than increasing it. Using this responsivity, along with the known (and itself unique) release profile of the nanoparticles we were able to time the UV exposure to tune the shape of the release profile, achieving a delivery profile with a constant dose and no initial burst release. Because the release of bound particles was incomplete, leaving some growth factor on the nanoparticles, it is possible that repeated UV exposures at carefully chosen times could be used to control the shape of the release profile over an extended time period.

In this work, a UV-sensitive nanoparticle was used to demonstrate the counter intuitive stimuli responsive behaviour and release profile shape tuning. However, the UV-responsivity is only specific to the nanoparticles used and not to this approach to controlling growth factor delivery. UV light scatters readily and therefore has limited penetration depth and is only practical for topical treatments.[92] However, stimuli responsive nanoparticle drug delivery is a popular field of research, with research being done on nanoparticles responding to variety of external stimuli, including near infrared (NIR) photo stimulation, which offers a greater penetration depth, as well as magnetic fields, electric fields, temperature changes, and ultrasound.[92] Future development of this delivery strategy could see incorporation with other stimuli responsive nanoparticles to allow for internal application *in vivo*, or else continuing with these specific nanoparticles it could be used topical hydrogel treatments such as for burn wounds or as an *in vitro* study tool.

Overall, this thesis described 5 distinct growth factor delivery profile options possible from the tissue-specific SAP hydrogels: the original slow burst/sustained profile observed from unmodified growth factor, short delay, long delay, the gradually increasing profile of nanoparticle bound growth factor, and the tuned to constant dose profile as a response to UV stimulus. And in all cases the modifications have been shown not to interfere with the delivery of unmodified growth factors. The delivery systems describe here are therapeutic additions to the SAP hydrogels, not replacements, they do not disrupt the SAP material and neither do the prevent additional growth factor delivery.

While the focus of this thesis has been material/system development and proof of concept of these novel drug delivery strategies, the biological impact of any drug delivery system, is always an important consideration. The work described in Chapter Seven, along with other work outside this thesis,[36,192] confirms that bioactivity of growth factors is maintained when modified by the SMCC chemical attachment method used here to achieve the short delay and stimuli responsive delivery. Direct assessment via MTT assay with murine

neurons in Chapter Eight demonstrated the maintained bioactivity of growth factors used in the emulsion electrospinning used to achieve the long delay, which has also been confirmed outside of this thesis.[238] Concurrent with the delivery system development approaches described above, further biological studies should be conducted to confirm the efficacy of these systems *in vivo*.

Currently the biological efficacy of unmodified growth factors delivered within SAPs, which do provide stabilisation for long-term delivery, is being assessed in ischemic brain injury in rats using methods described in Chapter Four and preliminary results show the benefit of using growth factor, in this case BDNF, and SAPs together (Figure 10.2). Cell transplants with both BDNF and SAP showed the best performance, in terms of both graft volume (Figure 10.2E) and reduced cortical atrophy (Figure 10.2F). In fact, cell transplants given with just BDNF were comparable to the cell grafts alone, likely due to the rapid degradation of BDNF early in the 36-week course experiment. However, when cells were delivered with SAP and BDNF, there was a statistically significant improvement compared to cells + SAP, indicating that the stabilising effect of the SAP allowed the BDNF growth factor to have a more pronounced effect on recovery. This results are very promising, and future studies will include similar investigation of the modified growth factor delivery systems discussed in this thesis *in vivo*.

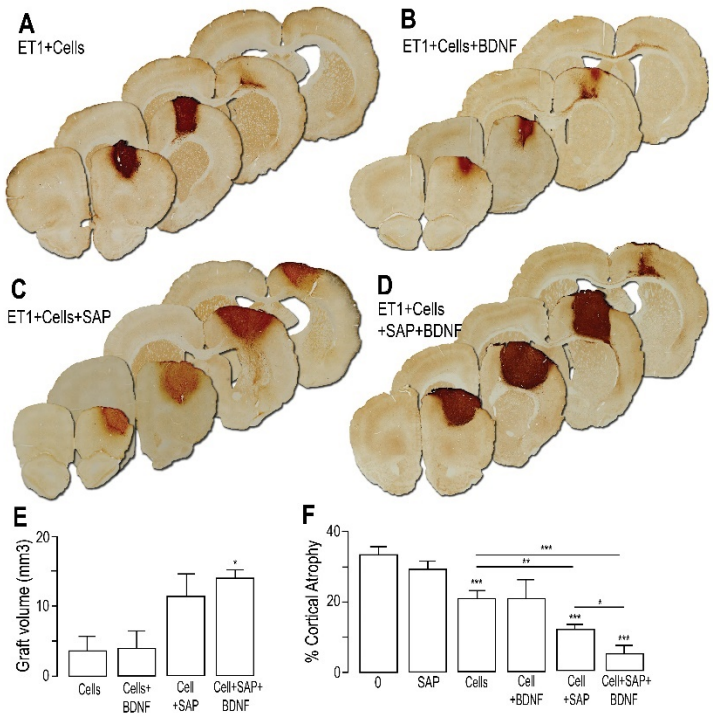

Figure 10.2: BDNF growth factor + SAP efficacy *in vivo* at 36 weeks. A-D: representative photomicrographs providing a coronal view of GFP+ (red) grafts within the cortex of cells alone (A), cells + BDNF (B), cells + SAP (C), and cells + BDNF + SAP (D) treatment of lesioned rats. E: Graft volume. F: Cortical atrophy. Data represent mean ± SEM, * $p < 0.05$, ** $p < 0.01$, *** $p < 0.001$.

In all three cases the novel delivery strategies described here were developed by applying materials and methods form other work in novel ways. There is no lack of diversity of materials being studied and used in tissue engineering, and the opportunities for novel combinations are correspondingly large. Future advancements in this field will involve the synergistic combinations of two or more materials, with each material contributing its own useful function. Appropriately, this approach to tissue engineering material development is itself mimetic of the ECM, an incredibly complex and specialised material able to perform many functions with contributions from its many constituent parts.

References

1. Frantz, C., Stewart, K.M. & Weaver, V.M. The extracellular matrix at a glance. *J Cell Sci* **123**, 4195-4200 (2010).
2. Engler, A.J., Sen, S., Sweeney, H.L. & Discher, D.E. Matrix elasticity directs stem cell lineage specification. *Cell*, 677-689 (2006).
3. Puschmann, T.B., Zanden, C., De Pablo, Y., Kirchhoff, F., Pekna, M., Liu, J. & Pekny, M. Bioactive 3D cell culture system minimizes cellular stress and maintains the in vivo-like morphological complexity of astroglial cells. *Glia* **61**, 432-40 (2013).
4. Lee, Y.-S. & Livingston Arinzeh, T. Electrospun nanofibrous materials for neural tissue engineering. *Polymers* **3**, 413-426 (2011).
5. Rim, N.G., Sin, C.S. & Hin, H. Current approaches to electrospun nanofibers for tissue engineering. *Biomed Mater*, 1-14 (2013).
6. Yan, C., Altunbas, A., Yucel, T., Nagarkar, R.P., Schneider, J.P. & Pochan, D.J. Injectable solid hydrogel: mechanism of shear-thinning and immediate recovery of injectable beta-hairpin peptide hydrogels. *Soft Matter* **6**, 5243-5156 (2010).
7. Smith, A.M., Williams, R.J., Tang, C., Coppo, P., Collins, R.F., Turner, M.L., Saiani, A. & Ulijn, R.V. Fmoc-diphenylalanine self assembles to a hydrogel via a novel architecture based on pi-pi interlocked beta-sheets. *Adv Mater* **20**, 37-41 (2008).
8. Nisbet, D.R. & Williams, R.J. Self-assembled peptides: Characterisation and in vivo response. *Biointerphases* **7**, 1-14 (2012).
9. Rodriguez, A.L., Parish, C.L., Nisbet, D.R. & Williams, R.J. Tuning the amino acid sequence of minimalist peptides to present biological signals via charge neutralised self assembly. *Soft Matter* **9**, 3915-3919 (2013).
10. Tayalia, P. & Mooney, D.J. Controlled growth factor delivery for tissue engineering. *Adv Mater* **21**, 3269-85 (2009).
11. Lee, K., Silva, E.A. & Mooney, D.J. Growth factor delivery-based tissue engineering: general approaches and a review of recent developments. *J R Soc Interface* **8**, 153-70 (2011).
12. Gudi, V., Skuljec, J., Yildiz, O., Frichert, K., Skripuletz, T., Moharregh-Khiabani, D., Voss, E., Wissel, K., Wolter, S. & Stangel, M. Spatial and temporal profiles of growth factor expression during CNS demyelination reveal the dynamics of repair priming. *PLoS One* **6**, e22623 (2011).
13. Edelman, E.R., Nugent, M.A. & Karnovsky, M.J. Perivascular and intravenous administration of basic fibroblast growth factor: vascular and solid organ deposition. *PNAS* **90**, 1513-1517 (1993).
14. Krewson, C.E. & Saltzman, W.M. Transport and elimination of recombinant human NGF during long-term delivery to the brain. *Brain Res* **727**, 169-181 (1996).
15. Allen, S.J., Watson, J.J., Shoemark, D.K., Barua, N.U. & Patel, N.K. GDNF, NGF and BDNF as therapeutic options for neurodegeneration. *Pharmacol Therapeut* **138**, 155-175 (2013).

16. Orive, G., Anitua, E., Pedraz, J.L. & Emerich, D.F. Biomaterials for promoting brain protection, repair and regeneration. *Nat Rev Neurosci* **10**, 682-692 (2009).

17. Horne, M.K., Nisbet, D.R., Forsythe, J.S. & Parish, C.L. Immobilized, three-dimensional nanofibrous scaffolds incorporating BDNF promote proliferation and differentiation of cortical neural stem cells *Stem Cells Dev* **19**, 843-852 (2010).

18. Levenberg, S., Burdick, J.A., Kraehenbuehl, T. & Langer, R. Neurotrophin-induced differentiation of human embryonic stem cells on three-dimensional polymeric scaffolds. *Tissue Eng* **11**, 506-512 (2005).

19. Kauhausen, J., Thompson, L.H. & Parish, C.L. Cell intrinsic and extrinsic factors contribute to enhance neural circuit reconstruction following transplantation in Parkinsonian mice. *J Physiol* **591**, 77-91 (2013).

20. Stockwell, J., Abdi, N., Lu, X., Maheshwari, O. & Taghibiglou, C. Novel central nervous system drug delivery systems. *Chem Biol Drug Des*, 507-520 (2014).

21. Choi, M.K., Taeyun; Chong, Kyuha; Yoon, Jonghee; Choi, Chulhee. Minimally invasive molecular delivery into the brain using optical modulation of vascular permeability. *PNAS* **108**, 9256-9261 (2011).

22. Wang, Y., Cooke, M.J., Sachewsky, N., Morshead, C.M. & Shoichet, M.S. Bioengineered sequential growth factor delivery stimulates brain tissue regeneration after stroke. *J Control Release* **172**, 1-11 (2013).

23. Rodriguez, A.L., Nisbet, D.R. & Parish, C.L. The potential of stem cells and tissue engineered scaffolds for repair of the central nervous system. in *Stem Cells and Cancer Stem Cells, Volume 4* 97-111 (Springer Netherlands, 2012).

24. Watt, F.M. & Huck, W.T.S. Role of the extracellular matrix in regulating stem cell fate. *Nat Rev Mol Cell Bio* **14**, 467-473 (2013).

25. Lutlof, M.P. & A, H.J. Synthetic biomaterials as instructive extracellular microenvironments for morphogenesis in tissue engineering. *Nat Biotechnol* **23**, 47-55 (2005).

26. Leipzig, N.D. & Shoichet, M.S. The effect of substrate stiffness on adult neural stem cell behavior. *Biomaterials* **30**, 6867-6878 (2009).

27. Unadkat, H.V., Hulsman, M., Cornelissen, K., Papenburg, B.J., Truckenmuller, R.K., Post, G.F., Uetz, M., Reinders, M.J.T., Stamatialis, D., van Blitterswijk, C.A. & de Boer, J. An algorithm-based topographical biomaterials library to instruct cell fate. *PNAS* **109**, 16565-16570 (2012).

28. Jaalouk, D.E. & Lammerding, J. Mechanotransduction gone awry. *Nat Rev Mol Cell Bio* **10**, 63-73 (2009).

29. Jang, J.-Y., Lee, S.W., Park, S.H., Shin, J.W., Mun, C.W., Kim, S.-H., Kim, D.H. & Shin, J.-W. Combined effects of surface morphology and mechanical straining magnitudes on the differentiation os mesenchymal stem cells without using biochemical reagents. *J Biomed Biotechnol*, 860652 (2011).

30. Li, Q., Cheung, W.H., Chow, K.L., Ellis-Behnke, R.G. & Chau, Y. Factorial analysis of adaptable properties of self-assembling peptide matrix on cellular proliferation and neuronal differentiation of pluripotent embryonic carcinoma. *Nanomedicine-UK* **8**, 748-756 (2012).

31. Wang, T.-Y., Bruggeman, K.A.F., Sheean, R.K., Turner, B.J., Nisbet, D.R. & Parish, C.L. Characterisation of the stability and bio-functionality of tethered proteins on bioengineered scaffolds: implications for stem cell biology and tissue repair. *J Biol Chem* **289**, 15044-15051 (2014).

32. Richards Grayson, A.C., Choi, I.S., Tyler, B.M., Wang, P.P., Brem, H., Cima, M.J. & Langer, R. Multi-pulse drug delivery from a resorbable polymeric microchip device. *Nat Mater* **2**, 767-772 (2003).

33. Sirianni, R.W., Olausson, P., Chiu, A.S., Taylor, J.R. & Saltzman, W.M. The behavioral and biochemical effects of BDNF containing polymers implanted in the hippocampus of rats. *Brain Res* **1321**, 40-50 (2010).

34. Sudhakar, M., Kancharla, R. & Rao, V.U. A review on sustained release injectable depot drug delivery systems. *Pharmanest* **4**, 142-158 (2013).

35. Li, X., Qian, Y., Liu, T., Hu, X., Zhang, G., You, Y. & Liu, S. Amphiphilic multiarm star block copolymer-based multifunctional unimolecular micelles for cancer targeted drug delivery and MRI imaging. *Biomaterials* **32**, 6595-6605 (2011).

36. Horne, M., K, Nisbet, D.R., Forsythe, J.S. & Parish, C.L. Three-dimensional nanofibrous scaffolds incorporating immobilized BDNF promote proliferation and differentiation of cortical neural stem cells. *Stem Cells Dev* **19**, 843-852 (2010).

37. Nisbet, D.R., Forsythe, J.S., Shen, W., Finkelstein, D.I. & Horne, M.K. A review of cellular response on electrospun nanofibers for tissue engineering. *J Biomater Appl* **24**, 7-29 (2009).

38. Wang, X., Ding, B. & Li, B. Biomimetic electrospun nanofibrous structures for tissue engineering. *Mater Today* **16**, 229-241 (2013).

39. Jayasinghe, S.N. Cell electrospinning: a novel tool for functionalising fibres, scaffolds and membranes with living cells and other advanced materials for regenerative biology and medicine. *Analyst* **128**, 2215-2223 (2013).

40. Wang, T.Y., Forsythe, J.S., Parish, C.L. & Nisbet, D.R. Biofunctionalisation of polymeric scaffolds for neural tissue engineering. *J Biomater Appl* **27**, 369-390 (2012).

41. Place, E.S., George, J.H. & Williams, C.K. Synthetic polymer scaffolds for tissue engineering. *Chem Soc Rev* **38**, 1139-1151 (2008).

42. Sell, S.A., Wolfe, P.S., Garg, K., McCool, J.M., Rodriguez, I.A. & Bowlin, G.L. The use of natural polymers in tissue engineering: A focus on electrospun extracellular matrix analogues. *Polymers* **2**, 522-553 (2010).

43. Kisiel, M., Martino, M.M., Ventura, M., Hubbell, J.A., Hilborn, J. & Ossipov, D. Improving the osteogenic potential of BMP-2 with hyaluronic acid hydrogel modified with integrin-specific fibronectin fragment. *Biomaterials* **34**, 704-12 (2013).

44. Huang, W., Zou, T., Li, S., Jing, J., Xia, X. & Liu, X. Drug-loaded zein nanofibers prepared using a modified coaxial electrospinning process. *PharmaSciTech* **14**, 675-681 (2013).

45. Zahedi, P., Karami, Z., Rezaeian, I., Jafari, S.-H., Mahdaviani, P., Abdolghaffari, A.H. & Abdollahi, M. Preparation and performance evaluation of tetracycline hydrochloride loaded wound dressing mats based on electrospun nanofibrous poly(lactic acid)/poly(e-caprolactone) blends. *J Appl Polym Sci* **124**, 4174-4183 (2012).

46. Hu, J., Tian, L., Prabhakaran, M., Ding, X. & Ramakrishna, S. Fabrication of nerve growth factor encapsulated aligned poly(ε-Caprolactone) nanofibers and their assessment as a potential neural tissue engineering scaffold. *Polymers* **8**, 54 (2016).

47. Chew, S.Y., Wen, J., Yim, E.K.F. & Leong, K.W. Sustained release of proteins from electrospun biodegradable fibers. *Biomacromolecules* **6**, 2017-2024 (2005).

48. Wittmer, C.R., Claudepierre, T., Reber, M., Wiedemann, P., Garlick, J.A., Kaplan, D. & Egles, C. Multifunctionalized electrospun silk fibers promote axon regeneration in central nervous system. *Adv Funct Mater* **21**, 4202 (2011).

49. Maleki, M., Latifi, M., Amani-Tehran, M. & Mathur, S. Electrospun core-shell nanofibres for drug encapsulation and sustained release. *Polym Eng Sci* **53**(2013).

50. Han, D. & Steckl, A.J. Triaxial electrospun nanofiber membranes for controlled dual release of functional molecules. *ACS Appl Mater Inter* **5**, 8241-8245 (2013).

51. Costoya, A., Concheiro, A. & Alvarez-Lorenzo, C. Electrospun Fibers of Cyclodextrins and Poly(cyclodextrins). *Molecules* **22**(2017).

52. Jordan, A.M., Viswanath, V., Kim, S.-E., Pokorski, J.K. & Korley, L.T.J. Processing and surface modification of polymer nanofibers for biological scaffolds: a review. *J Mater Chem B* **4**, 5958-5974 (2016).

53. Kim, S.E., Wallat, J.D., Harker, E.C., Advincula, A.A. & Pokorski, J.K. Multifunctional and Spatially Controlled Bioconjugation to Melt Coextruded Nanofibers. *Polym Chem* **6**, 5683-5692 (2015).

54. Cabanas-Danés, J., Huskens, J. & Jonkheijm, P. Chemical strategies for the presentation and delivery of growth factors. *J Mater Chem B* **2**, 2381-2394 (2014).

55. Wang, T.-Y., Forsythe, J.S., Nisbet, D.R. & Parish, C., L. Promoting engraftment of transplanted neural stem cells/progenitors using biofunctionalised electrospun scaffolds. *Biomaterials* **33**, 9188-9197 (2012).

56. DeForest, C.A.A., Kristi S. Cytocompatible click-based gydrogels with dynamically tunable properties through orthogonal photoconjugation and photocleavage reactions. *Nat Mater* **3**, 925-931 (2012).

57. Guvendiren, M., Lu, H.D. & Burdick, J.A. Shear-thinning hydrogels for biomedical applications. *Soft Matter* **8**, 260-272 (2012).

58. Giraud Guille, M.M., Helary, C., Vigier, S. & Nassif, N. Dense fibrillar collagen matrices for tissue repair. *Soft Matter* **6**, 4963-4967 (2010).

59. Zhao, W., Jin, X., Cong, Y., Yuying, L. & Fu, J. Degradable natural polymer hydrogels for articular cartilage tissue engineering. *J Chem Technol Biot* **88**, 327-339 (2013).

60. Collins, M.N. & Birkinshaw, C. Hyaluronic acid based scaffolds for tissue engineering: A review. *Carbohyd Polym* **92**, 1263-1279 (2013).

61. Li, R., Horgan, C.C., Long, B., Rodriguez, A.L., Mather, L., Barrow, C.J., Nisbet, D.R. & Williams, R.J. Tuning the mechanical and morphological properties of self-assembled peptide hydrogels via control over the gelation mechanism through regulation of ionic strength and the rate of pH change. *RSC Adv* **5**, 301-307 (2015).

62. Williams, R.J., Hall, T.E., Glattauer, V., White, J., Pasic, P.J., Sorensen, A.B., Waddington, L., McLean, K.M., Currie, P.D. & Hartley, P.G. The in vivo performance of an enzyme-assisted self-assembled peptide/protein hydrogel. *Biomaterials* **32**, 5304-10 (2011).

63. Javid, N., Roy, S., Zelzer, M., Yang, Z., Sefcik, J. & Ulijn, R.V. Cooperative self-assembly of peptide gelators and proteins. *Biomacromolecules* **14**, 4368-4376 (2013).

64. Song, B., Song, J., Zhang, S., Anderson, M.A., Ao, Y., Yang, C.Y., Deming, T.J. & Sofroniew, M.V. Sustained local delivery of bioactive nerve growth factor in the central nervous system via tunable diblock copolypeptide hydrogel depots. *Biomaterials* **33**, 9105-16 (2012).

65. Branco, M.C., Pochan, D.J., Wagner, N.J. & Schneider, J.P. The effect of protein structure on their controlled release from an injectable peptide hydrogel. *Biomaterials* **31**, 9527-9534 (2010).

66. Sakiyama-Elbert, S.E. & Hubbell, J.A. Controlled release of nerve growth factor from a heparin-containing fibrin-based cell ingrowth matrix. *J Control Release* **69**, 149-158 (2000).

67. Pakulska, M.M.M., Shane; Shoichet, Molly S. Designed protein delivery: From natural to engineered affinity-controlled release systems. *Science* **351**(2016).

68. Li, H., Ham, T.R., Neill, N., Farrag, M., Mohrman, A.E., Koenig, A.M. & Leipzig, N.D. A hydrogel bridge incorporating immobilized growth factors and neural stem/progenitor cells to treat spinal cord injury. *Adv Healthc Mater* **5**, 802-12 (2016).

69. Leipzig, N.D., Wylie, R.G., Kim, H. & Shoichet, M.S. Differentiation of neural stem cells in three-dimensional growth factor-immobilized chitosan hydrogel scaffolds. *Biomaterials*, 57-64 (2011).

70. Egawa, E.Y., Kato, K., Hiraoka, M., Nakaji-Hirabayashi, T. & Iwata, H. Enhanced proliferation of neural stem cells in a collagen hydrogel incorporating engineered epidermal growth factor. *Biomaterials*, 4737-4743 (2011).

71. Sakiyama-Elbert, S.E. & Hubbell, J.A. Development of fibrin derivatives for controlled release of heparin-binding growth factors. *J Control Release* **65**, 389-402 (2000).

72. Martino, M.M., Briquez, P.S., Ranga, A., Lutolf, M. & Hubbell, J.A. Heparin-binding domain of fibrin(ogen) binds growth factors and promotes tissue repair when incorporated within a synthetic matrix. *PNAS* **110**, 4563-4568 (2013).

73. Van Hove, A.H., Burke, K., Antonienko, E., Brown, E., 3rd & Benoit, D.S. Enzymatically-responsive pro-angiogenic peptide-releasing poly(ethylene glycol) hydrogels promote vascularization in vivo. *J Control Release* **217**, 191-201 (2015).

74. Hoffman, J.C. & West, J.L. Three-dimensional photolithographic patterning of multiple bioactive ligands in poly(ethylene glycol) hydrogels. *Soft Matter*, 5056-5063 (2010).

75. Wylie, R.G., Ahsan, S., Aizawa, Y., Maxwell, K.L., Morshead, C.M. & Stoichet, M.S. Spatially controlled simultaneous patterning of multiple growth factors in three-dimensional hydrogels. *Nat Mater* **10**, 799-806 (2011).

76. Luo, Y. & Shoichet, M.S. A photolabile hydrogel for guided three-dimensional cell growth and migration. *Nat Mater* **3**, 249-53 (2004).

77. Bencherifa, S.A.S., R Warren; Bhatta, Deen; Aranya, Praveen; Verbeke, Catia S; Edwardsa, David A; & Mooney, D.J. Injectable preformed scaffolds with shape-memory properties. *PNAS* **109**, 19590-19595 (2012).

78. Modepalli, V.N., Rodriguez, A.L., Li, R., Pavaluri, S., Nicholas, K.R., Barrow, C.J., Nisbet, D.R. & Williams, R.J. In vitro response to functionalised self-assembling peptide scaffolds for three-dimensional cell culture. *Biopolymers (Pept Sci)* **102**, 197-205 (2014).

79. Genove, E., Shen, C., Zhang, S. & Semino, C.E. The effect of functionalized self-assembling peptide scaffolds on human aortic endothelial cell function. *Biomaterials* **26**, 3341-3351 (2005).

80. Law, B., Weissleder, R. & Tung, C.-H. Peptide-based biomaterials for protease-enhanced drug delivery. *Biomaterials* **7**, 1261-1265 (2006).

81. Yoshida, R. & Okano, T. Stimuli-responsive hydrogels and their application to functional materials. in *Biomedical Applications of Hydrogels Handbook* 19-43 (Springer Science + Business Media, 2010).

82. Fairbanks, B., Singh, S.P., Bowman, C.N. & Anseth, K.S. Photodegradable, photoadaptable hydrogels via radical-mediated disulfide fragmentation reaction. *Macromolecules* **44**, 2444-2450 (2011).

83. Miyata, T., Asami, N. & Uragami, T. A reversibly antigen-responsive hydrogel. *Nature* **399**, 766-769 (1999).

84. Cha, C., Jeong, J.H., Shim, J. & Kong, H. Tuning the dependency between stiffness and permeability of a cell encapsulating hydrogel with hydrophilic pendant chains. *Acta Biomater* **7**, 3719-3728 (2011).

85. Zhang, R., Bowyer, A., Eisenthal, R. & Hubble, J. A smart membrane based on an antigen-responsive hydrogel. *Biotechnol Bioeng* **97**, 976-984 (2007).

86. Guiseppi-Elie, A., Brahim, S.I. & Narinesingh, D. A chemically synthesized artificial pancreas: release of insulin from glucose-responsive hydrogels. *Adv Mater* **14**, 743-746 (2002).

87. Matsumoto, A., Ishii, T., Nishida, J., Matsumoto, H., Kataoka, K. & Miyahara, Y. A synthetic approach toward a self-regulaed insulin delivery system. *Angew Chem*, 2166-2170 (2012).

88. van Bommel, K.J.C., Stuart, M.C.A., Feringa, B.L. & van Esch, J. Two-stage enzyme mediated drug release from LMWG hydrogels. *Org Biomol Chem*, 2917-2920 (2005).

89. Xiao, Y., Hong, H., Javadi, A., Engle, J.W., Xu, W., Yang, Y., Zhang, Y., Barnhart, T.E., Cai, W. & Gong, S. Multifunctional unimolecular micelles for cancer-targeted drug delivery and positron emission tomography imaging. *Biomaterials* **33**, 3071-3082 (2012).

90. Beck-Broichsitter, M., Thieme, M., Nguyen, J., Schmehl, T., Gessler, T., Seeger, W., Agarwal, S., Grenier, A. & Kissel, T. Novel 'nano in nano' composites for sustrained drug delivery: biodegradable nanoparticles encapsulated into nanofiber non-wovens. *Macromol Biosci* **10**, 1527-1535 (2010).

91. Xie, Z., Paras, C.B., Weng, H., Punnakitikashem, P., Su, L.C., Vu, K., Tang, L., Yang, J. & Nguyen, K.T. Dual growth factor releasing multi-functional nanofibers for wound healing. *Acta Biomater* **9**, 9351-9 (2013).

92. Mura, S., Nicolas, J. & Couvreur, P. Stimuli-responsive nanocarriers for drug delivery. *Nat Mater* **12**, 991-1003 (2013).

93. Shah, S., Sasmal, P.K. & Lee, K.B. Photo-triggerable hydrogel-nanoparticle hybrid scaffolds for remotely controlled drug delivery. *J Mater Chem B Mater Biol Med* **2**, 7685-7693 (2014).

94. Satarkar, N.S. & Zach Hilt, J. Hydrogel nanocomposites as remote-controlled biomaterials. *Acta Biomater* **4**, 11-6 (2008).

95. Satarkar, N.S. & Hilt, J.Z. Magnetic hydrogel nanocomposites for remote controlled pulsatile drug release. *J Control Release* **130**, 246-51 (2008).

96. Binder, D.K.S., Helen E;. Brain-derived neurotrophic factor. *Growth Factors* **22**, 123-131 (2004).

97. Airaksinen, M.S. & Saarma, M. The GDNF family: signalling, biological functions and therapeutic value. *Nat Rev Neurosci* **3**, 383-94 (2002).

98. Ni, W., Lin, M., Salinas, P., Savickas, P., Wu, S.L. & Karger, B.L. Complete mapping of a cystine knot and nested disulfides of recombinant human arylsulfatase A by multi-enzyme digestion and LC-MS analysis using CID and ETD. *J Am Soc Mass Spectrom* **24**, 125-33 (2013).

99. Zhang, T., Go, M.A., Stricker, C., Daria, V.R. & Tricoli, A. Low-cost photo-responsive nanocarriers by one-step functionalization of flame-made titania agglomerates withl-Lysine. *J Mater Chem B* **3**, 1677-1687 (2015).

100. Yu, L.M., Kazazian, K. & Shoichet, M.S. Peptide surface modification of methacrylamide chitosan for neural tissue engineering applications. *J Biomed Mater Res A* **82**, 243-55 (2007).

101. Nisbet, D.R., Moses, D., Gengenbach, T.R., Forsythe, J.S., Finkelstein, D.I. & Horne, M.K. Enhancing neurite outgrowth from primary neurones and neural stem cells using thermoresponsive hydrogel scaffolds for the repair of spinal cord injury. *J Biomed Mater Res A* **89**, 24-35 (2009).

102. Wang, T.Y., Bruggeman, K.F., Kauhausen, J.A., Rodriguez, A.L., Nisbet, D.R. & Parish, C.L. Functionalized composite scaffolds improve the engraftment of transplanted dopaminergic progenitors in a mouse model of Parkinson's disease. *Biomaterials* **74**, 89-98 (2016).

103. Thompson, L.H. & Parish, C.L. Transplantation of fetal midbrain dopamine progenitors into a rodent model of Parkinson's disease. *Methods Mol Biol* **1059**, 169-80 (2013).

104. Blakely, B.D., Bye, C.R., Fernando, C.V., Horne, M.K., Macheda, M.L., Stacker, S.A., Arenas, E. & Parish, C.L. Wnt5a regulates midbrain dopaminergic axon growth and guidance. *PLoS One* **6**, e18373 (2011).

105. Nisbet, D.R., Pattanawong, S., Ritchie, N.E., Shen, W., Finkelstein, D.I., Horne, M.K. & Forsythe, J.S. Interaction of embryonic cortical neurons on nanofibrous scaffolds for neural tissue engineering. *J Neural Eng* **4**, 35-41 (2007).

106. Costa, M., Dottori, M., Ng, E., Hawes, S.M., Sourris, K., Jamshidi, P., Pera, M.F., Elefanty, A.G. & Stanley, E.G. The hESC line Envy expresses high levels of GFP in all differentiated progeny. *Nat Methods* **2**, 259-60 (2005).

107. Denham, M., Parish, C.L., Leaw, B., Wright, J., Reid, C.A., Petrou, S., Dottori, M. & Thompson, L.H. Neurons derived from human embryonic stem cells extend long-distance axonal projections through growth along host white matter tracts after cerebral transplantation. *Front Cellular Neurosci* **6**(2012).

108. Sawamoto, K., Nakao, N., Kobayashi, K., Matsushita, N., Takahashi, H., Kakishita, K., Yamamoto, A., Yoshizaki, T., Terashima, T., Murakami, F., Itakura, T. & Okano, H. Visualization, direct isolation, and transplantation of midbrain dopaminergic neurons. *Proc Natl Acad Sci U S A* **98**, 6423-8 (2001).

109. Parish, C.L., Finkelstein, D.I., Drago, J., Borrelli, E. & Horne, M.K. The role of dopamine receptors in regulating the size of axonal arbors. *J Neurosci* **21**, 5147-57. (2001).

110. Gundersen, H.J., Bagger, P., Bendtsen, T.F., Evans, S.M., Korbo, L., Marcussen, N., Moller, A., Nielsen, K., Nyengaard, J.R., Pakkenberg, B., Sorensen, F.B., Vesterby, A. & West, M.J. The new stereological tools: disector, fractionator, nucleator and point sampled intercepts and their use in pathological research and diagnosis. *APMIS* **96**, 857-81 (1988).

111. West, M.J., Slomianka, L. & Gundersen, H.J. Unbiased stereological estimation of the total number of neurons in thesubdivisions of the rat hippocampus using the optical fractionator. *Anat Rec* **231**, 482-497 (1991).

112. Bye, C.R., Thompson, L.H. & Parish, C.L. Birth dating of midbrain dopamine neurons identifies A9 enriched tissue for transplantation into Parkinsonian mice. *Exp Neurol* **236**, 58-68 (2012).

113. Montoya, C.P., Campbell-Hope, L.J., Pemberton, K.D. & Dunnett, S.B. The "staircase test": a measure of independent forelimb reaching and grasping abilities in rats. *J Neurosci Methods* **36**, 219-28 (1991).

114. Kirik, D., Winkler, C. & Bjorklund, A. Growth and functional efficacy of intrastriatal nigral transplants depend on the extent of nigrostriatal degeneration. *J Neurosci* **21**, 2889-96. (2001).

115. Olsson, M., Nikkhah, G., Bentlage, C. & Bjorklund, A. Forelimb akinesia in the rat Parkinson model: differential effects of dopamine agonists and nigral transplants as assessed by a new stepping test. *J Neurosci* **15**, 3863-75 (1995).

116. Pettikiriarachchi, J.T.S.P., Clare L; Shoichet, Molly S; Forsythe, John S; Nisbet, David R. Biomaterials for brain tissue engineering. *Aust J Chem* **63**, 1143-1154 (2010).

117. Yanlian, Y., Ulung, K., Xiumei, W., Horii, A., Yokoi, H. & Shuguang, Z. Designer self-assembling peptide nanomaterials. *Nano Today* **4**, 193-210 (2009).

118. Zimmermann, D.R. & Dours-Zimmermann, M.T. Extracellular matrix of the central nervous system: from neglect to challenge. *Histochem Cell Biol* **130**, 635-53 (2008).

119. Tysseling-Mattiace, V.M., Sahni, V., Niece, K.L., Birch, D., Czeisler, C., Fehlings, M.G., Stupp, S.I. & Kessler, J.A. Self-assembling nanofibers inhibit glial scar formation and promote axon elongation after spinal cord injury. *J Neurosci* **28**, 3814-23 (2008).

120. Wang, X., Horii, A. & Zhang, S. Designer functionalized self-assembling peptide nanofiber scaffolds for growth, migration, and tubulogenesis of human umbilical vein endothelial cells. *Soft Matter* **4**, 2388 (2008).

121. Matson, J.B. & Stupp, S.I. Self-assembling peptide scaffolds for regenerative medicine. *Chem Commun (Camb)* **48**, 26-33 (2012).

122. Orbach, R.A.-A., Lihi; Zigerson, Sivan; Mironi-Harpaz, Iris; Seliktar, Drort*,†. Self-assembled Fmoc-peptides as a platform for the formation of nanostructures and hydrogels. *Biomacromolecules* **10**, 2646-2651 (2009).

123. Tang, C., Smith, A.M., Collins, R.F., Ulijn, R.V. & Saiani, A. Fmoc-diphenylalanine self-assembly mechanism induces apparent pKa shifts. *Langmuir* **25**, 9447-53 (2009).

124. Zhou, M., Smith, A.M., Das, A.K., Hodson, N.W., Collins, R.F., Ulijn, R.V. & Gough, J.E. Self-assembled peptide-based hydrogels as scaffolds for anchorage-dependent cells. *Biomaterials* **30**, 2523-30 (2009).

125. Wei, G. & Ma, P.X. Nanostructured biomaterials for regeneration. *Adv Funct Mater* **18**, 3568-3582 (2008).

126. Lindvall, O. & Kokaia, Z. Stem cell research in stroke: how far from the clinic? *Stroke* **42**, 2369-75 (2011).

127. Delavaran, H., Sjunnesson, H., Arvidsson, A., Lindvall, O., Norrving, B., van Westen, D., Kokaia, Z. & Lindgren, A. Proximity of brain infarcts to regions of endogenous neurogenesis and involvement of striatum in ischaemic stroke. *Eur J Neurol* **20**, 473-9 (2013).

128. Steinberg, G.K., Kondziolka, D., Wechsler, L.R., Lunsford, L.D., Coburn, M.L., Billigen, J.B., Kim, A.S., Johnson, J.N., Bates, D., King, B., Case, C., McGrogan, M., Yankee, E.W. & Schwartz, N.E. Clinical outcomes of transplanted modified bone marrow-derived mesenchymal stem cells in stroke: A phase 1/2a study. *Stroke* **47**, 1817-24 (2016).

129. Bang, O.Y., Lee, J.S., Lee, P.H. & Lee, G. Autologous mesenchymal stem cell transplantation in stroke patients. *Ann Neurol* **57**, 874-82 (2005).

130. Kondziolka, D., Steinberg, G.K., Wechsler, L., Meltzer, C.C., Elder, E., Gebel, J., Decesare, S., Jovin, T., Zafonte, R., Lebowitz, J., Flickinger, J.C., Tong, D., Marks, M.P., Jamieson, C., Luu, D., Bell-Stephens, T. & Teraoka, J. Neurotransplantation for patients with subcortical motor stroke: a phase 2 randomized trial. *J Neurosurg* **103**, 38-45 (2005).

131. Nelson, P.T., Kondziolka, D., Wechsler, L., Goldstein, S., Gebel, J., DeCesare, S., Elder, E.M., Zhang, P.J., Jacobs, A., McGrogan, M., Lee, V.M. & Trojanowski, J.Q. Clonal human (hNT) neuron grafts for stroke therapy: neuropathology in a patient 27 months after implantation. *Am J Pathol* **160**, 1201-6 (2002).

132. Cao, W. & Li, P. Effectiveness and Safety of Autologous Bone Marrow Stromal Cells Transplantation After Ischemic Stroke: A Meta-Analysis. *Med Sci Monit* **21**, 2190-5 (2015).

133. Tornero, D., Wattananit, S., Gronning Madsen, M., Koch, P., Wood, J., Tatarishvili, J., Mine, Y., Ge, R., Monni, E., Devaraju, K., Hevner, R.F., Brustle, O., Lindvall, O. & Kokaia, Z. Human induced pluripotent stem cell-derived cortical neurons integrate in stroke-injured cortex and improve functional recovery. *Brain* **136**, 3561-77 (2013).

134. Oki, K., Tatarishvili, J., Wood, J., Koch, P., Wattananit, S., Mine, Y., Monni, E., Tornero, D., Ahlenius, H., Ladewig, J., Brustle, O., Lindvall, O. & Kokaia, Z. Human-induced pluripotent stem cells form functional neurons and improve recovery after grafting in stroke-damaged brain. *Stem Cells* **30**, 1120-33 (2012).

135. Tatarishvili, J., Oki, K., Monni, E., Koch, P., Memanishvili, T., Buga, A.M., Verma, V., Popa-Wagner, A., Brustle, O., Lindvall, O. & Kokaia, Z. Human induced pluripotent stem cells improve recovery in stroke-injured aged rats. *Restor Neurol Neurosci* **32**, 547-58 (2014).

136. Kokaia, Z. & Lindvall, O. Stem cell repair of striatal ischemia. *Prog Brain Res* **201**, 35-53 (2012).

137. Qin, J., Gong, G., Sun, S., Qi, J., Zhang, H., Wang, Y., Wang, N., Wang, Q.M., Ji, Y., Gao, Y., Shi, C., Yang, B., Zhang, Y., Song, B. & Xu, Y. Functional recovery after transplantation of induced pluripotent stem cells in a rat hemorrhagic stroke model. *Neurosci Lett* **554**, 70-5 (2013).

138. Jensen, M.B., Yan, H., Krishnaney-Davison, R., Al Sawaf, A. & Zhang, S.C. Survival and differentiation of transplanted neural stem cells derived from human induced pluripotent stem cells in a rat stroke model. *J Stroke Cerebrovasc Dis* **22**, 304-8 (2013).

139. Jiang, M., Lv, L., Ji, H., Yang, X., Zhu, W., Cai, L., Gu, X., Chai, C., Huang, S., Sun, J. & Dong, Q. Induction of pluripotent stem cells transplantation therapy for ischemic stroke. *Mol Cell Biochem* **354**, 67-75 (2011).

140. Daadi, M.M., Maag, A.L. & Steinberg, G.K. Adherent self-renewable human embryonic stem cell-derived neural stem cell line: functional engraftment in experimental stroke model. *PLoS One* **3**, e1644 (2008).

141. Gomi, M., Takagi, Y., Morizane, A., Doi, D., Nishimura, M., Miyamoto, S. & Takahashi, J. Functional recovery of the murine brain ischemia model using human

induced pluripotent stem cell-derived telencephalic progenitors. *Brain Res* **1459**, 52-60 (2012).

142. Park, K.I., Teng, Y.D. & Snyder, E.Y. The injured brain interacts reciprocally with neural stem cells supported by scaffolds to reconstitute lost tissue. *Nat Biotechnol* **20**, 1111-7 (2002).

143. Bible, E., Chau, D.Y., Alexander, M.R., Price, J., Shakesheff, K.M. & Modo, M. The support of neural stem cells transplanted into stroke-induced brain cavities by PLGA particles. *Biomaterials* **30**, 2985-94 (2009).

144. Jin, K., Mao, X., Xie, L., Galvan, V., Lai, B., Wang, Y., Gorostiza, O., Wang, X. & Greenberg, D.A. Transplantation of human neural precursor cells in Matrigel scaffolding improves outcome from focal cerebral ischemia after delayed postischemic treatment in rats. *J Cereb Blood Flow Metab* **30**, 534-44 (2010).

145. Elias, P.Z. & Spector, M. Implantation of a collagen scaffold seeded with adult rat hippocampal progenitors in a rat model of penetrating brain injury. *J Neurosci Methods* **209**, 199-211 (2012).

146. Yu, H., Cao, B., Feng, M., Zhou, Q., Sun, X., Wu, S., Jin, S., Liu, H. & Lianhong, J. Combinated transplantation of neural stem cells and collagen type I promote functional recovery after cerebral ischemia in rats. *Anat Rec (Hoboken)* **293**, 911-7 (2010).

147. Liang, Y., Walczak, P. & Bulte, J.W. The survival of engrafted neural stem cells within hyaluronic acid hydrogels. *Biomaterials* **34**, 5521-9 (2013).

148. Bible, E., Qutachi, O., Chau, D.Y., Alexander, M.R., Shakesheff, K.M. & Modo, M. Neo-vascularization of the stroke cavity by implantation of human neural stem cells on VEGF-releasing PLGA microparticles. *Biomaterials* **33**, 7435-46 (2012).

149. Cheng, T.Y., Chen, M.H., Chang, W.H., Huang, M.Y. & Wang, T.W. Neural stem cells encapsulated in a functionalized self-assembling peptide hydrogel for brain tissue engineering. *Biomaterials* **34**, 2005-16 (2013).

150. Tysseling, V.M., Sahni, V., Pashuck, E.T., Birch, D., Hebert, A., Czeisler, C., Stupp, S.I. & Kessler, J.A. Self-assembling peptide amphiphile promotes plasticity of serotonergic fibers following spinal cord injury. *J Neurosci Res* **88**, 3161-70 (2010).

151. Winkler, C., Kirik, D. & Bjorklund, A. Cell transplantation in Parkinson's disease: how can we make it work? *Trends Neurosci* **28**, 86-92 (2005).

152. Rolls, A.S., Ravid; Schwartz, Michal. The bright side of the glial scar in CNS repair. *Nat Rev Neurosci* **10**, 235-241 (2009).

153. Lau, C.L., Kovacevic, M., Tingleff, T.S., Forsythe, J.S., Cate, H.S., Merlo, D., Cederfur, C., Maclean, F.L., Parish, C.L., Horne, M.K., Nisbet, D.R. & Beart, P.M. 3D electrospun scaffolds promote a cytotrophic phenotype of cultured primary astrocytes. *J Neurochem* **130**, 215-26 (2014).

154. Burda, J.E. & Sofroniew, M.V. Reactive gliosis and the multicellular response to CNS damage and disease. *Neuron* **81**, 229-48 (2014).

155. Levental, I., Georges, P.C. & Janmey, P.A. Soft biological materials and their impact on cell function. *Soft Matter* **3**, 299-306 (2007).

156. Kim, E.J., Park, S.Y., Lee, J.Y. & Park, J.H. Fucoidan present in brown algae induces apoptosis of human colon cancer cells. *BMC Gastroenterol* **10**, 96 (2010).

157. Dias, P.F., Siqueira, J.M., Jr., Vendruscolo, L.F., de Jesus Neiva, T., Gagliardi, A.R., Maraschin, M. & Ribeiro-do-Valle, R.M. Antiangiogenic and antitumoral properties

of a polysaccharide isolated from the seaweed Sargassum stenophyllum. *Cancer Chemother Pharmacol* **56**, 436-46 (2005).

158. Park, H.Y., Kim, G.Y., Moon, S.K., Kim, W.J., Yoo, Y.H. & Choi, Y.H. Fucoidan inhibits the proliferation of human urinary bladder cancer T24 cells by blocking cell cycle progression and inducing apoptosis. *Molecules* **19**, 5981-98 (2014).

159. Patel, M.K.M., B; Gallagher, K L; O'Brien, L; Hughes, A D. The antimitogenic action of the sulphated polysaccharide fucoidan differs from heparin in human vascular smooth muscle cells. *Thromb Haemost* **87**, 149-154 (2002).

160. Coussens, L.M. & Werb, Z. Inflammation and cancer. *Nature* **420**, 860-7 (2002).

161. Jones, M.K.W., Hongtao; Peskar, Brigitta M; Levin, Ellis; Itani, Rabiha M; Sarfeh, I James; Tarnawski, Andrezej S. Inhibition of angiogenesis by nonsteroidal anti-inflammatory drugs: Insight into mechanisms and implications for cancer growth and ulcer healing. *Nat Med* **5**, 1418-1423 (1999).

162. Cuzick, J.O., Florian; Baron, John A; Brown, Powel H; Burn, John; Greenwald, Peter; Jankowski, Janusz; La Vecchia, Carlo; Meyskens, Frank; Jörg Senn, Hans; Thun, Michael. Aspirin and non-steroidal anti-infl ammatory drugs for cancer prevention: an international consensus statement. *Lancet Oncol* **10**, 501-507 (2009).

163. Zhu, C., Cao, R., Zhang, S.X., Man, Y.N. & Wu, X.Z. Fucoidan inhibits the growth of hepatocellular carcinoma independent of angiogenesis. *Evid Based Complement Alternat Med* **2013**, 692549 (2013).

164. Demir Sezer, A.H., Fatih; Cevher, Erdal; Oğurtan, Zeki; Levent Baş, Ahmet; Akbuğ, Jülide Chitosan film containing fucoidan as a wound dressing for dermal burn healing: Preparation and in vitro/in vivo evaluation. *AAPS PmarmSciTech* **8**(2007).

165. Murakami, K., Aoki, H., Nakamura, S., Nakamura, S., Takikawa, M., Hanzawa, M., Kishimoto, S., Hattori, H., Tanaka, Y., Kiyosawa, T., Sato, Y. & Ishihara, M. Hydrogel blends of chitin/chitosan, fucoidan and alginate as healing-impaired wound dressings. *Biomaterials* **31**, 83-90 (2010).

166. Wolinsky, J.B., Colson, Y.L. & Grinstaff, M.W. Local drug delivery strategies for cancer treatment: gels, nanoparticles, polymeric films, rods, and wafers. *J Control Release* **159**, 14-26 (2012).

167. Soisuwan, S.W., Warangkana; Lirdprapamongkol, Kriengsak; Svasti, Jisnuson Eco-friendly synthesis of fucoidan-stabilized gold nanoparticles.pdf. *Am J Appl Sci* **7**, 1038-1042 (2010).

168. Huang, X., Li, S., Huang, Y., Wu, S., Zhou, X., Li, S., Gan, C.L., Boey, F., Mirkin, C.A. & Zhang, H. Synthesis of hexagonal close-packed gold nanostructures. *Nat Commun* **2**, 292 (2011).

169. Rao, S.K.P., Zoran; Du, Ziyun; Kim, Jong-Gwan; Fan, Meiyun; Jiao, Yan; Rosebush, Molly; Samant, Sandeep; Gu, Weikuan; Pfeffer, Lawrence M; Nosrat, Christopher A. Pro-inflammatory genes as biomarkers and therapeutic targets in oral squamous cell carcinoma. *J Biol Chem* **285**, 32512-32521 (2010).

170. Jang, J.-H., Schaffer, D.V. & Shea, L.D. Engineering biomaterial systems to enhance viral vector gene delivery. *Mol Ther* **19**, 1407-1415 (2011).

171. Wang, K., Hu, Q., Zhu, W., Zhao, M., Ping, Y. & Tang, G. Structure-invertible nanoparticles for triggered co-delivery of nucleic acids and hydrophobic drugs for combination cancer therapy. *Adv Funct Mater* **25**, 3380-3392 (2015).

172. Alexi, T., Borlongan, C.V., Faull, R.L., Williams, C.E., Clark, R.G., Gluckman, P.D. & Hughes, P.E. Neuroprotective strategies for basal ganglia degeneration: Parkinson's and Huntington's diseases. *Prog Neurobiol* **60**, 409-470 (2000).

173. Choi-Lundberg, D.L., Lin, Q., Chang, Y.-N., Chiang, Y.L., Hay, C.M., Mohajeri, H., Davidson, B.L. & Bohn, M.C. Dopaminergic neurons protected from degeneration by GDNF gene therapy. *Science* **275**, 838-841 (1997).

174. Géral, C., Angelova, A. & Lesieur, S. From molecular to nanotechnology strategies for delivery of neurotrophins: emphasis on brain-derived neurotrophic factor (BDNF). *Pharmaceutics* **5**, 127-167 (2013).

175. Kotterman, M.A. & Schaffer, D.V. Engineering adeno-associated viruses for clinical gene therapy. *Nat Rev Genet*, 445-51 (2014).

176. Björklund, A., Kirik, D., Rosenblad, C., Georgievska, B., Lundberg, C. & Mandel, R. Towards a neuroprotective gene therapy for Parkinson's disease: use of adenovirus, AAV and lentivirus vectors for gene transfer of GDNF to the nigrostriatal system in the rat Parkinson model. *Brain Res* **886**, 82-98 (2000).

177. Oliveira, S.L., Pillat, M.M., Cheffer, A., Lameu, C., Schwindt, T.T. & Ulrich, H. Functions of neurotrophins and growth factors in neurogenesis and brain repair. *Cytometry Part A* **83**, 76-89 (2013).

178. Pakulska, M.M.D., Irja Elliott; Obermeyer, Jaclyn M; Tuladhar, Anup; McLaughlin, Christopher K; Shendruk, Tyler N; Shoichet, Molly S. Encapsulation-free controlled release: Electrostatic adsorption eliminates the need for protein encapsulation in PLGA nanoparticles. *Sci Adv* **2**(2016).

179. Turner, P., Petch, A. & Al-Rubeai, M. Encapsulation of viral vectors for gene therapy applications. *Biotechnol Progr* **23**, 423-429 (2007).

180. Matthews, C., Jenkins, G., Hilfinger, J. & Davidson, B. Poly-L-lysine improves gene transfer with adenovirus formulated in PLGA microspheres. *Gene Ther* **6**, 1558-1564 (1999).

181. Kidd, M.E., Shin, S. & Shea, L.D. Fibrin hydrogels for lentiviral gene delivery in vitro and in vivo. *J Control Release* **157**, 80-85 (2012).

182. Schek, R.M., Hollister, S.J. & Krebsbach, P.H. Delivery and protection of adenoviruses using biocompatible hydrogels for localized gene therapy. *Mol Ther* **9**, 130-138 (2004).

183. Shin, S., Tuinstra, H.M., Salvay, D.M. & Shea, L.D. Phosphatidylserine immobilization of lentivirus for localized gene transfer. *Biomaterials* **31**, 4353-4359 (2010).

184. Kreppel, F. & Kochanek, S. Modification of adenovirus gene transfer vectors with synthetic polymers: a scientific review and technical guide. *Mol Ther* **16**, 16-29 (2007).

185. Lee, G.K., Maheshri, N., Kaspar, B. & Schaffer, D.V. PEG conjugation moderately protects adeno-associated viral vectors against antibody neutralization. *Biotechnol Bioeng* **92**, 24-34 (2005).

186. Rey-Rico, A., Venkatesan, J.K., Frisch, J., Schmitt, G., Monge-Marcet, A., Lopez-Chicon, P., Mata, A., Semino, C., Madry, H. & Cucchiarini, M. Effective and durable genetic modification of human mesenchymal stem cells via controlled release of rAAV vectors from self-assembling peptide hydrogels with a maintained differentiation potency. *Acta Biomater*, 118-27 (2015).

187. Gersbach, C.A., Coyer, S.R., Le Doux, J.M. & García, A.J. Biomaterial-mediated retroviral gene transfer using self-assembled monolayers. *Biomaterials* **28**, 5121-5127 (2007).

188. Adler-Abramovich, L., Vaks, L., Carny, O., Trudler, D., Magno, A., Caflisch, A., Frenkel, D. & Gazit, E. Phenylalanine assembly into toxic fibrils suggests amyloid etiology in phenylketonuria. *Nat Chem Biol* **8**, 701-6 (2012).

189. Copeland, R.A. Drug-target interactions: Stay tuned. *Nat Chem Biol* **11**, 451-452 (2015).

190. Timm, D.E., de Haseth, P.L. & Neet, K.E. Comparative equilibrium denaturation studies of the neurotrophins: nerve growth factor, brain-derived neurotrophic factor, neurotrophin 3, and neurotrophin 4/5. *Biochemistry-US* **33**, 4667-76 (1994).

191. Yang, W., Liu, Y., Liu, B., Tan, H., Lu, H., Wang, H. & Yan, H. Treatment of surgical brain injury by immune tolerance induced by intrathymic and hepatic portal vein injection of brain antigens. *Sci Rep* **6**, 32030 (2016).

192. Potas, J.R., Haque, F., Maclean, F.L. & Nisbet, D.R. Interleukin-10 conjugated electrospun polycaprolactone (PCL) nanofibre scaffolds for promoting alternatively activated (M2) macrophages around the peripheral nerve in vivo. *J Immunol Methods* **420**, 38-49 (2015).

193. Crompton, K.E., Goud, J.D., Bellamkonda, R.V., Gengenbach, T.R., Finkelstein, D.I., Horne, M.K. & Forsythe, J.S. Polylysine-functionalised thermoresponsive chitosan hydrogel for neural tissue engineering. *Biomaterials* **28**, 441-449 (2007).

194. Hempstead, B.L. Brain-derived neurotrophic factor: Three ligands, many actions. *Trans Am Clin Climatol Assoc* **126**, 9-19 (2015).

195. Innovagen. Peptide Property Calculator. (2015).

196. Dixon, S.J. & Stockwell, B.R. Drug discovery: engineering drug combinations. *Nat Chem Biol* **6**, 318-9 (2010).

197. Barker, R.A., Barrett, J., Mason, S.L. & Bjorklund, A. Fetal dopaminergic transplantation trials and the future of neural grafting in Parkinson's disease. *Lancet Neurol* **12**, 84-91 (2013).

198. Lindvall, O. & Hagell, P. Clinical observations after neural transplantation in Parkinson's disease. *Prog Brain Res* **127**, 299-320 (2000).

199. Bentley, D. & Caudy, M. Pioneer axons lose directed growth after selective killing of guidepost cells. *Nature* **304**, 62-5 (1983).

200. Raper, J. & Mason, C. Cellular strategies of axonal pathfinding. *Cold Spring Harb Perspect Biol* **2**, a001933 (2010).

201. Kiryushko, D., Berezin, V. & Bock, E. Regulators of neurite outgrowth: role of cell adhesion molecules. *Ann N Y Acad Sci* **1014**, 140-54 (2004).

202. Kleene, R. & Schachner, M. Glycans and neural cell interactions. *Nat Rev Neurosci* **5**, 195-208 (2004).

203. Richardson, P.M., McGuinness, U.M. & Aguayo, A.J. Axons from CNS neurons regenerate into PNS grafts. *Nature* **284**, 264-265 (1980).

204. David, S. & Aguayo, A.J. Axonal elongation into peripheral nervous system "bridges" after central nervous system injury in adult rats. *Science* **214**, 931-933 (1981).

205. Aguayo, A.J., Bjorklund, A., Stenevi, U. & Carlstedt, T. Fetal mesencephalic neurons survive and extend long axons across peripheral nervous system grafts inserted into the adult rat striatum. *Neurosci Lett* **45**, 53-8 (1984).

206. Johansson, S., Lee, I.H., Olson, L. & Spenger, C. Olfactory ensheathing glial co-grafts improve functional recovery in rats with 6-OHDA lesions. *Brain* **128**, 2961-76 (2005).

207. Thompson, L.H., Grealish, S., Kirik, D. & Bjorklund, A. Reconstruction of the nigrostriatal dopamine pathway in the adult mouse brain. *Eur J Neurosci* **30**, 625-38 (2009).

208. Newland, B., Newland, H., Werner, C., Rosser, A. & Wang, W.X. Prospects for polymer therapeutics in Parkinson's disease and other neurodegenerative disorders. *Prog Polym Sci* **44**, 79-112 (2015).

209. Nisbet, D.R., Yu, L.M., Zahir, T., Forsythe, J.S. & Shoichet, M.S. Characterization of neural stem cells on electrospun poly(epsilon-caprolactone) submicron scaffolds: evaluating their potential in neural tissue engineering. *J Biomater Sci Polym Ed* **19**, 623-34 (2008).

210. Nisbet, D.R., Rodda, A.E., Horne, M.K., Forsythe, J.S. & Finkelstein, D.I. Neurite infiltration and cellular response to electrospun polycaprolactone scaffolds implanted into the brain. *Biomaterials* **30**, 4573-80 (2009).

211. Nisbet, D.R., Forsythe, J.S., Shen, W., Finkelstein, D.I. & Horne, M.K. Review paper: A review of the cellular response on electrospun nanofibers for tissue engineering. *J Biomater Appl* **24**, 7-29 (2009).

212. Jeong, B., Kim, S.W. & Bae, Y.H. Thermosensitive sol-gel reversible hydrogels. *Adv Drug Deliv Rev* **54**, 37-51 (2002).

213. Nisbet, D.R., Crompton, K.E., Hamilton, S.D., Shirakawa, S., Prankerd, R.J., Finkelstein, D.I., Horne, M.K. & Forsythe, J.S. Morphology and gelation of thermosensitive xyloglucan hydrogels. *Biophys Chem* **121**, 14-20 (2006).

214. Nisbet, D.R., Rodda, A.E., Horne, M.K., Forsythe, J.S. & Finkelstein, D.I. Implantation of functionalized thermally gelling xyloglucan hydrogel within the brain: associated neurite infiltration and inflammatory response. *Tissue Eng Part A* **16**, 2833-42 (2010).

215. Lindvall, O. & Odin, P. Clinical application of cell transplantation and neurotrophic factors in CNS disorders. *Curr Opin Neurobiol* **4**, 752-7 (1994).

216. De Feo, D., Merlini, A., Laterza, C. & Martino, G. Neural stem cell transplantation in central nervous system disorders: from cell replacement to neuroprotection. *Curr Opin Neurol* **25**, 322-33 (2012).

217. Parish, C.L., Castelo-Branco, G., Rawal, N., Tonnesen, J., Sorensen, A.T., Salto, C., Kokaia, M., Lindvall, O. & Arenas, E. Wnt5a-treated midbrain neural stem cells improve dopamine cell replacement therapy in parkinsonian mice. *J Clin Invest* **118**, 149-160 (2008).

218. Lin, L.F., Doherty, D.H., Lile, J.D., Bektesh, S. & Collins, F. GDNF: a glial cell line-derived neurotrophic factor for midbrain dopaminergic neurons. *Science* **260**, 1130-2 (1993).

219. Hoban, D.B., Newland, B., Moloney, T.C., Howard, L., Pandit, A. & Dowd, E. The reduction in immunogenicity of neurotrophin overexpressing stem cells after intra-striatal transplantation by encapsulation in an in situ gelling collagen hydrogel. *Biomaterials* **34**, 9420-9 (2013).

220. Zhang, J.J., Tokatlian, T., Zhong, J., Ng, Q.K.T., Patterson, M., Lowry, W.E., Carmichael, S.T. & Segura, T. Physically associated synthetic hydrogels with long-term covalent stabilization for cell culture and stem cell transplantation. *Adv Mater* **23**, 5098-5103 (2011).

221. Tatard, V.M., D'Ippolito, G., Diabira, S., Valeyev, A., Hackman, J., McCarthy, M., Bouckenooghe, T., Menei, P., Montero-Menei, C.N. & Schiller, P.C. Neurotrophin-directed differentiation of human adult marrow stromal cells to dopaminergic-like neurons. *Bone* **40**, 360-73 (2007).

222. Clavreul, A., Sindji, L., Aubert-Pouessel, A., Benoit, J.P., Menei, P. & Montero-Menei, C.N. Effect of GDNF-releasing biodegradable microspheres on the function and the survival of intrastriatal fetal ventral mesencephalic cell grafts. *Eur J Pharm Biopharm* **63**, 221-8 (2006).

223. Nisbet, D.R.P.N., J; Shen, W; Horne, M K; Finkelstein, D I; and Forsythe, J S. The effect of surface hydrophilicity on the behavior of embryonic cortical neurons. *J Colloid Interface Sci* **299**, 647-655 (2006).

224. Gefen, A., Gefen, N., Zhu, Q., Raghupathi, R. & Margulies, S.S. Age-dependent changes in material properties of the brain and braincase of the rat. *J Neurotrauma* **20**, 1163-77 (2003).

225. Rosenblad, C., Martinez-Serrano, A. & Bjorklund, A. Glial cell line-derived neurotrophic factor increases survival, growth and function of intrastriatal fetal nigral dopaminergic grafts. *Neuroscience* **75**, 979-85 (1996).

226. Cotman, C.W., Hailer, N.P., Pfister, K.K., Soltesz, I. & Schachner, M. Cell adhesion molecules in neural plasticity and pathology: similar mechanisms, distinct organizations? *Prog Neurobiol* **55**, 659-69 (1998).

227. Fields, R.D. & Itoh, K. Neural cell adhesion molecules in activity-dependent development and synaptic plasticity. *Trends Neurosci* **19**, 473-80 (1996).

228. van Horne, C.G., Stromberg, I., Young, D., Olson, L. & Hoffer, B. Functional enhancement of intrastriatal dopamine-containing grafts by the co-transplantation of sciatic nerve tissue in 6-hydroxydopamine-lesioned rats. *Exp Neurol* **113**, 143-54 (1991).

229. Shukla, S., Chaturvedi, R., Roy, N. & Agrawal, A. Enhanced survival and function of neural stem cells derived dopaminergic neurons under influence of olfactory ensheathing cells in parkinsonian rats. *J Neurochem* **109**, 436-51 (2009).

230. Gage, F.H., Stenevi, U., Carlstedt, T., Foster, G., Bjorklund, A. & Aguayo, A.J. Anatomical and functional consequences of grafting mesencephalic neurons into a peripheral nerve "bridge" connected to the denervated striatum. *Exp Brain Res* **60**, 584-9 (1985).

231. Cui, Y.F., Hargus, G., Xu, J.C., Schmid, J.S., Shen, Y.Q., Glatzel, M., Schachner, M. & Bernreuther, C. Embryonic stem cell-derived L1 overexpressing neural aggregates enhance recovery in Parkinsonian mice. *Brain* **133**, 189-204 (2010).

232. Ourednik, V., Ourednik, J., Xu, Y., Zhang, Y., Lynch, W.P., Snyder, E.Y. & Schachner, M. Cross-talk between stem cells and the dysfunctional brain is facilitated by manipulating the niche: evidence from an adhesion molecule. *Stem Cells* **27**, 2846-56 (2009).

233. Mehanna, A., Mishra, B., Kurschat, N., Schulze, C., Bian, S., Loers, G., Irintchev, A. & Schachner, M. Polysialic acid glycomimetics promote myelination and functional recovery after peripheral nerve injury in mice. *Brain* **132**, 1449-62 (2009).

234. Rodriguez, A., Wang, T.-Y., Bruggeman, K.F., Horgan, C.C., Li, R., Williams, R., Parish, C.L. & Nisbet, D.R. In vivo assessment of grafted cortical neural progenitor cells and host response to functionalized self-assembling peptide hydrogels and implications for tissue repair. *J Mater Chem B* **2**, 7771-7778 (2014).

235. Gash, D.M., Zhang, Z. & Gerhardt, G. Neuroprotective and neurorestorative properties of GDNF. *Ann Neurol* **44**, S121-5 (1998).

236. Shi, J., Votruba, A.R., Farokhzad, O.C. & Langer, R. Nanotechnology in drug delivery and tissue engineering: from discovery to applications. *Nano Lett* **10**, 3223-30 (2010).

237. Li, R., Pavuluri, S., Bruggeman, K., Long, B.M., Parnell, A.J., Martel, A., Parnell, S.R., Pfeffer, F.M., Dennison, A.J., Nicholas, K.R., Barrow, C.J., Nisbet, D.R. & Williams, R.J. Coassembled nanostructured bioscaffold reduces the expression of proinflammatory cytokines to induce apoptosis in epithelial cancer cells. *Nanomedicine-UK* **12**, 1397-407 (2016).

238. Sing Yian Chew, R.M., Ahmet Hoke, Kam W. Leong. Aligned protein–polymer composite fibers enhance nerve regeneration: A potential tissue-engineering platform. *Adv Funct Mater* **17**, 1288-1296 (2007).

239. Bruggeman, K.F., Rodriguez, A.L., Parish, C.L., Williams, R.J. & Nisbet, D.R. Temporally controlled release of multiple growth factors from a self-assembling peptide hydrogel. *Nanotechnology* **27**, 385102 (2016).

240. van Dommelen, J.A., van der Sande, T.P., Hrapko, M. & Peters, G.W. Mechanical properties of brain tissue by indentation: interregional variation. *J Mech Behav Biomed Mater* **3**, 158-66 (2010).

241. A. J. Bruce Alberts, J.L., Martin Raff, Keith Roberts, and Peter Walter. in *Molecular Biology of the Cell, 4th edition* (Garland Science, New York, 2002).

242. Lozano, D., Gonzales-Portillo, G.S., Acosta, S., de la Pena, I., Tajiri, N., Kaneko, Y. & Borlongan, C.V. Neuroinflammatory responses to traumatic brain injury: etiology, clinical consequences, and therapeutic opportunities. *Neuropsychiatr Dis Treat* **11**, 97-106 (2015).

243. Faulkner, J.R., Herrmann, J.E., Woo, M.J., Tansey, K.E., Doan, N.B. & Sofroniew, M.V. Reactive astrocytes protect tissue and preserve function after spinal cord injury. *J Neurosci* **24**, 2143-55 (2004).

244. Kim, J.H. Brain-derived neurotrophic factor exerts neuroprotective actions against amyloid beta-induced apoptosis in neuroblastoma cells. *Exp Ther Med* **8**, 1891-1895 (2014).

245. Yang, W.H., Yang, C., Xue, Y.Q., Lu, T., Reiser, J., Zhao, L.R. & Duan, W.M. Regulated expression of lentivirus-mediated GDNF in human bone marrow-derived mesenchymal stem cells and its neuroprotection on dopaminergic cells in vitro. *PLoS One* **8**, e64389 (2013).

246. Pierchala, B.A., Milbrandt, J. & Johnson, E.M., Jr. Glial cell line-derived neurotrophic factor-dependent recruitment of Ret into lipid rafts enhances signaling by partitioning Ret from proteasome-dependent degradation. *J Neurosci* **26**, 2777-87 (2006).

247. Williams, A.J., Wei, H.H., Dave, J.R. & Tortella, F.C. Acute and delayed neuroinflammatory response following experimental penetrating ballistic brain injury in the rat. *J Neuroinflammation* **4**, 17 (2007).

248. Coelho, J.F., Ferreira, P.C., Alves, P., Cordeiro, R., Fonseca, A.C., Gois, J.R. & Gil, M.H. Drug delivery systems: Advanced technologies potentially applicable in personalized treatments. *EPMA J* **1**, 164-209 (2010).

249. Wang, T., Jiang, H., Wan, L., Zhao, Q., Jiang, T., Wang, B. & Wang, S. Potential application of functional porous TiO2 nanoparticles in light-controlled drug release and targeted drug delivery. *Acta Biomater* **13**, 354-63 (2015).

250. Kommireddy, D.S., Patel, A.A., Shutava, T.G., Mills, D.K. & Lvov, Y.M. Layer-by-layer assembly of TiO2 nanoparticles for stable hydrophilic biocompatible coatings. *J Nanosci Nanotechnol* **5**, 1081-1087 (2005).

251. Devanand Venkatasubbu, G., Ramasamy, S., Ramakrishnan, V. & Kumar, J. Folate targeted PEGylated titanium dioxide nanoparticles as a nanocarrier for targeted paclitaxel drug delivery. *Adv Powder Technol* **24**, 947-954 (2013).

252. Jiang, X.-s., Chen, J.-y. & Huang, N. Immobilizing collagen type I to TiO2 film for improvement of biocompatibility. *Front Mater Sci China* **2**, 276-280 (2008).

253. Barhoumi, A., Salvador-Culla, B. & Kohane, D.S. NIR-triggered drug delivery by collagen-mediated second harmonic generation. *Adv Healthc Mater* **4**, 1159-63 (2015).

Appendix A: Supplementary Information (Chapter Six)

Fluctuation data was calculated using the release rate data for the hourly release profile of BDNF and modified BDNF-Chitosan shown below.

Table 1: Hourly Release Rate Data

Time (hour)	BDNF (pg/hour)			BDNF-Chitosan (pg/hour)		
1	0.238854	0.427126	0.179313	0.367356	1.797767	0.356615
2	0.375561	0.503393	85.80665	2.237672	0.983898	0.452686
3	108.4237	54.73617	114.3919	7.825296	1.559592	3.392786
4	39.95618	19.94937	29.85885	11.48662	6.702689	1.298517
5	17.63363	18.53271	27.74342	41.97237	2.761074	6.432447
6	61.5629	47.42654	51.16976	18.99239	5.674232	18.15534
7	83.12487	66.95469	41.34791	41.66928	13.90233	3.486096
8	43.90452	36.00312	52.99514	46.95929	2.794707	44.25023
9	50.40296	61.11735	62.76371	52.635	26.89515	59.14041
10	49.26989	53.52608	45.87377	58.37618	39.79055	
11	48.52583	70.86419	61.5629	50.38608	30.99872	
12	90.76646	245.6232	169.472	95.41332	71.32155	

From the individual time point values, the absolute changes within each sample between each time point were calculated (change = magnitude of 'value at time point' – 'value at previous time point') and an average fluctuation value was found for each sample group.

Table 2: Point to Point Fluctuations in Hourly Release Rate Data

Time (hour)	BDNF (pg/hour)			BDNF-Chitosan (pg/hour)		
1	N/A	N/A	N/A	N/A	N/A	N/A
2	0.136707	0.076267	85.62733	1.870316	0.813869	0.096071
3	108.0481	54.23278	28.58526	5.587625	0.575694	2.9401
4	68.46752	34.7868	84.53306	3.66132	5.143097	2.094268
5	22.32255	1.41666	2.115435	30.48575	3.941615	5.13393
6	43.92927	28.89383	23.42634	22.97999	2.913158	11.72289
7	21.56198	19.52816	9.82185	22.6769	8.228099	14.66924
8	39.22035	30.95157	11.64723	5.290005	11.10762	40.76413
9	6.498435	25.11423	9.76857	5.675715	24.10044	14.89019
10	1.13307	7.591275	16.88994	5.741175	12.8954	
11	0.74406	17.33811	15.68913	7.990095	8.79183	
12	42.24063	174.759	107.9091	45.02724	40.32284	
AVERAGE	32.20934	35.88079	36.0012	14.27147	10.80306	11.53885

To compare fluctuation values between BDNF and BDNF-Chitosan sample groups a matrix was established comparing each BDNF sample to each BDNF-Chitosan sample, and in each comparison, the relative change in fluctuations compared to the BDNF samples was calculated (change = (BDNF-Chitosan – BDNF)/BDNF).

Table 3: Matrix Comparison of Fluctuations in Hourly Release Rate Data

VS	BDNF-Chitosan	Sample 1	Sample 2	Sample 3
BDNF	**Average Fluctuation**	*14.27147*	*10.80306*	*11.53885*
Sample 1	*32.20934*	-55.69%	-66.46%	-64.18%
Sample 2	*35.88079*	-60.23%	-69.89%	-67.84%
Sample 3	*36.0012*	-60.36%	-69.99%	-67.95%

From these comparative values the average change was calculated as -64.73% with a standard deviation of 4.98%. The negative change describes an average reduction in fluctuations.

Appendix B: Full Published Work (Chapter Four)

A. Rodriguez, T. Wang, K. Bruggeman, C. Horgan, R. Li, R. Williams, C. Parish, D. Nisbet, "*in vivo* assessment of grafted cortical neural progenitor cells and host response to functionalised self-assembling peptide hydrogels and the implications for tissue repair", *Journal of Materials Chemistry B*, 2014, vol. 2, pp. 7771-7778 - Reproduced by permission of The Royal Society of Chemistry (http://www.rsc.org/)

Journal of Materials Chemistry B

PAPER

View Article Online
View Journal | View Issue

Cite this: J. Mater. Chem. B, 2014, 2, 7771

In vivo assessment of grafted cortical neural progenitor cells and host response to functionalized self-assembling peptide hydrogels and the implications for tissue repair

A. L. Rodriguez,[a] T. Y. Wang,[b] K. F. Bruggeman,[a] C. C. Horgan,[a] R. Li,[c] R. J. Williams,[cd] C. L. Parish†*[b] and D. R. Nisbet†*[a]

Received 21st August 2014
Accepted 3rd October 2014

DOI: 10.1039/c4tb01391c

www.rsc.org/MaterialsB

Tissue specific scaffolds formed from minimalist *N*-fluorenylmethyloxycarbonyl self-assembling peptides (Fmoc-SAPs) have emerged as promising biomaterials due to their ease of synthesis and capacity to self-assemble *via* simple, non-covalent interactions into complex nanofibrous hydrogels. However, concerns remain over their biocompatibility and cytotoxicity for *in vivo* applications. Here, we demonstrate that these Fmoc-SAPs are biocompatible *in vivo* and well suited as a delivery vehicle for cell transplantation. In order to determine the effect of tissue specific parameters, we designed three Fmoc-SAPs containing varying bioactive peptide sequences derived from extracellular matrix proteins, laminin and fibronectin. Fmoc-SAPs delivering cortical neural progenitor cells into the mouse brain display a limited foreign body response, effective functionalization and low cytotoxicity for at least 28 days. These results highlight the suitability of Fmoc-SAPs for improved neural tissue repair through the support of grafted cells and adjacent host parenchyma. Overall, we illustrate that Fmoc-SAPs are easily engineered materials for use as a tool in cell transplantation, where biocompatibility is key to promoting cell survival, enhancing the graft–host interface and attenuation of the inflammatory response for improved tissue repair outcomes.

Introduction

Central nervous system (CNS) repair presents a significant challenge, given the limited regenerative capacity of neural tissue. Currently, following insult to the CNS, treatments are limited to pharmacotherapy or rehabilitation with the aim of slowing disease progression and reducing secondary damage; thereby reducing symptom severity, without actually repairing the induced damage.[1] Cell replacement therapy offers an attractive alternative, whereby cells are implanted into the site of injury in order to regenerate and repair damaged neural tissue, providing symptomatic relief to patients.[2]

Early transplantation trials have identified additional mechanisms for repair, where grafted cells have been shown to be neuroprotective by providing trophic support to the surrounding area, attenuating the inflammatory response, promoting endogenous stem cell neurogenesis and enhancing angiogenesis.[3–5] Biomaterials have emerged as potential adjuncts for such tissue repair by delivering a morphological and biochemical extracellular matrix (ECM) mimic that can support transplanted cells at an injury site, lessening the impact of further degeneration to surrounding tissue and ultimately repairing the induced damage. As such, there is a need for biocompatible, functionalized materials into which cells can be embedded as a vector for transplantation, and once implanted *in vivo*, can attenuate the inflammatory response and allow the transplanted cells to infiltrate the host tissue by creating a permissive graft–host interface.

With this in mind, an ideal biomaterial for cell transplantation would improve recovery by creating a favorable milieu for exogenous and endogenous cells.[6] This would involve controlling the inflammatory response associated with the primary insult and ensuing transplantation surgery, which includes local astrocyte proliferation that can ultimately result in distortion of the brain parenchyma and scarring.[7] We have previously demonstrated the potential of electrospun scaffolds to modulate the inflammatory response of the brain with limited immunogenic reactivity.[8] However, while these scaffolds were shown to mimic the ECM morphology and control the inflammatory response, their geometric constraints and fixed form does not allow them to readily interface with cells at

[a]*Research School of Engineering, The Australian National University, Canberra, 2601, Australia. E-mail: david.nisbet@anu.edu.au*

[b]*Florey Institute of Neuroscience & Mental Health, The University of Melbourne, Parkville, 3010, Australia. E-mail: clare.parish@florey.edu.au*

[c]*Centre for Chemistry and Biotechnology, Deakin University, Waurn Ponds, 3217, Australia*

[d]*School of Aerospace, Mechanical and Manufacturing Engineering, RMIT University, Melbourne, 3001, Australia*

† Both authors contributed equally to this work.

the edge of a lesion site, making them less attractive for cell transplantation within the brain.[8,9]

Nature utilizes supramolecular interactions to drive the self-organization of biological macromolecules such as peptides and proteins of the ECM.[10] These principles can be used to design synthetic peptides that can self-assemble into larger, complex structures, reminiscent of those found within living systems, providing a platform for the development of regenerative therapies.[11] Peptide based materials can be rationally designed to include features that emulate the ECM in an effort to reproduce the nanofibrous network of proteins, as well as provide control over the introduction of biochemical cues, such as the release of growth factors and presentation of integrin binding domains.[11,12]

A number of hydrogels formed from fibrous self-assembling peptides (SAPs) have been developed for various *in vitro* and *in vivo* applications.[11] Significant progress has been made by utilizing long, highly structured peptides, such as the commercially available RADA16, or peptide amphiphiles.[13,14] However, due to their lengthy amino acid chains, these peptides require a large number of steps to synthesize and purify – increasing cost and complexity whilst reducing yield. Consequently, considerable interest has surrounded the design of minimalist peptide sequences (1–10 residues), as these simple molecules retain the ability to self-assemble, whilst allowing the incorporation of bioactive sequences. Additionally, they enable the effect of individual amino acid modifications to be investigated, enabling fine control over the structure, assembly conditions and triggering mechanisms of the resulting macroscale hydrogel.[12,15,16]

A promising class of these materials is based on the assembly of SAPs capped at the N-terminal with fluorenylmethyloxycarbonyl (Fmoc). Fmoc-SAPs have been shown to self-assemble into nanofibers *via* non-covalent π–β interactions with the peptide sequence presented on the external surface of the fibrils at high density.[17,18] These fibrils then intertwine to form an entangled matrix hydrogel that has morphological and mechanical similarities to many types of ECM.[17,19] Fmoc-SAP hydrogels that morphologically emulate the native ECM are of particular interest due to their potential to effectively fill a void at the site of neural damage, readily interface with cells at the edge of the lesion site, attenuate the inflammatory response post implantation and structurally support the surrounding neural tissue.

Though the material characteristics and underlying self-assembly mechanism of Fmoc-SAPs have been thoroughly studied, investigation of their biological properties and how cells respond to their physical and biochemical stimuli has been limited – usually focusing on *in vitro* cell culture, incorporating the fibronectin based sequence, arginine-glycine-aspartate (RGD).[15,17,19–23] Additionally, research has typically focused on short di- and tripeptides, as the individual amino acid contributions in longer peptide sequences tend to inhibit spontaneous self-assembly under physiological conditions.[12] We have recently published novel approaches that allow core amino acid sequences of up to five residues in length to be embedded into the peptide backbone by the rational design of additional flanking residues; either through adjustment of pK_a or addition of aromatic/hydrophobic residues.[12,24] Using these methods, we have designed Fmoc-SAPs that contain peptide sequences based on the common ECM brain protein laminin: isoleucine-lysine-valine-alanine-valine (IKVAV) and tyrosine-isoleucine-glycine-serine-arginine (YIGSR).

We have previously demonstrated the functionality of the embedded peptide sequence in Fmoc-SAPs *in vitro*, compared to a morphologically and chemically similar system made from a scrambled control sequence.[24] Here, we examine the effect of these Fmoc-SAPs on primary cortical neural progenitor cells *in vivo*. In order to ascertain the effectiveness of these laminin peptide sequences *in vivo*, we also included an RGD containing Fmoc-SAP as a control, as fibronectin is known to promote cell adhesion and is not observed in significant amounts in the brain, allowing us to determine the tissue specificity of the Fmoc-SAPs.[25] Importantly, for the material to be effective, it must be well tolerated by both the host and implanted cells, and elicit a limited inflammatory response with limited or no formation of a glial scar. Therefore, the inflammatory response to these developed Fmoc-SAPs, as well as survival, migration and integration of the transplanted cortical neural progenitor cells were investigated in the intact brain. These results allow us to ascertain which peptide sequence has the most beneficial effect on endogenous and grafted cells *in vivo* for future application in the injured CNS.

Materials and methods

Solid phase peptide synthesis/mass spectrometry

Fmoc-SAPs were made using solid phase peptide synthesis (SPPS) in a custom rotating glass reactor vessel at a 0.4 mmol scale. Fmoc protected amino acids, hydroxybenzotriazole (HOBt), *O*-benzotriazole-*N*,*N*,*N*′,*N*′-tetramethyl-uronium-hexafluoro-phosphate (HBTU) and Wang based resins were purchased from GL Biochem (China). All other chemicals were purchased from Sigma-Aldrich. Dimethylformamide (DMF) was dried for a minimum of 2 hours prior to use with 4 Å molecular sieves.

Peptide synthesis was achieved by the stepwise deprotection of the N-terminal Fmoc group of the resin anchored amino acid using a solution of 20% piperidine in DMF, followed by a coupling step using a solution of the next Fmoc-amino acid in HOBt, HBTU and *N*,*N*-diisopropylethylamine (DIPEA) in DMF. This process of deprotection and coupling of amino acids was repeated until the desired peptide was synthesised. The final Fmoc group was not removed. Deprotection and coupling of amino acids was verified using a Kaiser test for the detection of free amines. Once SPPS of the desired sequence was complete, the Fmoc protected peptide and resin was washed with ethanol and left to dry under constant vacuum for 2 days. A cleavage solution of trifluoroacetic acid (TFA), 2.5% distilled water and 2.5% triethylsilane (TES) was prepared. The resin was left to stand in the solution for 2 hours. Following cleavage, the peptide solution was filtered through glass wool. Excess TFA was then evaporated using nitrogen until approximately 5 mL of peptide solution was left. The peptide was then precipitated,

followed by 5 washes in cold ether before being collected and allowed to dry under constant vacuum for 2 days. The peptide was then ground into a fine powder before being placed under constant vacuum for a further 7 days. Mass spectrometry was performed to verify synthesis of the desired peptide.

Fmoc-SAP gel preparation

Fmoc-SAPs were prepared at 20 mg mL^{-1}. Approximately 10 mg of the peptide was initially dissolved in 100 μL deionized water with 50 μL of 0.5 M sodium hydroxide (NaOH). The pH of the peptide solution was then slowly reduced by the dropwise addition of 0.1 M hydrochloric acid (HCl) until the pH of the media was achieved (typically 100–150 μL). The solution was continually vortexed throughout this process. Once a gel was formed at appropriate pH, Hank's buffered saline solution (HBSS) (Gibco) was added to make the gel up to 20 mg mL^{-1}. The pH of the Fmoc-SAPs was measured using a microprobe pH meter.

Fourier transform infrared spectroscopy

Fourier transform infrared spectroscopy (FTIR) was performed using an Alpha Platinum Attenuated Total Reflectance FTIR (Bruker Optics). 30 μL of Fmoc-SAP was placed on the single reflection diamond. The pressure applicator was used to spread the Fmoc-SAP over the crystal. Absorbance scans were taken at 0 minutes and 5 minutes, with 5 minutes showing higher resolution.

Circular dichroism spectroscopy

Circular dichroism (CD) was completed using a Chirascan CD Spectrometer (Applied Photophysics Limited). Fmoc-SAP solutions were prepared at 1 part in 200 with deionized water. A baseline scan for deionized water was completed and subtracted from the obtained peptide CD scans. The Fmoc-SAP solution was scanned from 350 to 170 nm at a step size of 1 and 1 nm bandwidth.

Rheology

Viscoelastic properties of the formed Fmoc-SAPs were assessed using a Kinexus Pro+ Rheometer (Malvern). A 20 mm smooth flat plate with a solvent trap was used. The Fmoc-SAP sample was placed on the rheometer plate at a gap size of 0.2 mm. Oscillatory strain of 0.1% strain was used with a frequency sweep of 0.1–100 Hz.

Atomic force microscopy

Atomic force microscopy (AFM) images of the Fmoc-SAPs were obtained using a Multimolde 8 (Bruker BioSciences Corporation, USA). For sample preparation, 15 μL Fmoc-SAP was applied on highly ordered pyrolytic graphite (HOPG) substrates (SPI, USA). The tips used were scanasyst-air probes with silicon tip on nitride lever (Bruker BioSciences Corporation, USA). The AFM was operated in peak force QNM. Calibration of deflection sensitivity, spring constant and tip radius of probes was done before sample imaging. Scan size was at 10 μm.

Transmission electron microscopy

Transmission electron microscopy (TEM) was performed on a HITACHI HA7100 TEM with LaB6 filament at 100 kV. Negative stains were performed to image the Fmoc-SAP samples. Formvar coated copper grids were glow discharged for 30 seconds at 15 mA. A drop of the Fmoc-SAP sample was placed on the grid for 30 seconds, after which any excess was blotted off using filter paper. The grid was then washed with a drop of water, any excess water blotted off and the wash repeated. The grid was then briefly placed in a drop of 0.75% uranyl formate, blotted off and placed in a second drop of uranyl formate for 20 seconds. Any excess stain solution was blotted off and the grid was allowed to dry overnight before imaging in the TEM.

Preparation of primary cortical cells for transplantation

All procedures were conducted in accordance with the Australian National Health and Medical Research Council's published Code of Practice for the Use of Animals in Research and experiments were approved by the Florey Institute of Neuroscience & Mental Health animal ethics committee. All mice were housed on a 12 hour light/dark cycle with *ad libitum* access to food and water. Adult female C57BL/6 mice were used as graft recipients while donor tissue for transplantation was obtained from timemated mice expressing green fluorescent protein (GFP) under the β-actin promoter. Animals were time mated overnight and visualization of a vaginal plug on the following morning was taken as embryonic day (E) 0.5. Embryos at E14.5 were collected in chilled L15 media. GFP+ embryos were selected, their brains removed and the cortices dissected to isolate GFP+ cortical primary tissue. The cortices were incubated for 20 minutes in 0.1% DNase and 0.05% trypsin in magnesium and calcium HBSS. The tissue was then washed gently 3 times with HBSS. The tissue was then dissociated and the cells re-suspended in HBSS with 0.1% DNAse at 200 000 cells per μL.

Implantation of self-assembling peptide hydrogels with cell transplantation

Mice received implants of cells in the presence or absence of Fmoc-SAPs (Fmoc-DIKVAV; Fmoc-FRGDF; Fmoc-DYIGSRF), $n = 6$ per group. Mice were anaesthetized with 5% isoflurane, and the level of anesthesia maintained at 2% for the duration of the surgery. Mice were placed in a stereotaxic frame, midline incisions were made in the scalp and craniotomies were performed overlying the striatum. Cells were mixed at a 1 : 1 ratio with HBSS or Fmoc-SAP prior to implantation into the striatum. A total of 2 μL (200 000 cells) were injected, using a fine glass capillary, at the following co-ordinates: 1.0 mm anterior and 2.5 mm lateral relative to bregma, and at a depth of 3.2 mm below the dural surface. After 28 days, mice were delivered a terminal dose of barbiturate and were transcardially perfused with warm saline followed by 4% paraformaldehyde (PFA). Brains were removed and post-fixed for 2 hours in 4% PFA before overnight cryo-preservation in 30% sucrose solution. The brains were then coronally sectioned at 40 μM in 12 series before free-floating immunohistochemistry was performed.

Immunohistochemistry

Free floating immunohistochemical procedures were performed as previously described.[26] Primary antibodies and dilution factors were as follows: chicken anti-GFP (GFP, 1 : 1000, Abcam), rabbit anti-GFAP (GFAP, 1 : 800, DAKO) and mouse anti-CD11b (1 : 100, AbD serotec). Secondary antibodies for direct detection were used at a dilution of 1 : 200—DyLight 488 conjugated donkey anti-chicken, DyLight 550 donkey anti-rabbit and DyLight 649 donkey anti-mouse (Jackson ImmunoResearch). Absolute cell counts and optical density measurements were carried out on a Leica fluorescent microscope (Leica CTR6000).

Assessment of grafts

Grafted cells, and the extent of their innervation were discernable by the presence of GFP+ staining. For all animals, total number of GFP+ cell, density (GFP+ cells per mm^3) and volume of innervation (mm^3) were quantified. Optical intensity was measured at two fields of view (FOV) for comparison of innervation between each group. This technique was also used for assessment of inflammation. ImageJ was used to determine the optical intensity of the fluorophore (488 for GFP; 550 for GFAP and 649 for CD11b) in each image at each FOV. This provides a relative comparison for the extent of innervation or elicited inflammatory response induced in each group.

Statistical analysis

One-way ANOVAs with Tukey *post-hoc* tests were used to identify statistically significant changes between groups. The data was also transformed in order to obtain equal variance and the tests repeated, however, this had no effect on the statistical information obtained. Statistical significance was set at a level of $P < 0.05$. Data represents mean ± standard error of the mean (SEM).

Results and discussion

Laminin and fibronectin based Fmoc-SAPs form nanofibrous hydrogels at physiological pH

Three Fmoc-SAPs containing laminin and fibronectin peptide binding domains were designed and optimized for self-assembly under physiological conditions (pH 7.4) *via* two previously developed approaches.[12,24] Fmoc-aspartate-isoleucine-lysine-valine-alanine-valine (Fmoc-DIKVAV) and Fmoc-aspartate-tyrosine-isoleucine-glycine-serine-arginine-phenylalanine (Fmoc-DYIGSRF) were designed *via* adjusting their pK_a with an N-terminal acidic residue, namely aspartate (Fig. 1A & B).[12] Alternatively, uncharged flanking aromatic residues were added to improve the stability of the assembly to give Fmoc-phenylalanine-arginine-glycine-aspartate-phenylalanine (Fmoc-FRGDF) (Fig. 1C).[24]

Fmoc-self-assembly occurs when individual peptide building blocks are optimally charged, undergoing π–π stacking between aromatic Fmoc groups and hydrogen bonding between the pendant peptide groups, to form individual nanofibers. The

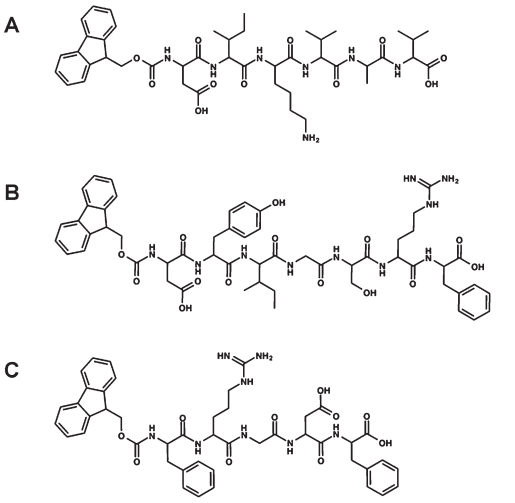

Fig. 1 Chemical structure of (A) Fmoc-DIKVAV, (B) Fmoc-DYIGSRF and (C) Fmoc-FRGDF.

short peptide chains assemble in anti-parallel β-sheets, yielding an overall π–β assembly (Fig. 2).

To ensure the underlying non-covalent and supramolecular interactions leading to π–β assembly were maintained with the insertion of bioactive peptide sequences, a series of materials characterization techniques were performed. AFM showed that each hydrogel presented a microscale fibrous network broadly

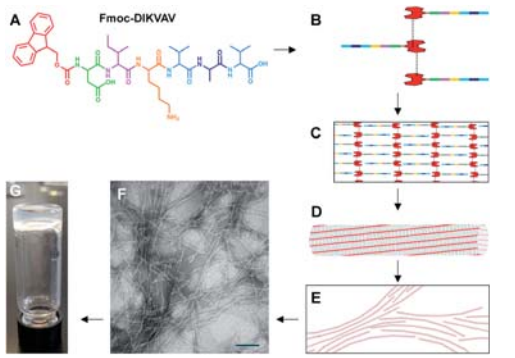

Fig. 2 Schematic of Fmoc-self-assembly process with Fmoc-DIKVAV. (A) Fmoc-DIKVAV structure as synthesized *via* solid-phase peptide synthesis. (B) Aromatic Fmoc terminal groups undergo π–π stacking. (C) The DIKVAV peptide chains undergo hydrogen bonding to form anti-parallel β-sheets. (D) A natural twist occurs to maintain this π–β assembly forming a hollow nanofiber with the DIKVAV sequence exposed on the outside of the fiber. (E) The nanofibers interact with each other forming a nanofibrous network as shown in (F), TEM of resulting Fmoc-DIKVAV hydrogel (scale bar 100 nm). (G) The material presents as a shear-thinning hydrogel.

analogous in scale, consisting of entwined linear features (Fig. 3A–C). TEM micrographs showed that in each case, fibrils nanometers in diameter and microns in length were formed and these appeared to orientate laterally, forming entanglements (Fig. 3D–F). Though the nanofibers were broadly conserved across all three systems, a more branched architecture was observed for Fmoc-DYIGSRF with fibers slightly larger in diameter than those seen for Fmoc-FRGDF and Fmoc-DIKVAV, potentially an effect of bundling fibers due to increased relative charge (Fig. 3C & F). Though IKVAV and YIGSR are both laminin based peptides, the observed differences in structure is a direct result of their unique amino acid sequence, apparent pK_a of the peptide, hydrophobicity of the sequence and resulting charge at physiological pH.[23]

In order to determine the viscoelastic properties of the hydrogels, parallel plate rheology was performed. The materials displayed characteristic viscoelastic gel properties, namely a storage modulus (G') greater than the loss modulus (G'') with both moduli independent of frequency (Fig. 4A–C).[17] The moduli varied across the three different sequences, attributed to the varying charges that appear throughout each unique sequence and the resulting ionic interactions between the individual fibrils. At the same concentration, Fmoc-DIKVAV showed the strongest rheological properties with a G' of 30 000 Pa (Fig. 4A). Fmoc-FRGDF and Fmoc-DYIGSRF were significantly weaker with a G' of ~100 Pa and ~200 Pa respectively, which could be a result of the morphological differences observed (Fig. 4B & C). Importantly, the range of moduli present is comparable to a range of soft tissues and could therefore be tuned for tissue specific applications.

Spectroscopic analyses of the Fmoc-SAP hydrogels were used to confirm that across each sequence the underlying π–β assembly was conserved. FTIR was used to investigate the presence of secondary structure by monitoring intermolecular 'peptide-like' interactions across the amide I region (Fig. 4D).[17] In each case, vibrations characteristic of this class of SAPs were observed. Anti-parallel β-sheet formation were observed with a major peak between 1630–1660 cm^{-1} and a minor peak between 1690–1710 cm^{-1}.[17,21] In addition, a broad feature at ~1650 cm^{-1} was observed, indicative of a random coil component.[21] Intra- and supramolecular interactions were analysed using CD (Fig. 4E). A general n–π* transition between 180 and 220 nm was observed in each sample, indicating the formation of anti-parallel β-sheets (Fig. 4E).[27] Transitions in the range of 230–270 nm arise due to the supramolecular alignment of individual fibers and are characteristic of Fmoc-SAPs.[28] Again, the CD spectrum for Fmoc-DYIGSRF indicates the presence of some random coil structures. However, together with the TEM and AFM images, the spectroscopic analysis confirms that π–β self-assembly is a robust mechanism that allows the formation of nanofibrous structures, despite the incorporation of varying bioactive peptide sequences, extending the peptide sequence, and altering the hydrophobicity and charge of the peptide sequence.

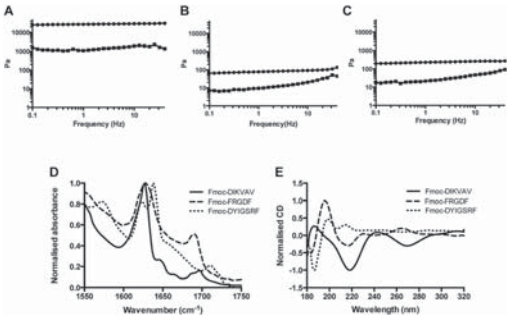

Fig. 4 Rheological analysis showing characteristic viscoelastic behavior, where G' (circles) is greater than G'' (squares) for (A) Fmoc-DIKVAV, (B) Fmoc-FRGDF and (C) Fmoc-DYIGSRF. (D) FTIR analysis of amide I region showing characteristic peaks for antiparallel β-sheets. (E) CD shows transition peaks at 220 nm for all the synthesized Fmoc-SAPs, suggesting the presence of β-sheets. Transitions in the 230–270 nm region represent supramolecular ordering and bundling of individual fibers.

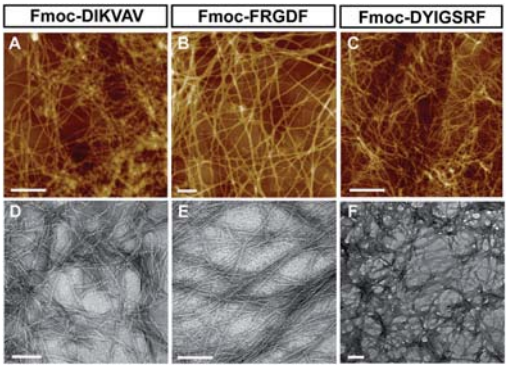

Fig. 3 (A–C) AFM (scale bar 500 nm) and (D–F) TEM (scale bar 100 nm) showing nanofibrous architecture of the three Fmoc-SAPs: Fmoc-DIKVAV, Fmoc-FRGDF and Fmoc-DYIGSRF.

Response of cortical neural progenitor cells upon transplantation into the mouse brain using Fmoc-SAPs

Fmoc-SAPs support the survival and migration of transplanted cortical neural progenitor cells in the intact brain. Following characterization of the Fmoc-SAPs, their capacity to support cell grafts *in vivo* was assessed in the intact brain. E14.5 cortical neural progenitor cells expressing GFP were stereotaxically injected into mouse brains (the striatum) in the absence or presence of Fmoc-SAPs. The grafted cells were identified by GFP staining within the mouse brain.

A GFP+ cell count showed no statistically significant difference in survival between cells alone and cells implanted together with Fmoc-SAPs, demonstrating that in each case the Fmoc-SAPs were non-cytotoxic (Fig. 5A). Not surprisingly, there was a trend for grafts in the presence of Fmoc-FRGDF to have the lowest GFP+ cell survival rate compared to Fmoc-DIKVAV and Fmoc-DYIGSRF (Fig. 5A). This is supported by the known

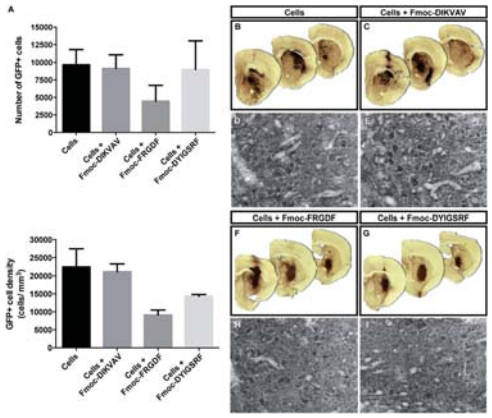

Fig. 5 (A) Number of GFP+ cells in the striatum 28 days after transplantation (top) and cell density of implanted GFP+ cells in graft core (bottom). Data represents mean + SEM. Photomontages of the mouse brain illustrating GFP+ grafts in (B) the absence, and presence of (C) Fmoc-DIKVAV, (F) Fmoc-FRGDF and (G) Fmoc-DYIGSRF. (D, E, H & I) show high power magnification (10×) of GFP+ grafts.

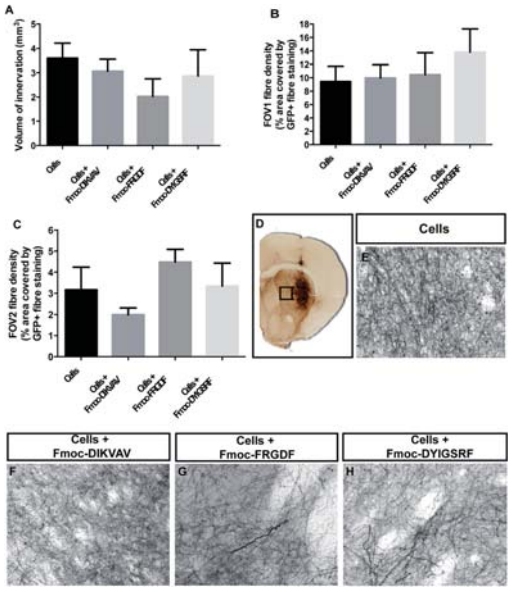

Fig. 6 (A) Volume of GFP+ graft innervation. (B & C) Percentage of GFP+ fibers in FOV1 and FOV2 respectively for each group, measured as optical density. (D) Section of single brain hemisphere showing example of fields of view (FOV) 1 (dashed line box) and 2 (solid line box) taken from the edge of the graft core, sequentially moving outwards. (E–J) Images of FOV2 used to measure optical density of GFP+ fibers and show fiber innervation. Data represents mean + SEM.

role of laminin, but not fibronectin, as a major constituent of the brain's ECM and modulator of neural differentiation and neurite extension.[29,30] This emphasizes the importance of designing a microenvironment that is specifically tuned to cellular requirements for tissue specificity. The density of cells within the graft core was assessed as an index of cell migration (GFP+ cells per mm^3, Fig. 5A). Similar to cell survival, graft cell density showed no significant difference between any groups (Fig. 5A).

With no statistical difference observed in cell survival or migration between grafts in the presence or absence of Fmoc-SAP, we have shown that these scaffolds are non-cytotoxic to grafted cells in the parenchyma. This result demonstrates the capacity for these non-toxic materials to support cells, potentially in a disease setting. The Fmoc-SAPs could help rebuild tissue by supporting the surrounding parenchyma, enhancing the graft–host interface at the lesion site to reduce any potential for secondary degeneration whilst also encouraging integration of transplanted cells with the host tissue.

Grafted cortical neural progenitor cells can innervate the host brain tissue in the presence of Fmoc-SAPs. Integration of transplanted cells within the host environment and reinnervation of damaged host tissue by transplanted cells have been identified as key issues in clinical trials for cell replacement therapy and are important goals in order to achieve lasting recovery and repair of neural circuitry.[31] Here, the volume of GFP+ graft innervation was determined in animals grafted with cells in the absence or presence of Fmoc-SAPs. No statistical difference in the level of innervation was observed between groups (Fig. 6A). Similar to cell survival, cells in the presence of Fmoc-FRGDF demonstrated the least capacity for innervation of the host brain, with the smallest volume of innervation (Fig. 6A).

Additionally, we assessed the density of GFP+ graft fiber innervation at two pre-determined fields of view (FOV1 and FOV2) away from the edge of the graft core (Fig. 6B–D). No significant difference was observed between the four groups, suggesting that the amount of neurite growth was not impeded by the Fmoc-SAPs (Fig. 6B & C). Together, this data confirms that implanted cells are capable of extending neurites into the surrounding parenchyma, unhindered by the presence of Fmoc-SAPs, highlighting their capacity as a useful tool for the delivery of cells in cell transplantation therapy.

Implantation of Fmoc-SAPs into the intact mouse brain does not result in glial scarring. A key concern impeding neural plasticity following CNS injury is the formation of the glial scar. The glial scar is comprised of reactive astrocytes and microglia that help form a fibrotic scar to seal off the injury, but also secrete inhibitory proteins that prevent axon regeneration.[32–34] To further assess the biocompatibility of Fmoc-SAPs in the brain, the inflammatory microglial and astrocytic response to the materials was investigated.

Fmoc-DIKVAV and Fmoc-DYIGSRF showed no increase in host-derived (GFP-) astrocytes (glial fibrillary acidic protein; GFAP+) compared to cells transplanted alone (Fig. 7A). Additionally, Fmoc-DIKVAV showed no increase in microglia

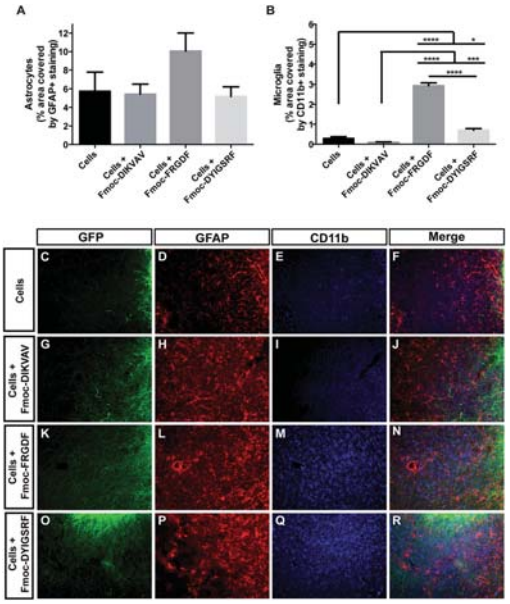

Fig. 7 Inflammatory response to cells transplanted alone and with Fmoc-SAPs measured as percentage of coverage of FOV at edge of graft (fluorescent optical density) (A) astrocytic response, (B) microglial response, (C–R) images of transplanted neural progenitor cells (GFP+; green), astrocytes (GFAP; red) and microglia (CD11b; blue). Data represents mean + SEM. *$P < 0.05$, *** and ****$P < 0.0001$.

(CD11b+) after 28 days (Fig. 7B). These results suggest that the host environment does not recognize these Fmoc-SAPs as "foreign material", with a limited immune response elicited over the course of 28 days (Fig. 7C–R). This is significant as these results emphasize the biocompatibility of these materials compared to other hydrogels, such as chitosan, that has been shown to be phagocytized by macrophages after 7 days *in vivo* due to the elicited foreign body response.[35]

After 28 days, Fmoc-FRGDF showed a trend towards enhanced astrocyte density compared to all other groups (Fig. 7A). In addition, Fmoc-FRGDF showed a statistically significant increase in microglia recruitment ($P < 0.05$) compared to cells alone and the laminin based Fmoc-SAP, Fmoc-DIKVAV ($P < 0.0001$) (Fig. 7B). Again, the control RGD sequence demonstrated the least biocompatibility for this application, however, as validated by the high GFP+ cell counts, the material itself is not cytotoxic (Fig. 5A). Rather, as previously suggested, the RGD signal is not suitable for presentation to cells in the CNS.

Previous studies have shown that Fmoc-peptides display neuroprotective properties where Fmoc-L-leucine protected both the mature and immature brain through the activation of PPARγ.[36] In addition, Fmoc-amino acids have been reported to have anti-inflammatory properties, inhibiting the recruitment of T-lymphocytes and neutrophils during an inflammatory response.[37] In line with these findings, here we demonstrated that after 28 days *in vivo* there was no glial scarring in the presence of any of the Fmoc-SAPs, indicating the inherent biocompatibility of these materials in the brain and their capacity to attenuate the inflammatory response. Importantly, this is the first study where Fmoc-SAPs have been used as a vehicle for the delivery and support of cell transplants *in vivo*. Their observed biocompatibility and lack of induced immune response promotes their suitability as a tool for cell transplantation in the brain.

Conclusion

Current research on Fmoc-SAPs has focused on understanding the material properties and underlying mechanisms of self-assembly of this system with their potential for biological applications being limited to small *in vitro* proliferation assays on cell lines. Here, we have demonstrated the utility of minimalist Fmoc-SAPs as biocompatible materials to support cell transplantation *in vivo*. We have developed three Fmoc-SAPs, containing varying ECM protein based peptides, for use as a delivery vehicle for neural progenitor cells for implantation into the intact mouse brain. The ability of the Fmoc-SAPs to maintain transplanted cell survival and the lack of induced immune response suggests their potential suitability for supporting residual host cells surrounding an injury site, as well as integration of newly transplanted cells. These results give us confidence that incorporating short amino acid sequences into Fmoc-SAPs allows the design of materials that can be easily and specifically tuned to a particular tissue and/or cellular requirement and demonstrates that Fmoc-SAPs could be used as a platform for the design of enhanced microenvironments to promote tissue repair.

Acknowledgements

The acknowledgements come at the end of an article after the We would like to thank Dr Navdeep Kaur and Joanne Lee (Centre for Advanced Microscopy, ANU) for their help and guidance in preparing negative stains for TEM imaging and Francesca Maclean and Shayanti Mukerhjee for thorough proof reading of the manuscript. This research was supported by funding from the National Health and Medical Research Council (NHMRC), Australia and the Australian Research Council. ALR was supported by an Australian Postgraduate Award; CLP was supported by an NHMRC Career Development Award, and subsequently Senior Medical Research Fellowship provided by the Viertel charitable Foundation, Australia; DRN was supported by an Australian Research Council Australian Postdoctoral Fellowship, and subsequently by a NHMRC Career Development Fellowship; and RJW is funded *via* an Alfred Deakin Research Fellowship. The Florey Institute of Neuroscience and Mental Health acknowledges the support from the Victorian Government's Operational Infrastructure Support Grant.

Notes and references

1 A. Bjorklund, *Novartis Found. Symp.*, 2000, **231**, 7–15; discussion 16–20.
2 C. L. Parish and L. H. Thompson, *J. Mol. Cell Biol.*, 2014, **6**, 54–63.
3 O. Lindvall and Z. Kokaia, *J. Clin. Invest.*, 2010, **120**, 29–40.
4 S. B. Dunnett and A. E. Rosser, *Neurobiol. Dis.*, 2014, **61**, 79–89.
5 O. Lindvall and Z. Kokaia, *Stroke*, 2011, **42**, 2369–2375.
6 J. T. S. Pettikiriarachchi, C. L. Parish, M. S. Shoichet, J. S. Forsythe and D. R. Nisbet, *Aust. J. Chem.*, 2010, **63**, 1143–1154.
7 D. R. Nisbet, J. A. Bourne and J. S. Forsythe, in *Biomaterials Developments and Applications*, ed. H. Bourg and A. Lisle, NOVA Publishers, 2010, pp. 453–463.
8 D. R. Nisbet, A. E. Rodda, M. K. Horne, J. S. Forsythe and D. I. Finkelstein, *Biomaterials*, 2009, **30**, 4573–4580.
9 T. Y. Wang, J. S. Forsythe, D. R. Nisbet and C. L. Parish, *Biomaterials*, 2012, **33**, 9188–9197.
10 R. Timpl and J. C. Brown, *BioEssays*, 1996, **18**, 123–132.
11 D. R. Nisbet and R. J. Williams, *Biointerphases*, 2012, **7**, 2.
12 A. L. Rodriguez, C. L. Parish, D. R. Nisbet and R. J. Williams, *Soft Matter*, 2013, **9**, 3915–3919.
13 V. M. Tysseling-Mattiace, V. Sahni, K. L. Niece, D. Birch, C. Czeisler, M. G. Fehlings, S. I. Stupp and J. A. Kessler, *J. Neurosci.*, 2008, **28**, 3814.
14 T. C. Holmes, S. de Lacalle, X. Su, G. Liu, A. Rich and S. Zhang, *Proc. Natl. Acad. Sci. U. S. A.*, 2000, **97**, 6728–6733.
15 R. Orbach, L. Adler-Abramovich, S. Zigerson, I. Mironi-Harpaz, D. Seliktar and E. Gazit, *Biomacromolecules*, 2009, **10**, 2646–2651.
16 R. Williams, A. Smith, R. Collins, N. Hodson, A. Das and R. Ulijn, *Nat. Nanotechnol.*, 2008, **4**, 19–24.
17 A. Smith, R. Williams, C. Tang, P. Coppo, R. Collins, M. Turner, A. Saiani and R. Ulijn, *Adv. Mater.*, 2008, **20**, 37–41.
18 H. Xu, A. K. Das, M. Horie, M. S. Shaik, A. M. Smith, Y. Luo, X. Lu, R. Collins, S. Y. Liem, A. Song, P. L. A. Popelier, M. L. Turner, P. Xiao, I. A. Kinloch and R. V. Ulijn, *Nanoscale*, 2010, **2**, 960–966.
19 C. Tang, A. Smith, R. Collins, R. Ulijn and A. Saiani, *Langmuir*, 2009, **25**, 9447–9453.
20 M. Zhou, A. Smith, A. Das, N. Hodson, R. Collins, R. V. Ulijn and J. Gough, *Biomaterials*, 2009, **30**, 2523–2530.
21 G. Cheng, V. Castelletto, R. R. Jones, C. J. Connon and I. W. Hamley, *Soft Matter*, 2011, **7**, 132601333.
22 V. Jayawarna, S. M. Richardson, A. R. Hirst, N. W. Hodson, A. Saiani, J. E. Gough and R. V. Ulijn, *Acta Biomater.*, 2009, **5**, 934–943.
23 D. J. Adams, L. M. Mullen, M. Berta, L. Chen and W. J. Frith, *Soft Matter*, 2010, **6**, 1971–1980.
24 V. N. Modepalli, A. L. Rodriguez, R. Li, S. Pavuluri, K. R. Nicholas, C. J. Barrow, D. R. Nisbet and R. J. Williams, *Pept. Sci.*, 2014, **102**, 197–205.
25 L. F. Reichardt and K. J. Tomaselli, *Annu. Rev. Neurosci.*, 1991, **14**, 531.
26 C. R. Bye, L. H. Thompson and C. L. Parish, *Exp. Neurol.*, 2012, **236**, 58–68.
27 S. M. Kelly, T. J. Jess and N. C. Price, *Biochim. Biophys. Acta, Proteins Proteomics*, 2005, **1751**, 119–139.
28 A. R. Hirst, S. Roy, M. Arora, A. K. Das, N. Hodson, P. Murray, S. Marshall, N. Javid, J. Sefcik and J. Boekhoven, *Nat. Chem.*, 2010, **2**, 1089–1094.
29 V. Tysseling, V. Sahni, E. Pashuck, D. Birch, A. Hebert, C. Czeisler, S. Stupp and J. Kessler, *J. Neurosci. Res.*, 2010, **88**, 3161–3170.
30 D. M. Ryan and B. L. Nilsson, *Polym. Chem.*, 2012, **3**, 18–33.
31 C. Winkler, D. Kirik and A. Björklund, *Trends Neurosci.*, 2005, **28**, 86–92.
32 A. Rolls, R. Shechter and M. Schwartz, *Nat. Rev. Neurosci.*, 2009, **10**, 235–241.
33 C. L. Lau, M. Kovacevic, T. S. Tingleff, J. S. Forsythe, H. S. Cate, D. Merlo, C. Cederfur, F. L. Maclean, C. L. Parish and M. K. Horne, *J. Neurochem.*, 2014, **130**, 215–226.
34 J. E. Burda and M. V. Sofroniew, *Neuron*, 2014, **81**, 229–248.
35 K. Crompton, D. Tomas, D. Finkelstein, M. Marr, J. Forsythe and M. Horne, *J. Mater. Sci.: Mater. Med.*, 2006, **17**, 633–639.
36 P. Maurois, S. Rocchi, N. Pages, P. Bac, J. P. Staples, P. Gressens and J. Vamecq, *Biomed. Pharmacother.*, 2008, **62**, 259–263.
37 R. M. Burch, M. Weitzberg, N. Blok, R. Muhlhauser, D. Martin, S. G. Farmer, J. M. Bator, J. R. Connor, C. Ko, W. Kuhn, B. A. McMillan, M. Raynore, B. G. Shearer, C. Tiffany and D. E. Wilkins, *Proc. Natl. Acad. Sci. U. S. A.*, 1991, **88**, 355–359.

Appendix C: Full Published Work (section 5.3)

Rui Li, Sivapriya Pavuluri, Kiara Bruggeman, Benjamin M. Long, Andrew J. Parnell, Anne Martel, Steven R. Parnell, Frederick M. Pfeffer, Andrew J.C. Dennison, Kevin R. Nicholas, Colin J. Barrow, David R. Nisbet, Richard J. Williams, "Coassembled nanostructured bioscaffold reduces the expression of proinflammatory cytokines to induce apoptosis in epithelial cancer cells", *Nanomedicine: Nanotechnology, Biology and Medicine*, 2016, vol. 12, pp. 1397-1407 – Reproduced with permission from Elsevier

BASIC SCIENCE

Nanomedicine: Nanotechnology, Biology, and Medicine
12 (2016) 1397–1407

Original Article

nanomedjournal.com

Coassembled nanostructured bioscaffold reduces the expression of proinflammatory cytokines to induce apoptosis in epithelial cancer cells

Rui Li, BSc[a,f], Sivapriya Pavuluri, PhD[a,g], Kiara Bruggeman, BSc[b], Benjamin M. Long, PhD[a], Andrew J. Parnell, PhD[c], Anne Martel, PhD[d], Steven R. Parnell, PhD[e], Frederick M. Pfeffer, PhD[a], Andrew J.C. Dennison, PhD[d,i], Kevin R. Nicholas, PhD[a,g], Colin J. Barrow, PhD[a], David R. Nisbet, PhD[b,1], Richard J. Williams, PhD[a,h,*,1]

[a]*Centre for Chemistry and Biotechnology, Deakin University, Waurn Ponds, Australia*
[b]*Research School of Engineering, The Australian National University, Canberra, Australia*
[c]*Department of Physics and Astronomy, University of Sheffield, United Kingdom*
[d]*Institut Laue Langevin, Grenoble, France*
[e]*Low Energy Neutron Source (LENS), Indiana University, Bloomington, IN, USA*
[f]*Coconut Research Institute of Chinese Academy of Tropical Agricultural Sciences, Wenchang, Hainan, China*
[g]*School of Medicine, Deakin University, Waurn Ponds, VIC, Australia*
[h]*School of Aerospace, Mechanical and Manufacturing Engineering and the Health Innovations Research Institute, RMIT University, Melbourne, Australia*
[i]*TU Berlin, Institut für Chemie, Berlin, Germany*

Received 29 September 2015; accepted 21 January 2016

Abstract

The local inflammatory environment of the cell promotes the growth of epithelial cancers. Therefore, controlling inflammation locally using a material in a sustained, non-steroidal fashion can effectively kill malignant cells without significant damage to surrounding healthy cells. A promising class of materials for such applications is the nanostructured scaffolds formed by epitope presenting minimalist self-assembled peptides; these are bioactive on a cellular length scale, while presenting as an easily handled hydrogel. Here, we show that the assembly process can distribute an anti-inflammatory polysaccharide, fucoidan, localized to the nanofibers within the scaffold to create a biomaterial for cancer therapy. We show that it supports healthy cells, while inducing apoptosis in cancerous epithelial cells, as demonstrated by the significant down-regulation of gene and protein expression pathways associated with epithelial cancer progression. Our findings highlight an innovative material approach with potential applications in local epithelial cancer immunotherapy and drug delivery.

Key words: Bionanotechnology; Self-assembly; Cancer; Supramolecular materials; Hydrogels; Tissue engineering

The use of designed, nanostructured materials for the treatment of cancers is a rapidly growing research area[1] as they can potentially mimic the tumor microenvironment.[2] A promising approach involves materials that can mediate the local tumor environment through attenuation of the inflammatory response,[3] while simultaneously providing a stable healthy extracellular matrix (ECM) mimic to promote regeneration.[4] The link between the inflammatory response and the promotion of cancers is well established; notably in endothelial cancers such as oral, pancreatic and colon.[5] Epidemiological studies have shown that chronic inflammation is a significant causative factor for these cancers; several studies showed promising anti-tumorigenic effects using non-steroidal anti-inflammatory drugs.[6] Hence, a therapeutic opportunity lies in developing a biocompatible material that can

This work was funded by an Australian Research Council (ARC) Discovery Project (DP130103131). N.M.R. instrumentation was provided through ARC funding (LE110100141). D.R.N. was supported by an NHMRC Career Development Fellowship (APP1050684). R.J.W. was supported via an Alfred Deakin Research Fellowship. Access to the facilities of the Centre for Advanced Microscopy (CAM) with funding through the Australian Microscopy and Microanalysis Research Facility (AMMRF) is gratefully acknowledged. A.J.C.D. was supported by the Swedish Research Council VR. Preliminary SANS measurements were performed at the Low Energy Neutron Source, Indiana. Access to the D33 instrument was provided by the Institut Laue-Langevin user access programme (8-03-826).

* Corresponding author at: School of Aerospace, Mechanical and Manufacturing Engineering and the Health Innovations Research Institute, RMIT University, Melbourne, Australia.
E-mail address: Richard.Williams@RMIT.edu.au (R.J. Williams).
[1] D.R.N. and R.J.W. contributed equally to this work.

http://dx.doi.org/10.1016/j.nano.2016.01.009
1549-9634/

Please cite this article as: Li R, et al, Coassembled nanostructured bioscaffold reduces the expression of proinflammatory cytokines to induce apoptosis in epithelial cancer cells. *Nanomedicine: NBM* 2016;12:1397-1407, http://dx.doi.org/10.1016/j.nano.2016.01.009

achieve a spatially confined, sustained, non-steroidal and selective suppression of the immune system.[7] A range of cancer therapies could benefit from this approach; such a material could provide an anti-tumoral void-filling support for the surrounding healthy tissue following surgical excision, or, alternatively, a topical treatment for the surface of a lesion.[8] Numerous examples exist of complex hierarchical ECM assemblies, formed by the self-organization of a range of cellularly secreted small molecules, that provide structure and function in living systems.[9] In particular, polysaccharides and fibrous proteins assemble to form networks that support multicellular systems and mediate cellular interactions with their surrounding microenvironment.[10] A family of sulfonated polysaccharides known as fucoidans have gathered increasing attention for their inherent biocompatibility and anti-inflammatory properties both *in vitro* and *in vivo*.[11] Importantly, several studies have also indicated the anti-mitogenic effects of fucoidans as they block cell cycle progression,[12] induce apoptosis and reduce tumorigenicity in several cancer cell lines.[13] However, the use of these biopolymers as a therapeutic is constrained by the high solubility of the polysaccharide chains, limiting their sustained functionality unless encapsulated in an external carrier[14] or presented on a two-dimensional (2D) surface.[15] The motivation for this work, therefore, was to present constrained fucoidan on the surface of a three dimensional (3D) ECM-like scaffold.

Hydrogels formed by bioinspired synthetic organic molecules known as self-assembling peptides (SAP) are highly suitable materials for cancer therapy,[16] as they have been shown to form nanofibrillar matrices of similar morphology[17] which are functional both *in vitro*[18] and *in vivo*[19] through the inclusion of bioactive and biocompatible peptide sequences in the SAP during synthesis.[20] The formation of SAP hydrogels is a thermodynamically driven process[21]; control over the organization of the structures formed is achieved through careful exploitation of assembly conditions, such as manipulation of the molecule's specific pKa,[22] biocatalysis[21] or the rate of assembly.[23] Such facile control over the final structures means that they are excellent candidates for use as tailored multicomponent adjuvant scaffolds. Key to such applications, SAPs have been shown to have multicomponent functionality, as the noncovalent forces that govern their assembly can be used to physically incorporate larger molecules such as proteins[24] or drugs[25] making them an ideal candidate material for the immobilization and functional presentation of the otherwise highly soluble fucoidan polysaccharides as part of a self-assembled matrix.

Methods

See Supplementary Information for full synthetic and analytical procedures.

Co-assembled hydrogel formation

Fmoc-FRGDF (10.0 mg) along with mixtures of 2 mg fucoidan (Marinova Pty Ltd, Cambridge, Tasmanian, Australia) was added to separate 4 mL glass vials. Milli-Q water (400 μL; purified by Milli-Q Advantage A10 System, Merck Millipore, Australia) was added into each vial, then pH increased by the addition of a minimal volume of 0.5 M NaOH while vortexing and then neutralized to pH 7.4 via dropwise addition of 0.1 M HCl (Asia Pacific Specialty Chemicals Ltd., Australia). Finally, 100 mM PBS (pH 7.4) was added into the solution to bring the total volume up to 1.0 mL, and used 48 h later.

NMR studies

Fmoc-FRGDF of 2.5 mg was added to a glass vial and dissolved in 0.5 mL of D_2O. The pH was increased using freshly prepared 0.5 M NaOD (NaOH in D_2O) and vortexed until a transparent solution was obtained. The resulting solution was transferred to a 5 mm NMR tube. ^1H, COSY, HMBC and HSQC spectra were collected on a Bruker AVANCE III 500 MHz FT-NMR spectrometer. ^{13}C resonances were elucidated using both heteronuclear multiple-bond correlation spectroscopy (HMBC) and heteronuclear single-quantum correlation spectroscopy (HSQC).

Small-angle neutron scattering (SANS)

SANS measurements were performed on the D33 instrument at the Institut Laue-Langevin, Grenoble, France[26] in fixed wavelength mode using a wavelength of 6 Å and a wavelength resolution of $\Delta\lambda = 10\%$ at detector distances of 2 m and 12 m to cover the Q-range 0.001-0.5 $Å^{-1}$. Data collected for the two detector distances were joined using the $GRAS_{ans}P$ package, reduced using the NIST SANS reduction macros[27] and the resultant SANS curves fit using the SASview package. A flexible cylinder model was used to fit the data. The data for Fmoc-FRGDF were fit using constraints on the scattering lengths of the buffer and peptide. Kratky analysis was performed using the NIST SANS analysis macros.[27] Contrast matching to fucoidan was performed by measuring SANS from a series of 10 mg/mL fucoidan solutions in H_2O/D_2O mixtures. SANS from the chosen concentration of 21.5% confirmed that there was no detectable scattering from the fucoidan solution. Peptide samples were measured in sealed 1 mm path-length Hellma cells.

Cell lines and culture conditions

The human tongue squamous cell carcinoma cell line (SCC25) cultures were obtained verified from ATCC and were maintained in DMEM-F12 complete medium containing 10% fetal bovine serum and 400 ng/mL hydrocortisone and penicillin/streptomycin. The human mammary fibroblast cell line (hMFC) cultures were maintained as described previously.[18a] Cell line cultures were maintained at 37 °C with 5% CO_2.

Reverse transcription and quantitative PCR

Total RNA was reverse-transcribed to generate complimentary DNA using Superscript III (Invitrogen) following the manufacturer's protocol. To challenge fucoidan, cells were stimulated with LPS (Sigma) at a concentration of 10 μg/mL in the complete media. Differential expression of the genes examined was listed in Supplementary Table 1. cDNA of 30 ng was used to perform quantitative real time PCR in a 20 μL reaction using SYBR Green (Biorad) on a CFX connect™ Real Time PCR detection system (Biorad). Primer oligosequences were designed using Primer3 PCR prime design tool (Whitehead Institute for Biomedical Research, Cambridge, MA, USA) and the gene specificity was checked using National Center for Biotechnology Information nucleotide database. Steps followed during QPCR to generate

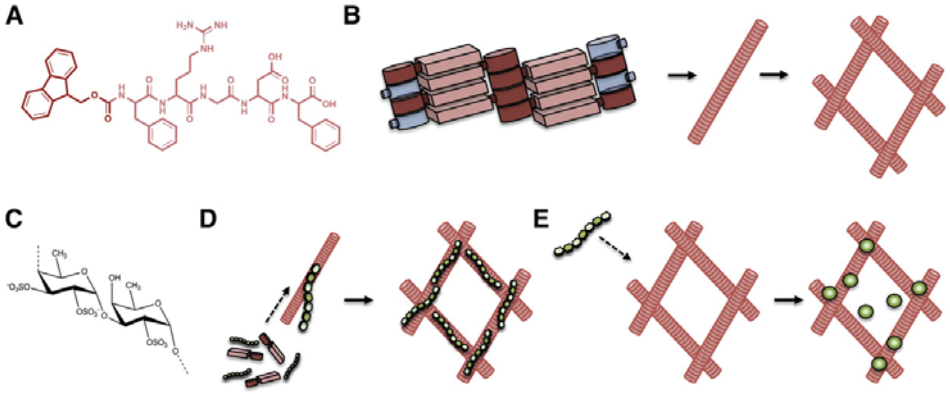

Figure 1. Cartoon of the coassembly mechanism (**A**) structure of Fmoc-FRGDF, (**B**) cartoon schematic showing the π stacking of Fmoc and the antiparallel interactions of the peptide which drive its assembly to fibrils that intertwine to form a scaffold, (**C**) structure of a fucoidan subunit, (**D**) co-assembly results in an interaction of fucoidan with fibrils, resulting in the presentation of the molecule over the surface of the scaffold. (**E**) The addition of fucoidan post-assembly however does not produce a surface decorated structure, instead it results in the formation of separate disordered fucoidan aggregates.

amplification curves include an initial denaturing step for 3 min at 95 °C, followed by 40 cycles of 95 °C for 10 s, 60 °C for 30 s and 72 °C for 30 s. The expression of each gene in terms of fold change was normalized to the housekeeping gene ACTB.

NFκB and CEP55 staining

SCC25 cells were treated without and with fucoidan (2 mg/mL) for 48 h. Cells were fixed with paraformaldehyde and permeabilized with 0.1% triton-X-100. Cells were blocked with 1% bovine serum albumin (BSA) in PBS for 1 h at room temperature and further treated with primary antibody (Rabbit polyclonal NFκB p65 antibody and Rabbit monoclonal CEP55 antibody, Abcam) overnight at 4 °C. Cells were further incubated with anti-rabbit Alexa Fluor 488 secondary conjugates for 1 h at room temperature. Following several washes cells were visualized under fluorescence microscope (Nikon).

Annexin V staining

SCC25 cells treated without and with fucoidan (2 mg/mL) for 48 h were stained with the Alexa Fluor® 488 annexin V/Dead Cell Apoptosis Kit (Life Technologies). Cells were also counter-stained with Hoechst dye to stain the live cells. Images were obtained through fluorescence microscopy (Nikon Eclipse Ti-S).

Results

The formation of two-component hydrogels and evaluation of (i) their biocompatibility and (ii) their effect on cancer cells

In order to form the scaffold to present fucoidan, we used a biocompatible minimalist pentapeptide sequence known to assemble via a π-β self-assembly mechanism, fluorenylmethoxycarbonyl (Fmoc) FRGDF (Figure 1).[17,18] Fmoc-FRGDF was synthesized using a standard solid phase Fmoc peptide synthesis methodology to yield a white crystalline powder (see electronic Supplementary Information). Fucoidan was supplied in a readily solubilized powder of similar consistency. We mixed both powders together and initiated self-assembly using a well-established pH switch methodology.[18a,22] The solution was then made up to a final concentration of 10 mg/mL Fmoc-FRGDF and 2 mg/mL fucoidan with Dulbeccos' modified Eagle medium (DMEM), and the hydrogel was allowed to form. When this was compared to a pure Fmoc-FRGDF hydrogel, both formed optically clear, stable hydrogels (Supplementary Figure 1, *A*).

Biocompatability of the systems was measured with 3D cell cultures of human mammary fibroblast cells as a control for healthy tissue, and the moderately differentiated oral tongue squamous cell carcinoma line SCC25.[28] Cell viability of hMFC on the hydrogels of Fmoc-FRGDF (0RGD) and hydrogels co-assembled with 2 mg/mL of fucoidan (2RGD) was determined using an MTS assay up to 72 h with no significant difference, whereas SCC25 cells showed a reduction in the number of viable cells (Figure 2, *A*). A live/dead cell assay performed at 48 h (to observe cell death mid-cycle) showed significant numbers of dead SCC25 cells, evenly distributed throughout the material (Figure 2, *B*). To observe which cells were apoptotic, SCC25 cells were cultured for 48 h prior to staining with Annexin V, propidium iodide and Hoechst stain to observe cell death mid-cycle (Figure 2, *C* and *D*).

Analysis of the two component self-assembly

Four samples were prepared: (1) *Fmoc-FRGDF*: a hydrogel formed by the pH triggered assembly at a concentration of 10 mg/mL; (2) *Co-Assembly*: whereby 10 mg/mL Fmoc-FRGDF and 2 mg/mL fucoidan were mixed in powdered form prior to application of a pH switch; (3) *Post-Assembly*: a preformed Fmoc-FRGDF hydrogel with a solution of fucoidan added 12 h post-assembly by mixing to the same final concentration as sample 2; and (4) *Fucoidan*: 2 mg/mL solution of fucoidan. As expected, samples 1-3 formed self-supporting hydrogels, whereas sample 4 remained a solution.

We visualized the structures formed in each sample with transmission electron microscopy (TEM) to determine the

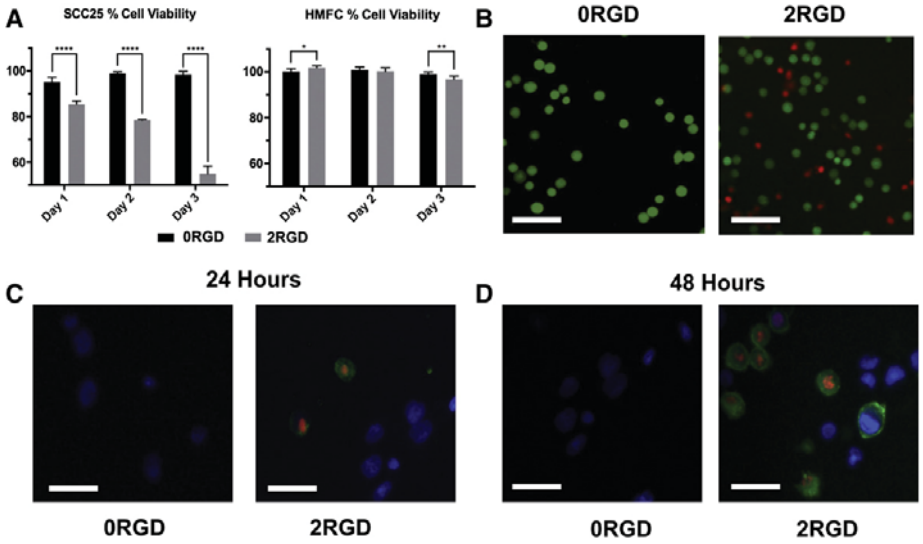

Figure 2. Biocompatability and the effect of the material on Cancer (SCC25) and healthy (hMFC) cell fate. (**A**) The relative viabilities of the cells on each scaffold over three days. SCC25 cells were seeded on the Fmoc-FRGDF hydrogel (0RGD) and 2 mg/mL fucoidan (2RGD) and incubated for 3 days. Calcein AM staining was performed to identify live cells (green) and propidium iodide was used to identify dead cells (red). Scale bars 125 μm. A minimum of 5 fields were captured for each treatment and number of live cells and dead cells were counted individually and percentage was calculated $*P = 0.05$, $**P = 0.01$, $***P = 0.001$, $****P = 0.0001$ ($n = 3$). (**B**) The distribution of SCC25 cells on day 3 on each hydrogel. (**C** and **D**) Apoptosis at 24 and 48 h. In order to determine the mode of cell death in the SCC25 cells, we stained the cells using Annexin V (green), propidium iodide (red) and Hoechst dye (blue). Live cells are identified by a nucleus stained only with Hoechst dye and appear only blue. Early apoptotic cells were stained green with nucleus blue and the late apoptotic cells stained in green with a red nucleus. Scale bars 50 μm.

underlying nanostructures and atomic force microscopy (AFM) to evaluate the microstructure of the system (Figure 3). Fourier transform infra-red spectroscopy (FTIR) was used to confirm that the peptide-like organization was not disrupted. This confirmed that the addition of fucoidan during the assembly process did not affect the molecular packing of the peptides into the anti-parallel β-sheets which drive these assemblies and result in peaks at ~1630 cm^{-1} and ~1690 cm^{-1} (Figure 3, *I*).[29] We then analyzed the chiral organization of the structures within the samples using circular dichroism (CD).[22,24a,30] Characteristic and retained transitions were observed in the region between 230 and 280 nm. The mechanical properties of the hydrogel samples were then compared by oscillatory rheometry (Figure 4, *G* and *H*). Typically, two-component hydrogels where one component does not otherwise self-assemble tend to yield an alternate molecular packing, resulting in a stiffer hydrogel.[31] Here though, the characteristic frequency sweeps of this class of system were retained, and each forms a hydrogel of comparable stiffness, indicating that the inclusion of fucoidan (at this concentration) does not interfere with the processes that determine the final stiffness of the resultant hydrogels.[24a,32]

Interaction of fucoidan and the SAP fibrils

To determine at the availability of the peptide sequence on the surface of the fibrils, we used ^{1}H NMR spectroscopic analysis. After the addition of NaOH to solubilize the peptide (pH = 10), ^{1}H NMR provided a clean spectrum with narrow line widths. However, upon gelation, the resonances associated with the Fmoc-group and the fifth phenylalanine residue (F_5) significantly broadened and were not visible. However, the dynamic motion of the RGDF–OH portion of the peptide is conserved in the fibrils, and resulted in narrow line widths for this portion of the peptide (Figure 3, *K*). SANS measurements of fully hydrated samples of Fmoc-FRGDF and the co-assembled systems were performed to investigate the nanostructures *in-situ* and to determine what effect the addition of fucoidan had on fibril radius. As SANS cannot distinguish features larger than approximately 17 nm under these conditions, the measurement was found to be insensitive to average fibril length. As SANS is sensitive to all structural features with sufficient contrast, we performed control measurements of 2 mg/mL fucoidan alone, which in 21.5% D_2O, was found to provide conditions for negligible scattering from fucoidan. In the samples presented here we used these conditions to observe only the scattering from the fibrils as the contributions from fucoidan could complicate the analysis. This approach enabled the differences in the scattering between Fmoc-FRGDF and the co-assembled system to be observed (Figure 3, *L*). Analysis of the scattering data was performed using both a model-independent approach and a flexible cylinder model in the SASview package (Supplementary Information). The model-independent approach found that fibril radius for the 0RGD sample was 48.8 ± 0.9 Å

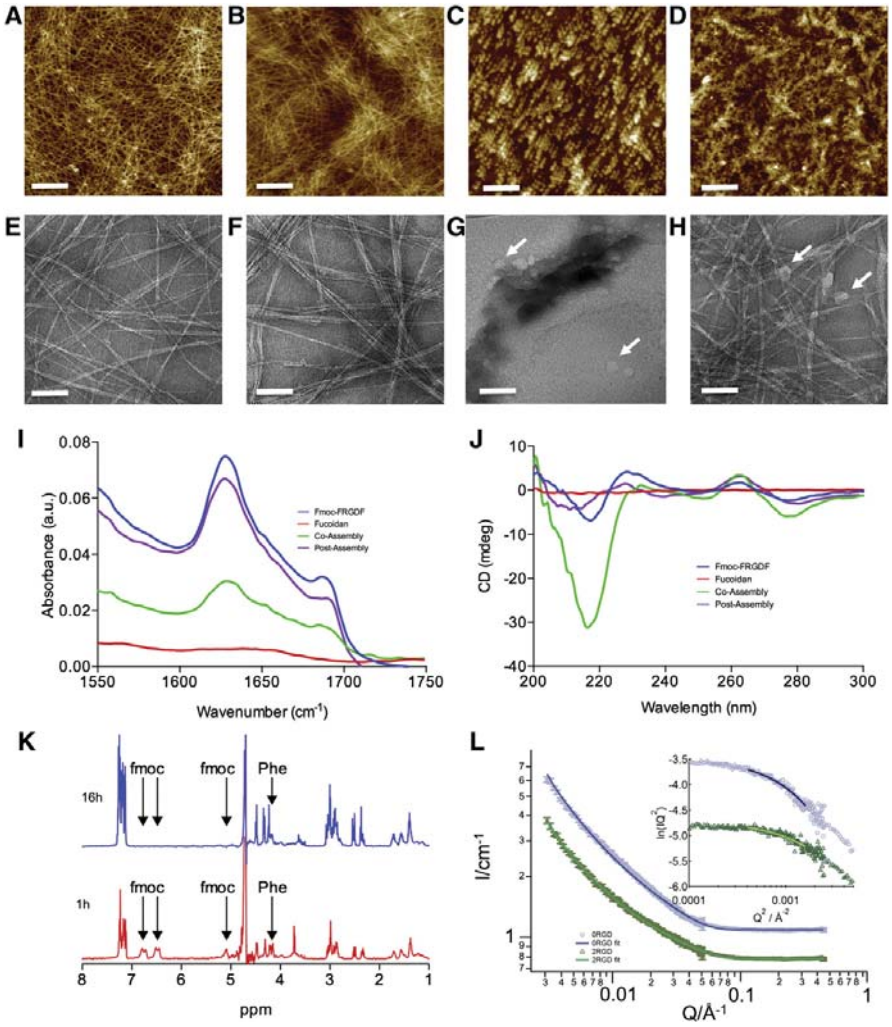

Figure 3. The underpinning structure and organization of the scaffold. AFM microscopy shows the structures formed by (**A**) Fmoc-FRGDF, (**B**) co-assembled with 2 mg/mL fucoidan, (**C**) a solution of fucoidan (**D**) post-addition fucoidan (scale bar represents 1 μm). (**E**-**F**) equivalent via negatively stained TEM. (**G**) Aggregates of fucoidan, which are similar to structures visible in post-addition (**H**), but not co-assembly (**F**) (scale bar represents 75 nm). (**I**) FTIR shows conserved antiparallel β-sheet formation. Fucoidan solution shows no overall structure. (**J**) CD shows increased supramolecular ordering of Fmoc-FRGDF when co-assembled. The transitions characteristic to this class of assembly are maintained across all the SAP containing samples, indicating the same chiral structure dominates. Co-assembly increases the magnitude of the transitions indicating an increase in supramolecular ordering whereas post-assembly disrupts structure. The solution of fucoidan has no overriding chiral signal. (**K**) NMR analysis shows that upon assembly Fmoc is completely removed from solution and the N-terminal (i.e., closets to Fmoc) Phe is partially removed from the solution as the assembly forms, indicating that the RGDF portion is still in solution, and presented on the surface of the assemblies. (**L**) Analysis of SANS using both a flexible cylinder model and model-independent Kratky analysis (inset) of the data show a reduction in the fibril radius when co-assembled with fucoidan. Plots are offset for clarity.

with this value reducing to 35.6 ± 1.1 Å for 2RGD. Similar values were found using model fitting with the initial fibril radius of 43.3 ± 0.1 Å, reducing to 33.7 ± 0.1 Å when the peptide was co-assembled with fucoidan. These values are consistent with the diameter of the previously reported subunit of these assemblies.[29] The model fitting approach also indicated that there was a densification of the fibril after co-assembly with the scattering length density of the fibrils increasing by 9.6%.

We adapted a previously described method of gold nanoparticle (GNP) synthesis,[33] creating GNP labeled fucoidan

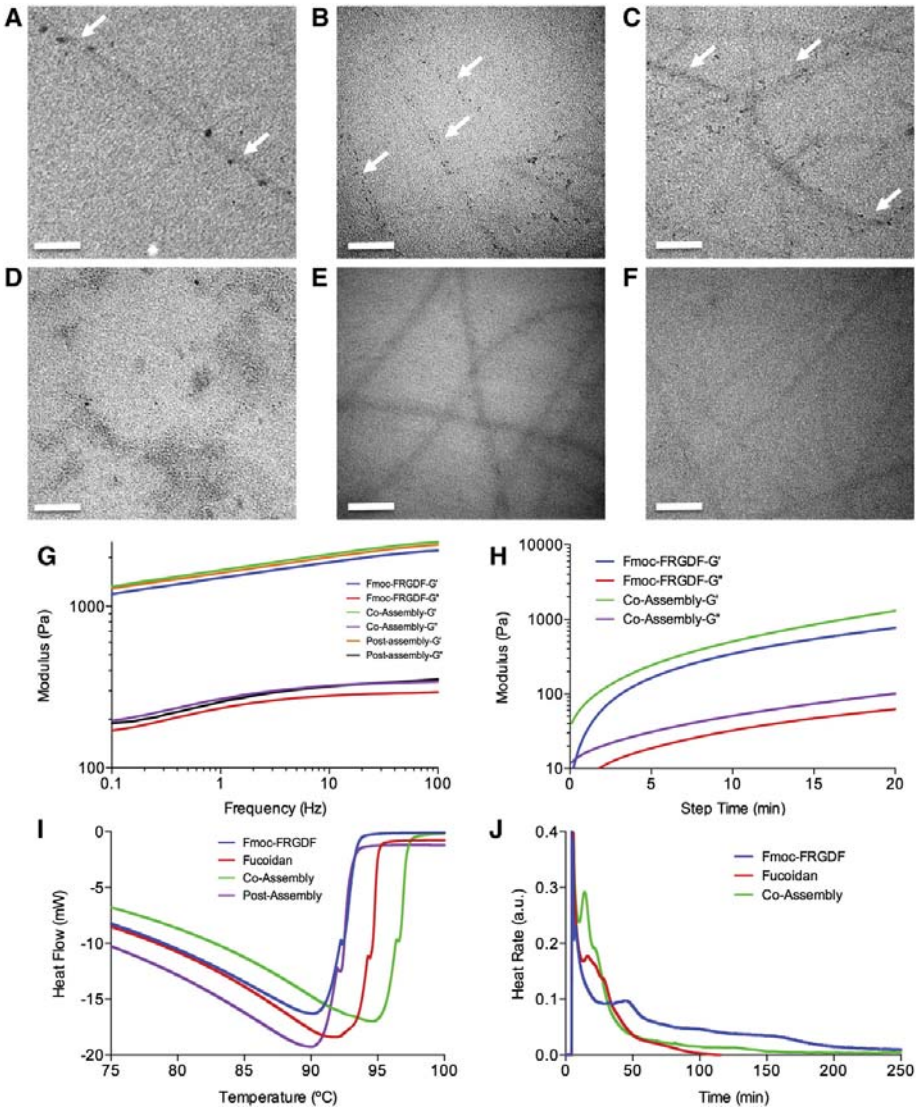

Figure 4. Location of fucoidan in relation to the fibrils and the effects on the final hydrogel: GNP labeled fucoidan shows co-localization along peptide fibrils (**A**) pre- and (**B** and **C**) post-washing of the hydrogel indicating strong associations between fucoidan and peptide fibrils. (**D**) GNP labeled fucoidan in solution. (**E**) Hydrogel co-assembled with unlabeled fucoidan and independent GNP shows no residual GNP post-washing. (**F**) Hydrogel co-assembled only with independent GNP shows no residual GNP post-washing (scale bar represents 100 nm). (**G**) rheological characteristics of hydrogels. (**H**) Rate of the formation of hydrogel is increased in co-assembly. (**I**) ITC shows increased rate of assembly with co-assembled samples (return of heat rate to 0). (**J**) DSC shows increased melting temperature of co-assembled system.

which can be readily visualized with TEM (Figure 4, *D*). Figure 4, *A-C* show TEM micrographs of the nanofibrils in close association with the GNP labeled fucoidan. Two control hydrogels were prepared to control against possible associations between independent gold nanoparticles and either fucoidan or the peptide fibrils. One control hydrogel contained a mixture of unlabeled fucoidan and the independent GNP (Figure 4, *E*), and the other containing only the independent GNP (Figure 4, *F*). All hydrogels were thoroughly washed with deionized water to remove any unbound nanoparticles from the hydrogel

Parallel plate rheometry was used to compare the rate of hydrogel formation.[34] When the materials were analyzed after 48 h, the final modulus were comparable across a range of frequencies and showed that the final mechanical properties of the scaffolds were similar (Figure 4, *G*). A fixed frequency time analysis showed that the co-assembled sample formed the hydrogel more rapidly with an order of magnitude increasing in stiffness at a specific time (Figure 4, *H*). Normalized isothermal titration calorimetry (ITC) thermograms (Figure 4, *I*) was used to monitor the time taken for the Fmoc-FRGDF network formation (i.e., where the heat rate returns to zero), and the co-assembled sample showed a rate enhancement of *ca.* 40% in the latter. Differential scanning caloriometry (DSC) analyses showed that co-assembly increased T_{gel} from 90.1 °C. to 94.6 °C, while the post-assembly addition did not show a similar increase in T_{gel} (Figure 4, *J*).

Biological mechanism of the fucoidan/peptide material

Immunostaining was performed on the cells cultured at 48 h to capture the process mid-cycle. SCC25 cells cultured on 0RGD were further counterstained with Hoechst dye to reveal NFκβ p65 co-localized with the nuclear stain. When the same experiment was performed upon the 2RGD hydrogel, however, no significant staining of NFκβ was observed.

To confirm that the material was effective at a gene expression level, we interrogated the mRNA regulation of genes in the NFκβ pro-inflammatory pathway using quantitative PCR [49] (see Supplementary Information for primer sequences). RNA was extracted from the cells under both conditions and quantified for the gene expression studies. We included the pro-inflammatory cytokines interleukin (IL) 1A, IL1B, IL6, IL8, and tissue necrotic factor (TNF), all transcribed as a key part of the NFκβ pro-inflammatory pathway and were therefore monitored as crucial regulators of tumorigenesis (Figure 5, *C*). The time point for studying gene expression was 48 h. At this time point, most of the SCC25 cells remained viable (~70%). In each case, there was significant downregulation in the expression of each pro-inflammatory gene on 2RGD when compared to the control. In order to confirm that the downregulation of the anti-inflammatory cytokines was not related to apoptosis, the housekeeping gene ACTB was monitored and showed the same level of expression in both situations. Then, to test the extent of this effect, we then challenged the cells with LPS, as this challenge has been shown to increase expression even if the cells were apoptotic. In each gene analyzed, the expression in the 0RGD system showed a significant increase, whereas the 2RGD was observed to be similar to the unchallenged sample.

Discussion

The formation of stable, functional biomaterials that can present biologically active sequences and molecules will play a significant role in a range of medical applications. Self-assembly has been shown to give rise to materials that are both biocompatible and functional, but have not yet fully realized their potential. The use of simple interactions between these structures and additional functional molecules offers several advantages. The spontaneous formation of multicomponent scaffolds with defined chemical properties allows materials to be formed in physiological conditions, conferring inherent biocompatibility.

To ensure that the material was biocompatible and non-toxic toward normal cell phenotypes, primary human mammary fibroblast cells (hMFCs) were also cultured on the SAP hydrogels (Figure 2, *A*). We chose these cell lines as fibroblasts and endothelial cancer cells have a close association in the tumor microenvironment,[35] and drugs that are solely cytotoxic also kill fibroblasts along with the target cells, a process which actually induces local tumorigenesis through the release of pro-cancerous factors.[5,36] In addition, the correct presentation of RGD is a requirement for the culture of both cell types, as the SCC25 oral cancer cells show over-expression of α5β1 integrin receptor.[37] The hMFC cells showed maintained equally high viability on both 0RGD and 2RGD, indicating that the inclusion of fucoidan did not negatively impact the cytotoxicity of the SAP matrix. However, the SCC25 cells showed significant numbers of dead cells in comparison. To verify that this mechanism was controlled apoptosis rather than necrosis, Annexin V staining was performed. While no cells in the 0RGD hydrogel were apoptotic, the results revealed that the majority of cells cultured on the 2RGD hydrogels were in a late apoptotic phase, with only a few cells found to be in the early apoptotic phase. Confident that the fucoidan within the material contributed toward the reduction of the number of cancer cells through the induction of controlled apoptosis, we set out to discover the mechanism by which it was distributed within the hydrogel. Ideally the material would retain the functional nanostructures formed by the Fmoc-SAP alone; however, the supramolecular ordering of self-assembled structures has been shown to be significantly altered in the presence of biological macromolecules such as proteins found in serum[24b] and the cytosol,[38] or when two or more complementary molecules are co-assembled.[31]

Using TEM and AFM analyses, we observed that the Fmoc-FRGDF formed a series of well-ordered bundles of striated nanofibrils underpinning a fibrous matrix (Figure 3, *A* and *E*), which were very similar to those in the co-assembled sample, though a more pronounced bundling of fibrils was observed (Figure 3, *B* and *F*). When the solution of fucoidan was examined, the analysis revealed the formation of a number of spherical structures with a diameter of ~20 nm (Figure 3, *C* and *G*). Finally, for the post-assembled hydrogel, a mixture of structures was observed, where spherical structures similar to those observed in the fucoidan solution (sample 4) were distributed at high density over the fibrillar network at both the nano- and microscales (Figure 3, *D* and *H*).

To determine if the molecular packing of the Fmoc-SAP within the fibrils was affected by the fucoidan, a series of spectroscopic analyses were performed, as co-assemblies in general have been demonstrated to promote inconsistent alternative organizational structures.[24b,38] The use of FTIR confirmed that the addition of fucoidan during the assembly process did not affect the molecular packing of the peptides into the desired anti-parallel β-sheets that drive these assemblies. Furthermore, the transitions observed via CD, shown to represent bundling between the fibrils driven by supramolecular

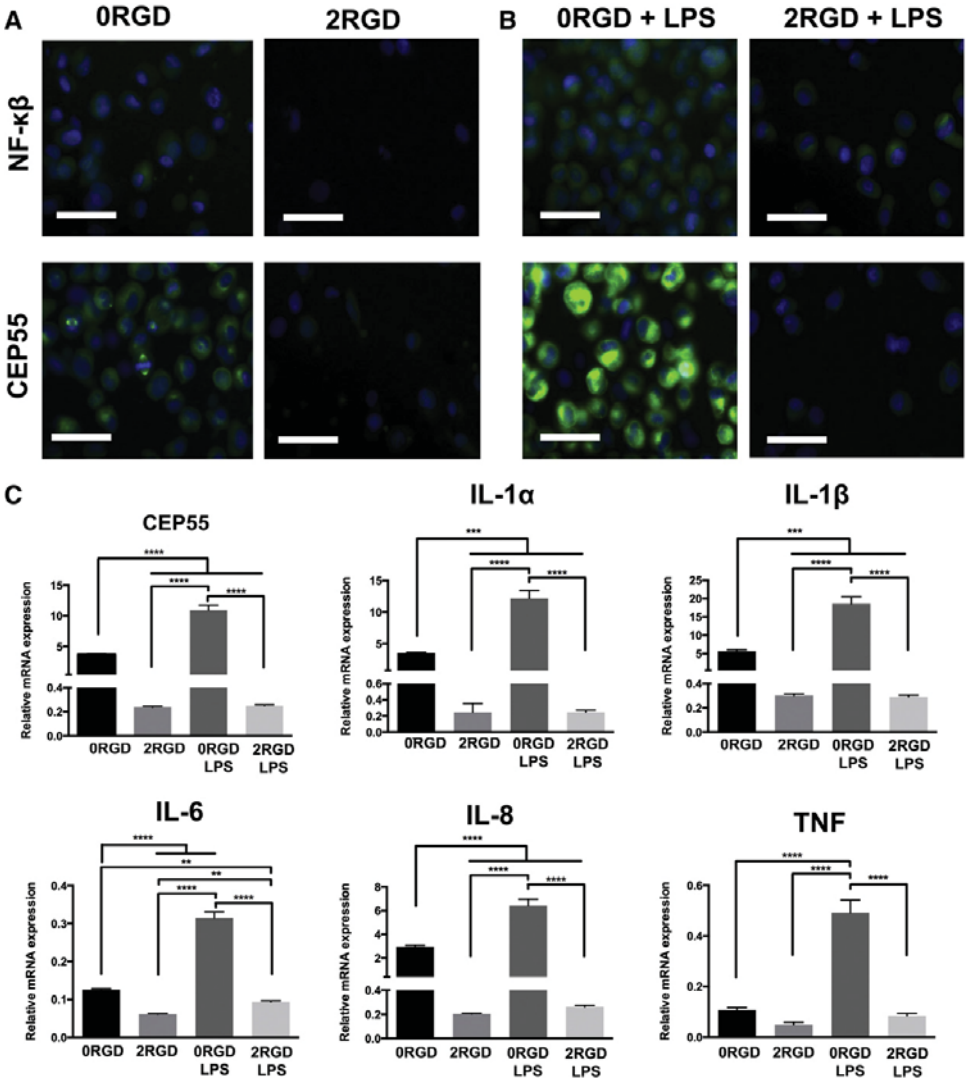

Figure 5. Co-assembled hydrogels inhibit the expression of proinflammatory cytokines and disrupts cell division on a gene and protein level. (**A**) Visualization of protein expression of fluorescent NFκβ p65 and CEP55 immunofluorescence analysis (green) in SCC25 cells localized with a nuclear counterstain of Hoechst dye (blue) cultured on the hydrogels for 48 h. (**B**) NFκβ p65 in the nucleus increased with 10 μg/mL of LPS stimulation in 0RGD cultures, whereas CEP55 expression was high in SCC25 cells irrespective of stimulation with LPS. Both signals were significantly reduced in cells cultured on the 2RGD hydrogels. Scale bars 25 μm. (**C**) Gene expression profiles of the pro-inflammatory cytokine response elements in LPS stimulated and non-stimulated SCC25 cells as determined by qPCR. Interestingly, in each case, gene expression was reduced on the 2RGD hydrogels compared with 0RGD. When LPS was used to stimulate the pro-inflammatory pathway, the expression increased significantly on 0RGD in each case, but remained comparable to the unchallenged cells on 2RGD. **P* = 0.05, ***P* = 0.01, ****P* = 0.001, *****P* = 0.0001.

interactions, are analogous to large macromolecules.[21,30] Importantly, when the co-assembled material was compared to Fmoc-FRGDF, the wavelength of the transitions within the spectra was unchanged, but the magnitude was increased, suggesting that the addition of fucoidan induced increased longitudinal ordering (Figure 3, *J*).[30] Conversely, the magnitude of the transitions was diminished in the post-assembled sample, possibly as a result of disruptions arising from the

mixing process, and potentially the unbound fucoidan forming aggregates increasing scattering in the far UV. The coassembly did not affect the mechanical properties of the resultant hydrogels; when the mechanical properties of the hydrogels were studied, the characteristic frequency sweeps of this class of system were retained, and each forms a hydrogel of comparable stiffness. Typically, two-component hydrogels where one component does not otherwise self-assemble tend to yield an alternate molecular packing, resulting in a stiffer hydrogel,[31] indicating that the inclusion of fucoidan (at this concentration) does not interfere with the processes that determine the final stiffness of the resultant hydrogels.[24a,32]

We hypothesized that the mechanism by which the fucoidan in the co-assembled sample was incorporated into the fibrillar network was through non-covalent interactions with amino acid(s) present on the surface of the fibrils. NMR data suggest restricted movement of the Fmoc and first phenylalanine due to assembly into nanotubes.[29] However, the dynamic motion of the RGDF–OH portion of the peptide is conserved in the fibrils and resulted in narrow line widths for this portion of the peptide. By integrating ^{1}H NMR resonances, it was concluded that <5 % of the RGD portion of the peptide was available in solution, and therefore available for interaction. It has been shown that a minimum spacing of ~440 nm between RGD epitopes is sufficient for effective cell attachment,[39] and the most effective cell interaction is achieved with well spaced clustered of epitopes.[40] As the entire fibril consists of closely packed Fmoc-FRGDF peptides, the limited availability of the RGD portion on the surface of the fibrils may in fact contribute to the observed cell attachment properties.[18a] We then employed small angle neutron scattering (SANS) analysis to look at the effect of the interaction with fucoidan on the fibril morphology. Although a slight reduction in radius is observed, the scattering fit suggests that the morphology of the fibril is broadly retained, as opposed to the formation of a secondary, self-sorted structure.[41] This retention of morphology coupled with an increase in density suggests that the fucoidan interaction is allowing the SAP fibril structure and morphology to be broadly retained, but is having an effect on the fibrils. This co-localization was confirmed by physically observing the location of fucoidan by labeling it with a gold nanoparticle that could be observed via TEM. After washing, GNP remained present only with the GNP labeled fucoidan, where they were observed in close association with the peptide fibrils. This indicated a strong and persistent co-localization of the fucoidan to the fibrils.

We observed that the co-assembled sample formed more quickly, possibly due to the bundling and co-location providing an increased driving force for assembly. In order to analyse the effects of this driving force on the time it takes the gel network to form, we used parallel plate rheometry to compare the rate of hydrogel formation.[34] When the materials were analyzed after 48 h, the final modulus was comparable across a range of frequencies, suggesting that the final mechanical properties of the scaffolds were similar (Figure 4, *G*). However, a fixed frequency time analysis showed that the co-assembled sample formed the hydrogel more rapidly (Figure 4, *H*). We then analyzed the sol–gel transition temperature (T_{gel}) to determine possible effects of this stabilization on the melting temperature of the hydrogels using a series of DSC analysis. These observations suggest further that the co-assembly process leads to a stabilization of the interfibrillar network. These results suggest that the fucoidan is enhancing the stability of the fibrils in the co-assembled system by increasing supramolecular order,[30] albeit without significantly increasing its stiffness (Figure 4, *G*).

Confident in the structure of our material, we decided to probe further its effect on the oral cancer cell line in further detail. Previous studies of the SCC25 cell line in comparison with normal human oral keratinocytes revealed significant over-expression of the pro-inflammatory cytokine response, upregulation of the cytokinesis promoting genes[42] and, in particular, increased expression of NFκβ useful here as an easily characterized component of a larger inflammatory pathway.[43] The uncontrolled G2 to M cell cycle progression is essential for oral cancer progression, and is characterized by an increase in the tumor size.[43] The transcription factors associated with this pathway, PLK1 and FOXM1, activate CEP55, a cytokinesis promoter identified as a key marker of tumor formation and progression.[44] Earlier CEP55 knockdown studies have revealed a reduction in cell proliferation and tumorigenicity of the cancer cells.[45] In addition, to further test the material and model the highly pro-inflammatory environment of the tumor, the cells were challenged with lipopolysaccharide (LPS), a powerful inflammatory agent, providing a valid assay for the progression of these cancer cell lines.[46] To investigate the mechanism inducing selective apoptotic effects in the cancer cells observed earlier (Figure 2) we performed a series of experiments to monitor the observed effects of the material on the protein expression of NFκβ and CEP55 (Figure 5, *A* and *B*). When the same experiment was performed upon the 2RGD hydrogel, however, no significant staining of NFκβ was observed suggesting that the material results in a significant reduction in the protein expression of NFκβ when compared to those stimulated by LPS. As expected, significant CEP55 protein expression was observed in SCC25 cells on the 0RGD hydrogel whereas the cells cultured on 2RGD hydrogels demonstrated little or no CEP55 protein expression, significantly this process was irrespective of stimulation with LPS, indicating that cytokinesis was effectively inhibited by the immobilized fucoidan (Figure 5, *A* and *B*). We then confirmed these observations with gene expression studies. As expected, when SCC25 cells were cultured on 0RGD with LPS, the response of each of the pro-inflammatory cytokines was significantly upregulated. However, when the same conditions were applied to the 2RGD hydrogel, there was a significant inhibition in the transcription of each of the cytokine promoting genes. Importantly, the expression in each of the cytokines analyzed was significantly less than that observed in the control, and comparable to the unchallenged 2RGD sample. NFκβ suppresses apoptosis by inducing the expression of a number of anti-apoptotic genes whose products include inhibitors of apoptosis (IAPs), and TNF receptor associated factor 1 (TRAF1) and TRAF2.[47] The mechanism behind the effect of this material could be due to the reduced activation and expression of anti-apoptotic products which protect the cells from apoptosis by blocking the apoptotic cascade and/or regulate other anti-apoptotic pathways.[48] We studied the materials potential as an effective anti-mitogenic agent.[12a] As shown in Figure 5, *C*, when the SCC25 cells were cultured on 2RGD compared to 0RGD a

significant downregulation of CEP55 mRNA expression was observed, again irrespective of LPS stimulation, as observed in the protein expression studies. However, when LPS was used to stimulate cells cultured on 0RGD hydrogel, a significant 50-fold inhibition of the CEP55 gene was observed with the 2RGD hydrogel. Therefore, the gene and protein data indicate that the inclusion of fucoidan allows the hydrogel to act as a powerful inhibitor of cytokinesis and the uncontrolled cell proliferation associated with this type of cancer, and potentially many others. We have shown for the first time that the self-assembly process is able to present a bioactive macromolecule, the anti-inflammatory polysaccharide fucoidan, so that the scaffold provides a non-toxic, biocompatible, yet potent environment to potentially treat a range of pro-inflammatory cancers. Future work in our laboratory will extend this study to other cell lines, and *in-vivo* studies. We suggest that this method to form materials can easily be adapted to treat a range of other disease states. We foresee that this simple yet powerful approach will develop further to allow researchers the convenient fabrication of inexpensive but complex materials which can be easily directed toward specific therapeutic outcomes.

Appendix A. Supplementary data

Supplementary data to this article can be found online at http://dx.doi.org/10.1016/j.nano.2016.01.009.

References

1. Ferrari M. Cancer nanotechnology: opportunities and challenges. *Nat Rev Cancer* 2005;**5**(3):161-71.
2. Quail DF, Joyce JA. Microenvironmental regulation of tumor progression and metastasis. *Nat Med* 2013;**19**(11):1423-37.
3. (a) Grivennikov SI, Greten FR, Karin M. Immunity, inflammation, and cancer. *Cell* 2010;**140**(6):883-99.
   (b) Conde J, Bao C, Tan Y, Cui D, Edelman ER, Azevedo HS, Byrne HJ, Artzi N, Tian F. Dual targeted immunotherapy via *in vivo* delivery of biohybrid RNAi-peptide nanoparticles to tumor-associated macrophages and cancer cells. *Adv Funct Mater* 2010 [n/a-n/a].
4. Cox TR, Erler JT. Remodeling and homeostasis of the extracellular matrix: implications for fibrotic diseases and cancer. *Dis Model Mech* 2011;**4**(2):165-78.
5. Coussens LM, Werb Z. Inflammation and cancer. *Nature* 2002;**420**(6917):860-7.
6. (a) Jones MK, Wang H, Peskar BM, Levin E, Itani RM, Sarfeh IJ, et al. Inhibition of angiogenesis by nonsteroidal anti-inflammatory drugs: insight into mechanisms and implications for cancer growth and ulcer healing. *Nat Med* 1999;**5**(12):1418-23.

(b) Cuzick J, Otto F, Baron JA, Brown PH, Burn J, Greenwald P, Jankowski J, La Vecchia C, Meyskens F, Senn HJ. Aspirin and non-steroidal anti-inflammatory drugs for cancer prevention: an international consensus statement. *Lancet Oncol* 1999;**10**(5):501-7.

7. (a) Yallapu MM, Jaggi M, Chauhan SC. Design and engineering of nanogels for cancer treatment. *Drug Discov Today* 2011;**16**(9):457-63.
   (b) Drury JL, Mooney DJ. Hydrogels for tissue engineering: scaffold design variables and applications. *Biomaterials* 2011;**24**(24):4337-51.
8. Wolinsky JB, Colson YL, Grinstaff MW. Local drug delivery strategies for cancer treatment: gels, nanoparticles, polymeric films, rods, and wafers. *J Control Release* 2012;**159**(1):14-26.
9. Geiger B, Bershadsky A, Pankov R, Yamada KM. Transmembrane crosstalk between the extracellular matrix and the cytoskeleton. *Nat Rev Mol Cell Biol* 2001;**2**(11):793-805.
10. Whitesides GM, Boncheva M. Beyond molecules: self-assembly of mesoscopic and macroscopic components. *Proc Natl Acad Sci U S A* 2002;**99**(8):4769-74.
11. (a) Dias PF, Siqueira Jr JM, Vendruscolo LF, de Jesus Neiva T, Gagliardi AR, Maraschin M, et al. Antiangiogenic and antitumoral properties of a polysaccharide isolated from the seaweed *Sargassum stenophyllum*. *Cancer Chemother Pharmacol* 2005;**56**(4):436-46.
    (b) Kim EJ, Park SY, Lee J-Y, Park JH. Fucoidan present in brown algae induces apoptosis of human colon cancer cells. *BMC Gastroenterol* 2005;**10**(1):96.
12. (a) Patel MK, Mulloy B, Gallagher KL, O'Brien L, Hughes AD. The antimitogenic action of the sulphated polysaccharide fucoidan differs from heparin in human vascular smooth muscle cells. *Thromb Haemost* 2002;**87**(1):149-54.
    (b) Park HY, Kim GY, Moon SK, Kim WJ, Yoo YH, Choi YH. Fucoidan inhibits the proliferation of human urinary bladder cancer t24 cells by blocking cell cycle progression and inducing apoptosis. *Molecules* 2002;**19**(5):5981-98.
13. Zhu C, Cao R, Zhang SX, Man YN, Wu XZ. Fucoidan inhibits the growth of hepatocellular carcinoma independent of angiogenesis. *Evid Based Complement Alternat Med* 2013;**2013**:692549.
14. Murakami K, Aoki H, Nakamura S, Nakamura S-i, Takikawa M, Hanzawa M, et al. Hydrogel blends of chitin/chitosan, fucoidan and alginate as healing-impaired wound dressings. *Biomaterials* 2010;**31**(1):83-90.
15. Sezer AD, Hatipoglu F, Cevher E, Oğurtan Z, Bas AL, Akbuğa J. Chitosan film containing fucoidan as a wound dressing for dermal burn healing: preparation and *in vitro/in vivo* evaluation. *AAPS PharmSciTech* 2007;**8**(2):1530-9932.
16. Worthington P, Pochan DJ, Langhans SA. Peptide hydrogels—versatile matrices for 3D cell culture in cancer medicine. *Front Oncol* 2015;**5**.
17. Rodriguez AL, Wang TY, Bruggeman KF, Horgan CC, Li R, Williams RJ, et al. *In vivo* assessment of grafted cortical neural progenitor cells and host response to functionalized self-assembling peptide hydrogels and the implications for tissue repair. *J Mater Chem B* 2014;**2**(44):7771-8.
18. (a) Modepalli VN, Rodriguez AL, Li R, Pavuluri S, Nicholas KR, Barrow CJ, et al. *In vitro* response to functionalized self-assembled peptide scaffolds for three-dimensional cell culture. *Pept Sci* 2014;**102**(2):197-205.
    (b) Zhou M, Smith AM, Das AK, Hodson NW, Collins RF, Ulijn RV, Gough JE. Self-assembled peptide-based hydrogels as scaffolds for anchorage-dependent cells. *Biomaterials* 2014;**30**(13):2523-30.
19. (a) Nisbet D, Williams R. Self-assembled peptides: characterisation and *in vivo* response. *Biointerphases* 2012;**7**(1):1-14.
    (b) Boekhoven J, Stupp SI. 25th anniversary article: supramolecular materials for regenerative medicine. *Adv Mater* 2012.
20. Rodriguez A, Wang T-Y, Bruggeman K, Li R, Williams R, Parish C, et al. Tailoring minimalist self-assembling peptides for localized viral vector gene delivery. *Nano Res* 2015:1-11.
21. Williams RJ, Smith AM, Collins R, Hodson N, Das AK, Ulijn RV. Enzyme-assisted self-assembly under thermodynamic control. *Nat Nanotechnol* 2009;**4**(1):19-24.
22. Rodriguez AL, Parish CL, Nisbet DR, Williams RJ. Tuning the amino acid sequence of minimalist peptides to present biological signals via charge neutralised self assembly. *Soft Matter* 2013;**9**:3915-9.
23. Li R, Horgan CC, Long B, Rodriguez AL, Mather L, Barrow CJ, et al. Tuning the mechanical and morphological properties of self-assembled peptide hydrogels via control over the gelation mechanism through regulation of ionic strength and the rate of pH change. *RSC Adv* 2015;**5**(1):301-7.
24. (a) Williams RJ, Hall TE, Glattauer V, White J, Pasic PJ, Sorensen AB, et al. The *in vivo* performance of an enzyme-assisted self-assembled peptide/protein hydrogel. *Biomaterials* 2011;**32**(22):5304-10.

(b) Javid N, Roy S, Zelzer M, Yang Z, Sefcik J, Ulijn RV. Cooperative self-assembly of peptide gelators and proteins. *Biomacromolecules* 2011;**14**(12):4368-76.
25. (a) Zhao F, Ma ML, Xu B. Molecular hydrogels of therapeutic agents. *Chem Soc Rev* 2009;**38**(4):883-91.
(b) Yang ZM, Xu KM, Wang L, Gu HW, Wei H, Zhang MJ, Xu B. Self-assembly of small molecules affords multifunctional supramolecular hydrogels for topically treating simulated uranium wounds. *Chem Commun* 2009;**35**:4414-6.
(c) Bhuniya S, Seo YJ, Kim BH. Ibuprofen-based hydrogelators: an approach toward anti-inflammatory drug delivery. *Tetrahedron Lett* 2009;**47**(40):7153-6.
26. Dewhurst CD. D33—a third small-angle neutron scattering instrument at the Institut Laue Langevin. *Meas Sci Technol* 2008;**19**(3):8.
27. Kline SR. Reduction and analysis of SANS and USANS data using IGOR Pro. *J Appl Crystallogr* 2006;**39**:895-900.
28. Rheinwald JG, Beckett MA. Tumorigenic keratinocyte lines requiring anchorage and fibroblast support cultured from human squamous cell carcinomas. *Cancer Res* 1981;**41**(5):1657-63.
29. Smith AM, Williams RJ, Tang C, Coppo P, Collins RF, Turner ML, et al. Fmoc-diphenylalanine self assembles to a hydrogel via a novel architecture based on pi-pi interlocked beta-sheets. *Adv Mater* 2008;**20**(1):37-41.
30. Hirst AR, Roy S, Arora M, Das AK, Hodson N, Murray P, et al. Biocatalytic induction of supramolecular order. *Nat Chem* 2010;**2**(12):1089-94.
31. Raeburn J, Adams DJ. Multicomponent low molecular weight gelators. *Chem Commun* 2015;**51**(25):5170-80.
32. (a) Adams DJ, Butler MF, Frith WJ, Kirkland M, Mullen L, Sanderson P. Tailoring gel strength by amino acid sequence in fmoc dipeptide hydrogels. *Soft Matter* 2009;**5**:1856-62.
(b) Cheng G, Castelletto V, Moulton CM, Newby GE, Hamley IW. Hydrogelation and self-assembly of fmoc-tripeptides: unexpected influence of sequence on self-assembled fibril structure, and hydrogel modulus and anisotropy. *Langmuir* 2009;**26**(7):4990-8.
33. Lirdprapamongkol K, Warisnoicharoen W, Soisuwan S, Svasti J. Eco-friendly synthesis of fucoidan-stabilized gold nanoparticles. *Am J Appl Sci* 2010;**7**(8):1038.
34. Williams RJ, Gardiner J, Sorensen AB, Marchesan S, Mulder RJ, McLean KM, et al. Monitoring the early stage self-assembly of enzyme-assisted peptide hydrogels. *Aust J Chem* 2013;**66**(5):572-8.
35. Sayes CM, Wahi R, Kurian PA, Liu Y, West JL, Ausman KD, et al. Correlating nanoscale titania structure with toxicity: a cytotoxicity and inflammatory response study with human dermal fibroblasts and human lung epithelial cells. *Toxicol Sci* 2006;**92**(1):174-85.
36. (a) Kalluri R, Zeisberg M. Fibroblasts in cancer. *Nat Rev Cancer* 2006;**6**(5):392-401.
(b) Olumi AF, Grossfeld GD, Hayward SW, Carroll PR, Tlsty TD, Cunha GR. Carcinoma-associated fibroblasts direct tumor progression of initiated human prostatic epithelium. *Cancer Res* 2006;**59**(19):5002-11.
37. Hamill KJ, Hopkinson SB, Hoover P, Todorović V, Green KJ, Jones JC. Fibronectin expression determines skin cell motile behavior. *J Investig Dermatol* 2012;**132**(2):448-57.
38. Kuang Y, Yuan D, Zhang Y, Kao A, Du X, Xu B. Interactions between cellular proteins and morphologically different nanoscale aggregates of small molecules. *RSC Adv* 2013;**3**(21):7704-7.
39. Massia SP, Hubbell JA. An RGD spacing of 440 nm is sufficient for integrin alpha V beta 3-mediated fibroblast spreading and 140 nm for focal contact and stress fiber formation. *J Cell Biol* 1991;**114**(5):1089-100.
40. Maheshwari G, Brown G, Lauffenburger DA, Wells A, Griffith LG. Cell adhesion and motility depend on nanoscale RGD clustering. *J Cell Sci* 2000;**113**(10):1677-86.
41. Morris KL, Chen L, Raeburn J, Sellick OR, Cotanda P, Paul A, et al. Chemically programmed self-sorting of gelator networks. *Nat Commun* 2013;**4**:1480.
42. (a) Nakano Y, Kobayashi W, Sugai S, Kimura H, Yagihashi S. Expression of tumor necrosis factor-alpha and interleukin-6 in oral squamous cell carcinoma. *Jpn J Cancer Res* 1999;**90**(8):858-66.
(b) Reuter S, Charlet J, Juncker T, Teiten MH, Dicato M, Diederich M. Effect of curcumin on nuclear factor kappaB signaling pathways in human chronic myelogenous K562 leukemia cells. *Ann N Y Acad Sci* 1999;**1171**:436-47.
43. Rao SK, Pavicevic Z, Du Z, Kim JG, Fan M, Jiao Y, et al. Pro-inflammatory genes as biomarkers and therapeutic targets in oral squamous cell carcinoma. *J Biol Chem* 2010;**285**(42):32512-21.
44. Waseem A, Ali M, Odell EW, Fortune F, Teh MT. Downstream targets of FOXM1: CEP55 and HELLS are cancer progression markers of head and neck squamous cell carcinoma. *Oral Oncol* 2010;**46**(7):536-42.
45. Tao J, Zhi X, Tian Y, Li Z, Zhu Y, Wang W, et al. CEP55 contributes to human gastric carcinoma by regulating cell proliferation. *Tumour Biol* 2014;**35**(5):4389-99.
46. Ko SC, Huang CR, Shieh JM, Yang JH, Chang WC, Chen BK. Epidermal growth factor protects squamous cell carcinoma against cisplatin-induced cytotoxicity through increased interleukin-1beta expression. *PLoS One* 2013;**8**(2):e55795.
47. Lin A, Karin M. NF-κB in cancer: a marked target. *Seminars in cancer biology*. Elsevier; 2003. p. 107-14.
48. Yamamoto Y, Gaynor RB. Therapeutic potential of inhibition of the NF-κB pathway in the treatment of inflammation and cancer. *J Clin Investig* 2001;**107**(2):135.
49. Yu C, Young S, Russo V, Amsden BG, Flynn LE. Techniques for the isolation of high-quality RNA from cells encapsulated in chitosan hydrogels. *Tissue Eng Part C Methods* 2013;**19**(11):829-38.

Appendix D: Full Published Work (section 5.4)

Alexandra L. Rodriguez, Ting-Yi Wang, Kiara F. Bruggeman, Rui Li, Richard J. Williams, Clare L. Parish, David R. Nisbet, "Tailoring minimalist self-assembling peptides for localized viral vector gene delivery", *Nano Research*, 2016, vol. 9, pp. 674-684 – Reproduced with permission from Springer

Nano Research
DOI 10.1007/s12274-015-0946-0
Research Article
ISSN 1998-0124
CN 11-5974/O4

Tailoring minimalist self-assembling peptides for localized viral vector gene delivery

Alexandra L. Rodriguez[1], Ting-Yi Wang[2], Kiara F. Bruggeman[1], Rui Li[3], Richard J. Williams[4], Clare L. Parish[2,§] (✉), and David R. Nisbet[1,§] (✉)

[1] *Research School of Engineering, The Australian National University, Canberra, ACT 2601, Australia*
[2] *Florey Institute of Neuroscience & Mental Health, The University of Melbourne, Parkville, VIC 3010, Australia*
[3] *Centre for Chemistry and Biotechnology, Deakin University, Waurn Ponds, VIC 3217, Australia*
[4] *School of Aerospace, Mechanical and Manufacturing Engineering and the Health Innovations, Research Institute, RMIT University, Melbourne, VIC 3001, Australia*
[§] *These authors contributed equally to this work.*

Received: 20 September 2015
Revised: 3 November 2015
Accepted: 15 November 2015

KEYWORDS
viral vectors,
gene therapy,
self-assembling peptides,
biomaterials

ABSTRACT

Viral vector gene delivery is a promising technique for the therapeutic administration of proteins to damaged tissue for the improvement of regeneration outcomes in various disease settings including brain and spinal cord injury, as well as autoimmune diseases. Though promising results have been demonstrated, limitations of viral vectors, including spread of the virus to distant sites, neutralization by the host immune system, and low transduction efficiencies have stimulated the investigation of biomaterials as gene delivery vehicles for improved protein expression at an injury site. Here, we show how N-fluorenylmethyloxycarbonyl (Fmoc) self-assembling peptide (SAP) hydrogels, designed for tissue-specific central nervous system (CNS) applications via incorporation of the laminin peptide sequence isoleucine–lysine–valine–alanine–valine (IKVAV), are effective as biocompatible, localized viral vector gene delivery vehicles *in vivo*. Through the addition of a C-terminal lysine (K) residue, we show that increased electrostatic interactions, provided by the additional amine side chain, allow effective immobilization of lentiviral vector particles, thereby limiting their activity exclusively to the site of injection and enabling focal gene delivery *in vivo* in a tissue-specific manner. When the C-terminal lysine was absent, no difference was observed between the number of transfected cells, the volume of tissue transfected, or the transfection efficiency with and without the Fmoc-SAP. Importantly, immobilization of the virus only affected transfection cell number and volume, with no impact observed on transfection efficiency. This hydrogel allows the sustained and targeted delivery of growth factors post injury. We have established Fmoc-SAPs as a versatile platform for enhanced biomaterial design for a range of tissue engineering applications.

Address correspondence to David R. Nisbet, david.nisbet@anu.edu.au; Clare L. Parish, clare.parish@florey.edu.au

TSINGHUA UNIVERSITY PRESS Springer

1 Introduction

Viral vector gene delivery plays a significant role in the development of therapeutic treatments for various diseases including cancer, autoimmune diseases, and neurodegenerative diseases [1, 2]. In particular, with limited capacity for self-repair in the brain and spinal cord, the delivery of neurotrophins to damaged central nervous system (CNS) has shown significant potential in delaying disease progression and promoting regeneration [3, 4]. Neurotrophic support provided to cells *in vivo* by various growth factors and cell-signaling molecules (such as brain-derived neurotrophic factor [5], nerve growth factor [6], and glial cell-derived neurotrophic factor [7]) can slow progressive neurodegeneration in disorders including Parkinson's disease and motor neuron disease. Evidence suggests that this approach can also limit the size of the injured area by protecting the surrounding parenchyma from secondary degeneration in acute insults such as stroke or traumatic brain injury, thereby improving the overall capacity for CNS regeneration [3].

Current strategies in growth factor delivery, however, are challenged by their short half-life, difficulty in penetrating the blood brain barrier, and susceptibility to enzymatic degradation, thereby requiring high concentrations of growth factors to achieve therapeutic benefit [8]. These limitations make the delivery of soluble growth factors, typically by invasive and cumbersome infusion kits, both inefficient and expensive [9]. As a result, viral vector gene delivery has been investigated as a means to achieve long-term delivery of neurotrophic factors at a site of injury through the introduction of DNA into cells for localized protein expression [10–14]. This approach overcomes the challenges presented by the delivery of soluble proteins, by providing a targeted source of growth factors for the neuroprotection of cells in and surrounding the injury site. Though there has been success in delivering genetic material for targeted therapeutic protein expression using viral vectors [3], there is a need to improve this technology with a localized and efficient gene delivery method for future clinical applications [1, 15]. For this reason, the use of biomaterials as sophisticated tools to overcome the issues associated with viral vectors has garnered significant attention [1].

Rationally designed biomaterials are powerful tools for regenerative medicine [16], primarily as adjuvant scaffolds that mimic the physical and biochemical properties of the extracellular microenvironment [17], such as those required to support neural cells for CNS repair [18]. Furthermore, they can be engineered to incorporate viral vectors for delivery of genetic material through encapsulation methods, including the use of nanoparticles and microspheres [19, 20], and/or attached via chemical functionalization [21, 22]. The covalent and/or non-covalent attachment of viral vectors [23–25] encourages binding of the vector to the material to limit vector spread, shield the vector from neutralization by the host immune system, and increase transduction efficiency [1].

Previous research has demonstrated that amine ($-NH_2$) moieties can enhance virus adsorption and cell attachment to the biomaterial surface, resulting in improved transduction efficiency [26]. This observation was attributed to the presence of positively charged amine ($-NH_3^+$) moieties reducing the electrostatic repulsion between the negatively charged membranes on the viral capsid and cell surface, enhancing the ability of the virus to attach to the cell membrane and deliver its genetic material [26]. Such examples highlight the utility of biomaterials as viral vector delivery vehicles. Recently, self-assembling peptides (SAPs) have also been demonstrated to effectively deliver genetic material to human mesenchymal stem cells in culture via recombinant adeno-associated virus [27]. However, the RADA16 SAP [28] used presents no biofunctionality, nor any capacity to immobilize the virus for controlled release. Here, we design a multifunctional biomaterial for both integrated tissue specificity and superior vector delivery ensuring improved overall tissue regenerative outcomes.

N-Fluorenylmethyloxycarbonyl (Fmoc)-peptides are a class of SAPs known to self-assemble through a robust mechanism driven by the intermolecular sharing of π electrons between Fmoc protecting groups, and stabilized by the antiparallel β-sheet interactions of the protected peptide sequence, a mechanism known as π-β self-assembly [29]. These assemblies take the form of hollow fibrils, measuring ~10–30 nm in diameter and

microns in length, that orientate themselves longitudinally into a network of interconnected bundles, forming a structural mimetic of the extracellular matrix [30]. We have shown that the mechanical properties of these Fmoc-SAPs can be easily tailored for tissue-specific applications through adjustment of the rate of assembly as well as the ionic concentration, without disturbing the nanofibrous morphology [31]. The biocompatibility of Fmoc-SAPs has been demonstrated across a range of sequences, and we have shown that optimal biocompatibility and functionality of the Fmoc-SAPs requires the incorporation of bioactive peptide sequences [30, 32–34]. Previously, in a demonstration of the utility of these materials in a neural context, we incorporated the laminin-based isoleucine–lysine–valine–alanine–valine (IKVAV) sequence (known to promote neuron survival, neural differentiation, and neurite extension [35]) into an Fmoc-SAP system [36], as we do again here, and have validated its performance *in vivo* [34]. This capacity to concomitantly present a bioactive peptide sequence at high density for directing cell behavior while also providing structural support through the self-assembled matrix makes Fmoc-SAP scaffolds a highly sophisticated class of biomaterials, ideal for tissue engineering in the CNS.

In this study, we hypothesized that these scaffolds could be used to nonspecifically immobilize viral vectors via reversible, noncovalent interactions between the SAP scaffold and the viral membrane by taking advantage of the chemical flexibility afforded via careful selection of the amino acids within the peptide sequence. As proof of principle, we used the previously designed Fmoc-DDIKVAV to deliver mCherry lentivirus *in vivo*, investigating its capacity for localized viral vector gene delivery. We subsequently improved on this design with the development of a second Fmoc-SAP, Fmoc-DDIKVAVK, engineered for the high-density presentation of $-NH_2$ functional groups at the C-terminus of the peptide. We show that by increasing the electrostatic interactions available for binding, we can enable focal gene delivery by limiting viral activity to the site of the hydrogel injection. Such technology could hold significant potential for the sustained and targeted delivery of growth factors to aid in tissue repair.

2 Experimental

2.1 Solid-phase peptide synthesis

Fmoc-SAPs were synthesized manually by solid-phase peptide synthesis (SPPS) as previously described [34]. SPPS was performed in a rotating glass reactor vessel at 0.4-mmol scale. Fmoc-protected amino acids, hydroxybenzotriazole, O-benzotriazole-N,N,N′,N′-tetramethyl-uronium-hexafluoro-phosphate, and Wang-based resins were purchased from GL Biochem (China). All other chemicals were purchased from Sigma-Aldrich.

2.2 Fmoc-self-assembling peptide hydrogel preparation

To prepare the Fmoc-SAP hydrogels, 10 mg of peptide was dissolved in 100 μL deionized water and 75 μL 0.5 M sodium hydroxide (NaOH). Hydrochloric acid (HCl, 0.1 M) was then used to reduce the pH of the peptide solution. HCl was added drop-wise until the solution reached ~pH 7.4 and formed a self-supporting hydrogel. The final volume of HCl added varied between 100 and 150 μL. Finally, the gel was made up to a final concentration of 20 mg/mL by addition of phosphate-buffered saline (PBS). The solution was vortexed throughout the entire procedure.

2.3 Transmission electron microscopy (TEM)

TEM images were obtained using a HITACHI HA7100 TEM. A LaB6 filament at 100 kV was used. Negative stains were performed to image the Fmoc-SAP samples as previously described [34].

2.4 Atomic force microscopy (AFM)

AFM was performed using a MultiMode 8 (Bruker BioSciences Corporation, USA) operated in peak force QNM with a scan size of 10 μm. Highly ordered pyrolytic graphite (HOPG) substrates (SPI, USA) were used for sample preparation. Fmoc-SAP hydrogel (15 μL) was applied to the HOPG substrates. Scanasyst-air probes with silicon tip on nitride lever (Bruker BioSciences Corporation) were used.

2.5 Fourier transform infrared (FTIR) spectroscopy

For FTIR spectroscopy, 30 μL of Fmoc-SAP hydrogel

sample at 20 mg/mL was placed on the single reflection diamond. An Alpha Platinum Attenuated Total Reflectance FTIR (Bruker Optics) was used to obtain scans from 1,550–1,750 cm^{-1}, corresponding to the amide I region. A background scan of deionized water was subtracted from the hydrogel data.

2.6 Circular dichroism (CD)

Fmoc-SAP hydrogels, prepared as described above at 20 mg/mL, were diluted at 1:200 in deionized water for CD. Approximately 400 μL was placed in the cuvette. Deionized water was used as the background scan and subtracted from the hydrogel CD data. All scans were taken from 350 to 170 nm at a step size of 1 and 1-nm bandwidth by using a Chirascan CD Spectrometer (Applied Photophysics Limited).

2.7 Rheology

A Kinexus Pro+ Rheometer (Malvern) was used to assess the viscoelastic properties of the previously prepared Fmoc-SAP hydrogels at 20 mg/mL with a 20-mm rough flat plate and solvent trap geometry. Approximately 200 μL of the hydrogel sample was placed on the geometry. A frequency sweep was performed from 0.1–100 Hz using an oscillatory strain of 0.1% at a 0.2-mm gap size.

2.8 Determination of lentiviral release and immobilization

To determine successful immobilization of the mCherry lentivirus, release of mCherry lentivirus from the two Fmoc-SAP hydrogels was compared. Samples (100 μL) of Fmoc-SAP hydrogels at 20 mg/mL were mixed with 1 μL of mCherry lentivirus (titer at 9.28×10^{10} copies/mL; GeneCopoeia) and placed in a 96-well plate. PBS (200 μL) was placed on top of the gel, and the plate was placed in an incubator (37 °C, 5% CO_2). The PBS was then collected and replaced with fresh PBS every 24 h for 5 days. The PBS supernatant was stored in a freezer until ready for analysis by an enzyme-linked immunosorbent assay (ELISA). An HIV Type 1 p24 Antigen ELISA 2.0 kit (ZeptoMetrix) was used to measure the amount of mCherry released. The ELISA was performed as per the manufacturer's instructions.

2.9 Implantation of mCherry virus with Fmoc-SAP

The Florey Institute of Neuroscience and Mental Health animal ethics committee approved all animal experiments with procedures conducted in accordance with the Australian National Health and Medical Research Council's published Code of Practice for the Use of Animals in Research. Adult Swiss mice were housed with a 12-h light/dark cycle and *ad libitum* access to food and water. Mice received stereotaxic implants of mCherry lentivirus alone ($n = 6$) or mCherry virus in the presence of Fmoc-DDIKVAV ($n = 6$) or Fmoc-DDIKVAVK ($n = 6$). Isoflurane (5%) was used to induce anesthesia, and 2% isoflurane was maintained for the duration of surgery. Mice were placed into a stereotaxic frame and a craniotomy performed for microinjections into the underlying striatum (coordinates: anterior +1.0 mm and lateral −2.3 mm, relative to Bregma). A fine-pulled micropipette coupled to a Hamilton syringe was used to inject virus or virus with Fmoc-SAP at a depth of 3.2 mm below the dura surface. For control animals, 1 μL of mCherry (10^9 UI/mL) was diluted in 1 μL sterile PBS and the total 2-μL suspension was implanted. Alternatively, the virus was mixed at a 1:1 ratio with either of the Fmoc-SAPs. After 21 days, mice were killed by an overdose of sodium pentobarbitone (100 mg/kg) and transcardially perfused with warm saline followed by 4% paraformaldehyde (PFA). After removal, mouse brains were post-fixed for 2 h in 4% PFA. Following fixation, brains were cryopreserved in a 30% sucrose solution overnight. The brains were coronally sectioned (40 μm at a 1:12 series) and immunohistochemistry against red fluorescent protein (rabbit anti-RFP, 1:1000, Rockland, USA) was performed to amplify the mCherry signal, using previously described methods [37]. Cell counts for mCherry virally infected cells (mCherry+), transduction volume, and density measurements were performed on a Leica microscope (Leica CTR6000) using LAS software. One-way ANOVAs with Tukey's post-hoc tests were used to identify statistically significant changes between groups. Statistical significance was set at $P < 0.05$. Data represent the mean ± standard error of the mean (SEM).

3 Results and discussion

3.1 Material characterization of the lysine-functionalized self-assembling peptide

An initial titration was performed to investigate any shifts in the apparent pK_a of the newly derived Fmoc-DDIKVAVK resulting from the addition of a K residue at the C-terminus, and the effect this could have on the pH of gelation (Fig. 1(a)) [36]. Although the addition of the K residue was observed to shift the pK_a (from ~7.0 to ~7.8), it indicated that self-assembly of this SAP could take place under physiological conditions (pH ~7.4). This was confirmed when both Fmoc-DDIKVAV and Fmoc-DDIKVAVK formed clear, self-supporting hydrogels at pH ~7.4 using the pH switch method previously described (Fig. 1(b)) [34].

The mechanical properties of both hydrogels were compared using parallel plate rheometry. Here, both gels demonstrated viscoelastic properties characteristic of previously described Fmoc-SAP hydrogels, where the storage modulus (G') is greater than the loss modulus (G'') and shows only a weak dependence on frequency (Figs. 1(c) and 1(d)) [36]. Fmoc-DDIKVAVK appeared to be a slightly stronger material than Fmoc-DDIKVAV (G' = 10,500 and 6,500 Pa, respectively), most likely the consequence of increased electrostatic interactions. The higher pK_a Fmoc-DDIKVAVK required more HCl addition to achieve gelation at physiological pH. The positively charged lysine groups attract negatively charged chloride ions from solution, which themselves attract further lysine groups attached to other fibrils. This increased electrostatic interaction enables stronger supramolecular interactions between the aligned fibrils, increasing the effective points of entanglement and resulting in a more rigid nanofibrous network [31].

AFM demonstrated that a microscale network was formed by both hydrogels, confirming that although the addition of a K residue shifted the pK_a slightly, self-assembly of the nanofibrous structures that underpinned the hydrogel was maintained at physiological pH (Figs. 2(a) and 2(d)). This modification in supramolecular ordering was further visualized using TEM, with Fmoc-DDIKVAVK exhibiting a higher

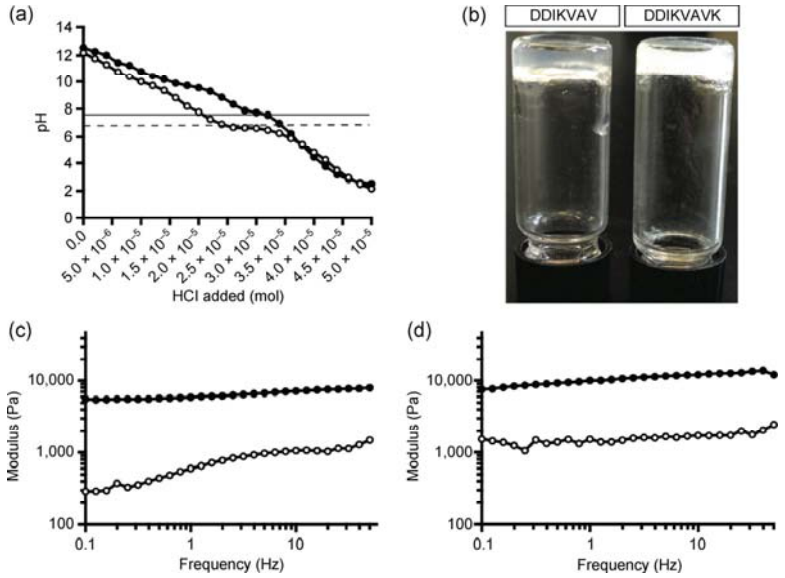

Figure 1 Fmoc-DDIKVAVK forms a hydrogel under physiological conditions. (a) Titration curve for Fmoc-DDIKVAV (open circles) and Fmoc-DDIKVAVK (closed circles) showing a slight shift in pK_a (Fmoc-DDIKVAV: dashed line; Fmoc-DDIKVAVK: solid line) that correlates with the expected pH range of self-assembly. (b) An inversion test demonstrates the gelation of the two Fmoc-SAPs using a pH switch. Rheological analysis for (c) Fmoc-DDIKVAV and (d) Fmoc-DDIKVAVK. Closed circles = G'; open circles = G''.

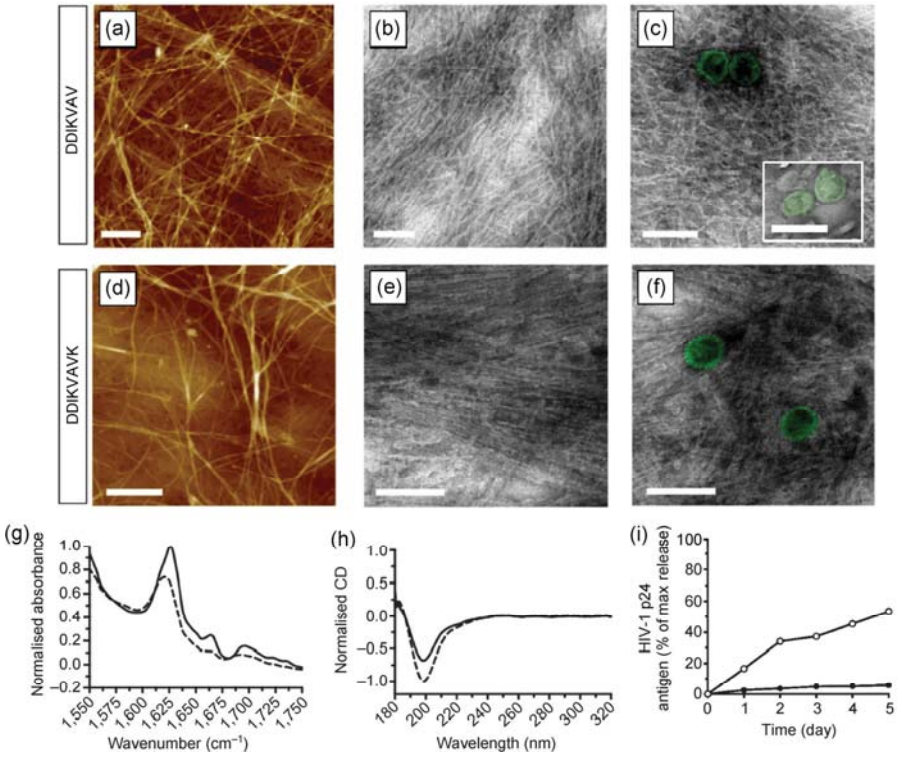

Figure 2 Microscopy images of Fmoc-SAPs show the nanofibrous structure of the gels, with spectroscopy confirming that the underlying π-β self-assembly mechanism is maintained with the addition of a K residue. A cumulative release profile confirms lentivirus immobilization in the presence of K. Fmoc-DDIKVAV nanofibrous network shown in (a) AFM image and (b) TEM image. (c) TEM image of lentivirus (green) embedded within the branched arrangement of the individual fibers, inset shows lentivirus alone. (d)–(f) Corresponding images for Fmoc-DDIKVAVK. Scale for AFM = 1 μm, TEM = 200 nm. (g) FTIR and (h) CD for Fmoc-DDIKVAV (solid line) and Fmoc-DDIKVAVK (dashed line). (i) A cumulative release profile for Fmoc-DDIKVAVK (closed circles) and Fmoc-DDIKVAV (open circles) over 5 days.

degree of alignment of the nanofibers compared to the more branched arrangement of Fmoc-DDIKVAV (Figs. 2(b) and 2(e)).

Finally, the effect of the addition of a K residue on the π-β assembly mechanism was characterized spectroscopically, using FTIR and CD. The FTIR spectra showed major peaks at 1,630 cm^{-1} and minor peaks at 1,690 cm^{-1}, representative of antiparallel β-sheets formed by hydrogen bonding between the peptide sequences (Fig. 2(g)) [36]. The CD spectra further supported the FTIR data, with a transition at 200 nm indicative of β-sheets in both Fmoc-DDIKVAV and Fmoc-DDIKVAVK (Fig. 2(h)) [29]. Importantly, the wavelength of the minima was not affected but increased in magnitude, indicating that the addition of the K residue did not affect the intermolecular π-β interactions, but did promote increased supramolecular ordering of the fibrils, as observed by TEM and AFM [36].

3.2 Assessment of virus retention in self-assembling hydrogels

Satisfied that the additional K residue was not adversely impinging on the assembly process, we proceeded to evaluate the material as a viral vector gene delivery vehicle. We blended lentiviruses into

preformed Fmoc-SAP hydrogels, and subsequently allowed them to reform gels at room temperature. Initial TEM images showed the lentiviral particles (80–100 nm in diameter) visibly embedded within the nanofibrous assembly of both Fmoc-SAPs (Figs. 2(c) and 2(f)). To investigate the retention of the lentiviral particles within the Fmoc-SAP scaffolds, and whether increased retention was induced by the additional positively charged residue, the release of the virus from the gels (in a static, physiological environment) was measured using an HIV-1 p24 antigen ELISA. Measured absorbance values were interpolated using a calibration curve of standard concentrations within the detection limits of the instrument and data above or below these limits were approximated as the minimum or maximum of the detection range, respectively.

Fmoc-SAP hydrogels (100 μL) were again mixed with the lentivirus and placed in a 96-well plate with 200 μL of PBS placed on top of each gel-virus sample. The plate was left in an incubator (37 °C, 5% CO_2) and 200 μL of PBS was removed and replaced every 24 h for 5 days. The isolated supernatant at each time point was analyzed with ELISA. The results showed an increase in lentiviral particle retention in the K-functionalized peptide hydrogel compared to Fmoc-DDIKVAV over 5 days, as revealed by the reduced detection of HIV-1 p24 (viral particles) in the supernatant (Fig. 2(i)). This result indicates that the addition of a positively charged K residue resulted in effective immobilization of the majority of the viral particles within the Fmoc-DDIKVAVK hydrogel (Fig. 3). This is important for the broad applicability of this method. Here, we have used a lentiviral vector as proof of concept; however, immobilization via electrostatic interactions with the negatively charged viral capsule could be utilized for any viral capsule such as adeno- and retroviruses.

3.3 *In vivo* assessment of self-assembling hydrogels as viral vector gene delivery vehicles

Upon confirmation of viral vector immobilization in Fmoc-DDIKVAVK hydrogels, we investigated the capacity of the Fmoc-SAP to localize viral vector delivery *in vivo*. mCherry lentivirus was loaded into the Fmoc-DDIKVAV and Fmoc-DDIKVAVK hydrogels, prior to stereotaxic injection into the mouse brain

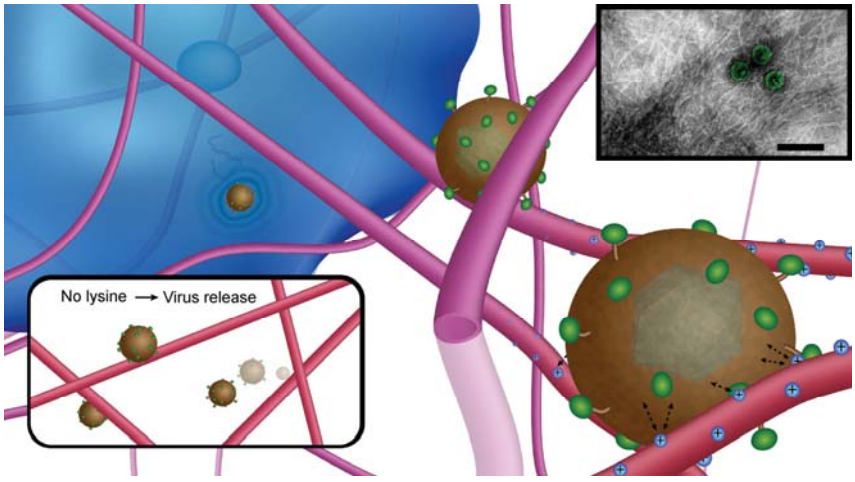

Figure 3 Charge-based immobilization of lentivirus within Fmoc self-assembling peptides is achieved through peptide functionalization with a K residue. When a K residue is added to the laminin-based self-assembling peptide sequence, Fmoc-DDIKVAV, the positive charges from the $–NH_2$ side groups immobilize the lentiviral vector via electrostatic interactions. This results in retention of the vector within the nanofibrous Fmoc-SAP network resulting in localized gene delivery to cells at the injection site. When no K is present, the virus is released from the Fmoc-SAP hydrogel. (TEM scale bar = 200 nm)

(striatum) and compared to delivery of virus alone. The Fmoc-SAP hydrogels were injected at a concentration of 10 mg/mL, and the amount of viral vector-mediated transfection was assessed after three weeks. A cell count of transduced (mCherry+) cells showed that delivery of the lentivirus in the absence of the Fmoc-SAPs resulted in the highest number of transduced cells with a statistically significant difference in the level of transduction between the Fmoc-DDIKVAVK and both of the other groups (Fig. 4(a)).

Additionally, a difference in volume of the mCherry+ area was observed with Fmoc-DDIKVAVK having the least mCherry coverage (Fig. 4(b)). There was no significant difference observed in the density of mCherry+ cells at the site of delivery between the three groups (Fig. 4(c)). Importantly, this result indicates that the capacity for transfection by the mCherry lentivirus was not compromised by the Fmoc-SAP hydrogels but simply achieved localized DNA delivery to the microenvironment surrounding the material without affecting the tropism of the virus. In particular, the introduction of a K residue resulted in the most focal delivery due to immobilization of the mCherry virus (Fig. 4(d)). This is noteworthy, as we have enhanced the properties of this sophisticated minimalist Fmoc-SAP system for our desired application in viral vector gene delivery for the CNS. The development of this adjuvant scaffold now offers the potential to deliver biologically relevant DNA (via viral vectors within SAPs) directly at the edge of a lesion (for example, post-traumatic brain injury or stroke) to enhance cell survival within the penumbra,

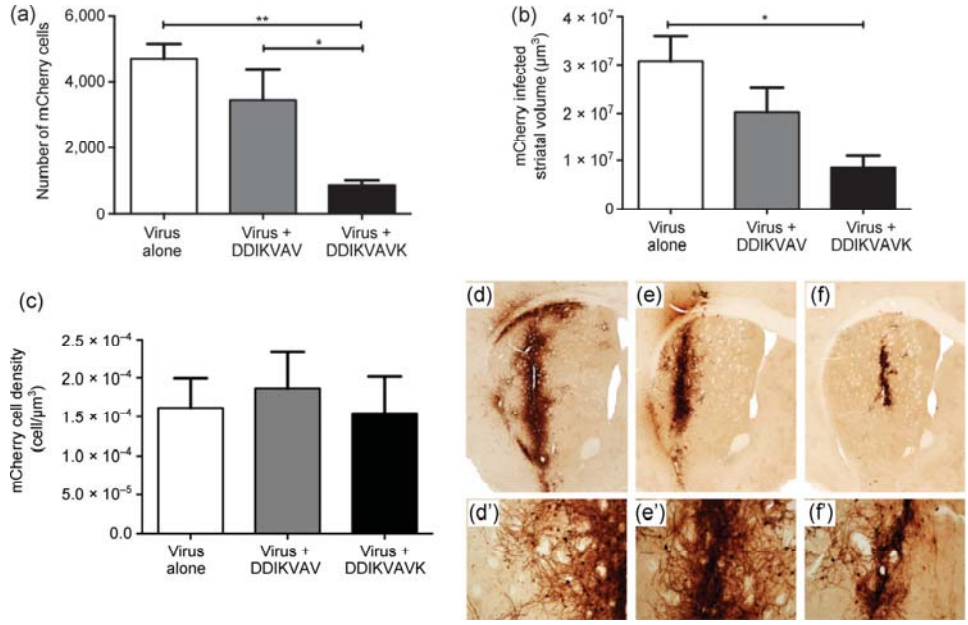

Figure 4 (a) Focal delivery of the mCherry lentivirus within an Fmoc-DDIKVAVK gel significantly reduced the number of mCherry+ cells in the host striatum. (b) Similarly, the volume of mCherry+ cells within the striatum was reduced with the addition of a K residue, demonstrating the ability of Fmoc-DDIKVAVK to immobilize the lentivirus and subsequently localize delivery of genetic material. (c) Consequently, the density of the mCherry+ cells was similar across all groups, demonstrating that the transduction efficiency of the delivered virus was not compromised by the presence of the Fmoc-SAPs. Data represent the mean + SEM. *$P < 0.05$, **$P < 0.01$. Chromogenic stain of mCherry+ cells in the mouse brain, illustrating the transduction efficiency following (d) direct viral vector delivery, (e) viral vector delivery with Fmoc-DDIKVAV, and (f) viral vector delivery with Fmoc-DDIKVAVK. Note the reduced volume of transduction with the addition of a K residue (5× magnification) (d')–(f'), high-power (20×) images of (d)–(f), illustrating transduced mCherry.

reducing its size and encouraging reinnervation. Delivery within the Fmoc-SAP hydrogel will also avoid neurite misrouting, antibody neutralization, and immune responses that increase as a result vector diffusion, as our scaffold will protect the virus from the host immune response through localized delivery. In addition to Fmoc-SAP's ability to support cells through its nanofibrous architecture, provide high-density presentation of bioactive peptides to direct cell behavior, and capacity for injection into a void, making intimate contact with the surrounding tissue, the designed hydrogel can now limit the spread of the viral vector to non-target tissues and deliver the desired genetic material to cells, providing long-term protein expression for therapeutic benefit.

4 Conclusion

Though viral vectors have emerged as useful tools for the delivery of genetic material, there is a need for a delivery mechanism that will shield the viral vector from the host immune system to improve transduction efficiency and achieve localized long-term therapeutic protein expression. In this work, we established the suitability of Fmoc-SAPs to focally deliver a viral vector into the brain without compromising the infectivity of the virus. The addition of a K residue demonstrated that the additional $-NH_2$ groups resulted in immobilization of the virus within the material, achieving localized transduction of the cells surrounding the injected Fmoc-SAP. With the added versatility of tissue specification through the high-density presentation of the laminin-based IKVAV sequence, such a material holds exciting promise as a valuable tool for continuing advances in gene therapy, particularly viral vector gene delivery for tissue engineering of the CNS.

Acknowledgements

Access to the facilities of the Centre for Advanced Microscopy (CAM) with funding through the Australian Microscopy and Microanalysis Research Facility (AMMRF) is gratefully acknowledged. We acknowledge NanoScope–Scientific Graphics and Illustration for kindly designing the virus immobilization schematic in Fig. 3. We would also like to thank Conor Horgan, Francesca Maclean and Anitha Parnneerselvan for thorough proof reading. Funding for this research was obtained from the National Health and Medical Research Council, Australia (NHMRC, No. APP1050684), and the Australian Research Council (ARC, No. DP130103131). A. L. R. was supported by an Australian Postgraduate Award; R. J. W. was funded via an Alfred Deakin Research Fellowship; C. L. P. was supported by Senior Medical Research Fellowship provided by the Viertel charitable Foundation, Australia; D. R. N. was supported by an ARC Australian Postdoctoral Fellowship, followed by an NHMRC Career Development Fellowship. The Florey Institute of Neuroscience and Mental Health acknowledges the support from the Victorian Government's Operational Infrastructure Support Grant.

References

[1] Jang, J.-H.; Schaffer, D. V.; Shea, L. D. Engineering biomaterial systems to enhance viral vector gene delivery. *Mol. Ther.* **2011**, *19*, 1407–1415.

[2] Wang, K.; Hu, Q. D.; Zhu, W.; Zhao, M. M.; Ping, Y.; Tang, G. P. Structure-invertible nanoparticles for triggered co-delivery of nucleic acids and hydrophobic drugs for combination cancer therapy. *Adv. Funct. Mater.* **2015**, *25*, 3380–3392.

[3] Allen, S. J.; Watson, J. J.; Shoemark, D. K.; Barua, N. U.; Patel, N. K. GDNF, NGF and BDNF as therapeutic options for neurodegeneration. *Pharmacol. Ther.* **2013**, *138*, 155–175.

[4] Orive, G.; Anitua, E.; Pedraz, J. L.; Emerich, D. F. Biomaterials for promoting brain protection, repair and regeneration. *Nat. Rev. Neurosci.* **2009**, *10*, 682–692.

[5] Horne, M. K.; Nisbet, D. R.; Forsythe, J. S.; Parish, C. L. Three-dimensional nanofibrous scaffolds incorporating immobilized BDNF promote proliferation and differentiation of cortical neural stem cells. *Stem Cells Dev.* **2010**, *19*, 843–852.

[6] Levenberg, S.; Burdick, J. A.; Kraehenbuehl, T.; Langer, R. Neurotrophin-induced differentiation of human embryonic stem cells on three-dimensional polymeric scaffolds. *Tissue Eng.* **2005**, *11*, 506–512.

[7] Kauhausen, J.; Thompson, L. H.; Parish, C. L. Cell intrinsic and extrinsic factors contribute to enhance neural circuit reconstruction following transplantation in Parkinsonian mice. *J. Physiol.* **2013**, *591*, 77–91.

[8] Oliveira, S. L. B.; Pillat, M. M.; Cheffer, A.; Lameu, C.; Schwindt, T. T.; Ulrich, H. Functions of neurotrophins and growth factors in neurogenesis and brain repair. *Cytomet. Part A* **2013**, *83A*, 76–89.

[9] Wang, T. Y.; Forsythe, J. S.; Nisbet, D. R.; Parish, C. L. Promoting engraftment of transplanted neural stem cells/progenitors using biofunctionalised electrospun scaffolds. *Biomaterials* **2012**, *33*, 9188–9197.

[10] Alexi, T.; Borlongan, C. V.; Faull, R. L. M.; Williams, C. E.; Clark, R. G.; Gluckman, P. D.; Hughes, P. E. Neuroprotective strategies for basal ganglia degeneration: Parkinson's and Huntington's diseases. *Prog. Neurobiol.* **2000**, *60*, 409–470.

[11] Choi-Lundberg, D. L.; Lin, Q.; Chang, Y.-N.; Chiang, Y. L.; Hay, C. M.; Mohajeri, H.; Davidson, B. L.; Bohn, M. C. Dopaminergic neurons protected from degeneration by GDNF gene therapy. *Science* **1997**, *275*, 838–841.

[12] Géral, C.; Angelova, A.; Lesieur, S. From molecular to nanotechnology strategies for delivery of neurotrophins: Emphasis on brain-derived neurotrophic factor (BDNF). *Pharmaceutics* **2013**, *5*, 127–167.

[13] Kotterman, M. A.; Schaffer, D. V. Engineering adeno-associated viruses for clinical gene therapy. *Nat. Rev. Genet.* **2014**, *15*, 445–451.

[14] Björklund, A.; Kirik, D.; Rosenblad, C.; Georgievska, B.; Lundberg, C.; Mandel, R. J. Towards a neuroprotective gene therapy for Parkinson's disease: Use of adenovirus, AAV and lentivirus vectors for gene transfer of GDNF to the nigrostriatal system in the rat Parkinson model. *Brain Res.* **2000**, *886*, 82–98.

[15] Lentz, T. B.; Gray, S. J.; Samulski, R. J. Viral vectors for gene delivery to the central nervous system. *Neurobiol. Dis.* **2012**, *48*, 179–188.

[16] Wei, G. B.; Ma, P. X. Nanostructured biomaterials for regeneration. *Adv. Funct. Mater.* **2008**, *18*, 3568–3582.

[17] Kim, T. G.; Shin, H.; Lim, D. W. Biomimetic scaffolds for tissue engineering. *Adv. Funct. Mater.* **2012**, *22*, 2446–2468.

[18] Rodriguez, A. L.; Nisbet, D. R.; Parish, C. L. The potential of stem cells and tissue engineered scaffolds for repair of the central nervous system. In *Stem Cells and Cancer Stem Cells*; Hayat, M. A., Ed.; Springer: Netherlands, 2012; Vol. 4, pp 97–111.

[19] Turner, P.; Petch, A.; Al-Rubeai, M. Encapsulation of viral vectors for gene therapy applications. *Biotechnol. Progr.* **2007**, *23*, 423–429.

[20] Matthews, C. B.; Jenkins, G.; Hilfinger, J. M.; Davidson, B. L. Poly-L-lysine improves gene transfer with adenovirus formulated in PLGA microspheres. *Gene Ther.* **1999**, *6*, 1558–1564.

[21] Kidd, M. E.; Shin. S.; Shea, L. D. Fibrin hydrogels for lentiviral gene delivery *in vitro* and *in vivo*. *J. Control. Release* **2012**, *157*, 80–85.

[22] Schek, R. M.; Hollister, S. J.; Krebsbach, P. H. Delivery and protection of adenoviruses using biocompatible hydrogels for localized gene therapy. *Mol. Ther.* **2004**, *9*, 130–138.

[23] Shin, S.; Tuinstra, H. M.; Salvay, D. M.; Shea, L. D. Phosphatidylserine immobilization of lentivirus for localized gene transfer. *Biomaterials* **2010**, *31*, 4353–4359.

[24] Kreppel, F.; Kochanek, S. Modification of adenovirus gene transfer vectors with synthetic polymers: A scientific review and technical guide. *Mol. Ther.* **2008**, *16*, 16–29.

[25] Lee, G. K.; Maheshri, N.; Kaspar, B.; Schaffer, D. V. PEG conjugation moderately protects adeno-associated viral vectors against antibody neutralization. *Biotechnol. Bioeng.* **2005**, *92*, 24–34.

[26] Gersbach, C. A.; Coyer, S. R.; Le Doux, J. M.; García, A. J. Biomaterial-mediated retroviral gene transfer using self-assembled monolayers. *Biomaterials* **2007**, *28*, 5121–5127.

[27] Rey-Rico, A.; Venkatesan, J. K.; Frisch, J.; Schmitt, G.; Monge-Marcet, A.; Lopez-Chicon, P.; Mata, A.; Semino, C.; Madry, H.; Cucchiarini, M. Effective and durable genetic modification of human mesenchymal stem cells via controlled release of rAAV vectors from self-assembling peptide hydrogels with a maintained differentiation potency. *Acta Biomater.* **2015**, *18*, 118–127.

[28] Wu, E. C.; Zhang, S. G.; Hauser, C. A. E. Self-assembling peptides as cell-interactive scaffolds. *Adv. Funct. Mater.* **2012**, *22*, 456–468.

[29] Smith, A. M.; Williams, R. J.; Tang, C.; Coppo, P.; Collins, R. F.; Turner, M. L.; Saiani, A.; Ulijn, R. Fmoc-diphenylalanine self assembles to a hydrogel via a novel architecture based on π–π interlocked β-sheets. *Adv. Mater.* **2008**, *20*, 37–41.

[30] Nisbet, D. R.; Williams, R. J. Self-assembled peptides: Characterisation and *in vivo* response. *Biointerphases* **2012**, *7*, 2.

[31] Li, R.; Horgan, C.; Long, B.; Rodriguez, A. L.; Mather, L.; Barrow, C. J.; Nisbet, D. R.; Williams, R. J. Tuning the mechanical and morphological properties of self-assembled peptide hydrogels via control over the gelation mechanism through regulation of ionic strength and the rate of pH change. *RSC Adv.* **2015**, *5*, 301–307.

[32] Zhou, M.; Smith, A. M.; Das, A. K.; Hodson, N. W.; Collins, R. F.; Ulijn, R. V.; Gough, J. E. Self-assembled peptide-based hydrogels as scaffolds for anchorage-dependent cells. *Biomaterials* **2009**, *30*, 2523–2530.

[33] Modepalli, V. N.; Rodriguez, A. L.; Li, R.; Pavuluri, S.; Nicholas, K. R.; Barrow, C. J.; Nisbet, D. R.; Williams, R. J. *In vitro* response to functionalized self-assembled peptide

scaffolds for three-dimensional cell culture. *Biopolym.: Pept. Sci.* **2014**, *102*, 197–205.

[34] Rodriguez, A. L.; Wang, T. Y.; Bruggeman, K. F.; Horgan, C. C.; Li, R.; Williams, R. J.; Parish, C. L.; Nisbet, D. R. *In vivo* assessment of grafted cortical neural progenitor cells and host response to functionalized self-assembling peptide hydrogels and the implications for tissue repair. *J. Mater. Chem. B* **2014**, *2*, 7771–7778.

[35] Silva, G. A.; Czeisler, C.; Niece, K. L.; Beniash, E.; Harrington, D. A.; Kessler, J. A.; Stupp, S. I. Selective differentiation of neural progenitor cells by high-epitope density nanofibers. *Science* **2004**, *303*, 1352–1355.

[36] Rodriguez, A. L.; Parish, C. L.; Nisbet, D. R.; Williams, R. J. Tuning the amino acid sequence of minimalist peptides to present biological signals via charge neutralised self assembly. *Soft Matter* **2013**, *9*, 3915–3919.

[37] Bye, C. R.; Thompson, L. H.; Parish, C. L. Birth dating of midbrain dopamine neurons identifies A9 enriched tissue for transplantation into Parkinsonian mice. *Exp. Neurol.* **2012**, *236*, 58–68.

Appendix E: Full Published Work (section 7.4)

Ting-Yi Wang, Kiara AF Bruggeman, Rebecca K Sheean, Bradley J Turner, David R Nisbet, Clare L Parish, "Characterization of the Stability and Bio-functionality of Tethered Proteins on Bioengineered Scaffolds IMPLICATIONS FOR STEM CELL BIOLOGY AND TISSUE REPAIR", *Journal of Biological Chemistry*, 2014, vol. 289, pp. 15044-15051 – Reproduced with permission from Elsevier

THE JOURNAL OF BIOLOGICAL CHEMISTRY VOL. 289, NO. 21, pp. 15044–15051, May 23, 2014

Characterization of the Stability and Bio-functionality of Tethered Proteins on Bioengineered Scaffolds

*IMPLICATIONS FOR STEM CELL BIOLOGY AND TISSUE REPAIR**

Received for publication, November 25, 2013, and in revised form, March 31, 2014 Published, JBC Papers in Press, April 3, 2014, DOI 10.1074/jbc.M113.537381

Ting-Yi Wang[‡], Kiara A. F. Bruggeman[§], Rebecca K. Sheean[‡], Bradley J. Turner[‡], David R. Nisbet[§1,2], and Clare L. Parish[‡1,3]

From the [‡]Florey Institute of Neuroscience & Mental Health, The University of Melbourne, Parkville, Australia, 3010 and the [§]Research School of Engineering, The Australian National University, Canberra, Australia, 0200

Background: Tethering proteins onto bioengineered scaffolds enables longterm delivery, however protein stability, release kinetics, and functionality over time remains unknown.
Results: Tethered proteins remain stable and functional for several months, capable of activating intracellular signaling pathways and influencing cell fate.
Conclusion: Tethered proteins are stable and functional long-term.
Significance: Such knowledge may have implications for promoting tissue repair.

Various engineering applications have been utilized to deliver molecules and compounds in both innate and biological settings. In the context of biological applications, the timely delivery of molecules can be critical for cellular and organ function. As such, previous studies have demonstrated the superiority of long-term protein delivery, by way of protein tethering onto bioengineered scaffolds, compared with conventional delivery of soluble protein *in vitro* and *in vivo*. Despite such benefits little knowledge exists regarding the stability, release kinetics, longevity, activation of intracellular pathway, and functionality of these proteins over time. By way of example, here we examined the stability, degradation and functionality of a protein, glial-derived neurotrophic factor (GDNF), which is known to influence neuronal survival, differentiation, and neurite morphogenesis. Enzyme-linked immunosorbent assays (ELISA) revealed that GDNF, covalently tethered onto polycaprolactone (PCL) electrospun nanofibrous scaffolds, remained present on the scaffold surface for 120 days, with no evidence of protein leaching or degradation. The tethered GDNF protein remained functional and capable of activating downstream signaling cascades, as revealed by its capacity to phosphorylate intracellular Erk in a neural cell line. Furthermore, immobilization of GDNF protein promoted cell survival and differentiation in culture at both 3 and 7 days, further validating prolonged functionality of the protein, well beyond the minutes to hours timeframe observed for soluble proteins under the same culture conditions. This study provides important evidence of the stability and functionality kinetics of tethered molecules.

Soluble proteins in their natural physiological environment execute their function and are then degraded by enzymes, oxidation, hydrolysis, and other reactions over relatively short periods of time, thereby losing their original bio-functionality. As such, repeated synthesis and delivery from the local environment is required for ongoing activity (1). When soluble proteins are extrinsically introduced *in vivo* to influence cellular responses (*e.g.* to promote tissue repair or influence disease progression) they are also only present for short periods of time (typically minutes to hours), due to diffusion into the local physiological environment and degradation. Hence methods of ongoing delivery must be employed which typically rely on the use of cumbersome catheters and infusion pumps. Consequently there is increasing interest to develop improved methodologies to enable the stable delivery of molecules and proteins, and to ensure these factors can be administered in temporally and spatially appropriate manners.

Work by us and others has already demonstrated that protein immobilization onto bioengineered scaffolds can provide means to control the localization of biological molecules, create longer lasting stimuli, and can be controlled by way of substrata (scaffold) degradation. We demonstrated that when tethered onto electrospun nanofibrous scaffolds both brain-derived neurotrophic factor (BDNF)[4] and glial-cell derived neurotrophic factor (GDNF) were capable of promoting neural stem cell proliferation and influencing differentiation *in vitro* to a greater extent than culturing cells in the presence of soluble protein (2, 3). Furthermore, we showed that tethered GDNF

* This research was supported by funding from the Australian Research council, Bethlehem Griffith Research Foundation, and the Australian National University Major Equipment Committee Fund.
[1] Both authors contributed equally to this work.
[2] Supported by an Australian Research Council Australian Postdoctoral Fellowship and subsequently an NHMRC Career Development Fellowship (APP1050684). To whom correspondence may be addressed: The Australian National University, Canberra. Tel.: +612-6125-7451; E-mail: david.nisbet@anu.edu.au.
[3] Supported by Senior Medical Research Fellowship provided by the Viertel Charitable Foundation, Australia. To whom correspondence may be addressed: Florey Institute of Neuroscience & Mental Health, The University of Melbourne, Parkville, Australia, 3010. Tel.: +613-9035-6526; Fax: +613-9347-0446; E-mail: cparish@unimelb.edu.au.

[4] The abbreviations used are: BDNF, brain-derived neurotrophic factor; E, embryonic day; ED, ethylenediamine; GDNF, glial-derived neurotrophic factor; iGDNF, immobilized glial-derived neurotrophic factor; iGDNF(v), immobilized glial derived neurotrophic factor scaffolds that have been exposed to vortexing; NSC, neural stem cell; PCL, poly ϵ-caprolactone; sGDNF, soluble glial-derived neurotrophic factor.

maintained long-term biofunctionality *in vivo*, supporting the survival, differentiation, and integration of transplanted neural stem cells for up to 28 days (3). Work by others has similarly demonstrated the benefit of tethered proteins. By way of example, photochemically bound nerve growth factor on microporous poly(2-hydroxyethylmethacrylate) was shown to encourage neurite outgrowth of PC12 cells (4); methacrylamide chitosan immobilized with rat interferon-γ promoted neural differentiation of adult neural stem/progenitor cells (5, 6); and tethered epidermal growth factor (EGF) on poly(methyl methacrylate)-*graft*-poly(ethylene oxide) significantly enhanced mesenchymal stem cell (MSC) spreading and survival compared with saturating concentrations of soluble EGF (7).

Despite evidence for the benefit of immobilized proteins, little attention has been paid to the amount of protein tethered to biomaterial surfaces, stability and longevity of tethered proteins, protein degradation rate, the release kinetics of tethered molecules, activation of intracellular signaling pathway, or the duration of functionality of the protein. Here we investigated the stability of a tethered protein, GDNF, its activation of intracellular signaling pathway, and its functionality using primary cultures isolated from the developing ventral midbrain, enriched with dopaminergic neurons. GDNF has been shown to promote the survival, differentiation, and neurite growth, most notably of dopaminergic neurons *in vitro* and *in vivo* (8, 9). GDNF has additionally been shown to delay degeneration of dopaminergic neurons in Parkinsonian animals as well as promote the survival and integration of these neurons following transplantation into animal models of the disease (10–13). GDNF therefore represents an example whereby prolonged protein delivery could have a significant impact on stem cell populations *in vitro*, disease progression and disease treatment. Our findings demonstrated long-term presence and functionality of GDNF, with no evidence of degradation or leaching, thereby highlighting the potential benefit of tethered molecules in applications such as tissue repair where prolonged exposure to trophic proteins is likely to be of benefit.

EXPERIMENTAL PROCEDURES

Synthesis of Electrospun Scaffolds—Electrospun fibers were produced from polycaprolactone (PCL, Mn 70–90k, Sigma Aldrich), dissolved in a 3:1 (v/v) solution of chloroform (Chem-Supply) and methanol (Chem-Supply), respectively. A home built electrospinner consisting of a syringe pump (KD-100, KD Scientific, Holliston) and an adjustable DC voltage power supply (Model RR 50-1.25R/230/DDPM, Gamma High Voltage Research, Ormond Beach, FL) was employed. Spinning was performed at room temperature using a 20 kV voltage, a 21-gauge needle, a 2 ml/h flow rate, and a 13 cm working distance. The duration of electro-spinning and collection onto a spinning mandrel resulted in two-dimensional (100 um) and three-dimensional (250–300 μm thick) scaffolds, as confirmed by scanning electron microscopy and previously reported (2). After collection, the scaffolds were dried in a vacuum oven at 37 °C overnight (Labec Laboratory Equipment, Australia) and stored in a desiccator prior to use. The scaffolds were then aminolysed by immersion in 0.05 M ethylenediamine (ED, Sigma Aldrich), diluted in 2-propanol (Merck Pty, Australia) for 15 min at room temperature with moderate stirring. The samples were subsequently washed three times with ice-cold distilled water, and sterilized in 70% ethanol for 15 min.

Scanning Electron Microscopy—To validate scaffold structure and assembly, samples were coated with ~2 nm of platinum by sputtering at 20 mA for 1 min. A scanning electron microscope was then used to visualize the morphology of the electrospun materials (Zeiss Ultra Plus FE-S.E., 7.5 μm aperture at 3 kV). A working distance of 3.4 mm and magnification of ×4950 was employed.

Confirmation of Aminolysation—Scaffolds treated with ED (Sigma Aldrich Pty Ltd) were dissolved in 100 μl of tetrahydrofuran and 100 μl of PBS, and reacted with 100 μl of fluorescamine (Molecular Probes, 10 mg/ml in acetone). The fluorescence was detected using a plate reader with ex/em = 390/475–490 nm. For the standard curve amine concentrations included 1.49×10^{-6}, 1.12×10^{-6}, 7.45×10^{-7}, 1.49×10^{-7}, 7.45×10^{-8}, 1.49×10^{-8}, 7.45×10^{-9}, and 0 mol/g of ED in PBS.

Protein Tethering on PCL Scaffolds—For immobilization of GDNF onto PCL scaffolds, 4-(*N*-maleimidomethyl) cyclohexane-1-carboxylic acid 3-sulfo-*N*-hydroxy-succinimide ester sodium salt (sulfo-SMCC, Sigma Aldrich) was used as a cross-linker. A 2.5 mg/ml sulfo-SMCC solution in PBS was gently shaken for an hour at room temperature and then filtered (0.22 mm filter). The PCL scaffolds, after treatment with ED, were immersed in the prepared sulfo-SMCC solution for 2 h at room temperature with gentle agitation, then transferred to a recombinant human GDNF solution (4 mg/ml; R & D Systems) overnight at 4 °C. To ensure that GDNF protein was attached and not simply absorbed onto the scaffolds some scaffolds were vortexed in PBS for minutes following protein immobilization. Amounts of tethered protein, stability, and functionality were compared between: PCL scaffolds (PCL), PCL scaffolds tethered with GDNF (PCL_iGDNF), and PCL scaffolds tethered with GDNF and vortexed (PCL_iGDNF(v)). GDNF was additionally tethered to aminolysed scaffolds in the presence of artificial cerebrospinal fluid (aCSF) to confirm stability and function in a biologically relevant fluid.

Enzyme-linked Immunoabsorbent Assay—Enzyme-linked immunoabsorbent assays (ELISA) were performed as described previously (3). In brief, PCL scaffolds, + GDNF attachment, were incubated in 1 mg/ml of goat anti-GDNF antibody (R & D Systems) containing 5% donkey serum in PBST (PBS containing 0.05% Tween-20) for 2 h at room temperature. The scaffolds were washed three times in PBST before being immersed in anti-goat horseradish peroxidase (HRP, 1:2000 in PBST solution containing 2% donkey serum) for 1 h. After three washes in PBST, scaffolds were placed in a 96-well plate where the bound HRP activity was assessed by color development using TMB microwell peroxidase system (R & D Systems). 30 μl of 1 M HCl was added to each well to stop the reaction, and the absorbance (at 450 nm) was measured with a microtiter plate reader (SpectraMax). A standard curve for GDNF was performed (0–10,000 pg/ml) from which the amount of bioavailable tethered GDNF protein per scaffold could be determined and compared across treatments. To determine the stability of tethered GDNF over time, scaffold samples were collected immediately

after protein attachment (day 0) and at 3, 7, 14, 28, and 120 days after attachment and storage in PBS and aCSF.

To assess whether tethered proteins were susceptible to proteolytic degradation of tethered proteins we treated iGDNF scaffolds with 0.25% trypsin (Invitrogen) for 10 min and compared the amount of GDNF present on PCL to non-trypsin-treated iGDNF scaffolds. Collected scaffolds and supernatant were stored at −80 °C until determination of protein levels by sandwich ELISA.

BET Surface Area Analysis of PCL Scaffolds—Brunauer-Emmett-Teller (BET) surface area analysis was performed using a micromeritics TriStar II surface area and porosity instrument to determine the surface area of the scaffolds (14), and subsequently the amount of GDNF tethered onto the PCL surface. 45 mg of untreated polymer scaffold was loaded into a dry 0.95-cm diameter sample tube and degassed under vacuum (0.15–0.3 mbar) at room temperature for 7 days on a micromeritics VacPrep 061 sample degas system. The degassed sample mass was determined to be 43 mg. The sample tube was then loaded into the instrument for adsorption analysis of nitrogen gas in a liquid nitrogen bath. The specific surface area was determined to be 3.0050 m^2/g. The weight of the punch biopsies (0.6 cm in diameter) on which GDNF was attached, and cells cultured, was 0.80 mg so the absolute surface area was $0.0008\ g \times 3.0050\ m^2/g = 0.0024\ m^2 = 24\ cm^2$.

Immunoblotting—The dopaminergic neural stem cell line, SN4741, was cultured in DMEM, 10% FBS, L-glutamine (2 mM), penicillin/streptomycin (50 units/ml), and glucose (0.6%). For analysis of intracellular GDNF signaling, 100,000 cells were seeded onto 12-well plates or PCL scaffolds. At 70% confluency the cells were changed into serum-free media with or without GDNF (soluble or immobilized). A standard curve of GDNF treatment (0, 3, 10, 30, 100 ng/ml), using the same cell line, was performed in parallel to quantify the levels of GDNF activity. Cells were stimulated with soluble GDNF (sGDNF, 30 ng/ml) for 60 min or 3 days, and tethered GDNF (iGDNF) for 1 day or 3 days prior to being lysed in ice-cold buffer containing 20 mM Tris-Cl, pH 7.5, 150 mM NaCl, 1% Triton X-100, 1% protease inhibitor mixture (Sigma), 50 mM NaF, and 0.2 mM Na_3VO_4 for 20 min on ice. Lysates were centrifuged at 14,000 rpm for 20 min at 4 °C to collect supernatants. Protein was quantified using the bicinchoninic acid assay kit (Pierce) using bovine serum albumin standards.

Protein (50 μg) was electrophoresed through 12.5% SDS-polyacrylamide gels and transferred to Immobilon PVDF-FL membrane (Millipore). Membranes were blocked with 5% skim milk in Tris-buffered saline with Tween-20 (TBST), pH 8.0, for 30 min and incubated with mouse pErk1,2 (1:2,000, #9106, Cell Signaling Technology) and rabbit total Erk1,2 (1:1,000, #9102, Cell Signaling Technology) antibodies in 3% BSA in TBST overnight at 4 °C. Blots were washed 3× in TBST for 10 min and incubated with IRDYe 680 and 800CW-conjugated secondary antibodies (1:10,000) followed by 3× washes in TBST for 10 min and detected using the Odyssey Classic infrared imaging system. Membranes were then stripped and re-probed with mouse anti β-actin (1:5000, Sigma). Blots were quantified by taking the ratio of pErk/Erk bands and subtracting background intensity.

Microdissection and Culturing of Ventral Midbrain Progenitors—All procedures were conducted in accordance with the Australian National Health and Medical Research Council's published Code of Practice for the Use of Animals in Research, and experiments were approved by the Florey Neuroscience Institute animal ethics committee. C57BL/6 mice were housed on a 12 h light/dark cycle with *ad libitum* access to food and water. Cells used for *in vitro* culturing were obtained from mice that were time mated overnight, with visualization of a vaginal plug on the following morning taken as embryonic day (E) 0.5. Ventral midbrain (VM) tissue was isolated at mouse embryonic day 11.5 (E11.5).

Pregnant mice (E11.5) were anesthetized with isoflurane prior to cervical dislocation. The collected embryos were immersed in chilled L15 medium (Invitrogen), the brains removed and ventral midbrain microdissected. Subsequently the tissue fragments were incubated in 0.1% DNase and 0.05% trypsin (in magnesium and calcium free Hank's buffered saline solution, HBSS) for 15 min followed by three gentle washes in HBSS. Finally, the tissue fragments were dissociated in N_2 media consisting of a 1:1 mixture of F12 and MEM supplemented with 15 mM HEPES buffer, 1 mM glutamine, 6 mg/ml glucose (Sigma-Aldrich), 1.5 mg/ml bovine serum albumin, and 1% N2 supplement (all purchased from Invitrogen). Cells were seeded at a density of 175,000 cells/cm^2 onto either poly-D-lysine-coated coverslips (in the presence or absence of soluble GDNF, 30 ng/ml) or PCL scaffolds (+ immobilized GDNF) and incubated at 37 °C in 5% CO_2 for 3 and 7 days. After 3 days and 7 days, the cells were fixed with 4% paraformaldehyde for 20 min, washed, and stored in PBS containing 0.025% sodium azide until the time of immunocytochemistry.

Immunocytochemistry—Fixed cultures were incubated overnight in the following primary antibodies (diluted in 0.3% Triton X and 5% donkey serum): mouse anti-β tubulin (TUJ1, 1:1500, Promega, neuronal marker), and rabbit anti-tyrosine hydroxylase (TH, 1:400 Pelfreeze, rate-limiting enzyme in dopamine synthesis and marker of dopaminergic neurons). Cultures were then washed for 10 min in PBS before the secondary antibodies were subsequently added and incubated for an hour at room temperature. Secondary antibodies (1:300 in PBS containing 0.3% Triton X and 2% of goat/donkey serum) were as follows: DyLight 488 donkey anti-rabbit (Jackson ImmunoResearch), DyLight 549 donkey anti-mouse (Jackson immunoResearch). After washing in PBS, Hoechst (1:1000 in PBS, nuclei marker) was applied for 5 min, followed by two washes. The samples were then slide mounted (Dako) and imaged using a fluorescence microscope.

Statistical Analysis—For all ELISAs, Western blots, and cell cultures ≥3 independent experiments were performed with three coverslips or scaffolds included for each condition in each experiment. For assessments of cell viability and differentiation, 10 fields of view per coverslip or scaffold were imaged using a Zeiss200 inverted microscope (images captured at 20x magnification). All data are expressed as mean ± S.D. Student's t-tests or one-way ANOVAs with Tukey post-hoc tests were used to show significant differences between groups with the level of significance set at 0.05.

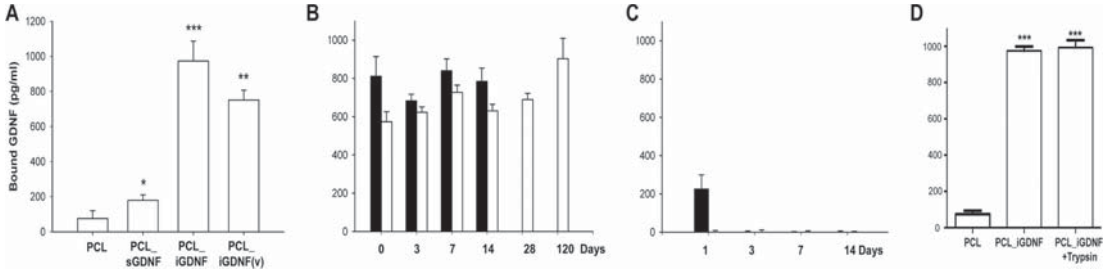

FIGURE 1. **Confirmation of protein tethering and stability on electrospun nanofibers.** *A*, immobilization of GDNF on PCL scaffolds (iGDNF) significantly increases the presentation of protein in culture. The majority of protein was covalently attached as reflected by vortexing to remove excess absorbed protein (iGDNF(v)). *B*, amount of GDNF presents on scaffolds at 0, 3, 7, and 14 days after attachment without vortexing (*black bars*) and at 0, 3, 7, 14, 28, and 120 days after attachment with vortexing (*white bars*). No significant decrease was observed in the amount of GDNF on the scaffolds over time, indicative of protein stability. *C*, small amount of GDNF was absorbed onto the scaffolds at the time of tethering, which leached from the biomaterial within the first day, and subsequently degraded. *D*, treatment of iGDNF scaffolds with trypsin had no effect on the amount of GDNF protein present compared with iGDNF alone, indicating that tethered GDNF was resistant to proteolysis. Data represent mean + S.E. *, $p < 0.05$; **, $p < 0.01$; ***, $p < 0.001$; one-way ANOVA with Tukey post-hoc test.

RESULTS AND DISCUSSION

Because of the high surface area to volume ratio, tuneable surface chemistry and biomimetic environment, electrospun scaffolds have been applied as a delivery system of biological molecules to influence cell behavior *in vitro* and *in vivo* (15, 16). As proof of principle, we previously demonstrated that the three-dimensional structure of electrospun PCL scaffolds could be exploited to deliver neurotrophins BDNF and GDNF *in vitro* to influence cell survival, proliferation, and differentiation (2, 3). Furthermore, implantation of GDNF functionalized scaffolds promoted the engraftment of neural transplants for up to 28 days (3). However in these former studies, and others like it exploring the benefits of tethered proteins, there remains insufficient knowledge pertaining to the amount of immobilized protein on the scaffold surface, the stability of the tethered protein, activation of intracellular signaling pathway, or the biofunctionality of the molecules over time. In the present study we examined the stability of immobilized GDNF on electrospun PCL scaffolds over 120 days (at 37 °C) and the biological effects on primary neurons in cultures. Specifically, we examined the ability of tethered GDNF protein to activate intracellular signaling pathways and to promote survival and dopaminergic differentiation of ventral midbrain cells for up to 7 days in culture.

Confirmation of Protein Immobilization and Maintained Presentation without Degradation—The electrospun PCL scaffolds were treated with ethylenediamine (ED) to produce amine groups on the fiber surface for protein (GDNF) attachment via a crosslinker, succinimidyl 4-(*N*-maleimidomethyl)-cyclohexane-1-carboxylate (SMCC) (2). The amount of fluorescamine on the scaffolds after aminolysation was measured to be 1.2×10^{-11} mol/g. Subsequent GDNF attachment onto the scaffolds (24 cm^2), via SMCC crosslinking, was confirmed by ELISA. Results showed significant levels of GDNF on the scaffold (PCL_iGDNF; 975 + 115 pg), compared with PCL scaffolds alone (75 + 45 pg; reflective of background readings) or in the absence of the SMCC crosslinker (PCL_sGDNF, 180 + 30 pg; reflective of physically absorbed GDNF into the scaffold), Fig. 1*A*. Furthermore we confirmed the benefit of utilizing 3D scaffolds, with significantly more (5-fold) GDNF attachment that observed on 2D PCL electrospun scaffolds (data not shown). In light of BET analysis, demonstrating a total surface area of 24 cm^2 for the 0.6 cm diameter PCL scaffold inserts used for protein attachment, and a total of 975 + 115 pg GDNF on the scaffold, we were able to estimate a total of 41 pg of tethered GDNF per cm^2 of PCL scaffolds.

To confirm that the majority of the protein was tethered, and not absorbed onto the scaffolds, we vortexed the scaffolds that had been immobilized with GDNF to shake off any protein embedded but not tethered to the PCL fibers. Under these conditions, no significant difference was seen in GDNF levels on PCL_iGDNF and PCL_iGDNF with vortexing (PCL_iGDNF: 975 + 115 pg, and PCL_iGDNF(v): 650 + 60 pg, respectively, Fig. 1*A*), indicating that the majority of the protein was covalently attached.

To examine the stability of tethered GDNF on scaffolds, the immobilized scaffolds were immersed in PBS for up to 120 days, with PCL scaffold samples collected at day 0 (*i.e.* upon completion of protein immobilization), day 3, 7, 14, 28, and 120 days and supernatant collected at days 1, 3, 7, and 14 days. All samples were stored at −80 °C prior to performing ELISAs. Importantly, we confirmed that freezing of scaffolds had no effect on the stability of the protein, with no significant difference observed in the amount of tethered protein at day 0 from fresh *versus* frozen PCL_iGDNF samples (975 + 115 pg and 810 + 100 pg, respectively, Fig. 1, *A* and *B*). Examination of PCL_iGDNF scaffolds, with or without vortexing, showed no significant difference in GDNF concentration over time (day 0, 3, 7, 14, 28, or 120 days), demonstrating that the protein remained tethered on the scaffold without degradation for at least 120 days (Fig. 1*B*) and thereby highlighting the potential application of these scaffolds for long-term protein presentation. Tethered GDNF stability was additionally confirmed in artificial cerebrospinal fluid (aCSF), with no difference in the level of GDNF present at 1 and 7 days, or from stability in PBS conditions (data not shown). Under these various culturing conditions, the degradation of covalently attached proteins is likely to occur through surface erosion of the electrospun scaffold. Hence, based upon our previous work, we anticipate pro-

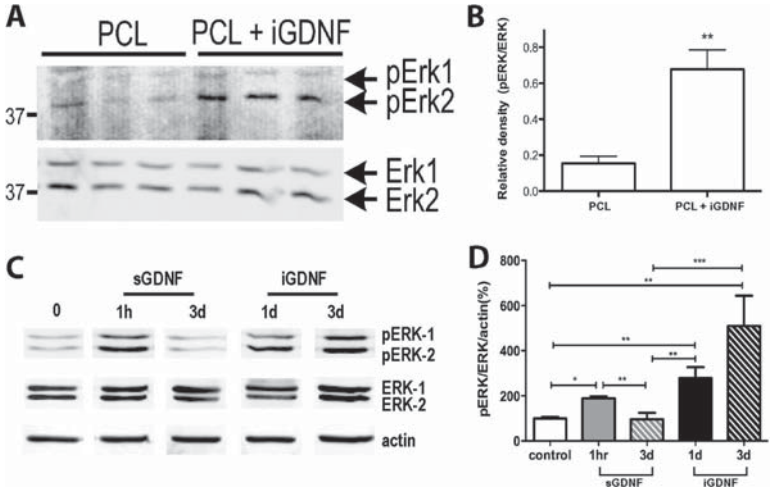

FIGURE 2. **Phosphorylation of intracellular ERK confirms functionality and longevity of tethered GDNF.** *A*, culturing of SN4741 neural cells on PCL+iGDNF, but not PCL alone, resulted in phosphorylation of intracellular Erk determined by immunoblot analysis, indictive of intracellular signaling in response to GDNF presentation. *B*, ratio of phospho-ERK/total ERK level. Tethered GDNF results in a 4.4-fold increase in pERK/ERK level compared with culturing on PCL. *C* and *D*, phospho-ERK levels were significantly elevated after 1 h of stimulation of SN4741 cells with soluble GDNF, but returned to basal levels within 3 days. By contrast culturing cells on iGDNF resulted in maintained elevated pERK levels (at 1 and 3 days in culture). Data represent mean + S.E. *, $p < 0.05$, **, $p < 0.01$; ***, $p < 0.001$, Student's *t* test and one-way ANOVA.

teins are likely to remain present in culture in excess of 12 months (17).

Results from the supernatant revealed that any absorbed protein leached from the scaffold within 24 h (225 + 75 pg, Fig. 1*C*), and was comparable to the difference observed between iGDNF (PCL_iGDNF: 819 + 100 pg, Fig. 2*B*) and vortexed iGDNF (PCL_iGDNF(v): 515 + 50 pg, Fig. 1*B*). Interestingly, GDNF was only marginally detectable in the supernatant at 3, 7, and 14 days, indicating that the protein measured in the supernatant after 24 h had likely degraded, and thereby further highlighting the benefit of protein tethering for biological applications.

Under biological setting proteases are responsible for the degradation of soluble proteins. To determine whether immobilized proteins may be susceptible to proteolytic degradation we treated iGDNF scaffolds with the protease trypsin and compared the amount of GDNF present to non-trypsinized iGDNF scaffolds. Results showed no significant difference in the amount of GDNF present following trypsin treatment, indicating that our tethered proteins were resistant to proteolysis (Fig. 1*D*).

Here we demonstrate the ability to covalently tether GDNF onto the surface of electrospun PCL scaffolds using the sulfo-SMCC protein crosslinking reaction. This linking is dependent on the protein of interest possessing sulfhydryls (thiols, -SH), which readily react with the maleimide group within the sulfo-SMCC at pH 6.5–7.5. However, it is still possible for maleimides to react with amines, such as those found on the N terminus of a protein or peptide (18). At pH > 7.5 the reactivity of maleimides to amines begins to increase and as our reactions were conducted in PBS (pH 7.4) the same chemistry can be used to tether a protein that does not possess a free sulfhydryl group, although the reaction will be slower. However, it should be noted that hydrolysis of the maleimide group is a possibility during such a conjugation. In this regard, the ability to tether a particular protein may therefore be dependent on the structure of the protein to be tethered (*i.e.* the binding affinity of the maleimide). Furthermore, while it may be possible to attach a number of different proteins using this approach it will also be important to ensure that such crosslinking does not interfere with the cellular accessibility of the protein surface. In this regard it may be necessary to assess other crosslinkers for protein attachment.

The Biofunctionality of Tethered GDNF on Cultured Neurons—Next we investigated the bio-functionality of tethered GDNF on a neural stem cell line in culture. Using the dopaminergic cell line (SN4741), known to express the GDNF receptors, c-ret and GFRa1, we examined the ability of tethered GDNF to induce intracellular phosphorylation of ErK1 and ErK2, key components of the GDNF-ErK signaling pathway. Comparable levels of total ErK1 and 2 could be detected in cells cultured on both PCL and PCL_iGDNF. However, the presence of GDNF significantly increased the phosphorylation of ErK (Fig. 2*A*), indicating that tethered GDNF was capable of mediating intracellular GDNF signaling. Quantification of band density revealed a significant (4.4-fold) increase in the ratio of phospho-ErK to total ErK following culturing on tethered GDNF, Fig. 2*B*. Next we examined the duration of functionality of tethered GDNF. While soluble GDNF (30 ng/ml) significantly increased pErK levels after 1 h of stimulation, by 3 days in culture pErK levels were not significantly different to untreated cultures, reflective of degradation of the GDNF protein. By comparison, tethered GDNF resulted in a significant increase in pErK levels at 1 day and was maintained for 3 days in culture (Fig. 2, *C* and *D*). GDNF has been demonstrated to be sufficient to promote cell survival, differentiation, and neurite growth of both rodent and human primary, neural, and pluripotent stem cells (19–26).

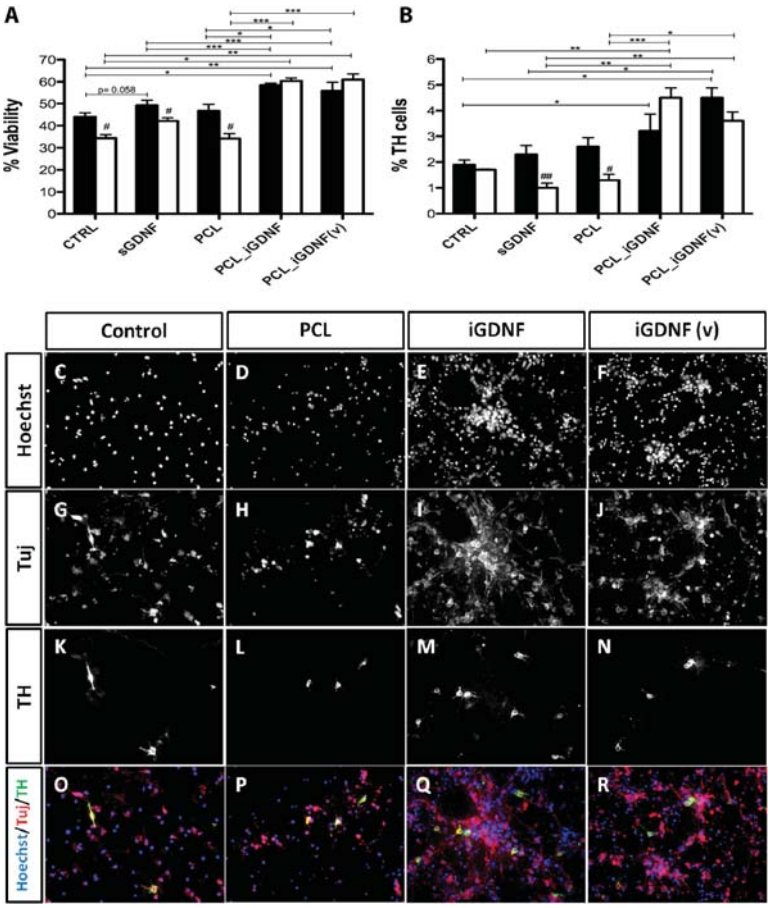

FIGURE 3. **GDNF immobilization enhances cell viability and differentiation.** *A*, GDNF protein tethering, with or without vortexting, significantly increased the viability and (*B*) proportion of tyrosine hydroxylase-immunoreactive (TH+) cells in ventral midbrain cultures, compared with soluble GDNF (sGDNF, at 7 days) and culturing under control conditions (PDL-coated plastic, control or PCL scaffolds, *PCL*). *Black bars*: 3 days *in vitro* (DIV), *white bars*: 7 DIV. Prolonged culturing (7DIV) resulted in a significant decrease in cell viability and TH cells, effects that could be prevented by maintained presentation of GDNF in culture. *C–F*, representative photomicrographs of Hoechst-labeled nuclei, *G–J*, TUJ+ neurons, *K–N*, TH+ dopaminergic neurons, and *O—R*, merged images of VM cells cultured on PDL-coated plastic (control), PCL, PCL with immobilized GDNF (PCL_iGDNF), and PCL with immobilized GDNF and vortexed (PCL_iGDNF(v)). Data represent mean + S.E. *, $p < 0.05$, **, $p < 0.01$, ***, $p < 0.001$. #, $p < 0.05$; ##, $p < 0.01$, 7 days in culture significantly different from same condition at 3 days in culture ($p < 0.05$). One-way ANOVA with Tukey post-hoc test.

These functions of GDNF have been additionally supported by increased phosphorylation of Erk. However to achieve these effects commonly requires repeated protein delivery, particularly in *in vivo* contexts. Here we demonstrate tethered protein is capable of activating intracellular Erk to a similar magnitude. Importantly however, the temporal expression and ability to maintain signaling (*i.e.* phospho-Erk levels) is sustainable, and may therefore present a superior method to prolong functional protein delivery for *in vitro* and *in vivo* applications.

Finally we examined the ability of tethered GDNF to not only induce an intracellular response, but also provide a prolonged effect on neural progenitors in culture. Here we demonstrate that soluble GDNF (added at the time of cell seeding) increased cell survival (and proportion of TH+ dopaminergic neurons) at 3 days, however viability significantly diminished thereafter to levels not different from untreated controls (Fig. 3, *A* and *B*), presumably reflecting insignificant GDNF levels in the media beyond this time. By contrast, tethering GDNF onto the scaffold surface significantly increased and maintained cell survival. After 3 days in culture, we demonstrated that tethered GDNF significantly improved the viability of VM cells (Hoechst labeled non-pyknotic nuclei) in culture compared with cells cultured on PDL coated plastic (56.37% + 0.96 and 44.04% + 1.78, respectively), or PCL scaffolds alone (46.74% + 2.86), Fig. 3. Similarly immobilized GDNF enhanced the number of tyrosine Hydroxylase immunoreactive (TH+) dopaminergic cells in culture, Fig. 3, *B*, *K–N*. After 7 days, cells cultured in the presence of immobilized GDNF showed no decrease in cell viability or the proportion of dopaminergic neurons compared with 3 days in culture, demonstrating maintained activity of

GDNF, while cells cultured on PCL alone showed significantly reduced viability over time (Fig. 3). These findings demonstrate the benefits of maintained presentation and functionality of tethered protein.

The development of assays to provide long-term presentation of molecules is important for increasing our understanding of physiological processes. Most *in vitro* studies focused on understanding the role of a given molecule in development, adult homeostasis, or disease rely on application of soluble proteins in culture; effects that are rapid and transient and often do not reflect the ongoing presentation of a protein that typically occurs in nature. In addition to providing a more relevant assay to understand these basal and pathophysiological functions, the use of tethered proteins can also aid in the development of new treatments. For example, long term delivery of GDNF *in vivo*, by way of protein tethering onto bioengineered scaffolds, such as microspheres, could be exploited to stall disease progression in PD, or promote the survival and integration of newly transplanted dopaminergic neurons for patients. The development of such protein/molecule tethering technologies will be dependent on ongoing validation of protein/molecule stability and function, using methodologies such as those described here.

CONCLUSION

Protein immobilization on the surface of tissue engineering scaffolds has been investigated for their potential to influence cellular responses *in vitro* and *in vivo*. While the benefits of tethered proteins have been recognized for some years now, there has been a notable lack of research concentrating on their stability and bio-functionality kinetics. Here we demonstrate, by way of GDNF as an example, that tethered proteins on electrospun scaffolds are stable for prolonged periods of time (with no evidence of degradation), activate intracellular signaling cascades, and maintain cellular effects (GDNF influencing cell viability and differentiation). These findings hold significant potential for the use of biomaterials in presenting and maintaining the activity of proteins *in vitro* and *in vivo*, and may impact on the ability to enhance tissue repair.

Acknowledgments—We thank Francesca Maclean for electrospinning and Dr. Francesca Ercole for assistance with the determination of attached amines. Access to the facilities of the Centre for Advanced Microscopy (CAM) with funding through the Australian Microscopy and Microanalysis Research Facility (AMMRF) is gratefully acknowledged.

REFERENCES

1. Tessmar, J. K., and Göpferich, A. M. (2007) Matrices and scaffolds for protein delivery in tissue engineering. *Adv. Drug Delivery Rev.* **59,** 274–291
2. Horne, M. K., Nisbet, D. R., Forsythe, J. S., and Parish, C. L. (2010) Three-dimensional nanofibrous scaffolds incorporating immobilized BDNF promote proliferation and differentiation of cortical neural stem cells. *Stem Cells Dev.* **19,** 843–852
3. Wang, T. Y., Forsythe, J. S., Nisbet, D. R., and Parish, C. L. (2012) Promoting engraftment of transplanted neural stem cells/progenitors using biofunctionalised electrospun scaffolds. *Biomaterials* **33,** 9188–9197
4. Kapur, T. A., and Shoichet, M. S. (2003) Chemically-bound nerve growth factor for neural tissue engineering applications. *J. Biomater. Sci. Polym. Ed.* **14,** 383–394
5. Leipzig, N. D., Wylie, R. G., Kim, H., and Shoichet, M. S. (2011) Differentiation of neural stem cells in three-dimensional growth factor-immobilized chitosan hydrogel scaffolds. *Biomaterials* **32,** 57–64
6. Leipzig, N. D., Xu, C., Zahir, T., and Shoichet, M. S. (2010) Functional immobilization of interferon-γ induces neuronal differentiation of neural stem cells. *J. Biomed. Mat. Res.* **93,** 625–633
7. Fan, V. H., Tamama, K., Au, A., Littrell, R., Richardson, L. B., Wright, J. W., Wells, A., and Griffith, L. G. (2007) Tethered epidermal growth factor provides a survival advantage to mesenchymal stem cells. *Stem Cells* **25,** 1241–1251
8. Haniu, M., Hui, J., Young, Y., Le, J., Katta, V., Lee, R., Shimamoto, G., and Rohde, M. F. (1996) Glial cell line-derived neurotrophic factor: selective reduction of the intermolecular disulfide linkage and characterization of its disulfide structure. *Biochemistry* **35,** 16799–16805
9. Consales, C., Volpicelli, F., Greco, D., Leone, L., Colucci-D'Amato, L., Perrone-Capano, C., and di Porzio, U. (2007) GDNF signaling in embryonic midbrain neurons *in vitro*. *Brain Res.* **1159,** 28–39
10. Nakajima, K., Hida, H., Shimano, Y., Fujimoto, I., Hashitani, T., Kumazaki, M., Sakurai, T., and Nishino, H. (2001) GDNF is a major component of trophic activity in DA-depleted striatum for survival and neurite extension of DAergic neurons. *Brain Res.* **916,** 76–84
11. Ortiz-Ortiz, M. A., Morán, J. M., Ruiz-Mesa, L. M., Bonmatty, R. G., and Fuentes, J. M. (2011) Protective effect of the glial cell line-derived neurotrophic factor (GDNF) on human mesencephalic neuron-derived cells against neurotoxicity induced by paraquat. *Environ. Toxicol. Pharmacol.* **31,** 129–136
12. Sandhu, J. K., Gardaneh, M., Iwasiow, R., Lanthier, P., Gangaraju, S., Ribecco-Lutkiewicz, M., Tremblay, R., Kiuchi, K., and Sikorska, M. (2009) Astrocyte-secreted GDNF and glutathione antioxidant system protect neurons against 6OHDA cytotoxicity. *Neurobiol. Dis.* **33,** 405–414
13. Alexi, T., Borlongan, C. V., Faull, R. L., Williams, C. E., Clark, R. G., Gluckman, P. D., and Hughes, P. E. (2000) Neuroprotective strategies for basal ganglia degeneration: Parkinson's and Huntington's diseases. *Prog. Neurobiol.* **60,** 409–470
14. Nisbet, D. R., Rodda, A. E., Finkelstein, D. I., Horne, M. K., Forsythe, J. S., and Shen, W. (2009) Surface and bulk characterisation of electrospun membranes: problems and improvements. *Colloids Surfaces. B, Biointerfaces* **71,** 1–12
15. Nisbet, D. R., Rodda, A. E., Horne, M. K., Forsythe, J. S., and Finkelstein, D. I. (2009) Neurite infiltration and cellular response to electrospun polycaprolactone scaffolds implanted into the brain. *Biomaterials* **30,** 4573–4580
16. Nisbet, D. R., Forsythe, J. S., Shen, W., Finkelstein, D. I., and Horne, M. K. (2009) Review paper: a review of the cellular response on electrospun nanofibers for tissue engineering. *J. Biomaterials Appl.* **24,** 7–29
17. Nisbet, D. R., Pattanawong, S., Nunan, J., Shen, W., Horne, M. K., Finkelstein, D. I., and Forsythe, J. S. (2006) The effect of surface hydrophilicity on the behavior of embryonic cortical neurons. *J. Colloid Interface Sci.* **299,** 647–655
18. Sharpless, N. E., and Flavin, M. (1966) The reactions of amines and amino acids with maleimides. Structure of the reaction products deduced from infrared and nuclear magnetic resonance spectroscopy. *Biochemistry* **5,** 2963–2971
19. Chen, Y., Ai, Y., Slevin, J. R., Maley, B. E., and Gash, D. M. (2005) Progenitor proliferation in the adult hippocampus and *substantia nigra* induced by glial cell line-derived neurotrophic factor. *Exp. Neurol.* **196,** 87–95
20. Enomoto, H. (2005) Regulation of neural development by glial cell line-derived neurotrophic factor family ligands. *Anat. Sci. Int.* **80,** 42–52
21. Lee, C. S., Tee, L. Y., Dusenbery, S., Takata, T., Golden, J. P., Pierchala, B. A., Gottlieb, D. I., Johnson, E. M., Jr., Choi, D. W., and Snider, B. J. (2005) Neurotrophin and GDNF family ligands promote survival and alter excitotoxic vulnerability of neurons derived from murine embryonic stem cells. *Exp. Neurol.* **191,** 65–76
22. Kauhausen, J., Thompson, L. H., and Parish, C. L. (2013) Cell intrinsic and extrinsic factors contribute to enhance neural circuit reconstruction following transplantation in Parkinsonian mice. *J. Physiol.* **591,** 77–91

23. Rosenblad, C., Martinez-Serrano, A., and Björklund, A. (1996) Glial cell line-derived neurotrophic factor increases survival, growth and function of intrastriatal fetal nigral dopaminergic grafts. *Neuroscience* **75,** 979–985
24. Björklund, A., Rosenblad, C., Winkler, C., and Kirik, D. (1997) Studies on neuroprotective and regenerative effects of GDNF in a partial lesion model of Parkinson's disease. *Neurobiol. Dis.* **4,** 186–200
25. Redmond, D. E., Jr., Elsworth, J. D., Roth, R. H., Leranth, C., Collier, T. J., Blanchard, B., Bjugstad, K. B., Samulski, R. J., Aebischer, P., and Sladek, J. R., Jr. (2009) Embryonic substantia nigra grafts in the mesencephalon send neurites to the host striatum in non-human primate after overexpression of GDNF. *J. Comp. Neurol.* **515,** 31–40
26. Rangasamy, S. B., Soderstrom, K., Bakay, R. A., and Kordower, J. H. (2010) Neurotrophic factor therapy for Parkinson's disease. *Progr. Brain Res.* **184,** 237–264

Appendix F: Full Published Work (not discussed in thesis)

Conor C Horgan, Alexandra L Rodriguez, Rui Li, Kiara F Bruggeman, Nicole Stupka, Jared K Raynes, Li Day, John W White, Richard J Williams, David R Nisbet, "Characterisation of minimalist co-assembled fluorenylmethyloxycarbonyl self-assembling peptide systems for presentation of multiple bioactive peptides", *Acta Biomaterialia*, 2016, vol. 38, pp. 11-22 – Reproduced with permission from Elsevier

Acta Biomaterialia 38 (2016) 11–22

Contents lists available at ScienceDirect

Acta Biomaterialia

journal homepage: www.elsevier.com/locate/actabiomat

Full length article

Characterisation of minimalist co-assembled fluorenylmethyloxycarbonyl self-assembling peptide systems for presentation of multiple bioactive peptides

Conor C. Horgan [a,1], Alexandra L. Rodriguez [a,1], Rui Li [b], Kiara F. Bruggeman [a], Nicole Stupka [c], Jared K. Raynes [d], Li Day [d,e], John W. White [f], Richard J. Williams [g,2,*], David R. Nisbet [a,2,*]

[a] Research School of Engineering, The Australian National University, Canberra 2601, Australia
[b] Centre for Chemistry and Biotechnology, Deakin University, Waurn Ponds 3217, Australia
[c] School of Medicine, Deakin University, Waurn Ponds 3217, Australia
[d] CSIRO Food and Nutritional Sciences, Werribee 3030, Australia
[e] AgResearch Ltd, Grasslands Research Centre, Palmerston North 4442, New Zealand
[f] Research School of Chemistry, The Australian National University, Canberra 2601, Australia
[g] School of Aerospace, Mechanical and Manufacturing Engineering, RMIT University, Melbourne 3001, Australia

ARTICLE INFO

Article history:
Received 29 November 2015
Received in revised form 17 April 2016
Accepted 26 April 2016
Available online 27 April 2016

Keywords:
Self-assembling peptides
Hydrogels
Co-assembly
Fmoc
Tissue engineering

ABSTRACT

The nanofibrillar structures that underpin self-assembling peptide (SAP) hydrogels offer great potential for the development of finely tuned cellular microenvironments suitable for tissue engineering. However, biofunctionalisation without disruption of the assembly remains a key issue. SAPS present the peptide sequence within their structure, and studies to date have typically focused on including a single biological motif, resulting in chemically and biologically homogenous scaffolds. This limits the utility of these systems, as they cannot effectively mimic the complexity of the multicomponent extracellular matrix (ECM). In this work, we demonstrate the first successful co-assembly of two biologically active SAPs to form a coassembled scaffold of distinct two-component nanofibrils, and demonstrate that this approach is more bioactive than either of the individual systems alone. Here, we use two bioinspired SAPs from two key ECM proteins: Fmoc-FRGDF containing the RGD sequence from fibronectin and Fmoc-DIKVAV containing the IKVAV sequence from laminin. Our results demonstrate that these SAPs are able to co-assemble to form stable hybrid nanofibres containing dual epitopes. Comparison of the co-assembled SAP system to the individual SAP hydrogels and to a mixed system (composed of the two hydrogels mixed together post-assembly) demonstrates its superior stable, transparent, shear-thinning hydrogels at biological pH, ideal characteristics for tissue engineering applications. Importantly, we show that only the coassembled hydrogel is able to induce *in vitro* multinucleate myotube formation with C2C12 cells. This work illustrates the importance of tissue engineering scaffold functionalisation and the need to develop increasingly advanced multicomponent systems for effective ECM mimicry.

Statement of Significance

Successful control of stem cell fate in tissue engineering applications requires the use of sophisticated scaffolds that deliver biological signals to guide growth and differentiation. The complexity of such processes necessitates the presentation of multiple signals in order to effectively mimic the native extracellular matrix (ECM). Here, we establish the use of two biofunctional, minimalist self-assembling peptides

* Corresponding authors.
E-mail addresses: richard.williams@rmit.edu.au (R.J. Williams), david.nisbet@anu.edu.au (D.R. Nisbet).
[1] Equal first author.
[2] Equal contribution.

http://dx.doi.org/10.1016/j.actbio.2016.04.038

(SAPs) to construct the first co-assembled SAP scaffold. Our work characterises this construct, demonstrating that the physical, chemical, and biological properties of the peptides are maintained during the co-assembly process. Importantly, the coassembled system demonstrates superior biological performance relative to the individual SAPs, highlighting the importance of complex ECM mimicry. This work has important implications for future tissue engineering studies.

1. Introduction

The successful application of biomaterials to tissue engineering requires the fabrication of carefully controlled physical and chemical properties presented on biologically relevant scales to promote cellular regeneration. The most promising candidates for tissue engineering should provide a three-dimensional (3D) microenvironment with support for cells as well as biochemical cues to promote and regulate cell behaviour such as cell adhesion, migration, proliferation and differentiation [1–3]. These biomaterials must also exhibit little or no immune response, and be biocompatible and non-cytotoxic after degradation [1,4]. These requirements present significant challenges in the design of tissue engineering materials, and provide the design inspiration for materials that can be applied to cell regeneration and repair.

Nanostructured 3D matrix scaffolds are some of the most promising and important biomaterials that have been applied to tissue engineering [4,5]. Developing design rules for these materials allows them to be purpose-built to provide a suitable cellular microenvironment that mimics the native ECM [1,2,4,6]. A variety of scaffolds have been investigated, including electrospun nanofibres [7–9], biologically derived and synthetic hydrogel scaffolds [10–16], and self-assembling peptide (SAP) hydrogel scaffolds [4,17,18].

SAP hydrogel scaffolds are a novel class of biomimetic materials consisting of structure forming low molecular weight peptide sequences [19,20]. SAP hydrogel scaffolds have proven to be particularly promising due to their inherent biocompatibility, tuneable mechanical and chemical properties, ability to fill irregularly shaped voids, and their porous, nanofibrous structure, making them ideal candidates for applications in regenerative medicine [4,21,22].

Recently, the potential of minimalist SAP systems for biomedical applications has gained much interest, due to their short length and ability to present biochemical cues at high densities through careful control of the amino acid sequence, allowing functionality to be included without sacrificing structure [17,21,23]. Understanding the mechanisms underpinning the structural formation of one group of these systems, fluorenylmethyloxycarbonyl (Fmoc) SAPs, has enabled the introduction of such biochemical cues via spontaneous assembly [23,24]. Here, under appropriate conditions, the Fmoc groups interact through π-π stacking, forming the backbone of the Fmoc-SAP structure, and the pendant peptides align through hydrogen bonding to form a network of stabilising β-sheets (Fig. 1) [25–27]. These assemblies subsequently stack to form nanotubes with the peptide sequence exposed at high density within beta strands [23,26,28]. Individual nanotubes then align longitudinally, resulting in the spontaneous formation of nanofibre bundles decorated with the peptide sequence of interest constituting the hydrogel scaffold [21]. The minimalist nature of Fmoc-SAP systems is advantageous as they are relatively inexpensive and quick to produce [21,24]. In addition, the Fmoc moiety itself has been shown to possess anti-inflammatory properties, a valuable property for the development of adjuvant scaffolds in cellular applications [29]. While a recent *in vitro* study has indicated the cytotoxicity of degradation products from high concentrations of Fmoc-F and Fmoc-FF due to the poor stability of these systems [30], and the possible formation of aggregates and nanocrystalline structures [31,32]; these studies, and recent work by our group have highlighted the need for optimisation and functionalization, thereby making these systems suitable for attachment based cell culture *in vitro* [33], and neural stem cell transplantation and viral vector delivery *in vivo* [34].

Another promising advantage of Fmoc-based SAP systems over other, longer SAP systems is their heightened potential for biofunctionalisation. Previously, biofunctionalisation of non-Fmoc peptides (such as RADA16) and peptide amphiphiles (PA), achieved through capping with short bioactive sequences (epitopes), has shown some promise in eliciting an improved cellular response *in vitro* and *in vivo* [17,35–37]. The capping of PAs with IKVAV in particular has seen selective promotion of cell differentiation, neurite extension, and neural differentiation, as well as reduced development of astrocytes (an inflammatory cell within the central nervous system (CNS)), indicating the formation of an appropriate cellular microenvironment for tissue engineering, in this case within the CNS [17,38–40]. While these results are promising, the relative size of the bioactive epitope to the PAs results in an inherently low-density presentation of the epitope [21,40,41]. What is more, work on biofunctionalised PAs has shown that density, rather than dimensionality, of the biofunctional epitope presentation plays a more important role in cell differentiation and is likely to play a wider role in the biofunctionality of the introduced material [35,42].

Our previous research has focused on the high-density presentation of RGD and IKVAV epitopes (Fig. 2a & b) [21,43,44]. The laminin-derived IKVAV and the fibronectin-derived RGD sequences are common components of the mammalian ECM [21,42,45]. These Fmoc peptides have been rationally designed to form SAP hydrogels at physiological pH [21], allowing for control of various cellular processes including survival, adhesion, differentiation, migration and proliferation [4]. Incorporation of these sequences has enabled us to develop an Fmoc-SAP scaffold that more closely mimics the ECM, both physically and chemically. However, while biofunctionalisation of SAP scaffolds represents a significant advancement in the development of cell scaffold materials, cellular control is somewhat limited in this instance by the presentation of a single biochemical cue [42].

The combination of multiple signals in a single, homogenous scaffold offers the potential for a synergistic effect on cellular response through the improved spatial and chemical arrangement of multiple bioactive signals [46]. A range of co-assembled systems, mixed, and self-sorting have been reported [22,47–50], however, bioactive co-assembly has only previously been investigated in PA systems, with limited success [46], and in an Fmoc-SAP system where a non-gelating Fmoc-RGD molecule was used to decorate fibrils of Fmoc-FF [51]. In each case, the mechanism by which the SAPs molecularly pack into the fibres is not well understood and the design of such co-assembled systems continues to prove challenging [52].

Here, we present a first step towards the development of truly co-assembled minimalist bioactive Fmoc-SAP scaffolds for the high-density presentation of multiple biochemical cues, in this

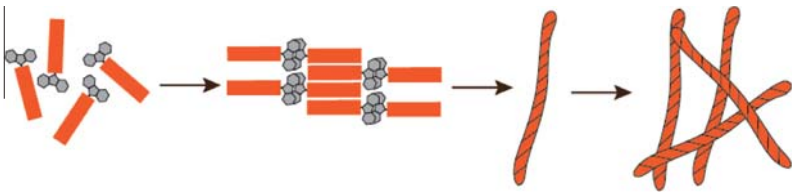

Fig. 1. Self-assembly of a minimalist Fmoc-SAP. Individual SAPs consist of an Fmoc group (grey) attached to the end of a short amino acid chain (red). Under appropriate conditions, the Fmoc groups then stack together while the peptides align, wrapping around to form a SAP nanofibre. These nanofibres then bundle together to form a hydrogel scaffold. (For interpretation of the references to colour in this figure legend, the reader is referred to the web version of this article.)

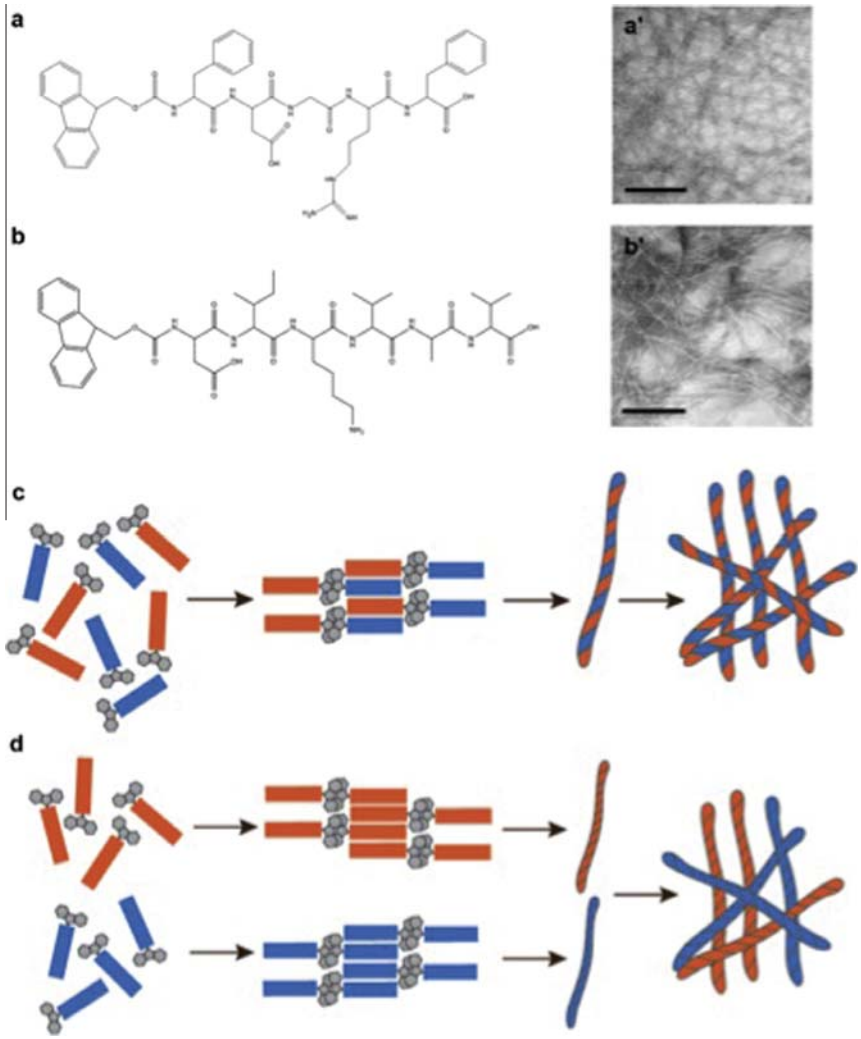

Fig. 2. (a, b) Structural formulae for the bioactive Fmoc-SAP sequences, (a) Fmoc-FRGDF, (b) Fmoc-DIKVAV with (a' & b') corresponding TEM images (scale = 200 nm). (c) π-β Co-assembly process where peptides are mixed prior to gelation and co-assembled via a pH switch method. (d) In contrast, the mixed assembly process results from the mixing of two previously prepared gels, giving rise to an inhomogeneous hydrogel.

case presenting both RGD and IKVAV in a single, co-assembled SAP system. In order to confirm the successful formation of co-assembled structures, we characterised the assembly process across all length scales; the molecular packing using Fourier transform infrared spectroscopy (FTIR), circular dichroism (CD) spectroscopy, and small-angle X-ray scattering (SAXS); the structures at longer length scales by transmission electron microscopy (TEM); and the bulk mechanical properties of the hydrogels by rheological measurements. We considered various co-assembled combinations of our two individual Fmoc-SAPs (Fmoc-FRGDF and Fmoc-DIKVAV) and distinguished the resulting co-assembled hydrogel structures (Fig. 2c) from both single Fmoc-SAP and parallel mixed Fmoc-SAP systems (Fig. 2d) to show that a unique homogenous nanofibrous hydrogel was obtained. Crucially, biological characterisation of these scaffolds demonstrated the superior biofunctionality of the co-assembled system over our other SAP systems, demonstrating the synergistic potential of simultaneously presenting multiple bioactive epitopes.

2. Materials and methods

2.1. Solid phase peptide synthesis (SPPS)

Fmoc-FRGDF and Fmoc-DIKVAV SAPs were made using solid phase peptide synthesis (SPPS) [53] in a custom rotating glass reactor vessel at a 0.4 mmol scale as described in [44]. Fmoc protected amino acids, Hydroxybenzotriazole (HOBt), O-Benzotriazole-N,N,N′,N′-tetramethyl-uronium-hexafluoro-phosphate (HBTU) and Wang based resins were purchased from GL Biochem (China). All other chemicals were purchased from Sigma-Aldrich. Dimethylformamide (DMF) was dried for a minimum of 2 h prior to use with 4 Å molecular sieves.

2.2. Single Fmoc-SAP hydrogel preparation

Peptide hydrogels were prepared at concentrations of 10 and 20 mg/mL using a method analogous to that described in [44], using 1.0× phosphate buffered saline (PBS) solution rather than Hank's buffered saline solution to take the hydrogels to the appropriate concentrations. Mass spectrometry was performed to confirm the desired peptide sequence was synthesised (Supplementary Fig. 1).

2.3. Mixed Fmoc-SAP hydrogel preparation

The mixed Fmoc-SAP hydrogel consisted of two different single Fmoc-SAP hydrogels, Fmoc-FRGDF and Fmoc-DIKVAV. In each case, the single Fmoc-SAP hydrogels were prepared as detailed above. The mixed Fmoc-SAP hydrogel was then prepared through the combination of the single Fmoc-SAP hydrogels over vortex. Fmoc-SAP hydrogels were combined in volumetrically equal ratios, with vortex mixing used to produce a single, heterogeneous hydrogel.

2.4. Co-Assembled Fmoc-SAP hydrogel preparation

The co-assembled Fmoc-SAP hydrogel was prepared in a similar manner to the single Fmoc-SAP hydrogels, however the single peptide used in hydrogel preparation was replaced with two different peptides, Fmoc-FRGDF and Fmoc-DIKVAV. These peptides were combined in equal mass ratios to a total mass of 5 mg. Hydrogel formation was then achieved as detailed in Section 2.2 above.

2.5. Transmission electron microscopy

Negative stain TEM was performed using a 125 kV Hitachi H7100FA electron microscope with a LaB_6 cathode as described in [44]. Nanofibre dimension and statistical analyses were performed as detailed in Section 3.

2.6. Titration

50 μL of 1 M NaOH was added dropwise to a vial containing 10 mg of peptide while mixed over vortex. Next, 200 μL of DI H_2O was similarly added dropwise over vortex. The pH of the solution was measured using an Oaktron pH 700 micro pH electrode (Thermo Scientific). 10 μL of 0.2 M HCl was added dropwise over vortex until the hydrogel solution reached pH 3. pH was measured after addition of each 10 μL of HCl.

2.7. Rheology

Rheological analysis was performed using a Kinexus Pro + Rheometer (Malvern). Approximately 0.5 mL of hydrogel sample was placed on a flat plate geometry with solvent trap (Upper Geometry: PU20 SR1351 SS, Lower Geometry: PLS55 C0177 SS). A gap distance of 0.2 mm was used and multiple frequency sweeps were performed for frequencies ranging from 0.1 to 100 Hz with a 0.1% strain at a constant temperature of 25 °C.

2.8. Fourier transform infrared spectroscopy

FTIR was completed using an Alpha Platinum ATR FTIR (Bruker Optics). 100 μL of peptide hydrogel was placed on the single reflection diamond and the pressure applicator used to adequately spread hydrogel over crystal surface. Absorbance scans of the amide I region (1550–1750 cm^{-1}) were obtained for each peptide, and a background buffer scan subtracted.

2.9. Circular dichroism

CD was completed using a Chirascan CD Spectrometer (Applied Photophysics Limited) from 180 nm to 320 nm with a step size of 0.5 and a 1 nm bandwidth as described in [44]. The resulting data was averaged and smoothed post-acquisition using software provided by Chirascan prior to analysis. Hydrogels were diluted 1 in 200 with de-ionized water to reduce scattering [23].

2.10. Small angle X-ray scattering

SAXS was performed using the SAXS/WAXS beamline at the Australian Synchrotron. Measurements were taken using two different camera lengths: 900 mm and 7000 mm with an X-ray wavelength of 1.0332 Å. These camera lengths enabled the scattering vector (q) to be measured across the range 0.008 –0.7 $Å^{-1}$. The diffraction pattern was recorded on a Pilatus 1 M detector (170 mm × 170 mm, effective pixel size of 172 μ × 172 μm), and processed using the Australian Synchrotron ScatterBrain software.

Hydrogel samples were prepared, as detailed above, two days prior to testing and stored in eppendorf vials. Prior to sample exposure, PBS backgrounds were loaded into 1.5 mm glass capillaries and sealed to prevent evaporation. Capillaries were then loaded into a custom mount designed to enable movement of the capillaries in two dimensions. Two 5-s exposures were taken for each sample background using the two different camera lengths. PBS backgrounds were then removed from the capillaries and replaced with hydrogel samples. Capillaries were then resealed and remounted for measurement. Multiple 5-s exposures were taken

for each sample on the two different camera lengths at different positions along the capillary length.

Repeated measurements for each sample on each camera length were averaged and the PBS background subtracted using ScatterBrain. q calibration was performed using air shot scattering curves, though the use of capillaries prevented standard intensity normalisation. To circumvent this issue, intensity normalisation was performed relative to a known scattering curve for de-fatted human serum albumin (DFHSA) at a protein concentration of 1 mg/mL. Due to weak scattering at higher q values, the background was scaled by 0.9 prior to subtraction from the sample scattering data. Data for each sample on the two different camera lengths were then combined using IgorPro, though data at the lower q range (obtained using the 7000 mm camera length) showed a linear scattering curve for all samples (likely due to aggregation) and so was discarded. Analysis of the scattering curves for each sample was performed across the q range 0.01 – 0.3 $Å^{-1}$. The intensity of the x-rays scattered from each sample, $I(q)$, was then compared to a number of theoretical form factors, $F(q)$, which result from the particle geometry. $I(q)$ can be described as the product of the number density of scattered objects (n_p), the form factor ($F(q)$), and the structure factor ($S(q) = 1$, for our dilute system), which describes interparticle interactions (Eq. (1)).

$$I(q) = n_p F(q) S(q) \quad (1)$$

$I(q)$ for each of our samples was compared to form factor models provided by the National Institutes of Standards and Technology (NIST) for use in conjunction with IgorPro, with the quality of the fit estimated using a chi-squared test [54]. These models included calculations of n_p, though structure factors had to be calculated separately. While structure factors are widely used to generate higher quality models of X-ray scattering intensity, IgorPro applies an average structure factor approximation, which rests on the assumption of homogeneous, monodisperse, spherical particles. As our samples consist of inhomogeneous, polydisperse, non-spherical particles, the use of an average structure approximation is inappropriate. Though structure factors for our samples could be calculated using polymer reference interaction site model (PRISM) theory, high-quality fits were obtained without the reliance on structure factors and they have hence been excluded from our calculations of $I(q)$ [55,56].

2.11. Cell culture

Sterile hydrogels for each of the single, mixed, and co-assembled peptide systems were prepared similar to the non-sterile hydrogel method previously detailed. However, the sterile hydrogels were prepared in sterile conditions with PBS replaced by high glucose Dulbecco's Modified Eagle Medium (DMEM) (Life Technologies, Melbourne, Australia) with 10% of fetal bovine serum (FBS). 400 μL of each hydrogel was then transferred to a 24-well plate and placed under UV light for 30 min for sterilisation prior to seeding with C2C12 mouse myoblasts, a skeletal muscle precursor cell line and commonly used model of myogenesis and skeletal muscle regeneration [57].

C2C12 skeletal muscle cells were maintained in high glucose Dulbecco's modified Eagle medium (DMEM) (Life Technologies, Melbourne, Australia) containing 10% fetal bovine serum (FBS), at 37 °C with 5% CO_2. 10,000 cells in 200 μL of cell culture media were then seeded onto each hydrogel system, with 3 independent experiments performed in duplicate for each hydrogel system.

2.12. DAPI and Actin Staining

Following 48 h in culture, C2C12 cells seeded on the four Fmoc-SAP systems were stained with the nuclear stain DAPI (Life Technologies Australia Pty. Ltd., VIC, Australia) and Phalloidin (Life Technologies Australia Pty. Ltd., VIC, Australia) an F-actin stain. Briefly, the upper media in each well was carefully aspirated and 200 μL of 4% paraformaldehyde (PFA, ProSciTech Pty. Ltd. QLD, Australia) was added and left at room temperature for 20 min to fix the cells and the gels. Then PFA was aspirated and the cells and gels were washed with 200 μL of PBS. Next, 200 μL of 0.1% Triton × 100 (ProSciTech Pty. Ltd., QLD, Australia) in PBS was added into each well and maintained at room temperature for 15 min to permeabilise the cells. Then the cells were stained with 200 μL of the mixture of DAPI and rhodamine phalloidin solution (Life Technologies Australia Pty. Ltd., VIC, Australia) (diluted 200 and 100 times, respectively) at room temperature for 60 min. DAPI and Rhodamine phalloidin were used according to manufacturer's instructions. Stained cells were observed under a fluorescent microscope (Nikon) at 20×. Three independent experiments in duplicate were performed for each hydrogel system.

3. Statistical methods

Nanofibre dimensions for each hydrogel were calculated based on TEM images using ImageJ. A selection of 10 width measurements across different nanofibres were taken from each of two images, corresponding to different samples of each peptide system, and a two-tailed T-test used to compare the mean width values between co-assembled and mixed systems. Nanofibre widths measured were then compared to the diameters measured using SAXS.

Nanofibre diameters were similarly modelled using SAXS, with mean and standard deviation values calculated from the optimal fitting model using Igor Pro. A two-tailed T-test was used to compare the mean width values between co-assembled and mixed systems.

4. Results

4.1. Titration

Titration of the single and co-assembled Fmoc-SAP systems (Fig. 3a) was employed to determine the pK_a of the dual peptide system as a predictor of gelation behaviour. The titration curves for the single and co-assembled Fmoc-SAP systems displayed multiple pK_a shifts (inflection points on the curves in as seen in Fig. 3a), between pH 7 and pH 9, with the titration curve for the co-assembled FRGDF-DIKVAV appearing as an average of the titration curves of the constituent single SAPs, Fmoc-FRGDF and Fmoc-DIKVAV.

4.2. Transmission electron microscopy

Nanofibrous structure formation and the network bundling for the mixed and co-assembled FRGDF-DIKVAV system was confirmed with negatively stained TEM (Fig. 3b & c). As expected, the Fmoc-SAPs yielded nanofibres with consistent morphology and diameters, with the characteristic nanoscale assemblies observed for each of the single Fmoc-SAP systems also prominent in the TEM micrographs of the mixed and co-assembled systems. The co-assembled system contained nanofibres with width dimensions of 13.1 nm ± 2.2 nm (mean ± standard deviation) (Fig. 3c), statistically significantly different ($p = 0.000014$) from the mixed system nanofibres of 9.6 nm ± 2.0 nm (Fig. 3b). The mixed system nanofibres display similar widths to both the FRGDF and DIKVAV systems, with width dimensions of 9.2 nm ± 1.4 nm and

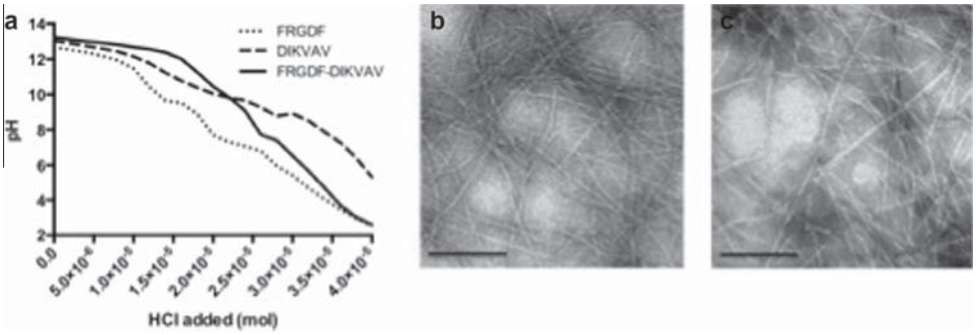

Fig. 3. (a) Titration curves showing shifts in pK_a for the individual peptides and FRGDF-DIKVAV combination. TEM images of (b) mixed and (c) co-assembled SAP hydrogels confirming nanofibre formation (scale = 200 nm).

Table 1
Hollow cylinder with polydisperse radius form factor model parameters for different peptide systems.

Parameter	FRGDF	DIKVAV	Mixed FRGDF-DIKVAV	Co-Assembled FRGDF-DIKVAV
Length (Å)	3015	2979	2900	3315
Mean Core Radius (Å)	24.25	20.65	23.40	29.71
Radial Shell Thickness (Å)	29.52	28.17	27.06	51.88
Radial Polydispersity	0.06	0.10	0.19	0.12
SLD Core ($Å^{-2}$)	1.31×10^{-5}	1.33×10^{-5}	1.36×10^{-5}	1.28×10^{-5}
SLD Shell ($Å^{-2}$)	9.94×10^{-6}	9.91×10^{-6}	9.94×10^{-6}	9.76×10^{-6}
SLD Solvent ($Å^{-2}$)	9.52×10^{-6}	9.49×10^{-6}	9.54×10^{-6}	9.49×10^{-6}
Chi-Squared (χ^2)	*4.40	1.62	1.88	1.02

* Though the χ^2 value here is high, this fit showed the best χ^2 value for FRGDF (see Supplementary Table 1).

9.5 nm ± 1.2 nm respectively. Importantly, these results corroborate the nanofibre diameters measured using SAXS (Table 1).

4.3. Rheology

Fig. 4 shows the storage moduli (G') and loss moduli (G") of the single, mixed, and co-assembled Fmoc-SAP systems as a function of applied frequency (Hz). All hydrogels displayed viscoelastic gel behaviour; with the storage moduli values higher than the loss moduli values with the range of frequencies measured. Viscoelastic behaviour remained essentially constant for each of the SAP systems at 25 °C and 37 °C (with minor differences displayed for the mixed and co-assembled SAP systems across the two temperatures).

For the single Fmoc-SAP systems, the G' value of Fmoc-DIKVAV was at $\sim 10^4$ Pa (Fig. 4b), in the appropriate range for application to tissue engineering, while the moduli for Fmoc-FRGDF were much lower (Fig. 4a). The G' value of the mixed FRGDF-DIKVAV system (Fig. 4c) was similar to that of single Fmoc-DIKVAV, whereas the ratio of G"/G' (the tan δ value) was similar to that of the single Fmoc-FRGDF system at 0.1–0.13 between 0.1 and 1 Hz. In contrast, the moduli for co-assembled FRGDF-DIKVAV showed a ~20% reduction relative to Fmoc-DIKVAV, but the tan δ was maintained (Fig. 4d).

4.4. Fourier transform infrared spectroscopy

FTIR spectra of each of the single, mixed, and co-assembled SAP systems are shown in Fig. 5a. In each case, a major peak at approximately 1630 cm^{-1} and a minor peak at approximately 1690 cm^{-1}.

4.5. Circular dichroism

CD spectra for the single and mixed SAP systems display local maximum bands at approximately 190 nm and/or local minimum bands at approximately 218 nm (Fig. 5b). However, the CD spectrum for the co-assembled system is inverted, displaying local minimum bands between 190 nm and 200 nm.

4.6. Small angle X-ray scattering

SAXS was used to determine a physical model of the nanofibres formed by each of the different SAP systems and identify differences between the nanofibres formed for each system. To determine the most suitable form factor model for our systems, different models were fitted to the experimental SAXS data, using fitting algorithms included in the NIST IgorPro software (Fig. 6).

TEM images were used to guide initial parameter values for the cylinder diameter and length, while the scattering length densities were adjusted to account for the use of these models for SAXS data. In each case, the optimal fit was achieved using the hollow cylinder with polydisperse radius form factor model (Fig. 6). The theoretical form factor model fit to the experimental data for each of the peptide systems enabled the physical properties of the peptide nanofibres to be determined (Table 1). In the single and mixed systems, the peptide nanofibres exhibit similar core and shell thicknesses of around 20–25 Å, and similar lengths, on the order of 3000 Å. However, for the co-assembled system, the mean core radius was increased to 29.7 Å and the radial shell thickness to 51.9 Å, closely agreeing with the nanofibre diameters observed in the TEM images (Fig. 3b and c). Statistical comparison of the nanofibre diameters modelled using SAXS demonstrated a statistically significant

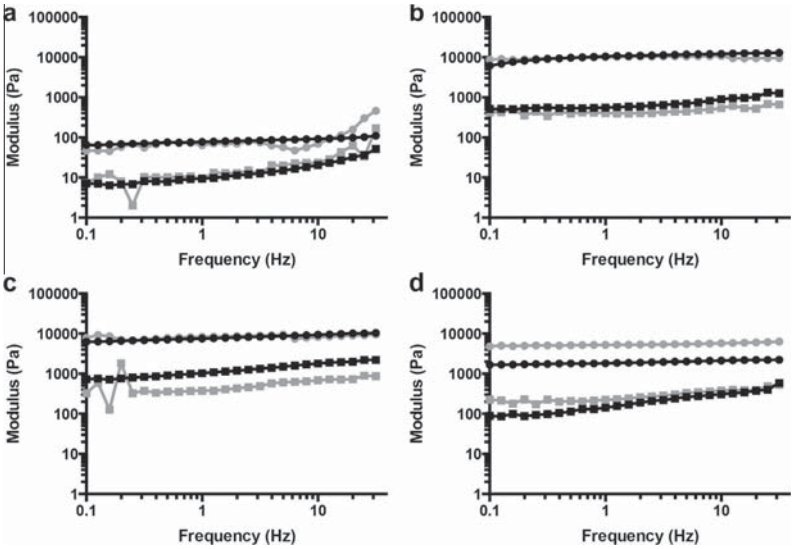

Fig. 4. Rheological data for single Fmoc-SAP sequences (a) FRGDF, (b) DIKVAV with comparison to (c) mixed and (d) co-assembled systems at 25 °C (black) and 37 °C (grey) (G' = circles; G" = squares).

increase (>75%) in core radius and shell thickness between the co-assembled nanofibres and those of the mixed and single SAP systems ($p < 0.0001$ in each case), as opposed to the average of the two observed in self-sorted systems [58].

4.7. Bioavailability investigation of Fmoc-SAP systems through 3D cell culture

3D cell cultures on the mouse skeletal muscle precursor cell line, C2C12 myoblasts, were performed for each of the SAP systems. Following 48 h of culture, myoblasts were visualised with DAPI (nuclear stain) and rhodamine phalloidin (F-actin stain) staining (Fig. 7). In each case seeded cells migrated into the gel matrix, rather than remaining on the surface, indicating the Fmoc-SAP hydrogels promoted C2C12 migration. Cells seeded onto the Fmoc-FRGDF hydrogel (Fig. 7a) were mostly mononuclear, with some multinucleated cells formed. In addition, limited cell spreading was observed. For the Fmoc-DIKVAV hydrogel (Fig. 7b) on the other hand, a much greater degree of cell spreading was observed, with many multinuclear cells formed, a few of which were beginning to elongate into myotube-like structures. The co-assembled FRGDF-DIKVAV hydrogel (Fig. 7d) displayed an even more remarkable effect on cell morphology, with numerous multinuclear cell clusters observed, as well as elongated multinucleated myotubes, which stained intensely for F actin. Unfortunately, the opacity of the mixed FRGDF-DIKVAV system (Fig. 7c) prevented clear imaging of the cells in the hydrogel, though it is clear that fewer myotube-shaped cells have formed in this system than the co-assembled system.

5. Discussion

This study has demonstrated the capacity of minimalist, functionalised Fmoc-SAPs to undergo co-assembly to form stable, nanofibrous hydrogel networks with enhanced biofunctionality. Physical and chemical characterisation of the co-assembled Fmoc-SAP systems indicate that the underlying assembly architecture is maintained during the co-assembly process, but that the nanofibrous network formed is physically and chemically distinct from the single and mixed Fmoc-SAP systems.

Nanofibrous architecture formation and pH-dependent gelation by the co-assembled Fmoc-SAP system was confirmed through titration, TEM, and rheology characterisation studies. The pH switch-triggered self-assembly of Fmoc-SAPs is determined by the pK_a of the peptide, which, in turn, is dependent on the composition of the peptide chain [21]. The peptide sequences of both Fmoc-SAPs was designed to allow assembly at physiological pH. The assembly of the Fmoc-SAPs is driven by the achievement of local thermodynamic minima to form a metastable structure [59]. Self-Sorted systems are usually achieved by having a difference in pKa to allow the preferential assembly of one or the other of the component [50]. In this case, however, the pKa of each fmoc-SAP has been designed in order to achieve assembly under physiological conditions and are closely matched. In each case, pK_a shifts between pH 7 and pH 9 indicate the ability of the system to form a stable hydrogel at physiological pH (~7.4), as was experimentally confirmed previously [21], with these results indicating the retained capacity of the Fmoc-SAPs within the co-assembled system to form a hydrogel under physiological conditions with no significant shifts.

TEM imaging of the nanofibrous networks demonstrated hydrogel formation in each case and that co-assembly resulted in nanoscale morphologies similar to the individual assemblies (Fig. 3c), rather than allowing a secondary type of structure to form [60]. Importantly, morphological differences were observed between the hydrogel-mixed and co-assembled FRGDF-DIKVAV systems, suggesting that the method of combination plays a role in determining the overall network structure.

Morphological differences between the mixed and co-assembled Fmoc-SAP systems were also apparent through differences in the elastic moduli for each system. The rheological properties of hydrogels are controlled by a number of parameters, including nanofibre stiffness, concentration, branching and number/type of entanglements [61]. Differences in the rheological

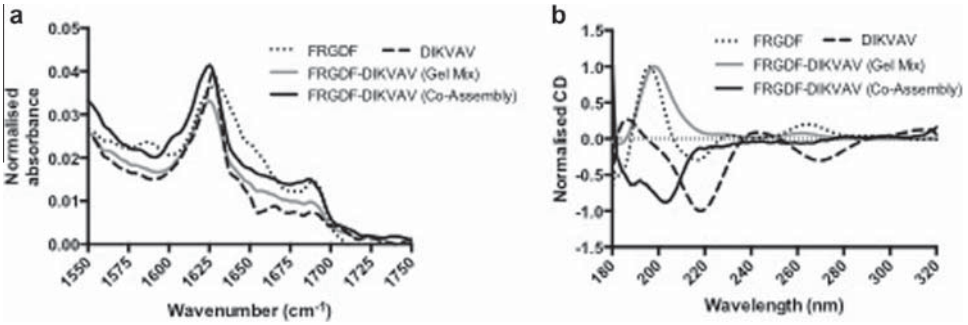

Fig. 5. (a) FTIR and (b) CD spectra for single, mixed, and co-assembled SAP hydrogels.

properties of each of the Fmoc-SAP systems therefore enable us to distinguish between the mixed and co-assembled systems. For the mixed system, the similarity of the G' value to that of Fmoc-DIKVAV and the similarity of the tan δ value to Fmoc-FRGDF suggests that the two Fmoc-SAPs co-existed as two separate non-interactive networks and both contributed to the overall rheological properties of the mixed system, which has been observed with other co-assembled systems [49]. On the other hand, the distinct moduli for the co-assembled system with a tan δ value similar to Fmoc-DIKVAV suggests that co-assembled FRGDF-DIKVAV is a cooperative system with modification to the fibril interaction, which influenced the type/number of entanglements formed, indicating a single aggregated structure exists as opposed to a cooperative network of two distinct components.

For successful *in vivo* applications as adjuvant cell scaffolds, it is essential that the hydrogel scaffold closely mimics the native ECM both in terms of the chemical signal presented and the physical support provided [40]. The elastic moduli of neural tissue ranges from 10^2 to 10^3 Pa while the moduli for connective and muscle tissues are $\sim 10^4$ Pa [62]. As such, Fmoc-SAP hydrogels with elastic moduli in these ranges have the potential to act as adjuvant ECM-mimetic cell scaffolds with appropriate properties for tissue engineering applications [63]. Importantly, these results indicate that the moduli of the co-assembled system are in the appropriate range for application to tissue engineering.

Spectroscopic analysis of the Fmoc-SAP systems demonstrates that the assembly is consistently driven by Fmoc- interactions, stabilised by a range of hydrogen bonds in a hierarchical assembly [26], supported by the structural similarities observed between the nanofibrous networks [64]. However, spectral differences between the co-assembled Fmoc-SAP system and the mixed and single Fmoc-SAP systems provide further evidence for the distinct nanofibrous structure formed through co-assembly.

In each case, the FTIR and CD spectra indicate the organisation of the molecules into a dominant structural ordering. However, the CD spectrum for the co-assembled system is inverted, a result of the π-π* Cotton effect from the Fmoc moiety, implying an opposite chirality of the co-assembled system with respect to the other peptide systems [65,66]. In addition, broad transitions in the 230–270 nm region for each of the systems (arising from numerous π-π* transitions) indicate the supramolecular alignment of the peptide nanofibres into a hydrogel scaffold [21]. The large transitions for the single Fmoc-FRGDF and Fmoc-DIKVAV hydrogels in this region indicate a high degree of fibre bundling [43]. The same effect is observed for the mixed and co-assembled SAP systems, though co-assembled FRGDF-DIKVAV displays smaller transitions relative to both the single and mixed SAP systems. This could be due to a reduced number of fibrils present due to a single population of heterogeneous structures.

Transitions present in the 180–220 nm region of the CD spectra for the single and mixed systems indicate the presence of β-sheets. On the other hand, the co-assembled FRGDF-DIKVAV system displayed a unique CD spectrum in this region, demonstrating an absorption shift of the minima from ~218 to 205 nm, and a greatly reduced maxima ~190 nm. This effect possibly arises from the novel interaction of aromatic and the carboxyl groups induced during the heterogeneous molecular packing of the penta- and hexapeptides [67], providing a means to spectroscopically distinguish the co-assembled system from the mixed system.

SAXS modelling of each Fmoc-SAP system provided further evidence that the underlying π-β architecture was maintained during co-assembly, resulting in the formation of unique, multicomponent nanofibres. Previous SAXS investigation of β-peptide oligomers indicated a good fit to a form factor model of a hollow cylinder with polydisperse radius to solutions of β-peptide oligomers, suggesting that simple cylindrical models can provide suitable fits for β-peptide solutions [68]. High quality fitting to this model was achieved for each of our Fmoc-SAP systems, aligning with previously observed model fitting for β-peptide oligomer solutions [68,69]. However, in our case, high quality fits were obtained without the need for associated structure factors.

Modelling of each of the Fmoc-SAP systems highlighted key differences between each of the assemblies, in particular distinguishing the co-assembled nanofibres from the other Fmoc-SAP systems. The distinct radial parameters observed for the co-assembled system (an increase in radial shell thickness of greater than 75% relative to the other peptide systems) are likely a result of larger, alternate packing than the formation of two self-sorted structures, modelled here by the mixed system [43]. The interaction of the two differently shaped and charged peptide sequences, requiring an increase in the radial shell thickness in order to achieve packing stability. Importantly, this suggests that the two SAPs are incorporated into a single structure, rather than forming a self-sorted heterogeneous system consisting of two separate homogeneous structures that would demonstrate properties closer to those of the mixed hydrogel [58]. This result supports the rheological measurements, where the co-assembled system was much weaker than the mixed or the Fmoc-DIKVAV systems, but stronger than the Fmoc-FRGDF, suggesting a distinct structure composed of the co-operative individual Fmoc-SAPs. The polydispersity in the cylinder (nanofibre) radius provides further confirmation of the formation of homogenous structures, with polydispersity values ranging between 0.06 and 0.12 for the single and co-assembled systems, indicating minimal variation in the cylinder radius along its length.

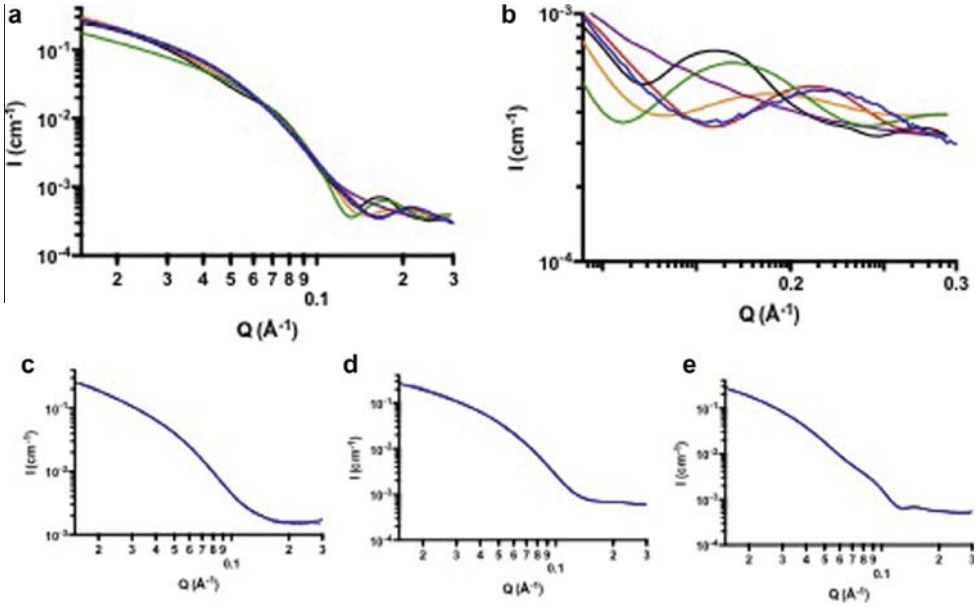

Fig. 6. (a) Scattering data obtained using SAXS for FRGDF (blue) showing various cylindrical models fitted to data including cylinder (green), cylinder with polydisperse radius (purple), hollow cylinder (black), flexible cylinder (orange) and hollow cylinder with polydisperse radius (red). The hollow cylinder with polydisperse radius is the best fit for our SAXS data as highlighted in (b) at higher Q values for FRGDF. Similar fits were obtained using this model for (c) DIKVAV, (d) mixed and (e) co-assembled hydrogel systems (blue = SAXS experimental data; red = hollow cylinder with polydisperse radius model). For all cylindrical model fits for DIKVAV, DIKVAV/FRGDF mixed and co-assembled systems see Supplementary Fig. 2. (For interpretation of the references to colour in this figure legend, the reader is referred to the web version of this article.)

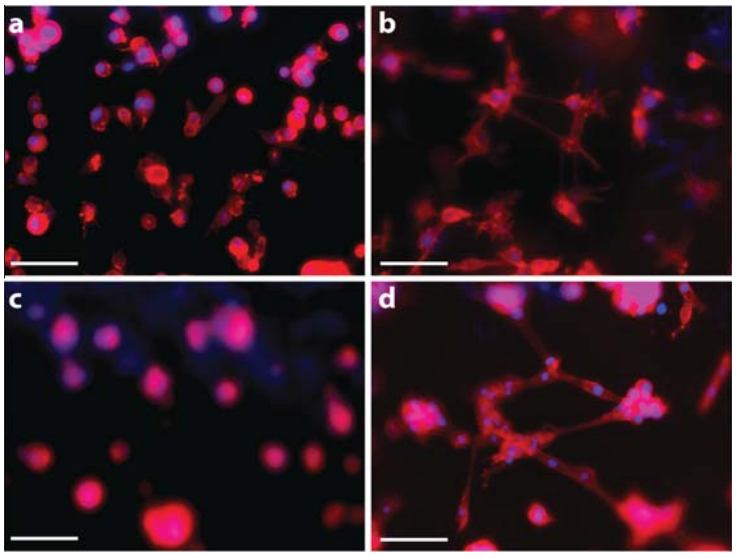

Fig. 7. DAPI/Rodamine phalloidin staining of C2C12 myoblasts maintained in high glucose DMEM plus 10% FBS at 48 h post seeding onto hydrogels of (a) Fmoc-FRGDF, (b) Fmoc-DIKVAV, (c) mixed FRGDF-DIKVAV, and (d) co-assembled FRGDF-DIKVAV (scale = 50 μm).

However, as expected for the mixed system, the polydispersity value increases to 0.19, suggesting a greater degree of inhomogeneity arising from the presence of two separate populations of fibrils.

C212 cell cultures demonstrated the enhanced bioactivity of the co-assembled Fmoc-SAP system relative to both the single and the mixed Fmoc-SAP systems, highlighting the benefit of incorporating multiple bioactive epitopes into a single nanofibrous network. C212 cells are known to proliferate as myoblasts but will withdraw from the cell cycle and fuse to form multinucleated myotubes under appropriate cell conditions [70]. Laminin-based substrates have been shown to support proliferation and myogenic differentiation of myoblasts [71], while fibronectin-based substrates have also demonstrated their ability to drive myogenesis [72]. Our results demonstrate the affinity of these cells for our laminin- and fibronectin-based SAP systems, with a clear preference for the co-assembled Fmoc-SAP system containing both laminin- and fibronectin-derived epitopes. Importantly, this result also demonstrates the advantages for the co-assembled SAP system relative to the mixed SAP system, with clearer gel formation, which has practical implications for the use of this co-assembled SAP system in tissue engineering applications.

Together, the results of these characterisation studies demonstrate the capacity of minimalist Fmoc-SAP systems to undergo co-assembly. While these results do not offer extensive insight into the exact molecular mechanisms that enable co-assembly in this system, we demonstrate, through the incorporation of bioactive epitopes, our functionalised Fmoc-SAPs offer superior biological performance in the co-assembled system over both the single and mixed systems. These results therefore illustrate the potential for application of co-assembled Fmoc-SAP systems to tissue engineering applications.

The co-assembly of Fmoc-SAPs however, offers additional benefits in the design and control of tissue engineering scaffolds through modulation of physical parameters. Our results for the co-assembled FRGDF-DIKVAV indicated gelation behaviour that lies between its constituent Fmoc-FRGDF and Fmoc-DIKVAV SAPs indicating a potential mechanism through which the gelation behaviour of co-assembled Fmoc-SAP systems can be tailored. Similarly, the rheological properties for co-assembled FRGDF-DIKVAV represent an intermediate between the weakest gel, Fmoc-FRGDF, and the strongest, Fmoc-DIKVAV. This range of material properties suggests an as yet unidentified opportunity for controlling the stiffness of Fmoc-SAP hydrogels, where the combination of Fmoc-SAPs in particular ratios (data not shown) could achieve the tuning required for select tissue engineering applications. Further modulation of hydrogel properties could be achieved through co-assembly, with SAXS results indicating an increase in fibre diameter relative to the other SAP systems. This increase in nanofibre width highlights the potential for co-assembly to permit greater control over fibril morphology, which has not been previously attained in other SAP systems. Through altering the relative ratios of the different SAPs present in the co-assembled system, we can potentially alter the nanofibre width, allowing us to selectively tune fibril morphology for tissue-specific ECMs.

Future studies on co-assembled Fmoc-SAPs can investigate both the enhanced bioactivity of the system as well as the potential mechanisms for control of the physical properties of the resultant hydrogel. For example, recent work on co-assembly in non-functionalised Fmoc-SAPs has indicated the importance of stabilization offered by neighbouring benzyl groups [52]. Such work may soon enable further co-assembled systems to be designed and developed. If successful, such studies could enable tissue engineering scaffolds to be tailored for tissue- or application-specific uses, enabling clinicians to select from a library of systems for individual patients or conditions.

6. Conclusions

In summary, novel co-assembled Fmoc-SAP systems were developed with the potential to present multiple bioactive epitopes and synergistically provide appropriate physical and chemical cues for cellular regeneration and repair. We demonstrate that two signals can be included into a nanofibrillar SAP hydrogel by mixing two preformed gels, or by co-assembling two distinct SAPs. In particular, we show for the first time the successful co-assembly of multiple bioactive SAP sequences into a single nanofibre scaffold. This process enables us to produce a tuneable biomaterial that can include multiple bioactive sequences in precisely defined ratios. Importantly, the observed increase in the width of the co-assembled nanofibres demonstrates a potential avenue for the tuning of fibril morphology through the co-assembly of multiple SAP systems, indicating the capacity for co-assembly to enable tuning of biomimetic SAP scaffolds to the ECM of particular tissues. This study similarly demonstrates the distinct biochemical properties of a co-assembled system for the concomitant presentation of unique signals to individual muscle precursor cells (C2C12 myoblasts) stimulating distinct cellular behaviours with regards to cell spreading and the formation of elongated, multinucleated myotube-like structures. This co-assembled system therefore provides a platform for a tuneable biomimetic material for future *in vitro* and *in vivo* tissue engineering applications.

Acknowledgements

Access to the facilities of the Centre for Advanced Microscopy (CAM) with funding through the Australian Microscopy and Microanalysis Research Facility (AMMRF) is gratefully acknowledged. SAXS experiments undertaken on the SAXS/WAXS beamline at the Australian Synchrotron, Victoria, Australia are also gratefully acknowledged. We would also like to thank F. Maclean and A. Panneerselvan for thorough proof reading of the manuscript. This research was supported by funding from the Australian Research Council (ARC, DP130103131). ALR was supported by an Australian Postgraduate Award; RJW was funded via an Alfred Deakin Research Fellowship; DRN was supported by a NHMRC Career Development Fellowship (APP1050684).

Appendix A. Supplementary data

Supplementary data associated with this article can be found, in the online version, at http://dx.doi.org/10.1016/j.actbio.2016.04.038.

References

[1] T.C. Holmes, S. de Lacalle, X. Su, G. Liu, A. Rich, S. Zhang, Extensive neurite outgrowth and active synapse formation on self-assembling peptide scaffolds, Proc. Natl. Acad. Sci. 97 (2000) 6728–6733.
[2] J.T.S. Pettikiriarachchi, C.L. Parish, M.S. Schoichet, J.S. Forsythe, D.R. Nisbet, Biomaterials for brain tissue engineering, Aust. J. Chem. 63 (2010) 1143–1154.
[3] J.L. Drury, D.J. Mooney, Hydrogels for tissue engineering: scaffold design variables and applications, Biomaterials 24 (2003) 4337–4351.
[4] D.R. Nisbet, R.J. Williams, Self-assembled peptides: characterisation and in vivo response, Biointerphases 7 (2012) 2.
[5] M.R. Hynd, J.N. Turner, W. Shain, Applications of hydrogels for neural cell engineering, J. Biomater. Sci. Polym. Ed. 18 (2007) 1223–1244.
[6] A. Atala, D.J. Mooney, Synthetic Biodegradable Polymer Scaffolds, Springer, 1997.
[7] L. Ghasemi-Mobarakeh, M.P. Prabhakaran, M. Morshed, M.H. Nasr-Esfahani, S. Ramakrishna, Electrospun poly(epsilon-caprolactone)/gelatin nanofibrous scaffolds for nerve tissue engineering, Biomaterials 29 (2008) 4532–4539.
[8] D.R. Nisbet, A.E. Rodda, M.K. Horne, J.S. Forsythe, D.I. Finkelstein, Implantation of functionalized thermally gelling xyloglucan hydrogel within the brain: associated neurite infiltration and inflammatory response, Tissue Eng. Part A 16 (2010) 2833–2842.

[9] N. Monteiro, D. Riberio, A. Martins, S. Faria, N.A. Fonesca, J.N. Moreira, et al., Instructive nanofibrous scaffold comprising runt-related transcription factor 2 gene delivery for bone tissue engineering, ACS Nano 8 (2014) 8082–8094.
[10] N.A. Peppas, K.B. Keys, M. Torres-Lugo, A.M. Lowman, Poly(ethylene glycol)-containing hydrogels in drug delivery, J. Control Rel. 62 (1999) 81–87.
[11] E.C. Tsai, P.D. Dalton, M.S. Schoichet, C.H. Tator, Synthetic hydrogel guidance channels facilitate regeneration of adult rat brainstem motor axons after complete spinal cord transection, J. Neurotrauma 21 (2004) 789–804.
[12] S. Suri, C.E. Schmidt, Cell-laden hydrogel constructs of hyaluronic acid, collagen, and laminin for neural tissue engineering, Tissue Eng. Part A 16 (2010) 1703–1716.
[13] T.W. Carone, J.M. Hasenwinkel, Mechanical and morphological characterization of homogeneous and bilayered poly(2-hydroxyethyl methacrylate) scaffolds for use in CNS nerve regeneration, J. Biomed. Mater. Res. B Appl. Biomater. 78 (2006) 274–282.
[14] X. Li, Z. Xiao, J. Han, L. Chen, H. Xiao, F. Ma, et al., Promotion of neuronal differentiation of neural progenitor cells by using EGFR antibody functionalized collagen scaffolds for spinal cord injury repair, Biomaterials 34 (2013) 5107–5116.
[15] Y. Liang, P. Walczak, J.W. Bulte, The survival of engrafted neural stem cells within hyaluronic acid hydrogels, Biomaterials 34 (2013) 5521–5529.
[16] P.X. Ma, Scaffolds for tissue fabrication, Mater. Today 7 (2004) 30–40.
[17] E.C. Wu, S. Zhang, C.A.E. Hauser, Self-assembling peptides as cell-interactive scaffolds, Adv. Funct. Mater. 22 (2012) 456–468.
[18] S. Zhang, Fabrication of novel biomaterials through molecular self-assembly, Nat. Biotechnol. 21 (2003) 1171–1178.
[19] F. Gelain, A. Horii, S. Zhang, Designer self-assembling peptide scaffolds for 3-d tissue cell cultures and regenerative medicine, Macromol. Biosci. 7 (2007) 544–551.
[20] A. Lakshmanan, S. Zhang, C.A. Hauser, Short self-assembling peptides as building blocks for modern nanodevices, Trends Biotechnol. 30 (2012) 155–165.
[21] A.L. Rodriguez, C.L. Parish, D.R. Nisbet, R.J. Williams, Tuning the amino acid sequence of minimalist peptides to present biological signals via charge neutralised self assembly, Soft Matter 9 (2013) 3915.
[22] A. Raspa, G.A.A. Saracino, R. Pugliese, D. Silva, D. Cigognini, A. Vescovi, et al., Complementary co-assembling peptides: from in silico studies to in vivo application, Adv. Funct. Mater. 24 (2014) 6317–6328.
[23] A.M. Smith, R.J. Williams, C. Tang, P. Coppo, R.F. Collins, M.L. Turner, et al., Fmoc-diphenylalanine self assembles to a hydrogel via a novel architecture based on π–π interlocked β-sheets, Adv. Mater. 20 (2008) 37–41.
[24] V. Jayawarna, M. Ali, T.A. Jowitt, A.F. Miller, A. Saiani, J.E. Gough, et al., Nanostructured hydrogels for three-dimensional cell culture through self-assembly of fluorenylmethoxycarbonyl–dipeptides, Adv. Mater. 18 (2006) 611–614.
[25] S. Kim, J.H. Kim, J.S. Lee, C.B. Park, Beta-sheet-forming, self-assembled peptide nanomaterials towards optical, energy, and healthcare applications, Small (2015).
[26] D. Zanuy, J. Poater, M. Sola, I.W. Hamley, C. Aleman, Fmoc-RGDS based fibrils: atomistic details of their hierarchical assembly, Phys. Chem. Chem. Phys. 18 (2016) 1265–1278.
[27] R.V. Ulijn, A.M. Smith, Designing peptide based nanomaterials, Chem. Soc. Rev. 37 (2008) 664–675.
[28] S. Fleming, R.V. Ulijn, Design of nanostructures based on aromatic peptide amphiphiles, Chem. Soc. Rev. 43 (2014) 8150–8177.
[29] R.M. Burch, M. Weitzberg, N. Blok, R. Muhlhauser, D. Martin, S.G. Farmer, et al., N-(Fluorenyl-9-methoxycarbonyl) amino acids, a class of antiinflammatory agents with a different mechanism of action, Proc. Natl. Acad. Sci. 88 (1992) 355–359.
[30] W.T. Truong, Y. Su, D. Gloria, F. Braet, P. Thordarson, Dissolution and degradation of Fmoc-diphenylalanine self-assembled gels results in necrosis at high concentrations in vitro, Biomater. Sci. 3 (2015) 298–307.
[31] A.D. Martin, J.P. Wojciechowski, M.M. Bhadbhade, P. Thordarson, A capped dipeptide which simultaneously exhibits gelation and crystallization behavior, Langmuir: ACS J. Surf. Colloids 32 (2016) 2245–2250.
[32] R.J. Williams, A.M. Smith, R. Collins, N. Hodson, A.K. Das, R.V. Ulijn, Enzyme-assisted self-assembly under thermodynamic control, Nat. Nanotechnol. 4 (2009) 19–24.
[33] R. Li, S. Pavuluri, K. Bruggeman, B.M. Long, A.J. Parnell, A. Martel, et al., Coassembled nanostructured bioscaffold reduces the expression of proinflammatory cytokines to induce apoptosis in epithelial cancer cells, Nanomed.: Nanotechnol., Biol. Med. 12 (2016) 1397–1407.
[34] A.L. Rodriguez, T.-Y. Wang, K.F. Bruggeman, R. Li, R.J. Williams, C.L. Parish, et al., Tailoring minimalist self-assembling peptides for localized viral vector gene delivery, Nano Res. 9 (2015) 674–684.
[35] G.A. Silva, C. Czeisler, K.L. Niece, E. Beniash, D.A. Harrington, J.A. Kessler, et al., Selective differentiation of neural progenitor cells by high-epitope density nanofibers, Science 303 (2004) 1352–1355.
[36] J.M. Anderson, A. Andukuri, D.J. Lim, H.-W. Jun, Modulating the gelation properties of self-assembling peptide amphiphiles, ACS Nano 3 (2009) 3447–3454.
[37] A.R. Cormier, X. Pang, M.I. Zimmerman, H.-X. Zhou, A.K. Paravastu, Molecular structure of RADA16-I designer self-assembling peptide nanofibres, ACS Nano 7 (2013) 7562–7572.
[38] E.J. Berns, S. Sur, L. Pan, J.E. Goldberger, S. Suresh, S. Zhang, et al., Aligned neurite outgrowth and directed cell migration in self-assembled monodomain gels, Biomaterials 35 (2014) 185–195.
[39] C.L. Lau, M. Kovacevic, T.S. Tingleff, J.S. Forsythe, H.S. Cate, D. Merlo, et al., 3D Electrospun scaffolds promote a cytotrophic phenotype of cultured primary astrocytes, J. Neurochem. 130 (2014) 215–226.
[40] J.B. Matson, S.I. Stupp, Self-assembling peptide scaffolds for regenerative medicine, Chem. Commun. 48 (2012) 26–33.
[41] J.D. Tovar, B.M. Rabatic, S.I. Stupp, Conducting polymers confined within bioactive peptide amphiphile nanostructures, Small 3 (2007) 2024–2028.
[42] T.G. Kim, H. Shin, D.W. Lim, Biomimetic scaffolds for tissue engineering, Adv. Funct. Mater. 22 (2012) 2446–2468.
[43] V.N. Modepalli, A.L. Rodriguez, R. Li, S. Pavuluri, K.R. Nicholas, C.J. Barrow, et al., In vitro response to functionalized self-assembled peptide scaffolds for three-dimensional cell culture, Pept. Sci. 102 (2014) 197–205.
[44] A.L. Rodriguez, T.Y. Wang, K.F. Bruggeman, C.C. Horgan, R. Li, R.J. Williams, et al., In vivo assessment of grafted cortical neural progenitor cells and host response to functionalized self-assembling peptide hydrogels and the implications for tissue repair, J. Mater. Chem. B 2 (2014) 7771–7778.
[45] F. Gelain, D. Silva, A. Caprini, F. Taraballi, A. Natalello, O. Villa, et al., BMHP1-derived self-assembling peptides: hierarchically assembled structures with self-healing propensity and potential for tissue engineering applications, ACS Nano 5 (2011) 1845–1859.
[46] K.L. Niece, J.D. Hartgerink, J.J.J.M. Donners, S.I. Stupp, Self-assembly combining two bioactive peptide-amphphile molecules into nanofibers by electrostatic interaction, J. Am. Chem. Soc. 125 (2003) 7146–7147.
[47] L.E. Buerkle, S.J. Rowan, Supramolecular gels formed from multi-component low molecular weight species, Chem. Soc. Rev. 41 (2012) 6089–6102.
[48] J.R. Xavier, T. Thakur, P. Desai, M.K. Jaiswal, N. Sears, E. Cosgriff-Hernandez, et al., Bioactive nanoengineered hydrogels for bone tissue engineering: a growth-factor-free approach, ACS Nano 9 (2015) 3109–3118.
[49] C. Colquhoun, E.R. Draper, E.G. Eden, B.N. Cattoz, K.L. Morris, L. Chen, et al., The effect of self-sorting and co-assembly on the mechanical properties of low molecular weight hydrogels, Nanoscale 6 (2014) 13719–13725.
[50] K.L. Morris, L. Chen, J. Raeburn, O.R. Sellick, P. Cotanda, A. Paul, et al., Chemically programmed self-sorting of gelator networks, Nat. Commun. 4 (2013) 1480.
[51] M. Zhou, A.M. Smith, A.K. Das, N.W. Hodson, R.F. Collins, R.V. Ulijn, et al., Self-assembled peptide-based hydrogels as scaffolds for anchorage-dependent cells, Biomaterials 30 (2009) 2523–2530.
[52] W. Liyanage, B.L. Nilsson, Substituent effects on the self-assembly/coassembly and hydrogelation of phenylalanine derivatives, Langmuir: ACS J. Surf. Colloids 32 (2016) 787–799.
[53] M. Amblard, J.-A. Fehrentz, J. Martinez, G. Subra, Methods and protocols of modern solid phases peptide synthesis, Mol. Biotechnol. 33 (2006) 239–254.
[54] S.R. Kline, Reduction and analysis of SANS and USANS data using IGOR Pro, J. Appl. Crystallogr. 39 (2006) 895–900.
[55] J.G. Curro, K.S. Schweizer, Theory of polymer melts: an integral equation approach, Macromolecules 20 (1987) 1928–1934.
[56] K.S. Schweizer, A. Yethiraj, Polymer reference interaction site model theory: new molecular closures for phase separating fluids and alloys, J. Chem. Phys. 98 (1993) 9053.
[57] N. Stupka, C. Kintakas, J.D. White, F.W. Fraser, M. Hanciu, N. Aramaki-Hattori, et al., Versican processing by a disintegrin-like and metalloproteinase domain with thrombospondin-1 repeats proteinases-5 and -15 facilitates myoblast fusion, J. Biol. Chem. 288 (2013) 1907–1917.
[58] J. Raeburn, D.J. Adams, Multicomponent low molecular weight gelators, ChemComm 51 (2015) 5170–5180.
[59] A. Wu, L. Isaacs, Self-sorting: the exception or the rule?, J Am. Chem. Soc. 125 (2003) 4831–4835.
[60] J.A. Foster, R.M. Edkins, G.J. Cameron, N. Colgin, K. Fucke, S. Ridgeway, et al., Blending gelators to tune gel structure and probe anion-induced disassembly, Chemistry 20 (2014) 279–291.
[61] J. Raeburn, A. Zamith Cardoso, D.J. Adams, The importance of the self-assembly process to control mechanical properties of low molecular weight hydrogels, Chem. Soc. Rev. 42 (2013) 5143–5156.
[62] K. Saha, A.J. Keung, E.F. Irwin, Y. Li, L. Little, D.V. Schaffer, et al., Substrate modulus directs neural stem cell behavior, Biophys. J. 95 (2008) 4426–4438.
[63] R. Li, C.C. Horgan, B. Long, A.L. Rodriguez, L. Mather, C.J. Barrow, et al., Tuning the mechanical and morphological properties of self-assembled peptide hydrogels via control over the gelation mechanism through regulation of ionic strength and the rate of pH change, RSC Adv. 5 (2015) 301–307.
[64] K.M. Eckes, X. Mu, M.A. Ruehle, P. Ren, L.J. Suggs, beta sheets not required: combined experimental and computational studies of self-assembly and gelation of the ester-containing analogue of an Fmoc-dipeptide hydrogelator, Langmuir: ACS J. Surf. Colloids 30 (2014) 5287–5296.
[65] E. Charney, H. Ziffer, U. Weiss, Optical activity of non-planar conjugated dienes-II transoid dienes, Tetrahedron 21 (1965) 3121–3126.
[66] W. Gaffield, Circular dichroism, optical rotary dispersion and absolute configuration of flavanones, 3-hydroxyflavanones and their glycosides, Tetrahedron 26 (1970) 4093–4108.
[67] L. Velluz, M. Legrand, M. Grosjean, Optical Circular Dichroism, Academic Press, 1965.
[68] C.L. Pizzey, W.C. Pomerantz, B.J. Sung, V.M. Yuwono, S.H. Gellman, J.D. Hartgerink, et al., Characterization of nanofibers formed by self-assembly of

beta-peptide oligomers using small angle X-ray scattering, J. Chem. Phys. 129 (2008) 095103.
[69] Y.M. Abul-Haija, S. Roy, P.W.J.M. Frederix, N. Javid, V. Jayawarna, R.V. Ulijn, Biocatalytically triggered co-assembly of two-component core/shell nanofibers, Small 5 (2014) 973–979.
[70] N.U. Nguyen, H.V. Wang, Dual roles of palladin protein in in vitro myogenesis: inhibition of early induction but promotion of myotube maturation, PLoS ONE 10 (2015) e0124762.
[71] K.J. Wilschut, H.P. Haagsman, B.A. Roelen, Extracellular matrix components direct porcine muscle stem cell behavior, Exp. Cell Res. 316 (2010) 341–352.
[72] R. Vaz, G.G. Martins, S. Thorsteinsdottir, G. Rodrigues, Fibronectin promotes migration, alignment and fusion in an in vitro myoblast cell model, Cell Tissue Res. 348 (2012) 569–578.